UNIVERSITÀ
DEGLI STUDI
DI PADOVA

Sede Amministrativa: Università degli Studi di Padova

Dipartimento di
Scienze Chimiche

CORSO DI DOTTORATO DI RICERCA IN: Scienze Molecolari
CURRICOLO: Chimica
CICLO XXXVI

Computational studies of complex fluid phases and polymeric membranes based on ionic liquid crystals

Tesi redatta con il contributo finanziario del CNR-DSCTM, CNR-ITM, Università degli studi di Padova

Coordinatore: Prof. Stefano Corni
Supervisore: dr. Giacomo Saielli
Co-Supervisore:dr. Alberto Figoli

Dottorando :Valerio Mazzilli

Computational studies of complex fluid phases and polymeric membranes based on ionic liquid crystals

Table of Contents

Introduction

In recent years, molecular simulations have emerged as a powerful tool for unraveling the intricate behaviors of complex molecular systems, shedding light on fundamental phenomena at the nanoscale. This thesis delves into the world of molecular simulations, exploring two fields: the molecular dynamics (MD) simulations of both atomic and coarse grained systems with increasing levels of complexity and the evaluation of NMR properties of heavy nuclei, like ^{129}Xe and ^{125}Te by means of relativistic Density Functioal Theory (DFT). The MD simulations performed were carried out to evaluate the goodness of the model employed in the reproduction of the macroscopic and experimental quantities, while the study of spectroscopic NMR properties is employed to assess the effectiveness of ^{129}Xe as a probe for different classes of substances. The objective of this work is the study of a specific class of materials: ionic liquid crystals, whose field of applications has grown broader in the past two decades[1]. Ionic liquid crystals (ILCs) are materials that share both the properties of ionic liquids (ILs), made of two distinct charged molecular entities, and the features of liquid crystals(LCs), which are materials capable of organizing themselves into ordered phases. The class of ILCs possess peculiar properties that are directly related to their double nature and the most interessant features are linked to the formation of anisotropic phases made of ionic channels employed in different field of technology such as membrane for separations, both gaseous and liquid, membranes for ions conduction and as optoelectronic materials[1]. The fundamental units of ILCs are made of two distinct molecular pairs: a cation and an anion, that provide the material with a ionic nature. Moreover, a large lipophilic moiety is usually found in the chemical structure of the ionic pair, this ensures the formation of an ordered phase, due to lipophilic interactions, that gives to the material the liquid crystal nature. The structures formed by the ILCs are directly linked to the subtle balance of electrostatic interactions and lipophilic interactions. These two interactions play a crucial role as the driving force in the formation of a phase over another. LCs are divided into two main classes: thermotropic and lyotropic, this separation holds also for ILCs. With the first class having a phase transition as temperature changes and the seconds having a phase transition as the concentration of the species changes, the focus of this thesis is on the behaviour of thermotropic LCs and ILCs. In addition to the study of ILCs materials, the parallel study of NMR spectroscopic properties of ^{129}Xe is investigated in different matrices.

Since ILCs have a broad range of applications, we have selected a subclass of ILCs that are employed as ion exclusion membranes for treatment of seawater to produce clean water. In order to achieve the objective set it was necessary to obtain the proper expertise and knowledge in the modeling and simulations of systems of increasing complexity. Starting from the simulations of systems composed of linear alkanes with increasing chain length, passing through the simulation of imidazolium based ILs, coarse grained simulations of discotic liquid crystals and charged discotic liquid crystals, the behaviour is evaluated for all these systems giving a special attention to the reproduction of experimental quantities and the discerning of phenomena that concur to the instauration of an ordered phase in charged systems composed of ionic pairs. ^{129}Xe NMR properties inside different media are evaluated for a slightly different class of materials: starting from xenon dissolved in simple linear alkanes, passing through the class of xenon in different dihalomethanes and ending with the xenon in a polymeric matrix, the effectiveness of ^{129}Xe employed as a molecular probe is tested.

The ILCs, objective of this study, whose complete informations are reported in the Gallic Acid Derivatives section , are composed of self assembling units that form disks that organize themselves into columnar hexagonal phases or gyroid phases[2] as the temperature changes by stacking multiple disks in different fashions. ILCs units studied are based on the ammonium derivatives of Gallic Acid, as cations, and tetrafluoroborate, [BF_4], as anions. Even though other cation-anion pairs exist, and produce different phase behaviour, we limited our

research to the one having [BF_4] as anion. Subtle changes in the cations structures produce relevant changes in the phase explored by the system, giving a broad featurization and applicability of the formed phases in different fields[3] [1]. This study focuses on the simulation of three different ammonium derivatives of the cation to search for structural and dynamical differences at the molecular level to be linked with the differences in the macroscopic ordering of the material. Moreover, the mechanism of columnar formation and salt exclusion is still not fully understood and it is an open challenge.

As aforementioned, the study of such complex systems should be investigated step by step by starting with simple systems and then increasing the complexity: therefore, we started with MD simulations of linear alkanes, then halomethanes with Xenon, then mixtures of short and long chain ionic liquids with increasing alkyl content to assess how well macroscopic quantities, like density and density modulations, are reproduced. Thermotropic behaviour of uncharged and charged simple models of discoti LCs are investigated to shed a light on the effect of miscibility of particles with different nature, nematogenic or non nematogenic, and the charged systems are studied to see how the nematogenic properties of the investigated systems change with the introduction of electrostatic interactions.

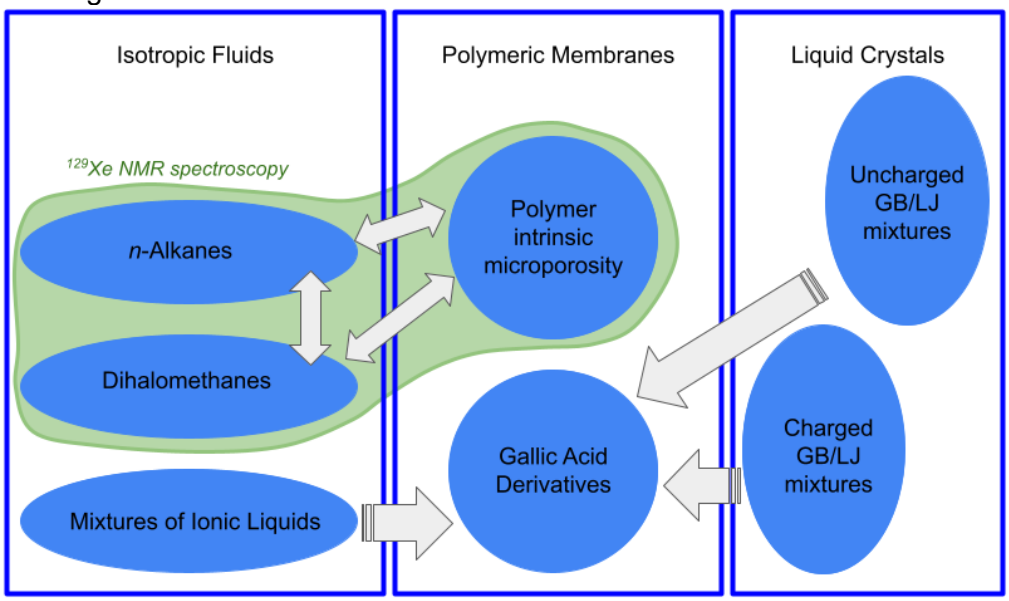

Figure 1 Scheme depicting the systems studied, starting from n-alkanes, dihalomethanes and mixtures of ionic liquids, which are the main fluid phases investigated for their reproduction of experimental quantities, left. In the center the polymeric matrices are depicted. The structural properties are investigated and related to the fluid phases systems, with particular interest in the evaluation of NMR spectroscopic properties, especially for polymer of intrinsic microporosity in relation to the alkanes and dihalomethanes systems. Gallic Acid derivatives systems link together the properties found for liquid crystalline systems and ionic liquids systems, with a behaviour found in both those classes of material

A schematic representation of the investigation topics can be seen in Figure 1. Such systems are also investigated in terms of ^{129}Xe NMR spectroscopy to unveil the relationship between the environment sensed by xenon atoms in the close proximity and the obtained chemical shifts. *n*-alkanes were, also, simulated in search of the right parameters to use for the modellation of long alkyl chains which are present in ILCs of interest and are responsible for the formation of lipophilic domains that act as spacers between the ionic domain inside ILCs. The simulations of ILs are performed to account for the lipophilic effect in the modulation of charged and non charged domains. These modulations are present, also, in the ILCs systems and are responsible for the formation of different phases mainly composed of channels spaced by alkyl domains. The study of uncharged and charged particles, as model for liquid crystalline and non liquid crystalline mixtures and for different ionic liquid crystals stoichiometric mixtures respectively, through coarse grained simulations is inserted in the field

of research of my supervisor [4]–[7]Having yet simulated prolate particles, here the focus is shifted to the simulation of oblate, or discotic, particles. The coronation of all these studies are found in the ILCs systems based on gallic acid derivatives which are the core of this thesis. ^{129}Xe NMR spectroscopic properties were also investigated with an increasing level of complexity of the material studied: starting from the *n*-alkanes systems a protocol that features quantum mechanical calculations based on density functional theory on configurations extracted from molecular dynamics simulations is followed. Changing the nature of the atoms, from all carbons and hydrogens in *n*-alkanes to carbons and halogens in dihalomethanes, the effect on the ^{129}Xe NMR chemical shift is evaluated in such systems which are still simple liquids. The final system on which the protocol for obtaining ^{129}Xe NMR chemical shifts is applied is a polymeric system employed in gas separation membranes.

Apart from the ^{129}Xe NMR properties the NMR properties of ^{125}Te are investigated in a collaboration with Prof. Orian and the PhD student under her supervision, Madabeni A., in a side work focused on the NMR spectroscopic properties of tellurium in different organotellurium halides.

This thesis is organized as follows: in the Section Methods and materials the protocol employed for the different MD simulations will be presented, starting from the *n*-alkanes systems followed by the simulations of different dihalomethanes and ionic liquids passing through polymer of intrinsic microporosity and ending with the ILCs systems made of ammonium gallic acid derivatives. After this first part of all-atom simulations a different section concerning the coarse grained simulation will provide all the relevant information on the uncharged and charged particles simulations used as models for LCs and ILCs. The last part of this section provides the information on the calculation of NMR spectroscopic properties, how the chemical shifts are calculated from extracted clusters and which is the procedure followed. The very last section of the method and material shows how the analyses of the different systems are performed. The Section Results features the results for the ^{129}Xe NMR properties in the beginning, followed by a small paragraph concerning the results obtained from the ^{125}Te NMR spectroscopy. After this part, the results for the imidazolium based ionic liquids and the results for the uncharged and charged coarse grained MD simulations of disks and spheres were reported. In the end, all the results for the ammonium derivatives gallic acid ILCs systems' simulations will be presented. The final chapter summarizes the conclusion of this work.

Methods and materials

In this chapter the methodologies and approaches employed will be discussed. Starting from the description of Molecular Dynamics (MD) principles, the simulated systems will be presented and the parameters used for their simulations will be listed. After this first section on classical mechanics, quantum mechanical methods based on Density Functional Theory (DFT) employed for the calculations of NMR shielding constant will be presented. Special attention on the method for the selection of configurations from MD simulations suitable for DFT calculations will be described. The employed level of theory for each system is, then, indicated. After this first part, where simulations and NMR calculations will be discussed, a different section will be presented in which it is explained how the different analyses were performed. In the end, a summary of the software used and the computational resources employed will be presented

MD simulations

Classical molecular dynamic (MD) simulations are performed on different systems. Both atomistic simulations (AA) and coarse-grained (CG) model potentials are used in this study. In this chapter, the general methodology and the parameters employed in the simulations will be discussed.

The MD simulations are obtained by solving Newton's second law of motion for each of the particles inside the system

$$F_i = m_i \cdot \ddot{r}_i$$

where F_i is the force acting on the *i*-th atoms being in the position r_i with acceleration $\ddot{r}_i$ having mass equal to m_i. The force is calculated as the gradient of the potential acting on each of the particles considered as:

$$F = -\nabla U$$

where U is the potential that is only a function of the atomic positions of the atoms, or particles, within the system. The functional form of U changes depending on the type of simulations that have to be performed. In the majority of cases where an AA MD simulation is intended to carry out, the term U is a sum of terms that are employed to model bonded and non-bonded interactions. The term U represents the total potential energy U_{TOT} and can be written as:

$$U_{TOT} = U_{bonded} + U_{non-bonded}$$

$$U_{TOT} = (U_{bonds} + U_{angle} + U_{dihedrals}) + (U_{LJ} + U_{electrostatic})$$

where U_{bonds} , U_{angle} , $U_{dihedrals}$ make the U_{bonded} part while U_{LJ} and $U_{electrostatic}$ are the $U_{non-bonded}$ part with U_{LJ} being the Lennard-Jones interaction potential and $U_{electrostatic}$ being the electrostatic interaction modeled through Coulomb potential. The non-bonded interactions are modeled through a harmonic potential for the bond and angle terms.The functional form employed in the AA MD simulations of this work is as follows:

$$U_{bonds}(r_{ij}) = \frac{1}{2} k_{ij}^{b} (r_{ij} - b_{ij})^2$$

where r_{ij} is the distance between *i*-th and *j*-th atoms, $k^b{}_{ij}$ is the characteristic spring constant of the harmonic oscillator and b_{ij} is the equilibrium distance;

$$U_{angle}(\theta_{ijk}) = \frac{1}{2}k^{\theta}_{ijk}(\theta_{ijk} - \theta^0_{ijk})^2$$

where θ_{ijk} is the angle formed by the *i*-th, *j*-th and *k*-th atoms, k^{θ}_{ijk} is the characteristic spring constant of the harmonic oscillator and θ^0_{ijk} is the equilibrium angle value. Dihedrals potential account for proper dihedral that models rotations around bonds, so-called torsionals, and improper dihedrals that model the deformations of atoms inside a ring. They are both implemented using Ryckaert-Bellemans potential that is of the form:

$$U_{dihedral}(\phi_{ijkl}) = \sum_{n=0}^{5} C_n(cos(\psi))^n$$

Where $\psi = \phi - 180°$ and C_n are different coefficients. The potential is calculated by the cosine expansion. The calculation of the dihedral potential does not take into account the contribution of the atoms that are less than 2 atoms apart. Only the first and fourth atoms of the dihedral contribute to the potential.

$$U_{LJ} = 4\epsilon_{ij}((\frac{\sigma_{ij}}{r_{ij}})^{12} - (\frac{\sigma_{ij}}{r_{ij}})^{6})$$

Dispersion interactions are calculated using Lennard-Jones potential where ϵ and σ are related to the depth of the potential well and the distance of particles in the minimum. The mixed terms ϵ_{ij} and σ_{ij} are obtained as the geometric average between the ϵ and σ of two self-interacting particles $(\epsilon_{ii}\ , \sigma_{ii}, \epsilon_{jj}\ , \sigma_{jj})$ as follows:

$$\epsilon_{ij} = (\epsilon_{ii}\ \cdot \epsilon_{jj})^{\frac{1}{2}}$$

$$\sigma_{ij} = (\sigma_{ii}\ \cdot \sigma_{jj})^{\frac{1}{2}}$$

Electrostatic interactions are accounted using Coulomb potential using particle-mesh-Ewald formulation as follows:

$$U_{electrostatic} \propto \frac{q_i q_j}{r_{ij}}$$

Where q_i and q_j are the partial charges of the *i*-th and *j*-th atoms respectively being at distance r_{ij}. Both LJ and electrostatic interactions are calculated also intramolecularly between atoms that are at least 3 bonds distant from each other. Interactions between atoms that are exactly 3 bonds apart are scaled by a factor of $\frac{1}{2}$ for both LJ and electrostatic potential. The set of all the functions that make up the potential U_{TOT} and the set of all the parameters (like $k^b{}_{ij}$,$\theta^0{}_{ijk}$, ...,σ_{ij},q_i) are the so-called Force Field (FF). In this work, The AA MD simulations are all carried out using the functional form of U_{TOT} aforementioned, if not stated otherwise, with the parameter employed taken from the OPLS-AA FF with slight variations or specific, yet known in the literature, adjustment. [8] The simulations are performed with the software GROMACS[9]–[11], if not stated otherwise.

All Atoms MD simulations

n-alkanes

Starting with the simplest system studied, a series of *n*-alkanes are simulated at different temperatures. The alkanes in consideration are linear alkanes: *n*-pentane, *n*-hexane, *n*-octane, *n*-decane, *n*-dodecane and *n*-tetradecane. The FF employed in the simulations of these systems is the one called L-OPLS from the work of Böckmann and co-workers.[12]This FF is optimized to reproduce the dynamical and structural properties of linear alkyl chains. In addition to the *n*-alkanes, a Xe atom is dissolved in each of the systems to produce configurations that are used to calculate the ^{129}Xe NMR spectroscopy properties, whose methods will be discussed later (pag. 24). The FF employed for the Xe atom is taken from Ref.[13]. Hereafter the parameters employed for the MD simulations will be presented.
All of the simulations are performed in the isothermal-isobaric ensemble, *NpT*. The integrator used for the equations of motion is leap-frog with a timestep of 1 fs. The cut-off for the LJ and short-range electrostatic interactions was set to 1 nm. Long range electrostatic interactions were handled using particle-mesh-Ewald method with an order of interpolation of 4. Each of the production runs consist of 60 ns and are performed after an equilibration run of 30 ns. The total number of alkanes' molecules in each system is 250. The number of atoms, *N*, varies accordingly to the alkyl chain length. The *n*-pentane system has 4251 atoms, while the *n*-tetradecane system has 11001 atoms. The equilibration runs use the simple Berendsen barostat [14] while the barostat for the production runs is the modified Berendsen barostat (V-rescale) [15] with isotropic coupling and the pressure was set to 1 bar. Different temperatures were simulated starting from low temperature systems and increasing the temperature for small chain alkanes, while longer chain alkanes were simulated at 300 K to sample for a liquid phase. A cubic box and periodic boundary conditions were used. The Table 1 reports the temperature at which each of the systems were simulated. The starting configurations were prepared using the software packmol [16] and the simulations were carried out using the software GROMACS.[9]

n-pentane	180	220	260	285	300	315
n-hexane	180	220	260	285	300	315
n-octane		220	260	285	300	315
n-decane					300	
n-dodecane					300	
n-tetradecane				285	300	

Table 1 Temperature in K of the different simulations performed

Dihalomethanes

Other organic liquids were studied and a set of simulations were performed on different dihalomethanes, CH_2X_2 with X= Cl, Br, I. These systems were simulated with and without Xe. The systems with Xe are employed in the study of ^{129}Xe NMR spectroscopic properties which will be discussed in more detail later (pag. 24). Systems without Xe are employed to check for dynamical and structural properties and in the validation of FF employed by comparing macroscopic quantities, like density or diffusion coefficients, to experimental values. The FF used is based on the OPLS-AA and the parameters were obtained using LigParGen [17], [18] and reported in Table 2. A small change in the FF parameter was operated to reproduce the experimental densities. For this reason, Van der Waals radius of Br and I were adjusted accordingly. The optimized values can be found in Table 2 indicated between parentheses at the corresponding site. Each of the simulated systems is composed of 1000 molecules of CH_2X_2 and an atom of Xe. The initial configurations were prepared using the software packmol and then minimized. The systems were simulated using GROMACS in the *NpT* ensemble with a pressure of 1 bar and at different temperatures. Each of the production runs are 10 ns long and they are preceded by an equilibration run of 5 ns. The integrator used for solving Newton's equations is the leap-frog method. The timestep was set to 1 fs and the cut-off for the LJ and short-range electrostatic interaction was set to 1 nm. Hydrogens are constrained to the equilibrium geometry using LINCS algorithm [19]. A cubic box with periodic boundary conditions was used. The simulated temperatures, reported in Table 3, for each of dihalomethanes studied were chosen to be in the range of temperatures whose data of density can be found in literature.

Molecule	Site	σ [nm]	ϵ [kJ/mol]	q [e]
CH_2Cl_2	Cl	0.3400	1.25520	−0.130
	C	0.3500	0.27614	−0.028
	H	0.2500	0.12552	0.144
CH_2Br_2	Br	0.3470 (0.35764)	1.96648	−0.160
	C	0.3500	0.27614	−0.081
	H	0.2500	0.12552	0.161
CH_2I_2	I	0.3550 (0.37914)	2.42672	−0.075
	C	0.3500	0.27614	−0.166
	H	0.2500	0.12552	0.158
	Xe	0.3948	1.89405	0.000

Table 2 FF parameter obtained from LigParGen. For the Br and I sites the optimized LJ radius is indicated in parentheses

CH_2Cl_2	250	275	300	
CH_2Br_2	250	275	300	325
CH_2I_2	250	275	300	325

Table 3 Temperature, in K, of the simulations of the different systems studied

Increasing the complexity of the studied systems, a series of simulations of imidazolium based ionic liquids with different alkyl chains content were performed. The systems were mixtures of two distinct ILs in different mole fractions. The IL with no alkyl chain is the 1,3-dimethylimidazolium bis(trifluoromethanesulfonyl)imide, $[C_1C_1im][Tf_2N]$, while the IL with a 12 carbon long alkyl chain is 1-dodecyl-3-methylimidazolium bis(trifluoromethanesulfonyl)imide $[C_{12}C_1im][Tf_2N]$. Hereafter, named C_1 and C_{12}, respectively, for simplicity. Their structural formulas are reported in Figure 2 where C_{12} is reported on the top and C_1 on the bottom alongside with the shared anion Tf_2N, sometimes called bistriflimide.

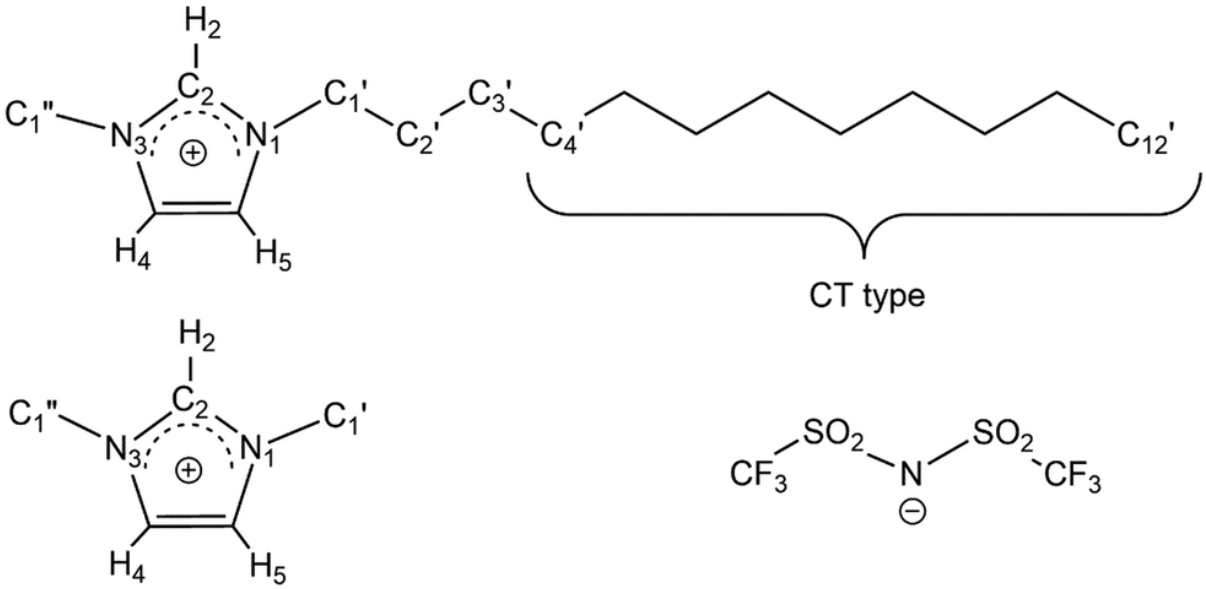

Figure 2 Structural formulas of C_{12}, top, C_1, bottom left, and anion Tf_2N, bottom right with the atoms explicitly indicated. Figure taken from Ref.[20]

The FF employed for the simulation of these systems is the one proposed by Ködderman and co-workers[21], which is a refinement of the FF developed by the group of Canongia Lopes[22] for short-chain imidazolium bistriflimide salts. This FF, even if it is not accounting for polarizability effects, is found to reproduce structural and dynamical properties as well. The parameters for the long alkyl chains are obtained by replicating the methylene parameter for the length of the chains involved. The simulations were carried out using GROMACS and the initial configurations were produced using packmol in large simulation boxes, approx. 14 nm in side length. Different mixtures of C_1 and C_{12}, starting with a C_{12} mole fraction $(\chi_{C_{12}})$ of 0.0 up to 1.0 with a step of 0.1, are simulated. The initial configurations were minimized and then simulated for 5 ns at T=800 K in the *NVT* ensemble. After this first step, 2 ns at T = 700 K, 2 ns at T = 600 K and 2 ns at T = 500 K were simulated in the *NpT* ensemble at *p*=1 atm using the Berendsen thermostat and barostat [14] to let the systems adjust its density. In the end, systems were equilibrated for 20 ns at T= 400 K in the *NpT* ensemble to evaluate the average box size that had to be fixed and employed in the final NVT simulations from which all the quantities were calculated. The runs for the productions were obtained in the *NVT* ensemble at T = 400 K using the leap-frog integrator for the Newton's equations and 1 fs timestep. Each production run consisted of $5x10^7$ steps providing trajectories of 50 ns. Cut-off distances for LJ and short-range electrostatic interactions were set to 1.4 nm. Long-range electrostatic interactions were handled using the particle-mesh-Ewald method with a grid for FFT of 0.16 nm. Simulations were carried out using cubic boxes and periodic boundary conditions. The Table 4 reports the information about the number of molecules $(N_{C_{12}}: N_{C_1})$, the box's side length (L) and the molar fraction of C_{12} $(\chi_{C_{12}})$ in the simulated systems. Systems with the higher content of C_1 have boxes' bigger side length that permit the calculation of the structure factor,

which will be discussed in the Analysis section, up to lower values of the minimum scattering vector q_{min} in the region of interest.

$\chi_{C_{12}}$	$N_{C_{12}}:N_{C_1}$	L [nm]	q_{min} [nm^{-1}]
0.0	3000 : 0	10.9143	1.151
0.1	2250 : 250	10.5338	1.193
0.2	1600 : 400	10.0122	1.255
0.3	1120 : 480	9.5021	1.322
0.4	600 : 400	8.2946	1.515
0.5	500 : 500	8.4570	1.486
0.6	400 : 600	8.6135	1.459
0.7	300 : 700	8.7651	1.434
0.8	200 : 800	8.9105	1.410
0.9	100 : 900	9.0517	1.388
1.0	0 : 1000	9.1886	1.368

Table 4 Relevant information about the simulations of the C_1-C_{12} systems. Bistriflimide anions are equal in number to the sum of C_{12} and C_1 molecules.

Polymer of intrinsic microporosity

The polymeric system studied belongs to the class of polymers of intrinsic microporosity, PIM. The specific PIM, target of this study, is a ethanoanthracene-based PIM synthesized by Tröger's base formation and thus abbreviated as PIM-EA-TB. The structure of the repeating monomer unit is reported in Figure 3**.** To study the effect of Xe and Xe content within the polymer matrix, three different Xe concentrations were employed.

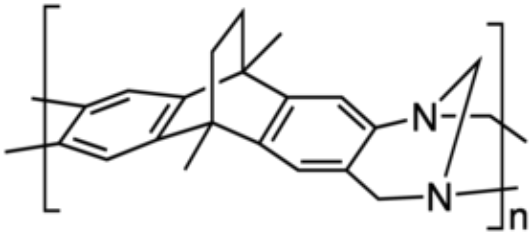

Figure 3 Chemical structure of the monomer of PIM-EA-TB

The simulations are performed using the Material Studio package of Biovia [23] and the COMPASS FF[24] The initial configurations are prepared using the Amorphous Cell module employing 5 polymeric chains composed of 15 repeating units. Theodorou/Suter method [25], [26], as implemented in Amorphous Cell module, was used to built the amorphous polymer packing. Every simulation box contained 400 Xe atoms randomly distributed as obstacles to avoid ring catenations during the chain growth. The packing and equilibration of the chains in the prepared systems follow the protocol in Ref.[27], yet known in literature. The protocol to perform the simulations is similar to the one presented in the work of Jansen and co-workers[28]. To provide a good sampling of regions probed by Xe, 5 independent boxes were built at the same density of 1.02 $\frac{g}{cm^3}$. In each of the different boxes prepared 3 different Xe concentrations were simulated with 1, 3 and 10 Xe atoms dispersed in the box, respectively. The number of atoms in the systems are between 3266 and 3275, depending on the Xe atoms dispersed within the polymer matrix. The simulations are performed at 303 K and 1 atm pressure using 1 fs time step with 4 x 10^6 steps producing 4 ns trajectories for each of the different boxes and Xe concentrations. All the simulations were performed with a 1 fs timestep using the Berendsen barostat and thermostat [14] with a time constant of 0.1 ps. Cubic box with periodic boundary conditions were applied to all three dimensions in all systems. A cut-off distance of 1.25 nm with a spline width of 1 Å was used to treat the van der Waals and the electrostatic interactions using a group based summation method [29]. The analysis and the cluster employed for the ^{129}Xe NMR calculations are obtained sampling the trajectory every 200 ps. The detail of the clusters' extraction will be presented later in the section Computational ^{129Xe} NMR spectroscopy

One of the most complex systems studied in this work are the ionic liquid crystals based on Gallic Acid derivatives. The IL units are composed of cations, which are the gallic acid derivative, and anions, tetrafluoroborate. The structures of the different Gallic Acid derivatives studied are reported in Figure 4.

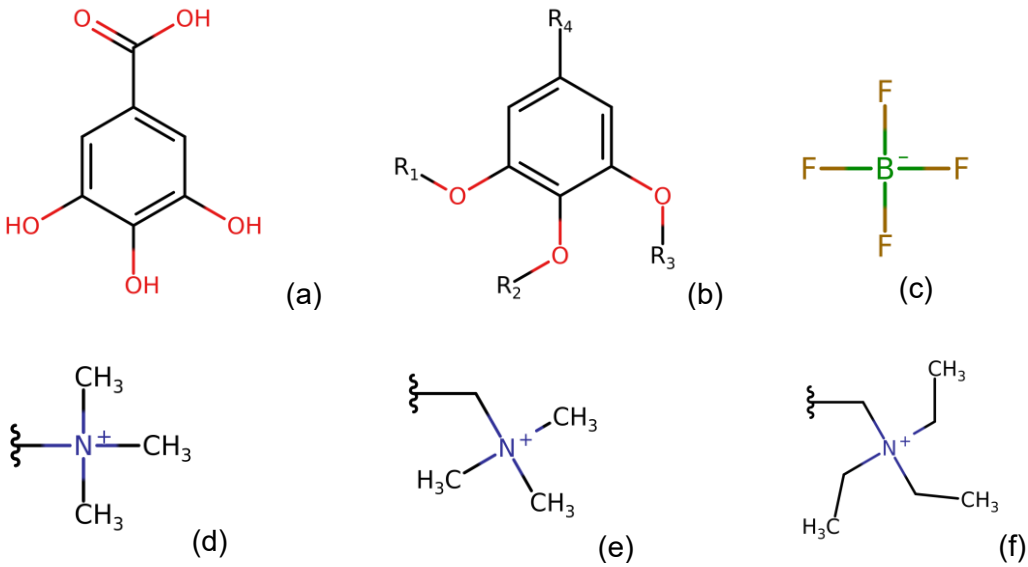

Figure 4 Chemical structure of the gallic acid, (a), structure of the gallic acid derivative unit, (b), with the tetrafluoroborate anion, (c). Together they make the IL units. R_1,R_2 and R_3 are all dodecyl substituents and R4 is one of the substituents reported on the bottom: (d), (e), (f).

The cations, whose structures are reported in Figure 4, are 3,4,5-tris(dodecyloxy)-N,N,N-trimethylbenzenamonium, (d), 3,4,5-tris(dodecyloxy)benzyltrimethylammonium, (e), and 3,4,5-tris(dodecyloxy)benzyltriethylammonium, (f). Their names here are abbreviated, for simplicity, as $PhNMe_3$, $BzNMe_3$ and $BzNEt_3$, respectively. Even though the structures of the cations are similar, their mesomorphic behaviour is very different. This study focuses on reproducing the thermotropic behaviour of the ILCs aggregates. For this reason a series of different simulations were carried out. The simulations are divided into “smaller systems” simulations and “bigger systems” simulations. While smaller systems simulations are employed to assess the goodness of the FF in reproducing the structure and behaviour of liquid crystalline phases, the bigger simulations are performed to enhance the statistic of calculated quantities and to get insight into microstructural and dynamic properties. These materials are self-assembled materials with highly hierarchical ordering effects taking place as the temperature changes, as the typical behaviour of thermotropic liquid crystals. The lower level of ordering is in the cation-anion arrangement as illustrated in Figure 5(a), where 4 cation-anion pairs arrange themselves into a disk-like structure. The disks, then stack on top of each other to form columns. The columns are organized in an hexagonal fashion, as depicted in Figure 5 (b). The phase of interest in this study is the Columnar hexagonal phase (Col_h).

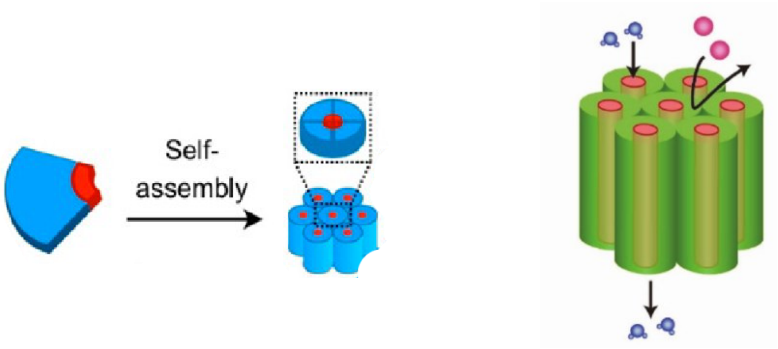

(a) (b)

Figure 5 Self assembly of 4 cation-anion pairs that produces a disk-like structure that stacks with other disks to form columns, (a). Image taken from [30]. *Hexagonal arrangement of the columns showing salt exclusion, (b). Image taken from Ref.*[31]

FF PARAMETERS

The parameters of the FF employed were taken from LigParGen[18]. Nonetheless, care should be exercised regarding the partial charges of the atoms since non-polarizable FF should be properly tuned to reproduce experimental results. For this reason the partial charges on the ring and the ammonium substituent were calculated using a QM approach. The structure used for QM calculations is the one reported in Figure 6 and consists of the Gallic acid unit with a methyl group instead of a dodecyl group as substituent on R1,R2 and R3. R4 are the substituent yet presented in Figure 4(d),(e) and (f).

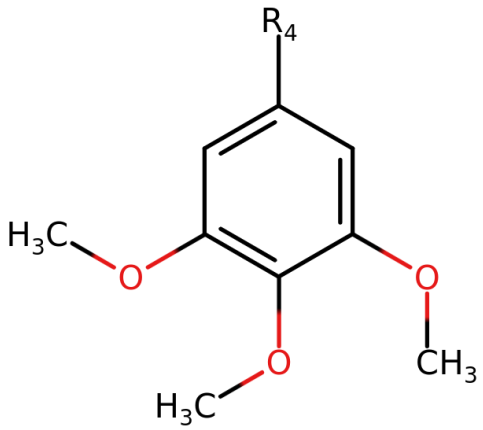

Figure 6 Molecular structure employed for the QM calculations

The protocol used in obtaining the atomic partial charges for these systems is the CHELPG method[32]. The approach consisted in a QM geometry optimization to have an equilibrated structure and then obtain the **CH**arges from **EL**ectrostatic **P**otential using a **G**rid based method, CHELPG. The software employed to perform QM calculations is Gaussian16 [33]. The level of theory for the geometry optimizations is **HF/6-31G(d)** which uses Hartree-Fock method and **6-31G(d)** basis set [34], [35], while the level of theory for the the charge determination through CHELPG uses Møller-Plesset expansion method truncated at second order, **MP2** [36]–[40], with the the triple-zeta Dunning's correlation consisten basis set [41], [42] ,**cc-pVTZ(-f)**.

INITIAL CONFIGURATIONS

Once the charges are obtained, a series of MD simulations on the smaller system could be ready to be performed. Nonetheless, the ordered system (Col_h) is taken as initial configurations to assess the melting of the ordered phase as the temperature is increased. Initial configurations are prepared as follows:

- building the discotic unit by assembling 4 cation-anion pairs, Figure 7(a)
- stack disks on top of each other with staggered units of Gallic Acid and anions Figure 7(b), forming a column Figure 7(c)
- arrange the columns in an hexagonal fashion Figure 7(d)

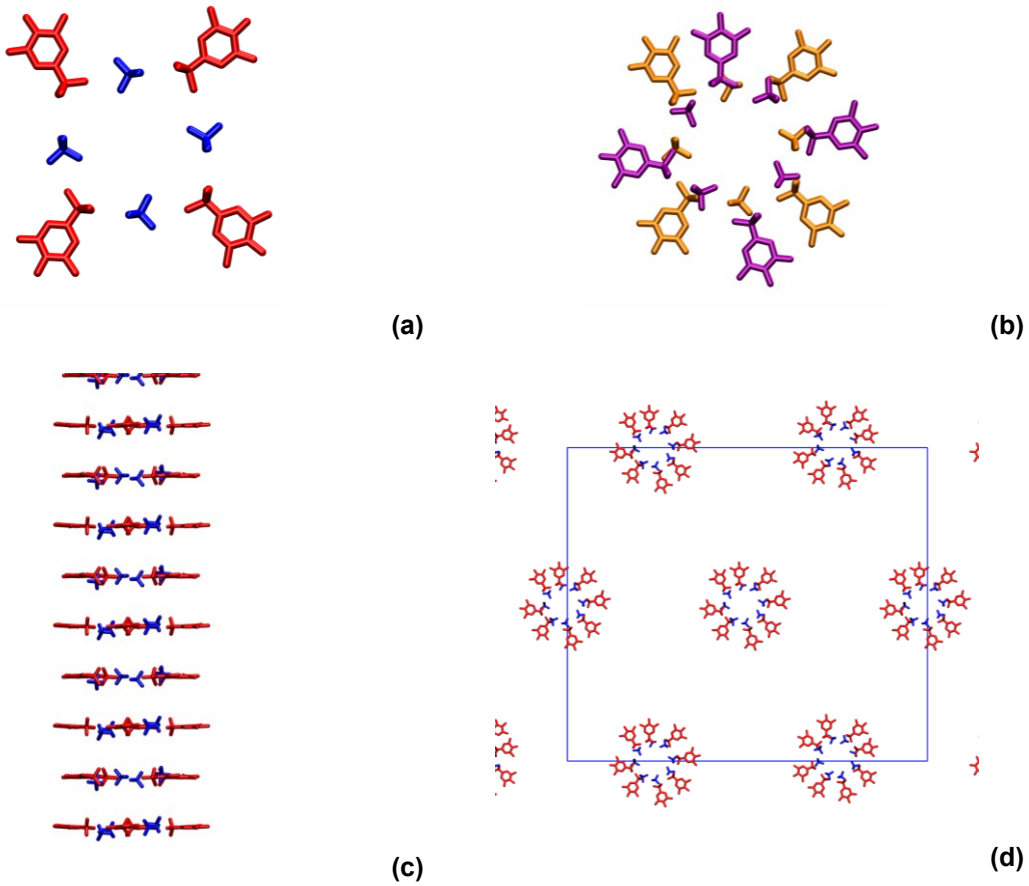

Figure 7 Discotic unit composed of 4 gallic acid derivatives, $PhNMe_3$, and 4 tetrafluoroborate anions, (a), respectively represented as red and blue sticks. Two discotic units stacked one on top of the other, (b), with the orange unit being below the purple one. Multiple stacked disks forming the column, (c), with the same color code of (a). Hexagonal arrangement of the columns seen from above with the simulation box indicated as blue line and with the closest periodic images represented, (d). All these images do not report the alkyl chains for simplicity.

It is important to stress that all the simulations were performed in a rectangular box whose dimensions in the plane perpendicular to the column direction are in the ratio of $1:\frac{2}{\sqrt{3}}$ to reproduce the hexagonal ordering. It is also noteworthy to say that for the building of the columns 20 disks are stacked for each of the columns built. The axis of the columns is along the *z*-direction and Figure 7(d) shows the XY plane. The minimum image of the box contains 4 columns.

SMALLER SYSTEMS' SIMULATIONS

Once the initial configurations were prepared a minimization was performed for each of the systems presented. After the minimization a series of short *NpT* simulations were carried out to properly equilibrate the system. The short *NpT* simulations were performed to relax the structure and have proper starting configurations. The timestep was set to 1 fs and the leap-frog algorithm was employed to solve Newton's equations with a 500000 steps trajectory for a total of 0.5 ns. The temperature was set to 200 K and the pressure to 15 bar to prevent the structure from being destroyed. The cut-of radii were set to 1 nm for both the van der Waals and electrostatic short range interactions. Particle mesh Ewald were employed to account for long-range electrostatic interactions. Berendsen thermostat and barostat were employed. Semi-isotropic coupling was employed to couple the fluctuations of the XY plane and decouple it from the Z direction fluctuations. Five subsequent relaxation runs were carried out before obtaining the initial configurations.

The simulations of dynamical and structural properties of ILs are often related to polarization effects. Nonetheless, the inclusion of polarizability effects in the simulations has the drawback of increasing the simulation's time. A common workaround is to scale the partial atomic charge by a scaling factor. Here we also used two sets of charges for the ILs constituents: the full charge and the scaled charge. A common scaling factor employed for these systems is 0.8 and thanks to a recent work [43], where they studied the $BzNEt_3$ system, we found that they had used 0.831 as scaling factor for charges. For this reason two sets of simulations were performed for each of the ILCs taken in exams. The main goal is to reproduce the transition temperature from the ordered phase to the isotropic phase.

Having the starting configurations ready, a series of simulations with increasing temperatures are carried out. Starting from 300 K and increasing the temperature in steps of 50 K the systems were brought up to 600 K, temperature at which the systems are found to be in a disordered isotropic phase. Each of the simulations uses the leap-frog integrator with 1 fs time step and 10^8 steps producing trajectories of 100 ns of which the last 50 ns are used for the analysis. They are simulated in the *NpT* ensemble with 1 bar pressure with semi isotropic coupling in the XY plane and Berendsen barostat. Cut-off for van der Waals and electrostatic interactions were set to 1.4 nm. Long range electrostatic interactions were handled using particle mesh Ewals method with an order of interpolation of 4 and 0.16 nm as the dimension of Fourier grid. Three dimensional periodic boundary conditions are applied and the number of atoms inside the simulation box are in the order of 45 thousands. Stretching of hydrogens was constrained using the LINCS algorithm. The analyses were performed sampling the trajectory every 100 ps. After the heating runs a series of analyses are performed to assess the existence of an ordered phase. Radial pair distribution function, diffusion coefficient and orientational order parameter $\langle P_2 \rangle$, illustrated in detail in the Analysis section, were employed for the phase assignment.

As will be illustrated in the Results section the rescaling of the charges by a factor of approximatively 0.8 [43] is found to be a suitable method to reproduce the experimental evidence and for this reason the FFs featuring the full charges are rejected and just the FF with the scale charge are adopted for all the remaining simulations. After the systems are in an high temperature isotropic state, they are brought back to the ambient temperature with temperature steps of 25 K using the same parameters aforementioned for the simulations.

BIGGER SYSTEMS' SIMULATIONS

Using the configurations obtained at 400 K in heating, bigger systems are built replicating the box 4 times in the XY plane resulting in initial configurations with 16 columns that appear as Figure 8. These bigger boxes are equilibrated for 100 ns at 400 K using the same parameters mentioned for the MD simulations of these systems. Once the bigger boxes are properly equilibrated different systems were built having the mentioned equilibrated configurations as starting points. The effect of a different anion other than BF_4 is evaluated by replacing the tetrafluoroborate molecules with chloride anions, whose FF parameters are taken from Ref [44], changing its partial charge by multiplying the scaling factor of 0.831. Apart from using another anion the effect of water addition is also evaluated for both the systems with Cl and BF_4. Different concentrations of water are added inside the ionic channels to probe the effect of channels' hydration and water dynamics. The FF parameters for the water are taken from the standard OPLS-AA [8]. The tip3p model is used and the charges are not rescaled. Substitution of BF_4 with Cl and addition of water molecules are obtained with the GROMACS' built-in function "insert-molecules".

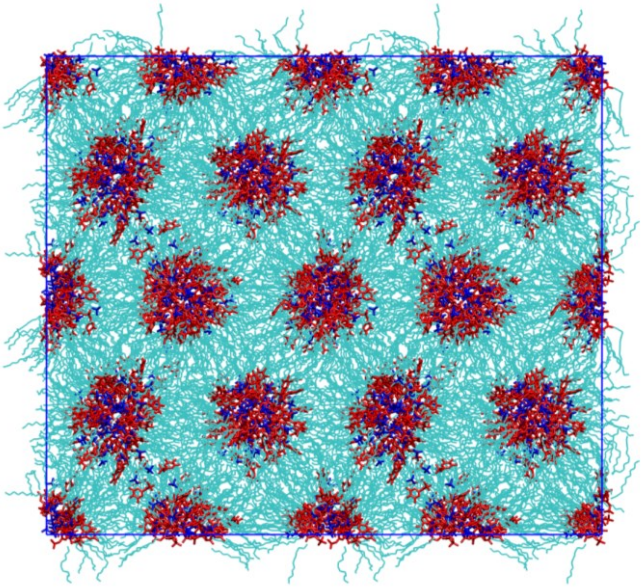

Figure 8 Box containing 16 columns of the extended systems. Anions are represented in blue, aromatic rings with the trimethylammonium moieties are represented in red and dodecyl chains are represented in cyan

The hydrated systems have a fixed number of molecules inside them and during this work will be referred as having fixed water concentrations even though the simulations are in *NpT* ensemble and the volume of the box changes, producing fluctuations in the concentrations. After the preparation of the initial configurations with just Cl, with BF_4 and water and with Cl and water, they are equilibrated with three *NpT* runs at 400 K and 1 bar with a time step of 0.01 fs for 500000 step followed by another run with a longer time step of 0.1 fs and the same number of steps and a third run with the timestep of 1 fs and number of steps equal to 5×10^7. After these equilibration runs, production runs are performed using 1 fs as a time step with 5×10^7 steps. The other parameters are invariant and are set to the ones previously reported. The systems with different water concentrations are indicated with the concentration of water. They are referred to as 0.39 M, 1.15 M and 3.32 M and have 455, 1340 and 3870 water molecules, respectively. To probe the behaviour of studied systems as a function of temperature a series of simulations, starting from 400 K, are performed. The temperature is decreased in steps of 20 K until 360 K is reached. Each temperature consists of 20 ns of equilibration and 20 ns of production with 1 fs as timestep. Other parameters are the same as for the aforementioned systems.

MEMBRANE MODEL

As the most complex system simulated, the model of a membrane was built using only the $BzNMe_3$ and BF_4 pairs as ILC. The initial configuration was built using the channels obtained from the simulations of smaller systems at 400 K as the central slab. Two layers of water are added on top and below the membrane. The representation of the system is reported in Figure 9. The height of the $BzNMe_3$ and BF_4 is about 8 nm while the water region height is 3 nm above and 3 nm below the central slab. The water molecules are 11480 and two systems, with different salts, were built. NaCl and $MgSO_4$ are the salts studied since they are the major component of the marine water and the target ions in water desalination membranes. The concentration of the ions in the water region is set to 0.5 M for both the salts tested and 104 ionic pairs of salt are randomly dispersed inside the water. Na, Mg and Cl ions use the standard OPLS parameters, while SO_4 parameters are taken from[45]. All the partial atomic charges of the ions are scaled by a factor of 0.831.

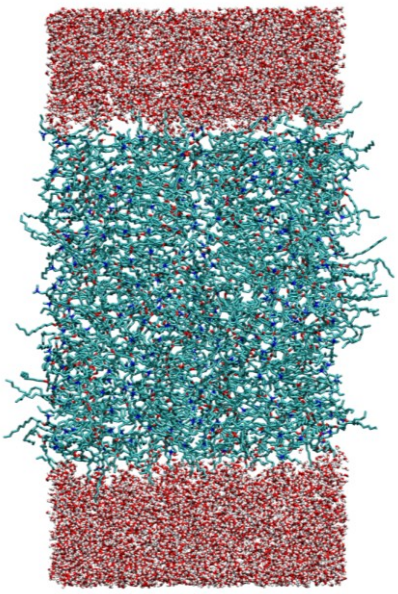

Figure 9 Initial configuration of the membranous system with the $BzNMe_3$ BF_4 ILC in the center and two layers of water above and below.

After the energy minimization, a small run consisting of 10^6 steps of 0.1 fs is carried out in the *NVT* ensemble to relax the structure of the liquid layers of water. To mimic the behaviour of a polymerized matrix the last carbon atoms of the alkyl chains are immobilized in space using the position restraint algorithm which implements an harmonic potential to keep the atoms fixed in place. After the equilibrations, simulations were performed at three different temperatures for the systems with both NaCl and $MgSO_4$ salts. The simulations at different temperatures have the same initial configuration and the simulated temperatures are 300 K, 350 K and 400 K. The integrator for the equation of motion is the leap-frog with 1 fs time step and 5 x 10^8 steps, resulting in 500 ns trajectories sampled every 10 ps. The cut-off for the close-range non bonded interactions was set to 1.4 nm with the particle mesh Ewald method to handle long-range electrostatic interaction with the order of interpolation of 4 and the grid space for fast Fourier transform set to 0.16 nm. The thermostat is the modified Berendsen thermostat, V-rescale[15], and the barostat is Parrinello-Rahman with the pressure of the systems being coupled in the XY plane and the value of pressure set to 1 atm. Three dimensional periodic boundary conditions were employed. LINCS algorithm[19] is used to constrain the bonds of the atoms with hydrogens and save computational time.

Using the membrane's initial configurations, bigger systems were built repeating the box 4 times in the XY plane. For these bigger systems the same parameter aforementioned was used for the simulations and only the temperature T= 350 K and T= 400 K were simulated. Small membranous systems were composed of approximately 80 thousand atoms, while bigger systems are composed of approximately 320 thousand atoms.

Coarse grained simulations of liquid crystals and ionic liquid crystals

To study the thermotropic behaviour of mixtures of nematogenic and non nematogenic particles a series of coarse grained MD simulations were carried out. Model particles for liquid crystals are discotic (an oblate ellipsoid) while non-nematogenic particles are represented as spheres. The aim of the coarse grained simulations performed is to model a system of ionic liquid crystals with oppositely charged particles. For this reason the simulations of the uncharged systems are needed to set a reference to be compared with the charged systems. Classical MD simulations were performed using the Gay-Berne (GB) potential implementation for the disks as described by Bates and Luckhurst [46] and the simple Lennard-Jones potential (LJ) for the spheres. The specific model used in this study, called GBII, features as parameters the four quantities κ, κ', μ, ν and is abbreviated as GB(κ, κ', μ, ν). GB potential is a direction dependent LJ pair potential. The dimensionless parameters determine the shape of the particles and their energy interactions. κ is the ratio of the face-to-face, σ_f, vs. the edge-to-edge contact distance, σ_e ; while the ratio of the face-to-face, ε_f, vs edge-to-edge well depth, ε_e, is the parameter κ'. μ and ν are the exponents in the expression of the energy. In this study the parameter are set to $\kappa = 0.345$, $\kappa' = 5.0$, $\mu = 1$ and $\nu = 2$. The selected parametrization uses an interaction potential which is scaled with respect to σ_0 and shifted with respect to σ_f. Discotic particles have the three diameters σ_e,σ_e,σ_f equal to 1.0, 1.0, 0.345 σ_0 units. Spherical particles have the three diameters all equal to 0.345 σ_0 units. Both particles are treated as special cases of biaxial GB particles with two, for the disks, and three, for the spheres, equal diameters. Mixed interactions between the discotic GB and the spherical LJ particles are handled following the work of Berardi *et al.* [47] as implemented in LAMMPS [48]. Care was exerted on a proper equilibration of the rotational temperature by removing the unphysical rotational degree of freedom [4], [6]. The scaled quantities are defined as follows: scaled potential energy $U^* = \frac{U}{\varepsilon_0}$, scaled distance $r^* = \frac{r}{\sigma_0}$, the scaled volume, $V^* = \frac{V}{\sigma_0^3}$, the scaled number density $\rho^* = \frac{N_{TOT}}{V^*}$, the scaled pressure, $p^* = \frac{p\sigma_0^3}{\varepsilon_0}$, the scaled moment of inertia, $I_\perp{}^* = \frac{I_\perp}{m\sigma_0^2}$, the scaled time, $t^* = \sqrt{\frac{\varepsilon_0}{m{\sigma_0}^2}}\,t$. The packing fractions is defined as $\eta = \frac{NV_m^*}{V^*}$ with $V_m{}^*$ being the scalar molecular volume. The simulations of charged GB-LJ mixtures features also the scaled charge $q^* = \frac{q}{\sqrt{4\pi\epsilon_0\varepsilon_0\sigma_0}}$ where ϵ_0 is the vacuum permittivity. All the aforementioned quantities are scaled with respect to m,ε_0 and $\sigma_0 = \sigma_e$ being the mass, the potential well depth and the contact distance, respectively. All these parameters are set to 1 to reduce the number of variable parameters. While σ_0 is used to scale quantities, σ_f is used to shift the GB potential. The masses of the two particles were also set to 1 since the structural properties and phase behaviour only depends on the space of coordinates and not on the space of momenta. Dynamical properties are not considered. The interaction potential as a function of the scaled distance between pairs of particles approaching edge-to-edge, face-to-face and edge-to-face is reported in Figure 10**.** It is important to note that the LJ-LJ pair, LJLJ, and GB-LJ pair approaching with the GB face side, $GBLJ_f$, have the same energy profile meaning that the interaction between two spheres and between a sphere approaching the face of a disk has the same functional dependence on the scaled distance.

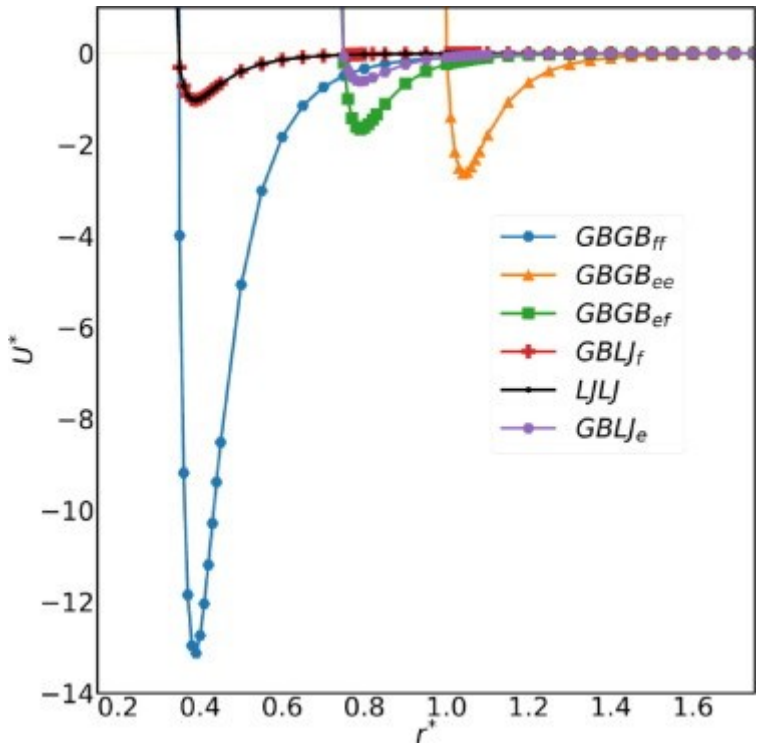

Figure 10 Scaled potential energy, U^*, as a function of scaled distance between particles, r^*. Curves are obtained by calculating the energy using simple configurations with two particles approaching.

MD simulations were run using the LAMMPS software package. All the simulated systems, both uncharged and charged, are simulated at the constant packing fraction $\eta = 0.5023$. Initial configurations were prepared as a high temperature isotropic mixed phase. Simulations were, then, run in cascade from the high temperature down to low temperature and then heated back to high temperature isotropic mixed phase to assess the presence of hysteresis. The simulations were carried out in the *NVT* ensemble using a timestep of 0.0005 scaled units and 10^6 steps for the trajectory productions of each of the temperatures simulated. Systems close to phase transitions employ up to $3\text{x}10^6$ steps. The total number of particles were above 5000 to achieve negligible size effects as reported in previous studies[6]. Cut-off for the van der Waals interactions was set to 1.6 scaled units and the temperature was controlled with a Nosé-Hoover thermostat[49], [50]. Uncharged GB-LJ simulations feature 11 systems with different molar fraction of GB particles, ranging from 0.0 to 1.0. For charged systems the cation:anion (GB:LJ) ratio of 1:2, 1:1 and 2:1 were selected with the values of scaled charge on GB particles changing from 0.5 q^*,1.0 q^* to 2.0 q^*. The correspondig charges of the LJ particles, to guarantee electroneutrality, are set accordingly and their values ranges from -0.35 to -4.0. The values of charges for the different systems studied are reported in Table 6, where the column $q^*_{\mathrm{GB}};q^*_{\mathrm{LJ}}$ reports the different charges combinations. The scaled point charges are at the center of mass of the particles and the close-range electrostatic interactions uses a cut-off of 4 scaled units, while the long-range electrostatic interactions were handled using the particle-particle particle-mesh solver[51] with an accuracy on the forces of 10^{-6} and grid size ranging between 48x48x48 for low charge systems and 144x144x144 for high charged systems. In Table 5 and Table 6 a summary of the simulations for the uncharged and charged systems are reported, respectively.

GB:LJ	N_{GB}:N_{LJ} (N_{TOT})	ρ^*	χ_{GB}
Pure GB	4096:0 (4096)	2.781	1.00
4:1	5324:1331 (6655)	3.375	0.80
3:1	3993:1331 (5324)	3.566	0.75
2:1	4394:2197 (6591)	3.937	0.67
1:1	2744:2744 (5488)	4.970	0.50
4:6	2916:4374 (7290)	5.898	0.40
1:2	2197:4394 (6591)	6.738	0.33
1:3	1331:3993 (5324)	8.196	0.25
1:4	1331:5324 (6655)	9.419	0.20
1:9	1000:9000 (10000)	13.424	0.10

Table 5 Particle ratios, GB:LJ, number of particles, N_{TOT}, scaled density, ρ^*, and GB molar fractions, χ_{GB}, of the uncharged systems studied

GB:LJ	N_{GB}:N_{LJ} (N_{TOT})	ρ^*	q^*_{GB};q^*_{LJ}
1:2	2197:4394 (6591)	6.738	0.5; -0.25
			1.0; -0.5
			2.0; -1
1:1	2744:2744 (5488)	4.970	0.5; -0.5
			1.0; -1.0
			2.0; -2.0
2:1	4394:2197 (6591)	3.937	0.5; -1.0
			1.0; -2.0
			2.0; -4.0

Table 6 Particle ratios, GB:LJ, number of particles, N_{TOT}, scaled density, ρ^*, GB and LJ particles' charge combinations, q^*_{GB};q^*_{LJ}

Computational ^{129}Xe NMR spectroscopy

The NMR spectroscopic properties of ^{129}Xe dispersed in different matrices were evaluated using QM DFT calculations on configurations obtained from classical MD simulations. The protocol followed to obtain the chemical shifts is the same for all the systems studied with a slightly different level of theory adjusted to optimize the computational cost for the QM DFT calculations. The software employed to obtain NMR spectroscopic quantities is ADF [52], [53]. Through QM DFT calculations it is possible to obtain the shielding constant of Xe in different media. The chemical shift value of Xe in a system, $\delta_{Xe@system}$, is obtained as the difference between the shielding constant of Xe in gas phase and the shielding constant of Xe dispersed within the system of interest as:

$$\delta_{Xe@system} = \sigma_{Xe(g)} - \sigma_{Xe@system}$$

Nonetheless, the calculation of the shielding constant of gaseous xenon, taken as the reference, is obtained from the calculation of Xe in vacuum, a purely single-point DFT calculation of an isolated atom, while $\sigma_{Xe@system}$ is obtained from structures generated by classical MD simulations (see below) Therefore, it is, sometimes, better to take into account the shielding constant of Xe dispersed in different media and use it as the reference to calculate the chemical shift in order to have a comparable computational protocol for both the reference and the system. The experimental chemical shifts can then be compared by simply calculating the differences of the experimental chemical shifts of the Xe in the two different media.

The shielding constants are calculated on configurations extracted from the MD trajectory. Since the close proximities of Xe are responsible for the magnetic response, just the closest atoms near the xenon should be included in the DFT calculations. Moreover, the local structure of atoms around Xe is of extreme importance in the calculations of NMR spectroscopic properties due to an external polarization on the Xe electron cloud. For this reason the density of the systems was a crucial parameter to be reproduced in MD simulations in order to have a good representation of the xenon surroundings. Given all that, DFT calculations were performed on the first shell of atoms around Xe. The first shell was obtained by the inspection of the radial distribution functions (RDFs), explained in more detail later in this chapter, between atomic pairs. RDFs are calculated between the Xe and all the non-hydrogen atoms of the system of interest. RDFs usually have a first peak at short distance which indicates the radius of the first shell of atoms around the reference atom, in this case the Xe. The position of the first minimum after the peak was chosen as the distance measure, around the xenon, to select atoms for the cluster needed in the DFT calculations. In Figure 11**(a)** the RDF of Xe and C in liquid hexane is reported with the position of the minimum after the first peak indicated as a horizontal dashed red line.
Figure 11 (b) shows an extracted cluster of Xe@hexane system, Figure 11 (c) shows an example of cluster for the Xe@dihalomethane system. One of the Xe@PIM clusters is reported Figure 11 (d). The cut-off radius employed for the extraction is obtained from the corresponding RDF while Figure 11 it is reported just the RDF of Xe-C pairs for simplicity.

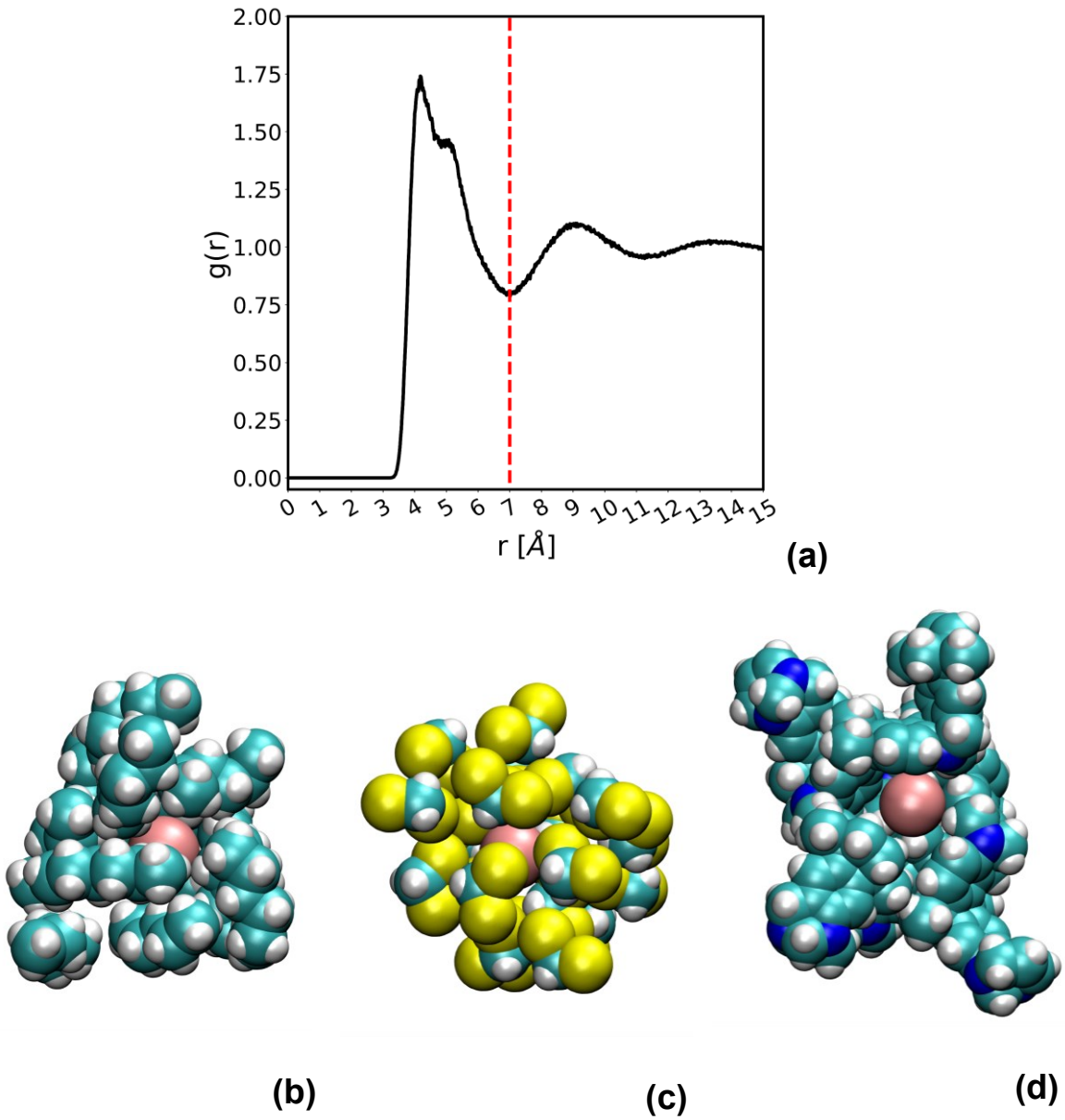

Figure 11 RDF between Xe and C in the hexane system with the minimum after the first peak indicated as a horizontal dashed red line, ***(a)****. Example of one of the clusters extracted from the different systems studied: Xe@n-hexane, Xe@dichloromethane, Xe@PIM;* ***(b), (c), (d)*** *respectively. Xe is represented in pink, C in cyan, N in blue, Cl in yellow and H in white.*

The procedure to extract clusters is based only on geometrical considerations. For each of the studied systems the position of minimum after the first peak is taken as the cut-off radius for the discrimination of atoms belonging to the cluster. If an atom, different from hydrogen, has a distance shorter than the cut-off radius the residue whose atom belongs to is taken as a whole and included into the cluster. For *n*-alkanes and dihalomethanes' systems this procedure is simple and straightforward. For the polymeric system a slightly different strategy on cluster extractions is followed. Since the polymer is made of repeating monomeric units, only the closest units are used for the DFT calculations. As for the simple liquids systems, *n*-alkanes and dihalomethanes, the RDF between Xe with C and Xe with N is used for the determination of the cut-off radius. The units that belong to the cluster are selected. However, monomers are connected to other monomers to form the polymeric chains with bonds between carbons of different monomers. To reduce the number of atoms and, thus, decreasing the time

for DFT calculations, only the monomer having an atom closer than the cut-off radius are selected and the bonds with the missing carbon atoms are replaced with bonds with aromatic hydrogens. In Figure 12 the structure of the monomer is depicted with the hydrogens used as substitutes for the C-C bonds between monomers explicitly indicated.

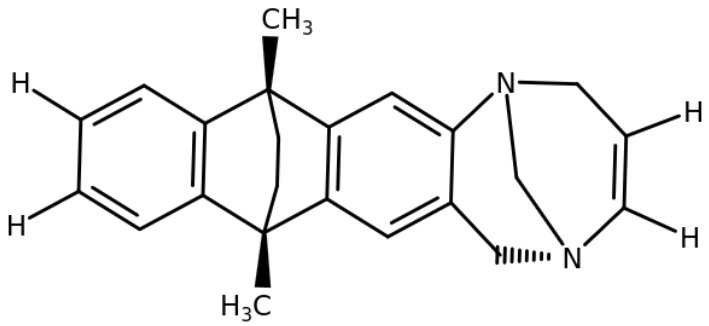

Figure 12 Structure of a monomer of PIM-EA-TB in which the bonds of the carbons with the previous and subsequent units are replaced with bond with aromatic hydrogens, explicitly indicated

Clusters were extracted every 200 ps in the *n*-alkanes systems and in the PIM-EA-TB systems, while for the dihalomethanes systems every 100 ps a cluster was extracted. The cut-off for the cluster extractions were found to be 6.5 Å for dichloromethane and dibromomethane, while diiodomethane had 7 Å. 7 Å is the cut-off radius found also for *n*-alkanes and PIM-EA-TB systems.

Once the clusters were extracted from MD trajectories a series of tests were run on a subset of clusters to choose the right level of theory to calculate the NMR shielding constant bearing in mind that the computational demand is a parameter to take into consideration given that huge number of clusters extracted from MD simulations. The calculation of shielding constant of heavy nuclei is performed using the software ADF with the zeroth order regular approximation (ZORA) to include relativistic effects [54]–[57]. Following the series of work of Saielli and co-workers [58], [59] it is found out that the generalized gradient approximation functional (GGA) BLYP [60]–[63] and the valence quadruple zeta with 4 polarization functions (QZ4P) basis set for Xe atoms are a good compromise between obtained shielding constant and computational time. Since Xe is not covalently bonded with any atoms, NMR properties mainly depend on the description of the Xe and for this reason the Xe atoms will always have the QZ4P basis set representation in this study. The basis sets for the atoms surrounding the Xe are adjusted from system to system. It is well known that hybrid functionals perform much better in the prediction of NMR properties, although being more demanding regarding the computational time. For ^{129}Xe in organic environments BHandHLYP hybrid functional has been found to give results rather close to the CCSD(T) values for model Xe-benzene dimer [64]. We have tested BHandHLYP functionals on some selected configurations of dihalomethanes' systems. The chemical shifts obtained were improved in the right direction and magnitude to have an almost quantitative agreement with experimental data. However, the computational cost was too demanding especially for thousands of clusters with hundreds of atoms inside. The BHandHLYP protocol took between 20 and 100 times the time elapsed for a calculation having the BLYP functional employed.

Different levels of theory were employed for the NMR shielding constant calculations.

For Xe@alkanes systems ZORA BLYP with scalar coupling is employed with a QZ4P basis set for Xe and SZ with the 1s electrons of C and H frozen. For Xe@dihalomethanes ZORA BLYP with spin-orbit coupling is employed with QZ4P basis set for Xe. All electrons TZ2P is used for C and H and 2p, 3p, and 4p frozen core TZ2P is the basis set for Cl, Br and I atoms, respectively. Xe@PIM features QZ4P for Xe and 1s frozen core TZP for C and N.

Computational ^{125}Te NMR spectroscopy of organotellurium halides

During my PhD me and my supervisor collaborated with Prof. Orian and Mr. Andrea Madabeni, the PhD student under her supervision, on the calculation of ^{125}Te NMR chemical shifts in different organotellurium halides. They managed to obtain QM optimized structures of different organohalotellurides. On these structures different levels of theory were employed to obtain the best fitting line for the whole series in search for the best functional that could reproduce the experimental data over a broad range of ppm. The structures of the different Organohalotellurides investigated are reported in Figure 13**.** Organotellurium halides, as the name suggests, features organic molecules bound to Te and one or more bonds between Te and halogen atoms (Cl, Br, I), indicated in Figure 13 as X.

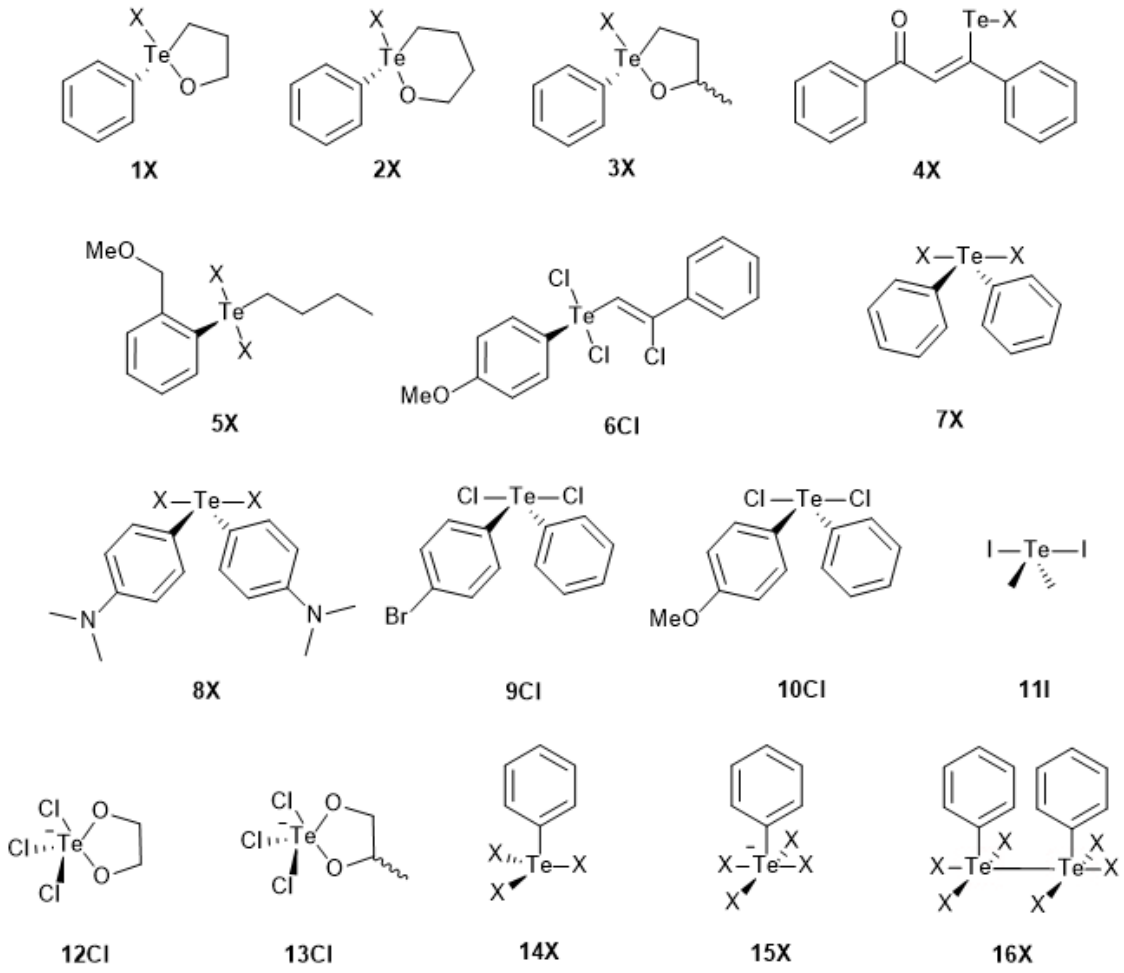

Figure 13 Chemical structures of the different organotellurium halides investigated. Compounds i*X were studied with different halogens, i.e. X=Cl, Br and I based on experimental ^{125}Te NMR chemical shift availability*

All structures shown in Figure 13 were fully optimized using density functional theory (DFT) methods as implemented in Amsterdam Density Functional (ADF) software.[52], [53]. The OPBE functional [65] was employed for the optimization in combination with the zeroth-order regular approximation (ZORA) to take into account scalar relativistic effects, which are mandatory in the presence of heavy nuclei. For a small subset of compounds we also run

optimization using the BLYP-D3(BJ) functional which includes the empirical correction for dispersive interactions. The TZ2P basis set was used for all the elements. It is a large uncontracted triple-ζ quality set of Slater-type orbitals (STOs) and is augmented with two sets of polarization functions on each atom. In addition, core electrons were described with the frozen-core approximation: up to 1s for C, O and Cl, up to 3p for Br and up to 4p for I . This level of theory, denoted **ZORA-OPBE/TZ2P** has already been employed with success in studies of the structural and electronic properties of organochalcogenides with the heavy selenium and tellurium nuclei.[66]. NMR shielding constants of Te nucleus were calculated by using several functionals combined with the all-electron quadruple-ζ quality QZ4P basis set. All NMR calculations include spin orbit-relativistic effects, which were accounted for by using the zeroth-order regular approximation (ZORA). The overall selected level of theory is abbreviated as **SO-ZORA-DFT/QZ4P-ae//ZORA-OPBE/TZ2P**. The NMR shift values presented are calculated as differences between the shielding value of the reference, Me_2Te, and the shielding value of the molecule of interest. The different functionals employed in the calculation of shifts were:
BP86[67], [68], KT1, KT2[69], mPW[70], [71], OPBE[65], BLYP[72]–[75] and SSB-D[76], [77]. The SSB-D and OPBE functionals were also tested with the inclusion of ethanol as implicit solvent. The goodness of the selected level of theory were evaluated using statistical parameters, explained in the Analysis section, obtained from the linear fit of calculated vs. experimental data.

Analysis

In this section the different methodologies and approaches used in the analysis will be discussed in more detail.

The microstructural order of the systems were evaluated using the Radial Distribution Functions between particle pairs, often referred as $g(r)$ or, more generally, to RDFs. This function, also known as pair correlation function, gives the probability density of finding a tagged particle at a certain distance with respect to a reference particle. It is calculated as the increment of tagged particles, dn_t, as the incremental volume containing the particles, dV, is increased. It is written as:

$$g(r) = \frac{dn_t}{dV \cdot \rho}$$

where ρ is the bulk density of the particles calculated over the whole box. In the case of a three dimensional (3D) $g(r)$ the dV quantity is the volume of the different spherical shells around the reference particle and it is calculated as $dV = 4\pi r^2 \cdot dr$. The integration of the $g(r)$ function between $r_1$and r_2 gives the number of particles belonging to the spherical shell determined by r_1 and r_2. The pair correlation function could be calculated not only in three dimensions, but also in two and one dimension. Since some of the studied systems possess anisotropic ordering it will be useful to evaluate such quantities with respect to a certain plane or a certain direction. For this reason two dimensional (2D) $g(r)$ are calculated for the columnar systems of the acid gallic derivatives to assess the existence of columns and to evaluate the dimensions of ionic channels. Moreover, parallel and perpendicular pair correlation functions calculated with respect to the LC phase director, $g(r_\parallel)$ and $g(r_\perp)$ respectively, are evaluated for the coarse grained GBLJ systems. $g(r_\parallel)$ is calculated taking in consideration GB particles in a small cylinder around the reference particle with its axis parallel to the phase director. On the contrary, $g(r_\perp)$ is calculated taking in considerations GB particles in a thin plane perpendicular to the phase director around the reference particle. RDFs are employed in the determination of clusters' radii using the first shell of atoms around Xe as previously illustrated in Computational ^{129}Xe NMR spectroscopy section. The pair correlation functions were calculated in different manners, depending on the systems studied. The 3D RDFs for the *n*-alkanes, dihalomethanes, ILs and gallic acid derivatives systems were calculated using the gmx rdf utility of the analysis suite of the software GROMACS. Also the two dimensional pair correlation functions, employed in the analysis of the gallic acid derivative systems, were calculated using the analysis package of GROMACS[9]. For the GBLJ systems $g(r)$, $g(r_\parallel)$ and $g(r_\perp)$ are calculated using a self-made code written in FORTRAN90.

Even though pair correlation function does not have a direct experimental quantity to be compared with, $g(r)$ could be linked to the structure factor $S(q)$ obtained by x-ray or neutron diffraction experiments. The structure factor gives an indication of the modulations in the density that can be observed in the bulk phase. From the simulations, the structure factor can be calculated using the analysis software TRAVIS[78], [79] starting from the theoretical structure factor $I(q)$ as:

$$I(q) = \sum_{i=1}^{N}\sum_{j=1}^{N} x_i x_j f_i(q) f_j(q) H_{ij}(q)$$

where q is the wavevector modulus, i and j are the indices running over all N atoms in the system, x_i and x_j are the molar fractions of i and j atom types, and $f_i(q)$ and $f_j(q)$ are the atomic scattering factors for atoms i and j . $H_{ij}(q)$ is the partial structure factor between atom types i and j, defined as:

$$H_{ij}(q) = 4\pi\rho_0 \int_0^{r_{max}} r^2 (g_{ij}(r) - 1) \frac{sin(qr)}{qr} dr$$

where $g_{ij}(r)$ is the pair correlation function between i and j atom pairs, r_{max} is the maximum sampled distance for the calculations of $g_{ij}(r)$, always set at less than half of the simulation box length to avoid artifacts due to periodic images, and ρ_0 the atomic number density. The structure factor, $S(q)$, is calculated:

$$S(q) = \frac{I(q)}{(\sum_{j=1}^{N} x_i f_i(q))^2}$$

This method was employed to obtain the structure factor of mixtures ILs and compare it with the experimental quantities. Since the $g_{ij}(r)$ is calculated up to radii equal to half of the simulation box length, the minimum wavevector probed for each system depends on the maximum evaluated distance. For this reason, studied ILs systems with a small content of alkyl chains possess bigger boxes compared to the systems with higher alkyl chains content. Table 4 shows that the systems with 0.0 up to 0.3 molar fraction of C_{12} needed bigger simulation boxes to obtain smaller scattering values as the inferior limit since the region of interest to compare the results with the experimental data lies in the region of wavevector less than 2 $Å^{-1}$

Other structural analysis relies on the evaluation of three different order parameters: The heterogeneity order parameter, the second rank orientational order parameter and the hexatic order parameter. The reduced heterogeneity order parameter, HOP, gives a quantitative measure of the mixing/de-mixing of two types of particles in a mixture. It is defined, by Voth and Wang[80], as:

$$\hat{h} = \frac{1}{N_s} \sum_{i=1}^{N_s} \sum_{j=1}^{N_s} exp(-\frac{{r_{ij}}^2}{2\xi^2})$$

where N_s is the total number of sites, i.e. the number of particles, r_{ij} is the distance between the sites i and j and ξ is equal to $\sqrt[3]{1/\rho}$ with ρ being the number density. The $\hat{h}$ shows finite size effect with its value growing from 1 up to 15.7495 as N_s grows from 1 to 729. Systems with N_s greater than 1728 have their $\hat{h}$ equal to 15.7596. This value is the heterogeneity order parameter for ideal uniform systems, $\hat{h}_0$, and it is taken as reference in the calculation of the reduced heterogeneity order parameter, HOP, as:

$$HOP = \hat{h} - \widehat{h_0}$$

HOP values range between 0, where the system does not segregate particles and the sites are evenly distributed, and values greater than 0, indicating that in the systems there is presence of clustered particles. The analysis of HOP is performed on the uncharged GBLJ system to assess for a demixing process of particles. HOP is also evaluated in the alkyl moieties of ILs systems to search for clustering of lipophilic domains. The analysis is performed using a self-made code written in FORTRAN90.

The second rank orientational order parameter $\langle P_2 \rangle$, is one of the other order parameters evaluated to probe the systems' structure and check for a nematic ordering arising from the systems. $\langle P_2 \rangle$, calculated only for the disks, is obtained as the maximum eigenvalue of the Q tensor defined as:

$$Q_{\alpha\beta} = \langle(\sum_i (3u_\alpha^i u_\beta^i) - \delta_{\alpha\beta})/2\rangle$$

where u_α^i is the projection of the i-th component of the molecular vector onto the α-th laboratory axis, and $\delta_{\alpha\beta}$ is the Kronecker's delta. For GB systems the molecular axis is the one corresponding to the short axis of the disk, while for the gallic acid derivatives the molecular axis is taken as the vector perpendicular to the plane of the aromatic ring. This order parameter gives the information about the orientations of the particles within the system. The value equal to 0 means that no preferred orientation is found in the system and so it is isotropic, while values close to 1 indicate that the system has particles perfectly aligned with a certain vector known as the director.

The last of the order parameters evaluated is the hexatic order parameter $\langle\Psi_6\rangle$. $\langle\Psi_6\rangle$ is calculated as the ensemble average of the particle hexatic order parameter for the i-th disk which is calculated as:

$$\Psi^i{}_6 = \frac{1}{n}\sum_i^n e^{6i\theta}$$

with n being the number of disks in a volume around the particle i and θ is the angle, projected on the plane perpendicular to the director, between the vector connecting particle i with its neighbor and a reference axis. This order parameter has been introduced by Nelson and Halperin[81] for a bidimensional lattice but it can be conveniently adapted to a tridimensional system by taking the volume surrounding the reference particle as a thin cylinder with a thickness and radius slightly larger than the size of a GB disk. In the case of this study 0.35 σ_0 and 1.20 σ_0 have been used for the size parallel and perpendicular to the director, respectively. The analysis of this parameter was employed only for the GBLJ systems to search for an hexagonal arrangement of the disks. The analysis was performed using a self-made code written in FORTRAN90. The order parameters were used to determine the transition temperatures isotropic-to-nematic, $T_{I\to N}$, and nematic-to-columnar, $T_{N\to Col}$, in the GBLJ systems. If no hysteresis is detected at phase transition, the transition temperature is estimated as the average between the two consecutives temperatures where the order parameter jumps from approximately 0 to a significantly larger volume with an error given by half the temperature step. In case where hysteresis could not be removed, that it is for some nematic-to-columnar transitions, we estimated the temperature of the phase transition (T_{PT}^*) as an average between the highest temperature of the heating run, before the transition (T_h^*) and the lowest of the cooling run (T_c^*), also before the transition using equation:

$$T_{PT}^* = T_c^* + T_h^* - \sqrt{T_c^* \cdot T_h^*}$$

as reported by Lindeberg and Patey [82]

Concerning the uncharged GBLJ systems, during the first year of my PhD course I worked on a method to identify the LC and isotropic, ISO, phases in boxes containing GB and LJ particles. I employed the HOP to determine a temperature of demixing, T_{dem}^*, at which the LJ particles segregate to form a phase composed mainly of LJ spheres, called isotropic phase (ISO), and the discotic particles form a liquid crystalline phase composed mainly of GB particles. T_{dem}^* is obtained from the trend of HOP as a function of reduced temperature. When HOP increases the system is found to start the demixing process of particles. Systems above the T_{dem}^* result in uniformly distributed LJ particles, while when the temperature is below T_{dem}^*, HOP parameter increases and two distinct regions in the same box are found: LC and ISO. When two phases are present a mole fraction specific for each phase can be defined as $\chi_\alpha^P = \frac{N_\alpha^P}{N^P}$ where α identifies the GB or LJ particles and P is the phase, either LC or ISO. For example χ_{GB}^{LC} represents the mole fraction of GB particles in the LC phase of a de-mixed two-phases

system. Following this reasoning also the $\langle P_2 \rangle$ parameters could be calculated just for the LC phase. Even though HOP parameters were employed to assess for a demixing process, the particles' belonging to a phase or another was achieved by counting particles around a reference particle and compare that number to average values obtained from the integration of $g(r)$. The two phases, LC and ISO, were quantitatively identified and separated as follows: for each particle, either GB or LJ, in order to decide whether the particle belongs to the GB-rich phase (LC phase) or to the LJ-rich phase (ISO phase), we counted the LJ neighbors within a given threshold distance, r_{TH}, from the reference particle. If this number is lower than a given limit, N_1, the particle is considered to belong to the GB-rich phase; instead, if it is higher than a second limit, N_2, then it is considered to belong to the LJ-rich phase; finally, if the number of LJ particles is included between these two limits above, the particles are taken as part of the interphase. To calculate the two limits, N_1 and N_2, we first evaluate the integral, over $4\pi r^2 dr$ and up to the threshold distance r_{TH} defined above, of the radial distribution function of the distance between two LJ particles at each temperature and for each systems; let us call this value as N_{TH}. After some testing, we observed that a clear identification of the two phases can be generally obtained for all systems and all temperatures by setting r_{TH} equal to 1.5 and the two threshold N_1 and N_2 to 2/5 and 2/3, respectively, of N_{TH}. This procedure allows to clearly identify the two phases in the box as can be appreciated by the inspection of the Figure 14**,** showing a low temperature snapshot of the simulation box of a mixture of non-charged disks and spheres in mole ratio GB:LJ=1:1, alongside the extracted phases, LC and ISO. Also the interphase is shown in the figure.

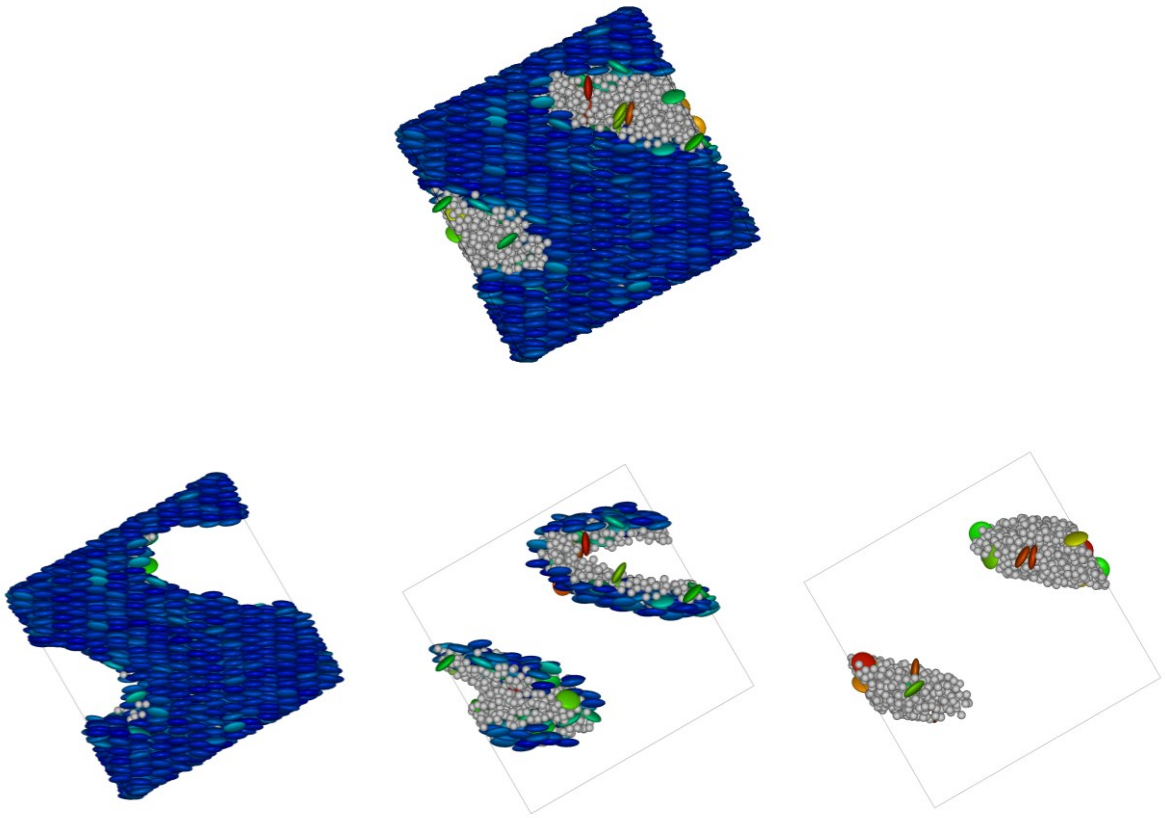

Figure 14 Snapshot of the GB:LJ =1:1 system at $T^* = 2.00$, top, with the LC phase, bottom left, and ISO phase, bottom right, depicted. At the bottom in the center the interphase is shown.

Another structural factor observed, especially in IL systems, is the isoperimetric quotient (IQ), or sphericity, of the lipophilic domains. This dimensionless number, between 0 and 1, measures how spherical a closed surface is in space. This value is calculated using the domain analysis function of the software TRAVIS which implements the radical Voronoi tessellations for the estimation of the domain extent using van der Waal's radii in the construction of Voronoi cells as previously described in the work of Kirchner and coworkers [83] concerning simulations of different IL than the one studied here. The Voronoi domains are composed of multiple sites centered on atom positions and around which a polyhedron is built considering the radius of the different atoms. Voronoi polyhedra, or cells, share faces with neighboring polyhedra. Cells that share a desired common property, i.e. being of a certain atom type, and have a face in common are assigned to a domain. Once the domain is defined the contribution from the different cells could be computed and a value of surface area and volume is obtained permitting the quantification of the isoperimetric quotient as:

$$IQ = (\frac{r_{sph}(V)}{r_{sph}(A)})^6$$

where $r_{sph}(V)$ and $r_{sph}(A)$ are the radii corresponding to an equivalent sphere with a volume V and one with a surface area, A, respectively. The sixth power is employed to obtain integer exponents and IQ simplifies to $36\pi\frac{V^2}{A^2}$ where V and A are the quantities extracted from the domain analysis.

Dynamical properties were evaluated calculating the diffusion coefficient from the linear interpolation of the mean squared displacements (MSDs). MSDs as a function of time of particles of different types are obtained through the function msd of GROMACS. All MSDs were visually inspected and the proper range of fitting was chosen. Moreover, 2D and 1D MSDs were calculated to evaluate the mobility of the ILCs species along the columnar axis or in the plane perpendicular to it. The relation between MSDs and diffusion coefficient is:

$$MSD = 2 \cdot N \cdot D \cdot t$$

where N account for the dimensionality of the MSD, 1 for 1D, 2 for 2D and 3 for isotropic 3D and t is the time. We fitted $MSD(t)$ to obtain the slope of the line and thus the diffusion coefficient D.
Fitted series were evaluated using different statistical parameters, especially in the determination of the best protocol for the ^{125}Te NMR chemical shift calculation. The parameter employed were:
Mean Error, ME

$$ME = \frac{1}{N}\sum_{i}^{N}(y_i^{EXP} - y_i^{CALCD})$$

Mean Absolute Error, MAE

$$MAE = \frac{1}{N}\sum_{i}^{N}(|y_i^{EXP} - y_i^{CALCD}|)$$

with y_i^{EXP} being the *i*-th experimental observation and y_i^{CALCD} the *i*-th calculated one, summed over the N data samples;
Corrected Mean Absolute Error, cMAE

$$cMAE = \frac{1}{N}\sum_{i}^{N}(|f(x_i) - y_i^{CALCD}|)$$

Root Mean Squared Error, RMSE

$$RMSE = \sqrt{\frac{1}{N}\sum_{i}^{N}(f(x_i) - y_i^{CALCD})^2}$$

where $f(x_i)$ is the y_i value obtained from the linear regression fit of the complete data set; and finally the coefficient of determination, R^2

$$R^2 = 1 - \frac{\sum_i^N (f(x_i) - y_i^{CALCD})^2}{\sum_i^N (\bar{y} - y_i^{CALCD})^2}$$

where $\bar{y}$ is the mean value of y_i^{CALCD}.
Here is a summary of the software used and the machines running simulations/calculations.

The simulations were run using the software GROMACS[9]–[11], LAMMPS[84] and MATERIAL STUDIO[23]. NMR calculations were performed using the software ADF [52], [53]. Some of the geometry optimizations and QM calculations were run on Gaussian16[33]. Starting configurations were prepared using the software packmol [16]. The analysis of the different properties of the systems were performed using the software package TRAVIS[78], [79] or built-in functions in GROMACS. Moreover, self-made code for specific analysis is written in FORTRAN90 or Python3. Several python modules were employed for analysis of systems like the standard scientific computing packages Numpy[85], Scipy [86] and a specific modulus for atomic trajectories analysis, MDAnalysis[87], [88]. The images of the AA systems are obtained using the software VMD[89], while the images for the GBLJ systems were obtained using the software QMGA.[90] Other kind of images manipulations are performed using the software GIMP[91].

Simulations and DFT calculations were performed on high performance computing (HPC) facilities. The HPC clusters of the chemical department of the university of Padua, C3P[92], were employed as the main machine for the calculation. Gibbs and Curie clusters were mainly used, with a maximum of 32 cores employed in the calculations of bigger systems. Gibbs' nodes are built with 1 x CPU Intel Xeon 24 Core, 256 GB of RAM, and OS Scientific Linux release 6.6. Curie's nodes implement the GPU acceleration for the calculation of some of the interactions and were mainly used for the MD simulations of AA systems, especially those of Gallic Acid derivatives. Curie's node specifics are 2 x CPU Intel Xeon Gold 5218 (*16 cores*), 192 GB of RAM, 2 x GPU Tesla V100 16 GB of RAM, Infiniband, OS CentOS 6.5. Apart from the HPC of the chemical department, different projects grant access to CINECA's HPC through ISCRA projects. ISCRA projects are divided into two categories: ISCRA C, which grants a modest quantity of computational time, and ISCRA B, which grants a large quantity of computational time. Both project classes give access to top-tier HPC systems and the hours are obtained after winning a call for proposal. I was a collaborator of dr. Saielli in two ISCRA C and one ISCRA B projects, whose reference numbers are HP10CUC24I, HP10CQB2Q7 for the C projects and HP10B8AOVV for the B project. Moreover, I also obtained, as P.I., an ISCRA C project (HP10C0H432). CINCECA's HPC cluster used was MARCONI100 and GALILEO100, using at maximum 1 node of 32 cores and GPU acceleration. GALILEO100, whose specific features can be found at Ref. [93] was employed

mainly for the NMR calculation through ISCRA C projects. MARCONI100 was accessed thanks to ISCRA B project and was employed for the AA MD simulations, the full specifications are reported in the CINECA's dedicated page [94].Finally a part of the simulations of xenon in alkanes and dihalomethanes were run on the Open-Stack based cloud of CloudVeneto [95] permitting the simulations ov virtual machines with adjustable resource allocation

Results

Xe@n-alkanes

During the first year of my PhD journey I simulated systems of different *n*-alkanes. Initially, Two FF were tested and the densities of the systems were evaluated and compared to the experimental results. The two FF tested were AMBER94 [96] and L-OPLS [12]. The densities and diffusion coefficients obtained with AMBER94 FF deviates greatly from the experimental values and for this reason this FF was discarded. On the contrary, the densities obtained from the simulations featuring the L-OPLS FF produce very accurate estimation of the systems' densities. Figure 15 the trend of densities as a function of carbon atoms, thus chain length, is reported for the systems being simulated at 300 K and for the two FF employed.

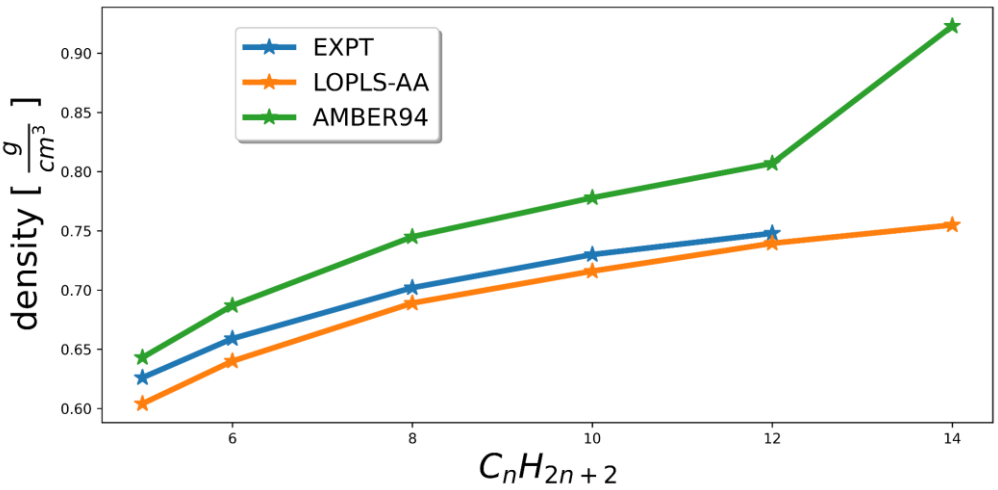

Figure 15 Density as a function of alkyl's chain length for the two FF tested: green for AMBER94 and orange for L-OPLS. Blue curve represents experimental data taken from Ref.[97]

Using the L-OPLS FF three different temperatures were simulated and the densities were compared to the experimental one. Figure 16**(a)** shows the relation between density and chain length for the three temperatures tested. It appears that the deviation of calculated values from the experimental ones was less than 3%. It is important to stress that the L-OPLS FF is a FF built for long alkyl chains, however, the densities of the systems with short chains are reproduced satisfactorily. A work by Cibulka [98] proposed a parametric model that relates the densities of different *n*-alkanes and alkanols with the temperature built using all the data present in literature. The parametric relation is as follows:

$$\rho(T) = \rho_c(1 + \sum_{i=1}^{N} a_i(1 - \frac{T}{T_c})^{\frac{i}{3}})$$

Where ρ_c and T_c are the critical density and critical temperature, respectively, characteristic for each of the different alkanes. Cibulka's model uses the critical densities taken from ESDU international [99] while the critical temperatures are taken from the work of Ambrose and Walton [100]. a_i are different coefficients specific for each of the molecules taken into consideration. The densities obtained from simulations were compared to the densities obtained from Cibulka's model to assess the goodness of the FF employed. The results of comparison between Cibulka's densities and densities obtained from simulations are shown in Figure 16**(b)**

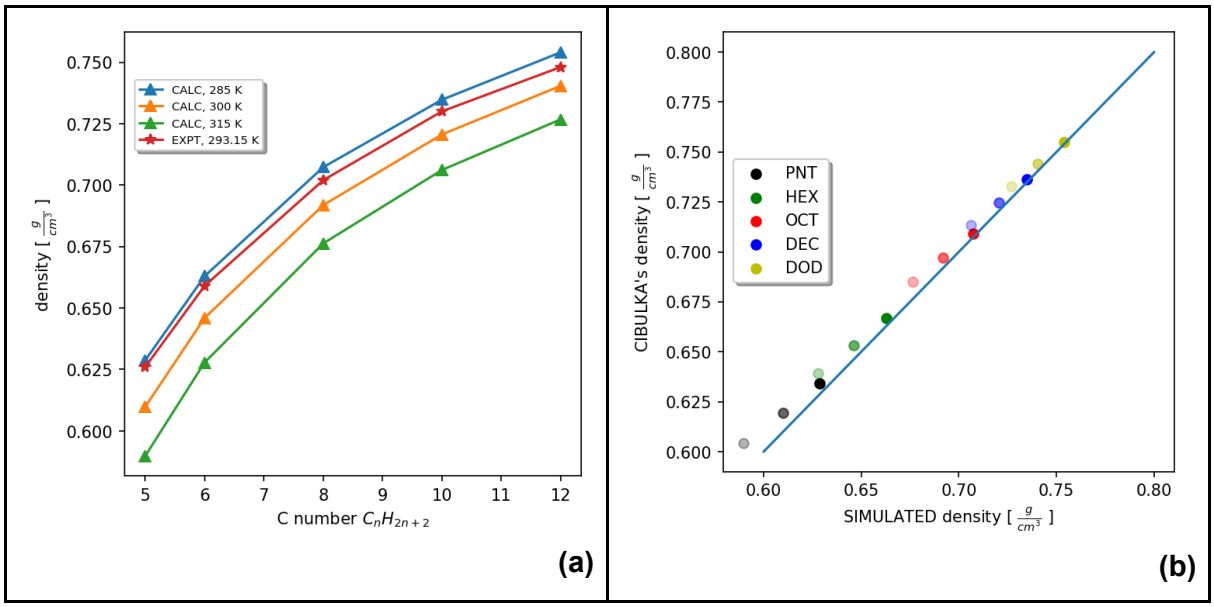

Figure 16 Density as a function of alkyl length for the three different temperatures compared to the experimental values [97] *, measured at 293.15 K,* ***(a)****. The same calculated densities on* ***(a)*** *are reported in* ***(b)*** *and compared with the densities obtained from Cibulka's model. Different alkanes are represented with different colors: the lighter the color the lower the temperature.*

The correlation between simulated densities and Cibulka's densities, Figure 16**(b)**, shows that there is a perfect match of the densities, at 300 K, when regarding longer chains, like dodecane or decane. Smaller systems and systems simulated at lower temperatures possess a slightly lower density than what expected, however the relative errors are lower than 5%. The reproduction of the macroscopic density implicitly suggests that the microstructure of the simulated system is likely to be similar to the real microstructure. The self diffusion coefficients of *n*-alkanes, reported in Table 7, show a pretty accurate representation of the experimental values for MD simulations, with relative error on the calculated quantities ranging from 13% to 28%. The simulated systems appear more viscous than the experiments with the quantities obtained from the simulations being lower than their real counterparts. The values obtained using the AMBER94 FF, omitted here, were way more different than their experimental counterpart producing bigger deviations from the experimental values. This, together with the great deviations in densities, permitted the exclusion of the AMBER94 as an effective FF in the representation of the microstructural and dynamical features of n-alkanes' systems. The coefficients of diffusion were calculated also for the atom of Xe dispersed within the systems of different *n*-alkanes. Table 8 reports the values of calculated diffusion coefficients alongside some of the diffusion coefficients for Xe@*n*-alkanes found in literature. The relative errors on the estimation of the coefficients for octane, decane and tetradecane are 3%, 19% and 13% respectively.

n-alkane	Expt. D x 10^{-9} [m^2/s]	Calcd. D x 10^{-9} [m^2/s]	Ref.
n-pentane	5.45	4.573	[101]
n-hexane	4.25	3.290	[102]
n-octane	2.00	1.738	[101]
n-decane	1.31	0.979	[101]
n-dodecane	0.814	0.630	[103]
n-tetradecane	0.56	0.399	[104]

Table 7 Experimental and calculated self diffusion coefficients of the different n-*alkanes studied alongside the reference of their experimental values*

	Expt. D x 10^{-9} [m^2/s] 303.15 K	Calcd. D x 10^{-9} [m^2/s] 300 K	
Xe@*n*-pentane		7.553	
Xe@*n*-hexane		6.978	
Xe@*n*-octane	5.15	4.977	[105]
Xe@*n*-decane	3.43	2.766	[105]
Xe@*n*-dodecane		1.674	
Xe@*n*-tetradecane	1.90	1.672	[105]

Table 8 Experimental and calculated diffusion coefficients of Xe dispersed within the n-*alkanes systems. The values for octane, decane and tetradecane have their experimental values available in literature*

Once the proper FF was chosen and the simulations run, the extraction of clusters for the DFT calculations was performed following the method of extraction reported in the section Computational ^{129Xe} NMR spectroscopy and using 7 Å as the cut-off radius for the cluster extraction, obtained from radial pair distribution functions between carbon atoms and Xe. The results of the calculated chemical shifts, $\delta_{CALCD.}$, vs. the experimental chemical shifts, $\delta_{EXPT.}$, are reported in the Figure 17. The figure shows the correlation of the calculated and experimental chemical shifts with the green line being the fitted curve and the black line being the line of perfect correlation. Experimental data are taken from Ref. [105].

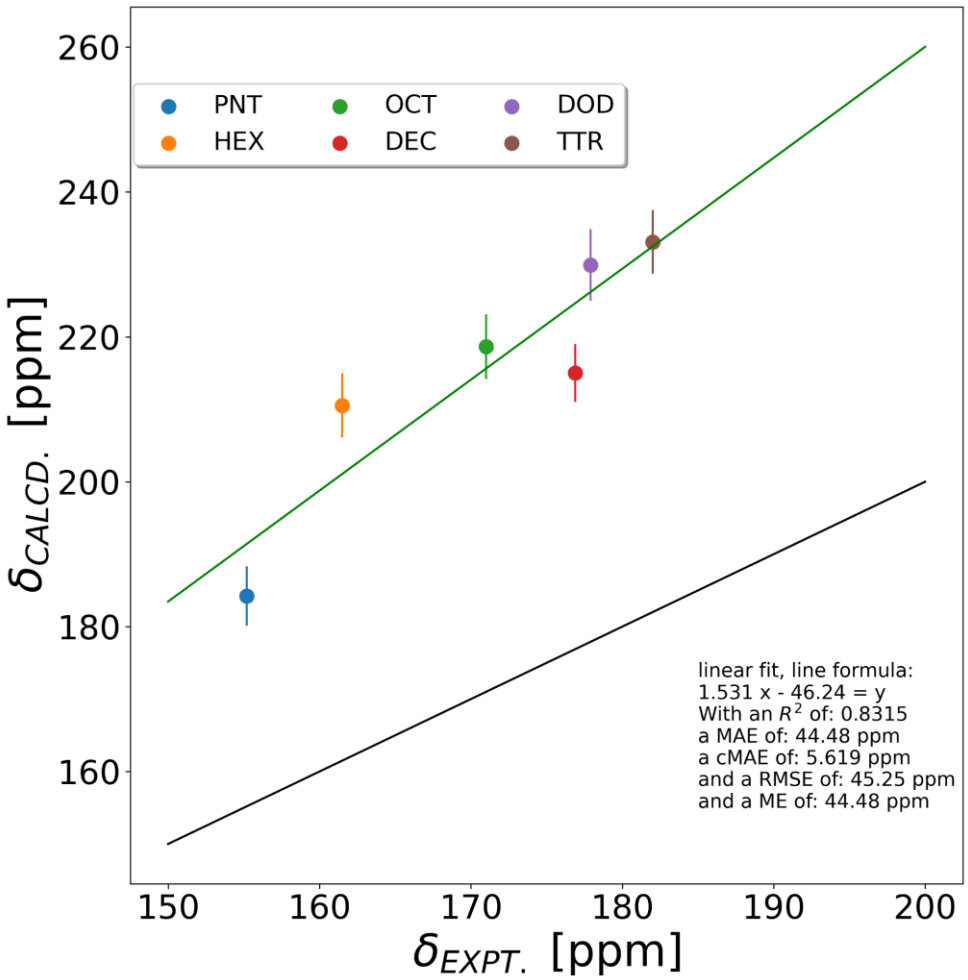

Figure 17. Experimental, x-axis, vs calculated chemical shifts. Statistical parameters of the linear fitting are reported in the bottom right part of the graph. The line for each of the points represents the error on the calculated NMR chemical shift obtained as the error on the average.

The calculated chemical shifts appear to be higher than the experimental counterpart with a deviation of the calculated values of approx. 45 ppm with respect to the experimental. The deviation has been estimated as Mean Error, Mean Absolute Error and Root Mean Squared Error, ME, MAE and RMSE respectively and all these parameters give the value of 45. The evaluation of the chemical shifts as a function of temperature for a subset of alkanes produces similar results. The calculated chemical shifts are higher if compared to the experimental values with approximately 55 ppm of overestimation. The trend of the chemical shifts as a function of temperature are reported in Figure 18**.**

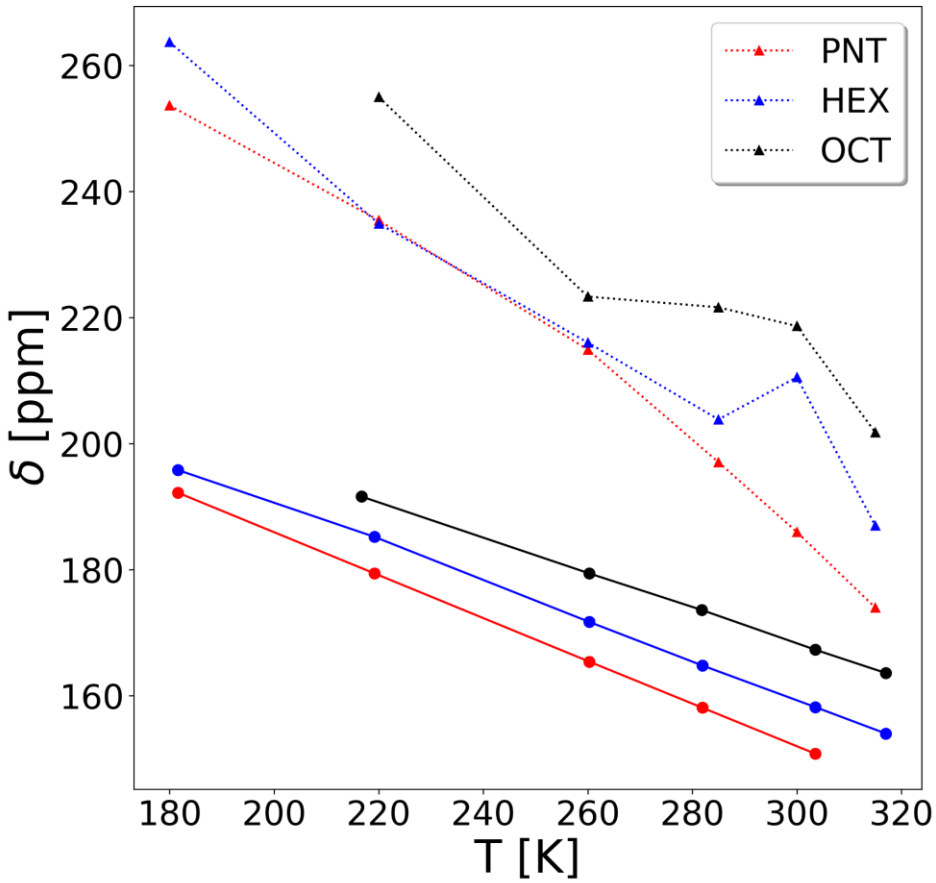

Figure 18 Calculated, triangles, and experimental, circles, chemical shifts as a function of temperature for the n*-pentane,* n*-hexane and* n*-octane. Experimental chemical shifts are taken from Ref.* [106]. *Lines are guides for the eyes*

The calculated chemical shifts obtained from MD configurations appear to give an overestimation even though the densities are correctly reproduced. This holds true also for the other systems presented and studied: Xe@dihalomethanes and Xe@PIM-EA-TB. Taking into consideration the systematic error and using the value of shielding constant obtained for the Xe@hexane as the reference value, the results for the other systems improves and the results could be compared quantitatively with their experimental counterparts.

Xe@dihalomethanes

The study of NMR properties of ^{129}Xe in different dihalomethanes (CH_2X_2 , X=Cl, Br, I) was carried out during my second year and we collaborated with the group of Prof. Castiglione. We published a paper, Ref. [107], of a joint work where they performed experiments and me and dr. Saielli executed MD simulations and DFT calculations. OPLS-AA was used as FF for the simulations. The key parameter used to check for FF goodness was the density of the different dihalomethanes' species. In Figure 19 the densities as a function of temperature are reported, both calculated and experimental.

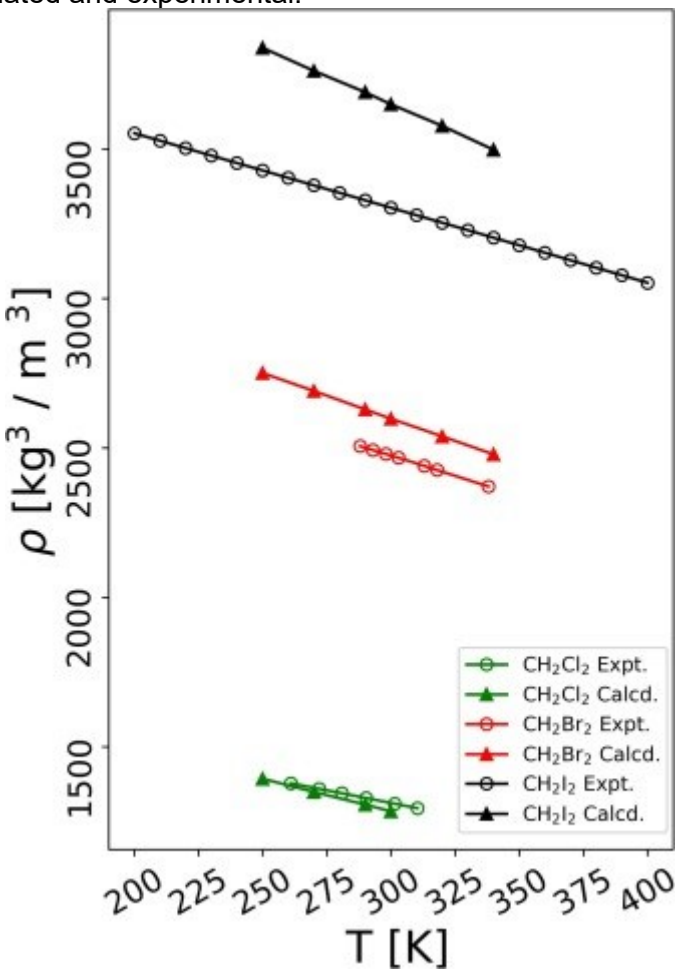

Figure 19 Experimental, empty circles, and calculated, full triangles, densities of the different dihalomehtanes studied as a function of temperatures. Experimental density values of CH_2Cl_2 are taken from the Refs.[108], [109]*, while for CH_2Br_2 and CH_2I_2 the values are taken from Ref.* [110] *and Ref.* [111]*, respectively. Lines are a guide to the eye*

The calculated densities obtained for the CH_2Cl_2, green triangles in Figure 19, almost overlap perfectly to the experimental values, empty green circles, with the discrepancy of calculated-experimental density being less than 2% at 300 K. For dihalomethanes with heavier halogens the differences between simulated and experimental quantities are larger with the simulated quantities being denser than the experimental. A first set of DFT calculations based on systems with densities reported in Figure 19 was performed and the results are reported in Figure 20 where chemical shifts are represented as a function of temperature. Experimental NMR chemical shifts were measured by the group of Prof. Castiglione and are reported in the figure as points connected with lines. Figure 20 **(left)** reports the calculated data as is, while in Figure 20**(right)** all the calculated quantities, full triangles, are scaled by a factor of 84.26 ppm. The scaling was carried out by moving the calculated chemical shifts such as the calculated

and experimental chemical shifts for the CH_2Cl_2 perfectly overlaps. Part of this discrepancy it is recovered with this operation, considering that the method of calculating the shielding constant (a Xe atom in vacuum at a purely quantum chemical level for the reference, and an average over time using clusters generated by a classical MD simulation for xenon in solution) do not represent exactly the same level of theory, which might introduce systematic deviations in the shielding constant. The scaling factor was calculated as the average distance between the calculated and experimental xenon chemical shifts at the temperatures investigated (250 K, 270 K, and 300 K).

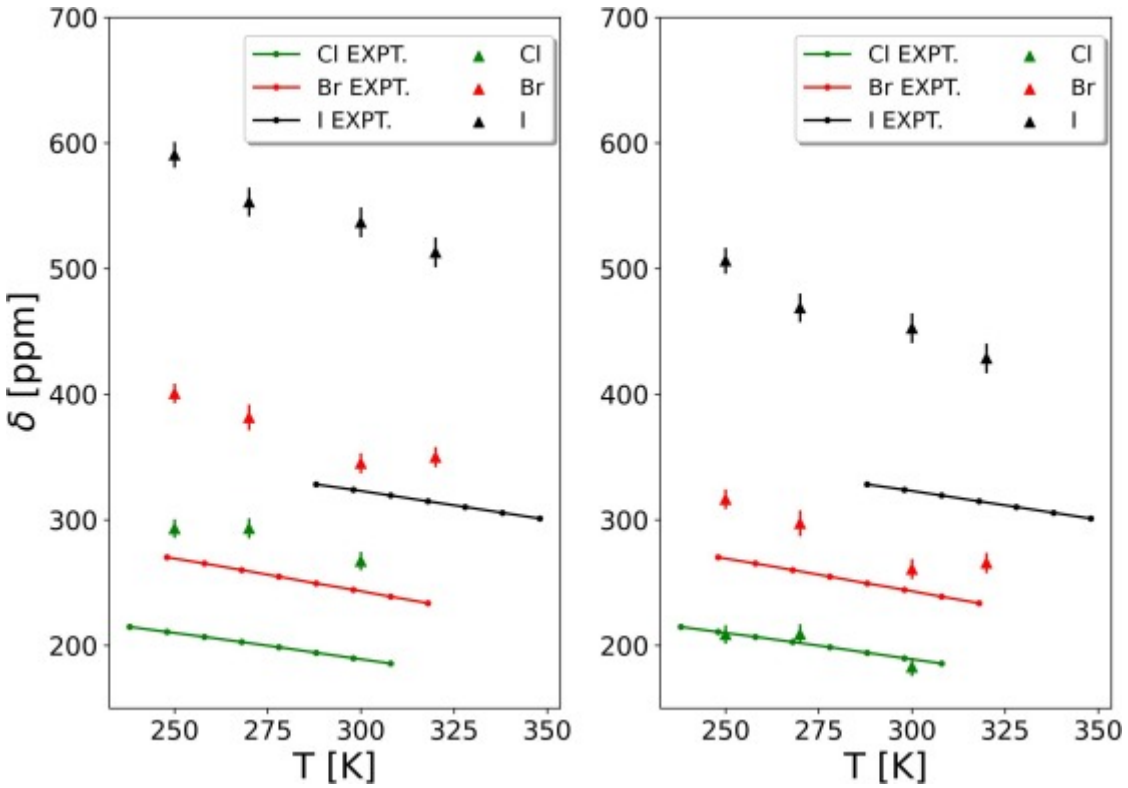

Figure 20 ^{129}Xe chemical shift of xenon dissolved in dihalomethanes as a function of temperature. Triangular markers represent the calculated chemical shift values obtained from the simulations employing the original OPLS FF, left panel. Calculated values scaled by 84.26 ppm with respect to the dichloromethane results, right panel. Vertical bars are the error of the average, ranging from 7 to 12 ppm. Full dots represent experimental values and the lines are simply a guide to the eye

Even though the rescaling permits to match experimental and calculated quantities for CH_2Cl_2 there is, still, an overestimation of chemical shift for CH_2Br_2 and CH_2I_2 with the quantities obtained for iodine derivatives being overestimated by more than 50%. To verify whether the large discrepancy in the calculated chemical shift values of Xe@CH_2I_2 (and to a less extent of Xe@CH_2Br_2), even when rescaled with the values in CH_2Cl_2 as a reference, was due to the error in the diiodomethane and dibromomethane densities, we ran an additional set of simulations for diiodomethane and also for dibromomethane after changing the Lennard-Jones radius to a proper value that reproduces the experimental density. To this end, we first ran a series of simulations at 300 K varying the LJ radius in steps of 0.01 Å, from 3.48 Å to 3.58 Å for Br, and from 3.57 Å to 3.80 Å for I. Each simulation lasted 10 ns and the average density was then evaluated over the last 5 ns. Using these data, we determined that the radius giving the correct density for each of the two solvents at 300 K was 3.5764 Å for Br in CH_2Br_2 and 3.7914 Å for I in CH_2I_2. We then ran again all the simulations of Xe@CH_2X_2 (X = Br, I) at various temperatures using the new set of parameters. The effect of adjusting the LJ radii impacted also on the dynamical properties of dihalomethanes. The calculated and experimental values of diffusion coefficient, D, for the dihalomethanes' molecule and for Xe

are reported in Table 9. It can be seen that the agreement between calculated and experimental quantities is almost quantitative.

Sample	*D*(Xe) (m^2/s) – Expt.	*D*(^{1}H) (m^2/s) – Expt.	*D*(Xe) (m^2/s) – Original OPLS FF	*D*(molecule) (m^2/s) – Original OPLS FF	*D*(Xe) (m^2/s) – Modified OPLS FF	*D*(molecule) (m^2/s) – Modified OPLS FF
CH_2Cl_2	3.96×10^{-9}	3.17×10^{-9}	3.90×10^{-9}	3.70×10^{-9}	–	–
CH_2Br_2	1.96×10^{-9}	1.42×10^{-9}	2.56×10^{-9}	1.44×10^{-9}	3.09×10^{-9}	1.30×10^{-9}
CH_2I_2	0.85×10^{-9}	4.77×10^{-10}	0.72×10^{-9}	0.97×10^{-9}	1.18×10^{-9}	0.84×10^{-9}

Table 9 Experimental diffusion coefficients and calculated, both with original OPLS FF and modified OPLS FF. The error on the experimental quantities is estimated to be ±5%

The overall effect of reproducing experimental densities reflects in an improvement of calculated chemical shifts. Therefore, the effect of the density of the solvent is very important and it has a significant impact on the outcome of the computational protocol. The new chemical shifts, obtained on clusters from the simulations with the adjusted LJ radii, are reported in Figure 21 using the same scaling process aforementioned. However, it remains to be investigated how the precise orientation of the solvent molecules, with respect to the xenon atom in the solvation shell, affects the NMR chemical shift. To this end, a series of simple DFT calculations were performed on dimers configurations made of Xe and a single molecule of CH_2X_2.

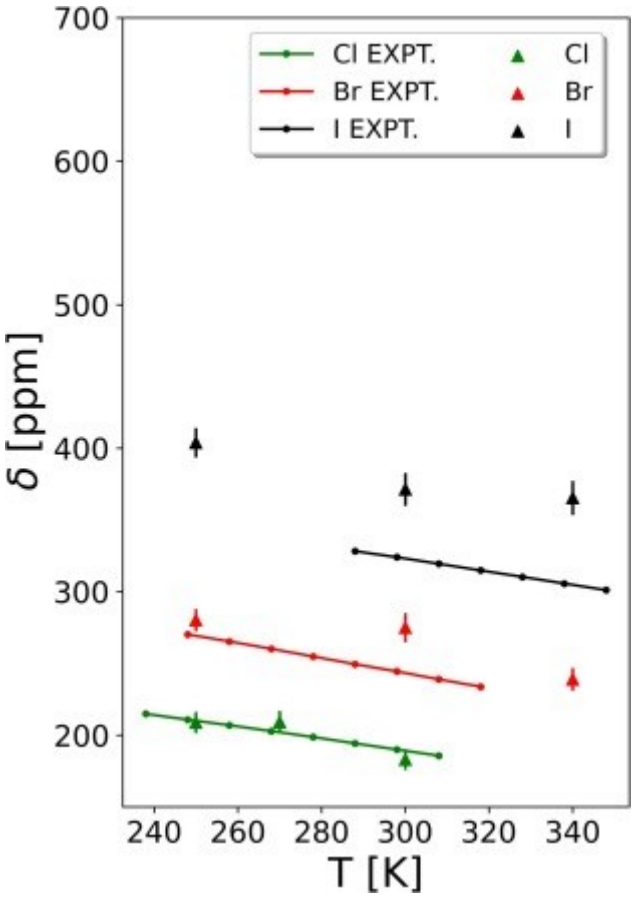

Figure 21 ^{129}Xe chemical shift of xenon dissolved in dihalomethanes as a function of temperature. Chemical shifts of CH_2Br_2 and CH_2I_2 are obtained on clusters extracted from the MD trajectories featuring the modified LJ radii

In Figure 22 we show the results of the chemical shift calculation, with respect to the free Xe atom, of model dimers composed of a xenon atom and a dihalomethane molecule. The geometrical arrangements considered are with the CX_2 side and the CH_2 side approaching xenon (left and middle panel in Figure 22) and a case where the C-X bond is collinear with the X-Xe distance vector (right panel in Figure 22).

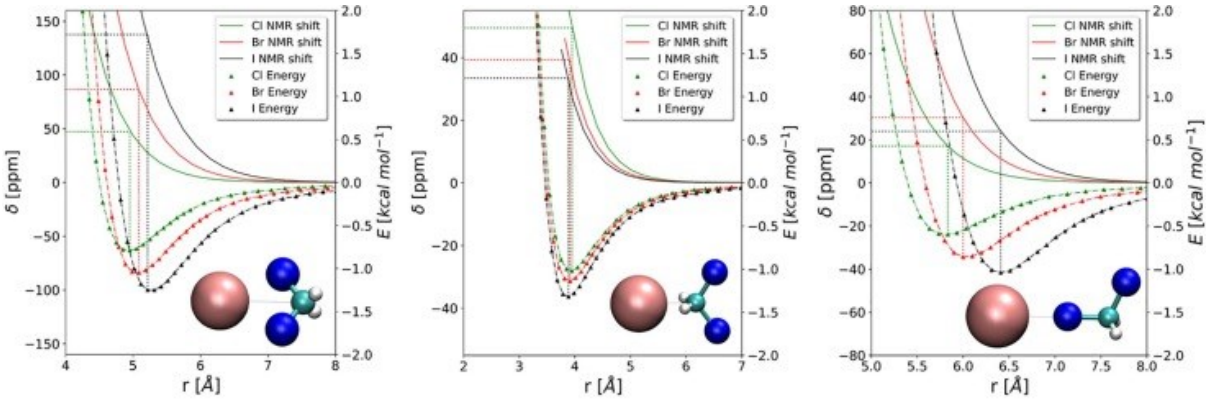

Figure 22 Calculated interaction energies and chemical shift for model pairs of Xe and dihalomethane in three different geometrical arrangements.

Although these results cannot be quantitatively compared with the experiment since the dimer is a too simple approximation of the bulk phase structure, the results of these model

calculations are informative. First of all, a non-trivial result is that the interaction energy at the distance of equilibrium is slightly larger when the xenon approaches the dihalomethane from the H_2-C side, rather than from the X_2-C side. This trend is especially evident for dichloromethane. It is likely the result of a strong polarization of the bonds, due to the electronegativity, which in turn induces stronger dipole-induced dipole interactions with xenon thanks to a closer approach distance when facing the hydrogens atoms. However, while the equilibrium distance in the Xe···H_2-C is almost the same for all three solvents, it changes significantly within the Xe···X_2-C geometry. The chemical shift of xenon at the equilibrium distance, calculated for the two geometries, gives two opposite trends: for the Xe···H_2-C geometry (hydrogen side) the relative chemical shift is δ(Xe@CH_2Cl_2) > δ(Xe@CH_2Br_2) > δ(Xe@CH_2I_2) which is the opposite of the experimental trend. In contrast, for the Xe···X_2-C geometry (halogen side approach) due to the different equilibrium distances, the experimental trend is qualitatively correct, δ(Xe@CH_2I_2) > δ(Xe@CH_2Br_2) > δ(Xe@CH_2Cl_2). This result indirectly confirms that the average geometry obtained in solution from the MD simulations, featuring a stronger solvation of xenon from the halogen atoms with respect to the hydrogens of the dihalomethanes, is qualitatively correct. Moreover, we also tested the energy of interaction and the corresponding xenon chemical shift dependence, for a geometry where Xe is collinear with the X-C bond. This might be interesting because of the extraordinary deshielding of ^{129}Xe in diiodomethane. The results are shown in Figure 22 (right panel) and it is clear that this arrangement is not able to provide a qualitatively correct trend for the xenon chemical shift since the value calculated at the equilibrium distance follows the order δ(Xe@CH_2Br_2) > δ(Xe@CH_2I_2) > δ(Xe@CH_2Cl_2).

Xe@PIM-EA-TB

During my second year I visited the laboratories of the Institute of Membrane Technology of the National Research Council (CNR-ITM) in Rende, where I collaborated with dr. Tocci on a study aimed at obtaining the NMR chemical shifts of ^{129}Xe dispersed in a polymeric matrix. Here the results of the ^{129}Xe NMR spectroscopy inside a polymer of intrinsic microporosity (PIM-EA-TB) are presented. The chemical structure of the monomer, the representation of a chain of 9 monomers and one of the simulation boxes with the highest Xe content are reported in Figure 23.

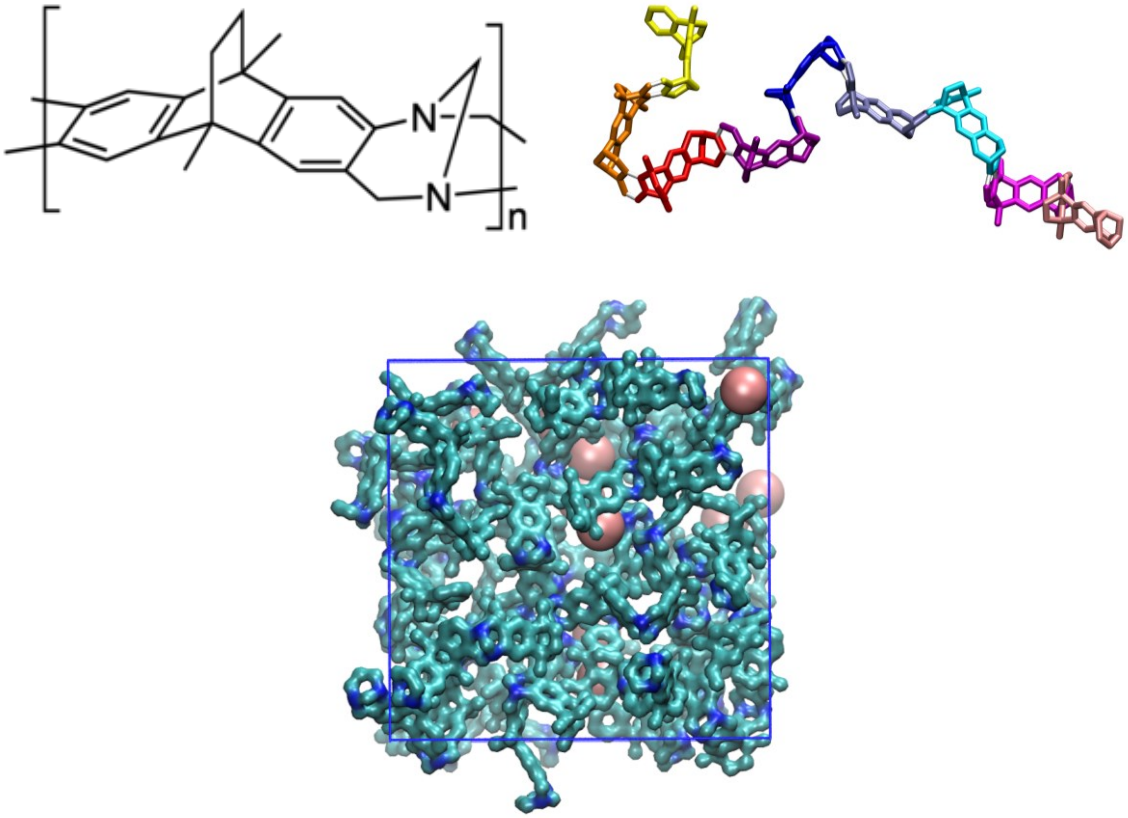

Figure 23 Structural formula of the monomer of PIM-EA-TB, upper left, and 9-monomers chain with each monomer colored differently, upper right. On the bottom the simulation box is reported with C and N represented in cyan and blue, respectively. Xe atoms are pink spheres. In all the images hydrogens were omitted for clarity.

The employment of RDFs to determine the first shell of any atoms around the Xe gives the distance of 7 Å as the first minimum, as can be seen in Figure 24**(a).** This quantity is used to determine the minimum radius of the cluster to be extracted. The clusters appear as illustrated in Figure 24**(b).** The intrinsic microporosity of the polymer and its voids distributions permit Xe atoms to experience the cavities, pockets and empty regions of the polymeric matrix. Different environments affect the ^{129}Xe NMR properties, especially in the close proximity. The more atoms are close to the Xe the higher is the deshielding effect, producing higher chemical shifts due to the electron withdrawing effects. The distribution of the calculated chemical shifts is reported in Figure 25 where the system with different Xe concentrations are evaluated both separately and as a whole. The distribution of shifts appears unsymmetrical with a peak at low chemical shifts and a long tail at higher chemical shifts. The mean values, reported in the legend of Figure 25, are obtained as the average of all the calculated chemical shifts of the

systems having the same Xe content. Since the produced configurations follow the proper partition function of the ensemble in which they are simulated, the sampling is considered uniform and for this reason the chemical shift is calculated as arithmetic mean.

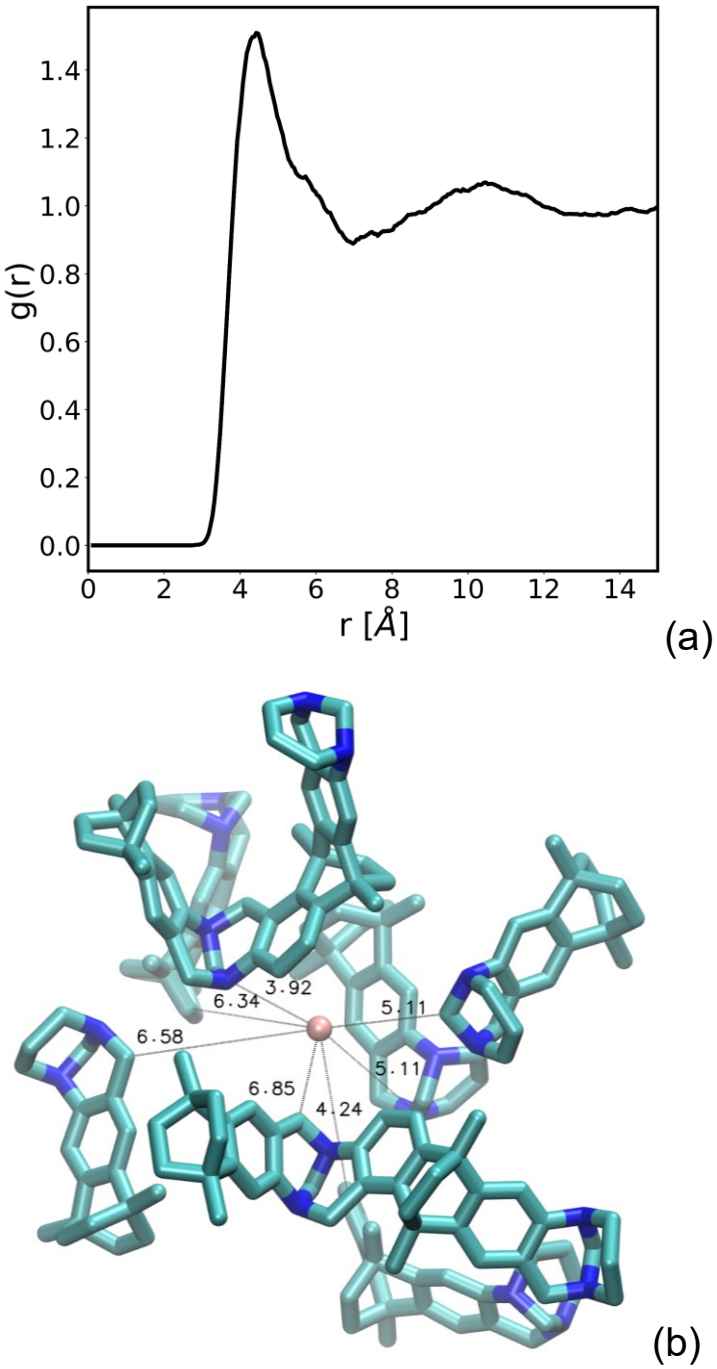

Figure 24 Radial distribution function calculated between the Xe and all the C and N present in the systems, (a). Sample of an extracted cluster comprising Xe, in the center, surrounded by monomers and oligomers with the distances of the closest residues indicated in Å, (b)

If the chemical shifts are calculated as the difference between the shielding constant of Xe in vacuum and the shielding constant of Xe in PIM ($\sigma_{Xe(g)}$-$\sigma_{Xe@PIM}$), the obtained chemical shift values for the systems with 1, 3 and 10 Xe are 168.7, 180.34 and 172.15 ppm, respectively. The distributions of chemical shifts for the different systems studied is shown in Figure 25 with

the arithmetic mean indicated as vertical lines. These values are higher than what is found in literature experimentally, 109.7 ppm [28], with a relative error of about 50% on the calculated values. The shielding constant of Xe gas is obtained as if the Xe is in vacuum with nothing around it, this could introduce a bias in the obtained chemical shift values producing higher chemical shifts due to the much more shielded Xe in vacuum with respect to the Xe in a different medium. Setting as reference the shielding constant of Xe in a different system could improve the results toward values with a smaller error and permitting also to compare the chemical shifts obtained as the difference of their experimental chemical shifts. If we employ as reference the shielding constant of Xe in hexane ($\sigma_{Xe@hexane}$),already mentioned in Xe@n-alkanes section, this improves the chemical shift obtained providing an error on its value of about 15% (c.a. 5 ppm). The shielding constants of Xe@hexane are obtained using the same level of theory employed for the calculation of the Xe@PIM shielding constant and the difference is compared to the difference of experimental chemical shifts. All these values are reported in Table 10.

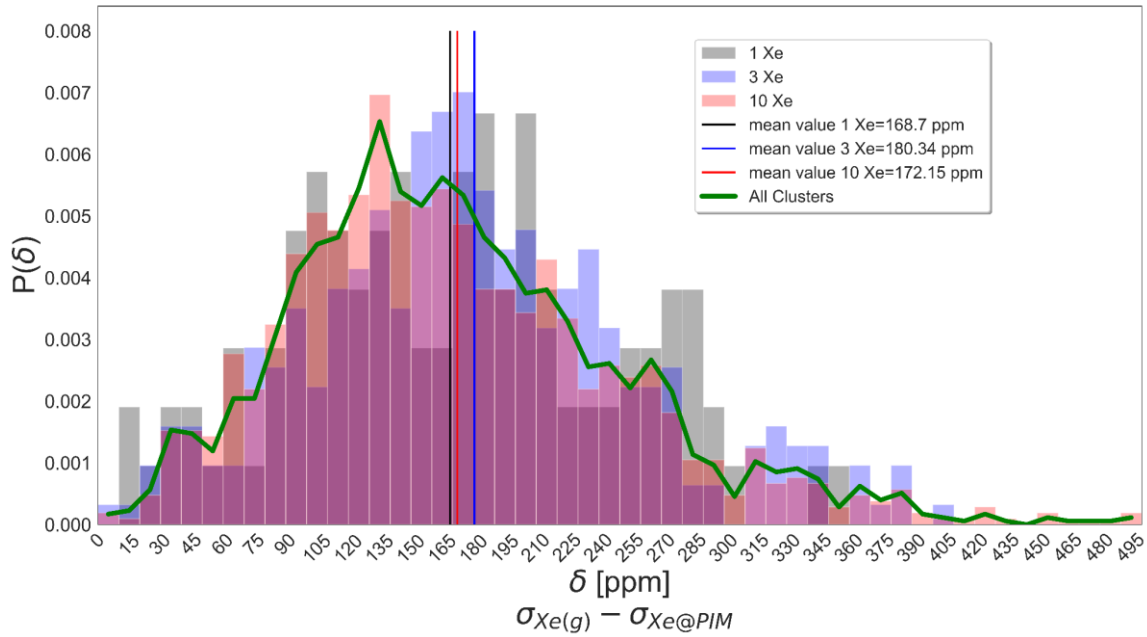

Figure 25 Probability distribution of the calculated chemical shifts of the systems with 1 Xe, 3 Xe and 10 Xe depicted with grey, blue and red bars respectively. The green curve is the probability distribution of all the calculated chemical shifts. Mean values for 1, 3 and 10 Xe are the black, blue and red vertical lines with the value indicated in the legend. Superimposition of bars produce different colors

# of Xe	δ [ppm] $\sigma_{Xe(g)}$-$\sigma_{Xe@PIM}$	δ [ppm] $\sigma_{Xe@PIM}$-$\sigma_{Xe@hexane}$	EXPT. δ [ppm] $\delta_{Xe@PIM}$ extrapolated at 0 bar [28]	EXPT. δ [ppm] $\delta_{Xe@PIM}$ - $\delta_{Xe@hexane}$ [112]
1 Xe	168.7	-50.58	109.7	-51.8
3 Xe	180.34	-38.94	109.7	-51.8
10 Xe	172.15	-47.13	109.7	-51.8
average	173.73	-45.55	109.7	-51.8

Table 10 Chemical shifts of Xe@PIM calculated as $\sigma_{Xe@PIM}$-$\sigma_{Xe@hexane}$ and as $\sigma_{Xe@PIM}$-$\sigma_{Xe@hexane}$. The experimental chemical shift is reported for Xe@PIM ($\delta_{Xe@PIM}$) and as difference $\delta_{Xe@PIM}$ - $\delta_{Xe@hexane}$

The main contribution to the shielding values, and thus on the obtained shifts, is ascribed to the close surroundings of Xe atoms. Figure 26 depicts the 2D map of chemical shift vs mean atoms distance from the Xe at the center of the cluster. The 4 closest atoms near Xe are considered for the distance evaluation and their mean value is the distance values reported in the Figure 26. It can be seen that the clusters having a great shift value are the one with atoms closer to the Xe, while shift values close to 0 ppm are found for Xe being in an almost empty region of space. In the figure Figure 26 two example clusters are reported for the high shift and low shift case, indicating that for low shift values the Xe does not have any atom in ~4.5 Å around it.

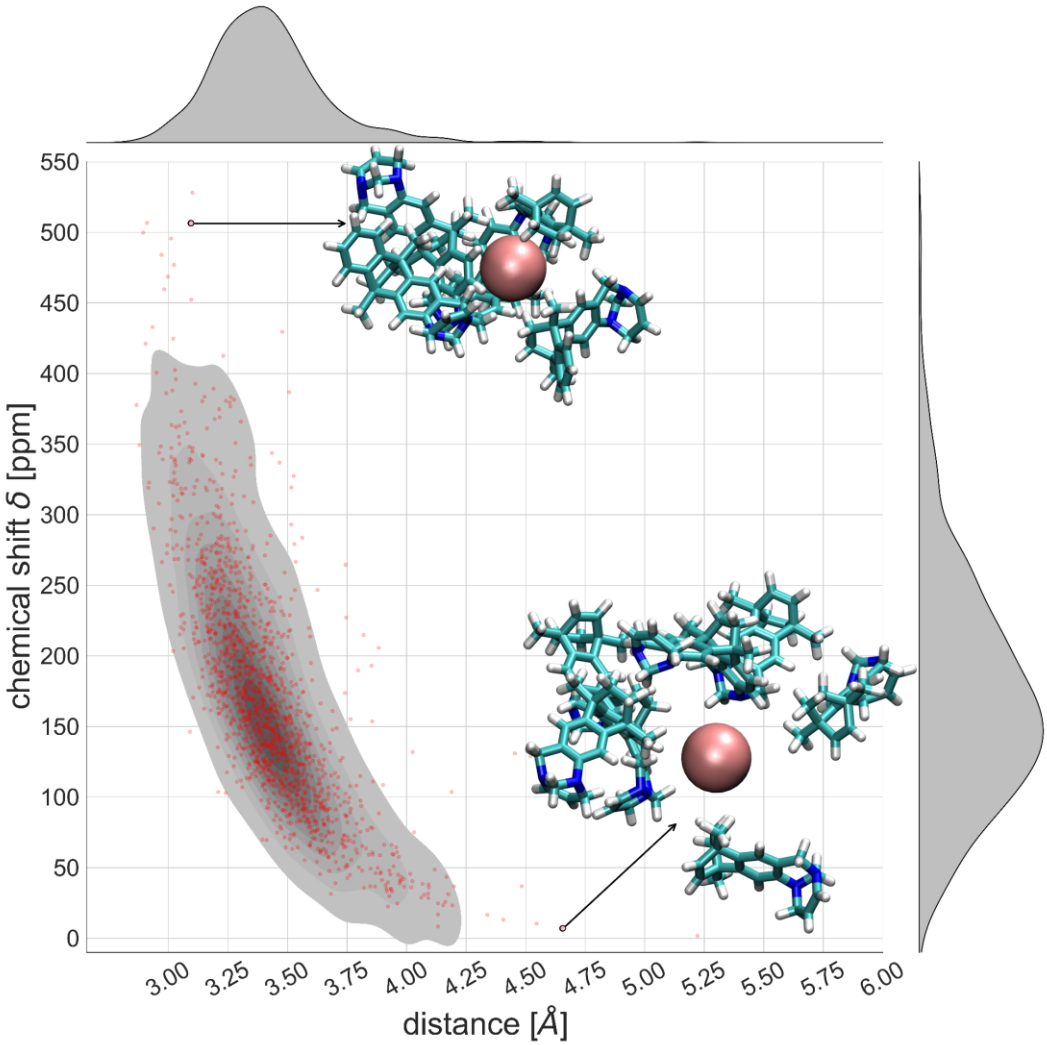

Figure 26 Two dimensional distribution map of the chemical shifts as a function of the mean distance of the four closest atoms to the central Xe. The map uses grayscale to indicate the more populated area of the plot. The darker the color the more observations are found. On the right and top of the figure histograms show the chemical shift and distance distributions with respect to the central Xe atom, respectively. Red dots are the observations. Two examples of clusters are reported for the high shift region, top, and low shift region, bottom. The color code for atomic models is the same as in Figure 23 with hydrogens represented in white

The calculated chemical shifts for Xe in PIM gives results that are in agreement on what is found in literature, meaning that the Xe atoms preferentially reside near the atoms and inside the pockets created by the polymer structure. When near other nuclei the Xe is deshielded more, producing higher shift values like in the case of the cluster represented at the top of the

Figure 26. The effect of Xe content on the shifts is found not to strongly depend on Xe concentration, but this holds true also for experimental evidence, where the chemical shift of ^{129}Xe increases by about 10 ppm with the increasing of Xe nominal pressure from 0 kPa to 110 kPa. Taking as reference the Xe in a different, denser, environment improves the chemical shift calculated permitting to obtain almost the quantitative value of chemical shift.

NMR chemical shifts of ^{125}Te in organotellurium halides

Apart from the calculation of NMR spectroscopic properties of Xe in different matrices, me and my supervisor collaborated with Prof. Orian's group in the calculation of NMR chemical shifts of another heavy nucleus: ^{125}Te. This investigation is the subject of a manuscript which is in preparation.

In order to calculate the chemical shift of organotellurium halides, different chemical scaffolds were selected to provide an overview over different classes of halides. Referring to Figure 13 the compounds were grouped in mono- (1 – 4), di- (5 – 11) and trihalides (12 – 14). Tetrahalides were also included since it was proved that, in solution, trihalides 14 can dissociate producing the tetrahalide anion 15.[113] Lastly, also dimer structures of 14X, 16X, were investigated as plausible systems in solution according to previous studies.[113] The choice of molecular compounds was guided by three main factors: 1) only organotellurides were considered, thus inorganic halides were excluded from the investigation. In order to expand the number of substrates, also compounds without a formal C – Te bond were included (12, 13) as long as an organic ligand was present (12Cl and 13Cl); 2) Experimental chemical shifts of the species were available; 3) Priority was given to structures with the same chemical scaffold but with different halogens. Some compounds were included even if only one halide species was experimentally available (i.e. 6, 9, 10, 11, 12 and 13). All other compounds were studied for at least two different halogens X, spanning Cl, Br and, when available, I. The complete set of studied molecules are distributed over a window of 1000 ppm. For this reason the analysis of correlation of experimental vs. calculated chemical shifts was employed to determine the best functional in reproducing experimental trends. On these optimized structures, a series of NMR calculations were performed using different GGA functionals to assess a reliable protocol in determining the shielding constants of Tellurium-halides. The results of these calculations are condensed in Table 11, where ME, MAE, cMAE, RMSE and R^2 values are reported for each of the GGA functional tested. The solvent effect of EtOH on NMR shielding was accounted for on two of the tested functionals, OPBE and SSB-D.

Statistical Parameter	BLYP	BP86	KT1	KT2	mPW	OPBE	OPBE + SOL EtOH	SSB-D	SSB-D + SOL EtOH
ME	-1.158	55.92	-20.93	-27.1	28.68	14.36	140.3	-130.8	-20.56
MAE	87.06	87.47	71.21	74.39	74.76	65.19	144	130.8	43.85
cMAE	83.25	76.12	65.71	66.69	73.63	61.94	55.37	48.42	45.65
RMSE	100.8	94.11	84.31	83.67	91.09	80.01	72.68	63.28	56.45
R^2	0.9106	0.9230	0.9304	0.9329	0.9270	0.9417	0.9525	0.9532	0.9650

Table 11 Statistical parameters of the correlation between experimental and calculated chemical shifts of the complete set of molecules presented in Figure 13

Since ME accounts for positive and negative differences between calculated and experimental values, it represent the set's average deviation from the unitary line. On the contrary, the MAE, which accounts only for absolute differences, is an esteem of the average distances of points from the unitary line. cMAE is calculated as MAE but the absolute differences are evaluated not between points and unitary line but between points and a fitting line, indeed. RMSE is another parameter that gives an esteem of the average distances of the points from the fitted line, giving more weight to outsider values, since they are squared. Finally, the goodness of

linear regression can be evaluated by looking at R^2 values. All the tested functionals provide a R^2 above 0.9, nonetheless the highest values, not accounting for EtOH solvent, are spotted for OPBE and SSB-D functionals. OPBE values fall in the right place, with a ME of c.a. +15 ppm, slightly overesteeming the shift values due to more deshielded Te. Moreover, the average differences between experimental and calculated values are on the order of 60 ppm for both MAE and cMAE, with some outsider values that increases the RMSE value to 80 ppm. On the contrary, SSB-D ME and MAE values suggest more shielded Te nuclei, having all the calculated shifts lying below the unitary line. It is worth to note that the cMAE of SSB-D is among the smallest, suggesting that shift values are narrower distributed around the linear fit compared to other functionals. The effect of solvent was tested for the functionals that possessed the highest values, OPBE and SSB-D. Taking into account the solvent increases the shift values by c.a 110 ppm for both the functionals OPBE and SSB-D with more deshielded Te nuclei. Regarding at the statistical parameters of the systems with solvent addition it can be seen that the solvent addition highly increases the estimation of the OPBE shifts, ME and MAE c.a. 140 ppm, while the SSB-D shifts fall in the right range with an underestimate of the shifts, that is -20 ppm on average, while the average distance between calculated and experimental values being c.a. 40 ppm. The solvent improves the correlation of experimental and calculated shift values, as can bee seen from the cMAE, RMSE and R^2 values. cMAE and RMSE lowers when the solvent is considered, thus, implying that the values are more narrowed distributed around the fitting line, also the R^2 values increases, indicating a better linear fitting. Taking in count all these considerations we evaluated the SSB-D functional with the inclusion of EtOH solvent as the best choice in reproducing the behaviour of the studied species. The complete set of data, with the unitary line and linear fitting, is depicted in Figure 27 just for the SSB-D + SOL (EtOH). These values are indicated in Table 12, alongside experimental values and their references. The correlation plots for the other functionals are not reported here. A relevant part of this work focused on the assessment of the chemical shifts for the 14X structures reported in Figure 13. These structures, studied by Casagrande and coworkers[113], when in solution produce anionic species. For this reason the case study for these molecules were investigated using the structures 14X, 15X and 16X, syn and anti configurations.

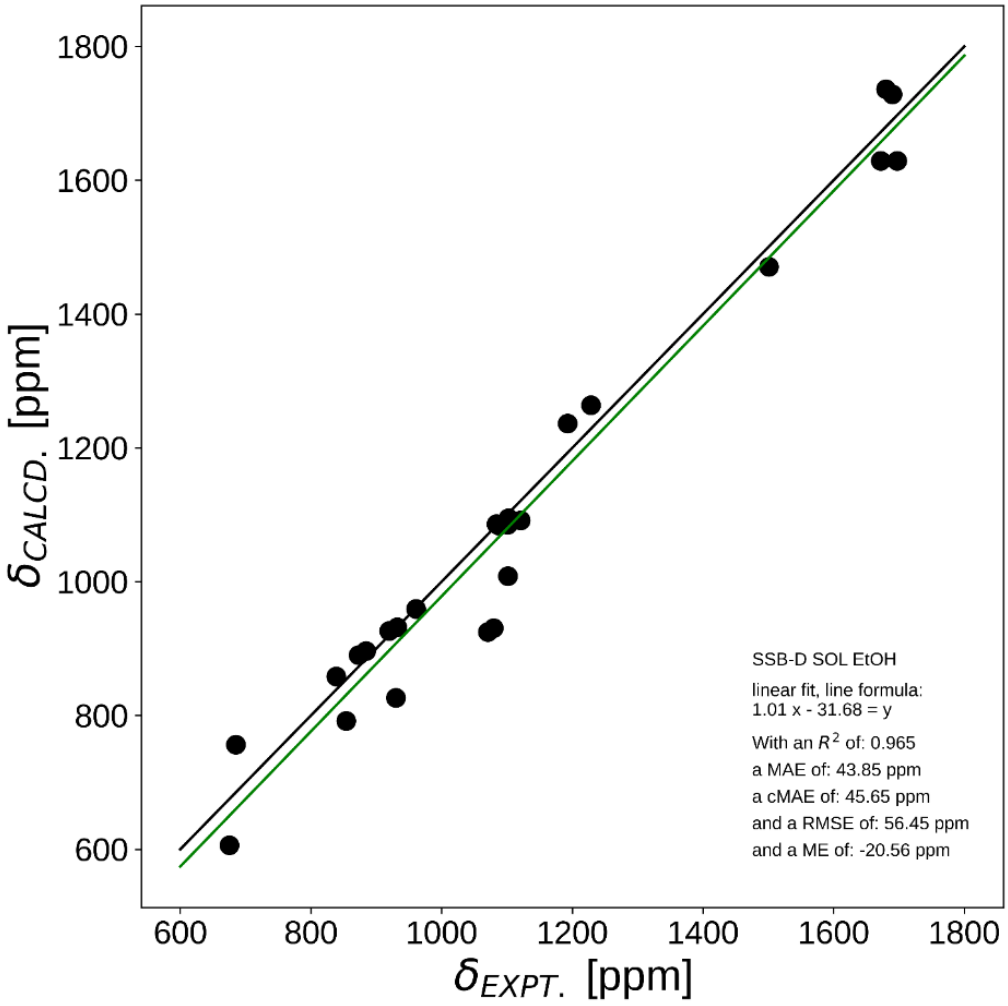

*Figure 27 Correlation plot of calculated ($\delta_{CALCD.}$) and experimental ($\delta_{EXPT.}$) chemical shifts for the whole set of studied organotellurium halides. Black line is the unitary line, green line is the linear fit with the formula indicated in the figure. The level of theory for geometry optimization and NMR calculation are **ZORA-SSB-D(SolEtOH)/QZ4P** ; **ZORA-OPBE/TZ2P**, respectively*

The correlation plot for the chemical shifts of these structures is represented in Figure 28. The protocol employed is the one reported as the best: ZORA-OPBE/TZ2P for geometry optimization and ZORA-SSB-D(EtOH)/QZ4P for NMR calculations. As can be seen from Figure 28 the trihalogenated molecules, 14X triangles, produce the biggest discrepancy between the experimental and calculated shifts of about 350 ppm. This suggests that the trihalogenated species are not the one attributed to the experimental shifts. Moreover, their correlation is inverted having $\delta_{14Cl} > \delta_{14Br} > \delta_{14I}$ for experimental values while for calculated one the trend is $\delta_{14I} > \delta_{14Br} > \delta_{14Cl}$. The dimeric syn and anti structures, 15X crosses and diamonds, produces the right correlation but their calculated values are still overestimated by about 200 ppm. The anionic tetrahalogenated species, 16X circles, are the best in reproducing the experimental trend, with a correct correlation and a difference between calculated and experimental chemical shifts of about 30, 40 and 100 ppm for 16Cl, 16Br and 16I, respectively. This subset of molecules were also optimized accounting for dispersion interactions with ZORA-BLYP-D3(BJ)/TZ2P level of theory and the shifts calculated with ZORA-SSB-D(EtOH)/QZ4P level of theory.

Name	EXPT	CALCD.	Ref.	NAME	EXPT	CALCD.	Ref
1Cl	1088	1083.76	[114]	7Cl	919.7	926.38	[115]
1Cl	1084	1086.06	[114]	7Br	884.3	896.54	[115]
1Br	1106	1092.09	[114]	7I	838.5	858.3	[115]
1Br	1102	1094.69	[114]	8Cl	960.9	959.24	[115]
3Cl	1101	1085.07	[114]	8Br	932.1	931.75	[115]
3Br	1121	1091.43	[114]	8I	872.8	890.19	[115]
4Cl	1697	1628.89	[116]	9Cl	1070.6	924.78	[117]
4Br	1672	1628.89	[116]	10Cl	1079.6	930.53	[117]
4I	1501	1470.60	[116]	11I	675	606.22	[117]
5Cl	930	826.26	[118]	12Cl	1680	1735.98	[118]
5Br	685	756.27	[118]	13Cl	1690	1728.49	[118]
6Cl	854	791.75	[118]	15Cl	1228.5	1263.74	[113], [117]
				15Br	1192.9	1236.46	[113], [117]
				15I	1101.4	1008.33	[113], [117]

Table 12 Calculated and experimental chemical shifts of all the species obtained with the SSB-D(SolEtOh) level of theory. The experimental values are taken from the corresponding work indicated in the Ref. columns

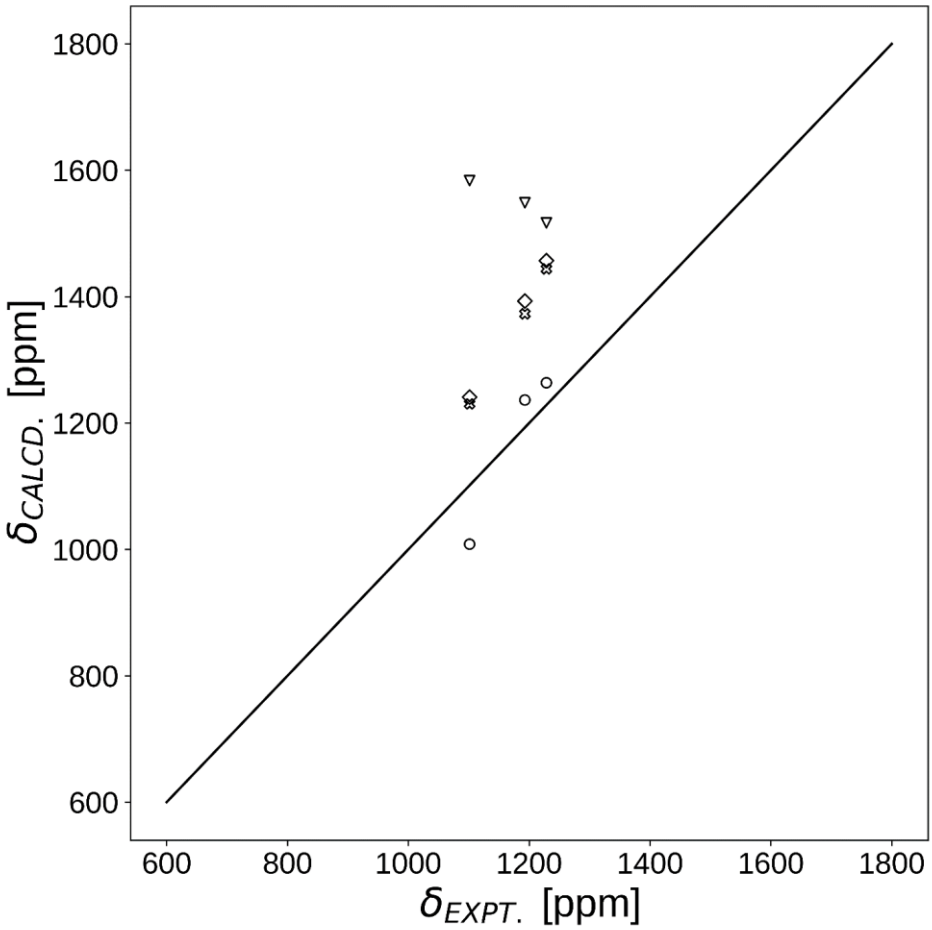

Figure 28 Correlation plot of calculated ($\delta_{CALCD.}$) and experimental ($\delta_{EXPT.}$) chemical shifts for the subset of 14X, 15X, 16X syn and anti structures. Black line is the unitary line; triangles are the 14X trihalogenated species, circles are the 15X anionic species, crosses and diamonds are 14X dimeric structures, syn and anti respectively. The same level of theory reported in Figure 27 is used

The behaviour of calculated shifts using this approach is similar to the one already discussed: 14X structures produce bigger differences between calculated and experimental shifts that are c.a. 500, 600 and 1000 ppm for 14Cl, 14Br and 14I, respectively. The correlation for these shifts is also inverted. 15X and 16X structures produce rightly correlated shifts trend with the values of 16X structures being higher that the one found for anionic tetrahalogenated one, 15X structures. Even though the functional employed accounted for dispersion interactions, the best functional to obtain optimized structures is the OPBE and the overall level of theory declared as the best among the the tested one is ZORA-OPBE/TZ2P for geometry optimization and ZORA-SSB-D(EtOH)/QZ4P for NMR calculations.

Mixtures of long-chain and short-chain imidazolium / bistriflimide salts

The study of ionic liquid mixtures with different alkyl content was pursued during the second year of my PhD thanks to the financial support through the bilateral agreement CNR-NSFC 2021-2022, NSFC grant No. 22011530390 between the Italian National Research Council and the Natural Science Foundation of China. The study was in collaboration with Prof. Yanting Wang and produced the paper in Ref.[119].
The aim of the work was to reproduce the experimental structure factor $S(q)$ and to investigate structural and dynamic features of mixtures of C_1 and C_{12} cations with bistriflimide anions. The close range order of cations and anions id investigated through RDFs and Figure 29 shows the $g(r)$ between anion-anion, (a), cation-cation, (b) and cation-anion,(c).

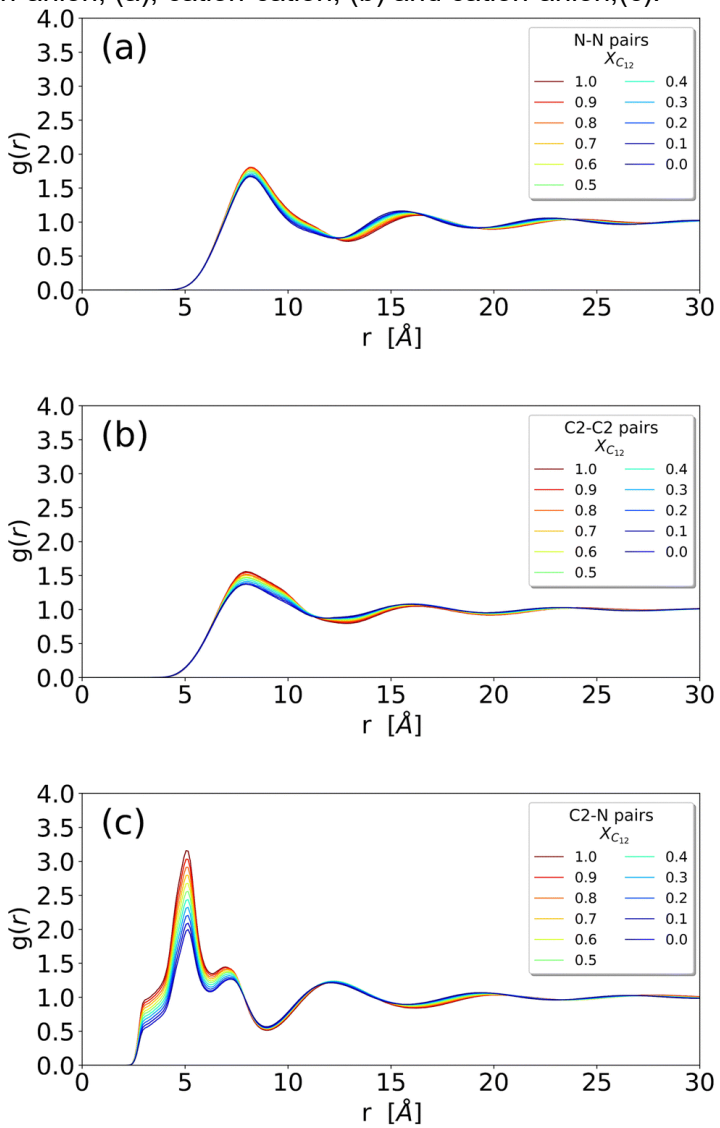

Figure 29 (a) RDF of the N–N distance between two anions; (b) RDF of the C_2–C_2 distance between two imidazolium heads (irrespective of being [$C_{12}C_1$im] or [C_1C_1im]); (c) RDF of the N–C_2 distance between an anion and an imidazolium head (irrespective of being [$C_{12}C_1$im] or [C_1C_1im]) (see Figure 2 for atom labelling)

By looking at the RDFs of the ionic moieties of the ILs it can be seen that the close range ordering pattern of anion-cation pairs, Figure 29**(c),** is present in all the systems with increasing intensity of the first peak in the $g(r)$ as the alkyl content is increased. A closer inspection reveals an interesting trend: in Figure 30 we show the cation–anion RDF (calculated between the carbon C_2 on the cationic ring and the nitrogen on the anion) for various systems. The RDFs are normalized with respect to the height of the first peak at around 5 Å (Figure 30 **(a)**) and with respect to the height of the second peak at around 7 Å (Figure Figure 30**(b)**) in order to better see the relative positions of the peaks. It is clear that, by increasing the mole fraction of C_{12}, the peaks shift towards shorter distances, indicating a stronger cation–anion interaction. This is clear both in Figure Figure 30**(a)** where, though the maximum does not change significantly, the sides of the peak at around 5.5 and 4.5 Å are shifting to the left with increasing C_{12} mole fraction, and more clearly in Figure 30**(b)** where the maximum of the peak is clearly dependent on the mixture composition. Therefore, it appears that the growth of the alkylic domains is responsible for a stronger structuring of the polar network.

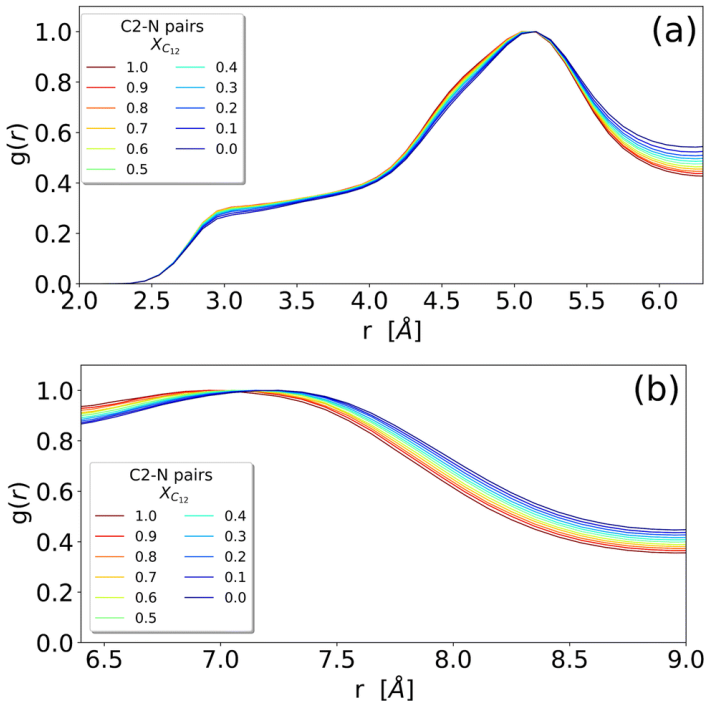

Figure 30 Enlarged versions of the (c) panel of Figure 29 representing the RDF of the N–C_2 distance between an anion and an imidazolium head (irrespective of being [$C_{12}C_1$im] or [C_1C_1im]). RDFs are normalized by the height of the respective peaks: (a) the peak around 5 Å and (b) the peak around 7 Å.

A certain degree of chain aggregation appears early with increasing the C_{12} mole fraction. To have a deeper understanding of the aggregation of alkyl chains, a feature which has been extensively documented for pure ILs both from MD simulations[120]–[122] and experiments [123], we have calculated the HOP, explained in the Analysis section. This parameter measures the degree of aggregation of particles in a given volume. For a perfect random distribution of positions, it is scaled to zero by subtracting the asymptotic values. A HOP larger than 1 indicates a certain degree of aggregation of the particles. In Figure 31 we show the trend of the HOP of the terminal methyl group on the alkyl chain of the [$C_{12}C_1$im] cation for various compositions.

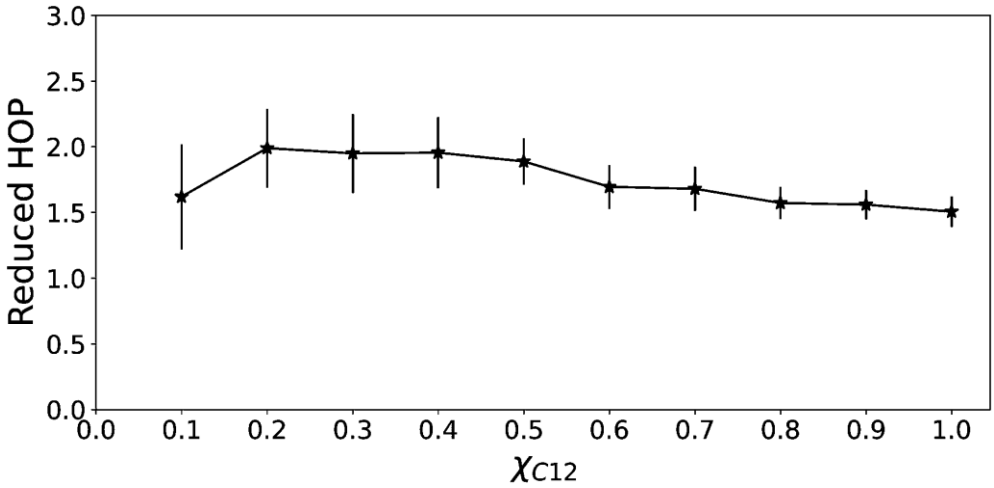

Figure 31 Heterogeneity order parameter of the terminal methyl of the alkyl chain of C_{12} as a function of the C_{12} mole fraction.

As we can see, it appears that the HOP goes through a weak maximum. This profile suggests a competition between two opposite trends. On the one hand, at low C_{12} mole fractions, the "hydrophobic" effect favours the aggregation of the relatively few alkyl chains and the ensuing nano-segregation from the ionic parts. This mechanism was proposed already by Wang and co-workers in Ref. [124] where the authors observed that the nano-segregation of alkyl chains in pure ILs is mostly driven by the strong electrostatic interactions of the ionic parts which "push" away the non-polar moieties, rather than by VDW interactions among the chains themselves. This aggregation increases with increasing C_{12} mole fraction. However, at the same time, the methyl terminal group used as a probe of the chain aggregation is also diluted within the increasingly large alkyl domains. Therefore, the HOP appears only slightly varying with the composition due to these two opposite effects.

To further shed light on this issue, domain analysis was performed according to the theoretical description reported in the Analysis section. Figure 32 shows the domain's volume *versus* its IQ, which is used to describe the sphericity of a domain in IL simulations. The closer to 1 the numerical value, the more spherical in shape the domain is. A large deviation from 1 indicates an aspheric domain. The calculated volumes and IQs suggest that, as expected, the size of the alkyl domains as well as the distribution of sizes increases with increasing C_{12} concentration, as suggested by the spread of the volume values for large C_{12} compositions. At the same time, the domains always appear far from a spherical shape, which can be attributed to the possibility of the alkyl chains to align roughly parallel to each other. To get insight into the chains' arrangement within the alkyl domains, a distance-orientation analysis is performed for the system with composition x_{C12} = 0.80 as a representative example.

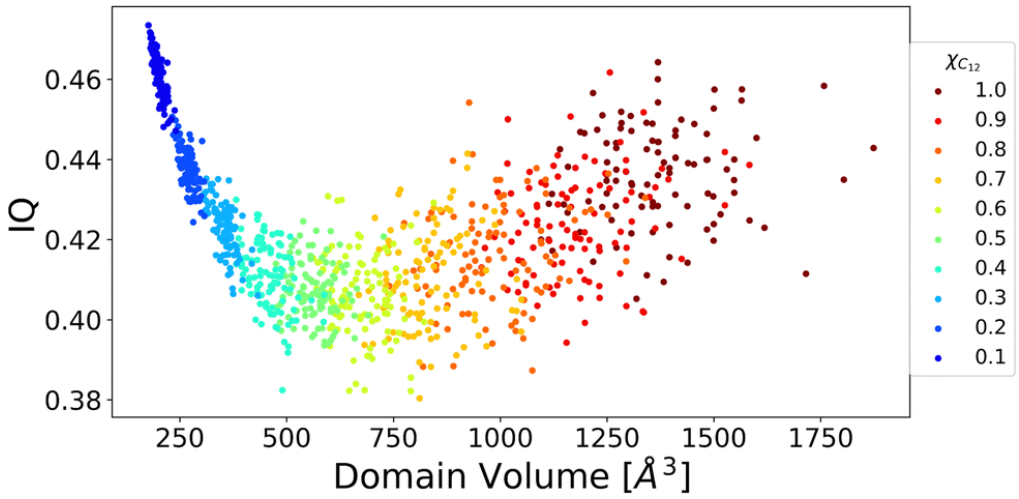

Figure 32 Domain's volume vs. isoperimetric quotient for all the mixed systems

The chains in these domains are in fact more likely to be aligned parallel or antiparallel to each other as it can be seen from Figure 33, where the probability distribution of distance and orientation of side chains is reported. The probability exhibits a clear peak in intensity at a relatively close distance between the alkyl chains for orientations with cos(θ) = ±1, which corresponds to the two vectors highlighted in Figure 33 being parallel or antiparallel.

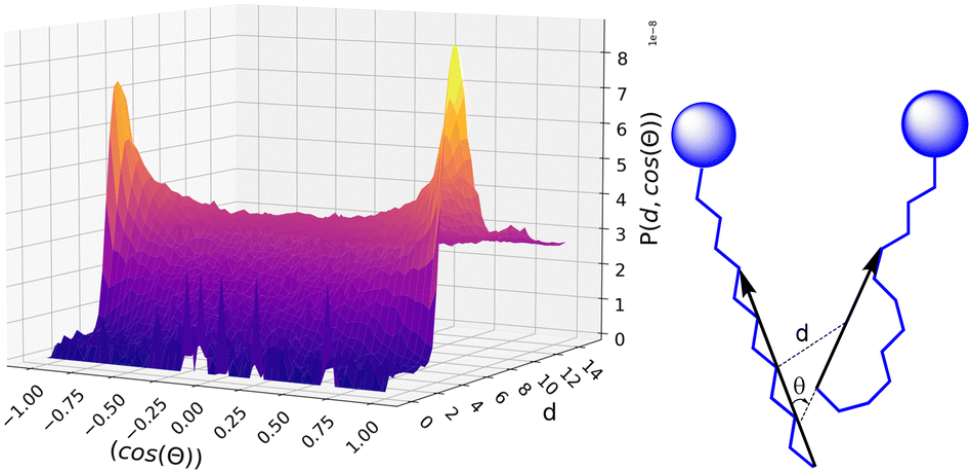

Figure 33 Probability distribution to find a pair of chains as a function of their mutual distance and orientation, as defined in the scheme on the right, for the system with composition x_{C12} of 0.80

To conclude the structural analysis, the calculated X-ray structure factor $S(q)$ for all the systems is shown in Figure 34. For pure C_1, a simple fluid with no nano-domain segregation, we observe that the whole region between the smallest available wavevector (1.151 nm^{-1}) up to about 7 nm^{-1} is completely flat, indicating that no inhomogeneities are present in the fluid, as in simple organic molecular solvents. In contrast, for pure C_{12}, we observe a well-defined intense pre-peak centered at around 2.3 nm^{-1}, nonetheless still quite broad due to the liquid nature of the phase. On decreasing the mole fraction x_{C12}, we observe a broadening of the pre-peak, a shift to lower q values and, most important, a gradual decrease of the intensity until the pre-peak disappears for systems with x_{C12} = 0.1 and 0, at least within the range of wavevectors available from the simulations. Remarkably, the loss of intensity does not show any abrupt change, but rather decreases regularly with the composition.

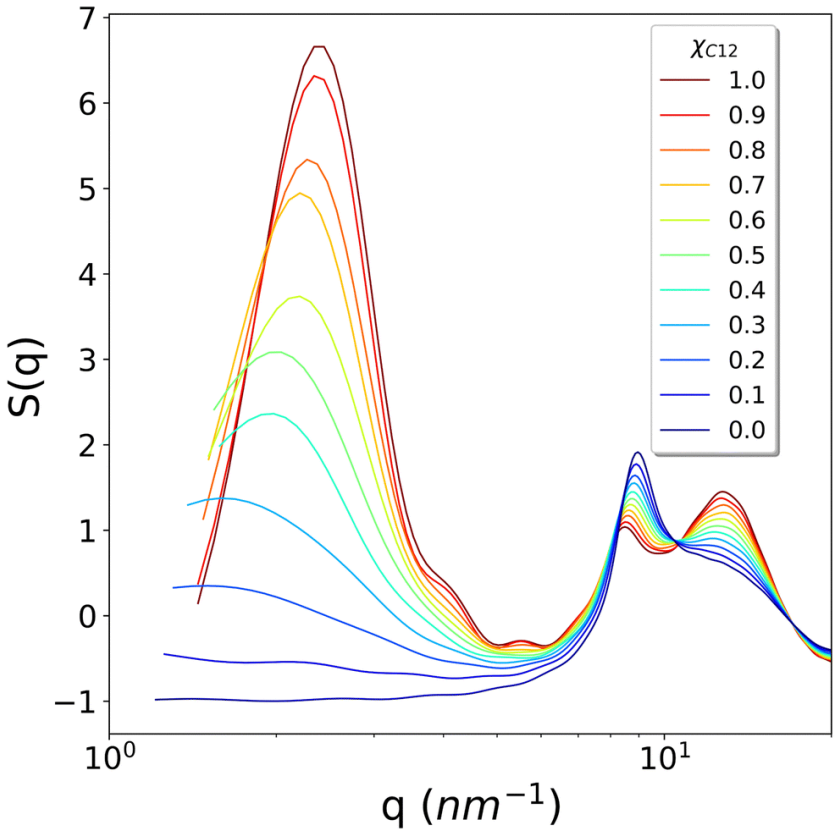

Figure 34 The calculated $S(q)$ as a function of the wavevector q for all the studied systems.

The calculated profiles well reproduce the experimental trends reported by Russina and coworkers [125] who measured small angle X-ray scattering of $[C_{12}C_1im]/[C_1C_1im][Tf_2N]$ mixtures and noticed the growth of a peak in the region with q < 3 nm^{-1}. This behaviour of $S(q)$ is explained by Russina and coworkers by means of interacting pseudospherical aggregates. The pre-peak's q position contains the information about the distance between interacting pseudospherical aggregates while its broadening determines whether this distance peaked around certain values as in rich C_{12} mixtures, or it spans several q values as the content of C_{12} decreases. The substantial increment of the pre-peak, as the C_{12} mole fraction is increased, is therefore due to a "structuring" effect (akin to the hydrophobic effect when a non-polar molecule is solvated by water) of the ionic domains where the alkyl domains act as spacers. Again, this interpretation is also consistent with the proposed predominant role of the electrostatic interactions as the driving force for the nano-segregation in pure ILs reported in Ref. [124]. To further examine this issue, we have calculated the contributions to the total $S(q)$ coming from cation–cation, anion–anion, cation–anion, chain–cation, chain–anion and chain–chain correlations. They are reported in Figure 35 for the system with composition $\chi_{C_{12}} = 0.80$ as an example. As it can be observed, the strongest positive contribution comes from anion–anion correlations, while the cation–cation correlations are also significant but negative. Weaker contributions are obtained from the chains. This confirms the interpretation of the alkyl domains being a sort of structuring agent of the ionic polar network, which, in turn, is the main resource responsible for the scattering intensity in the pre-peak region.

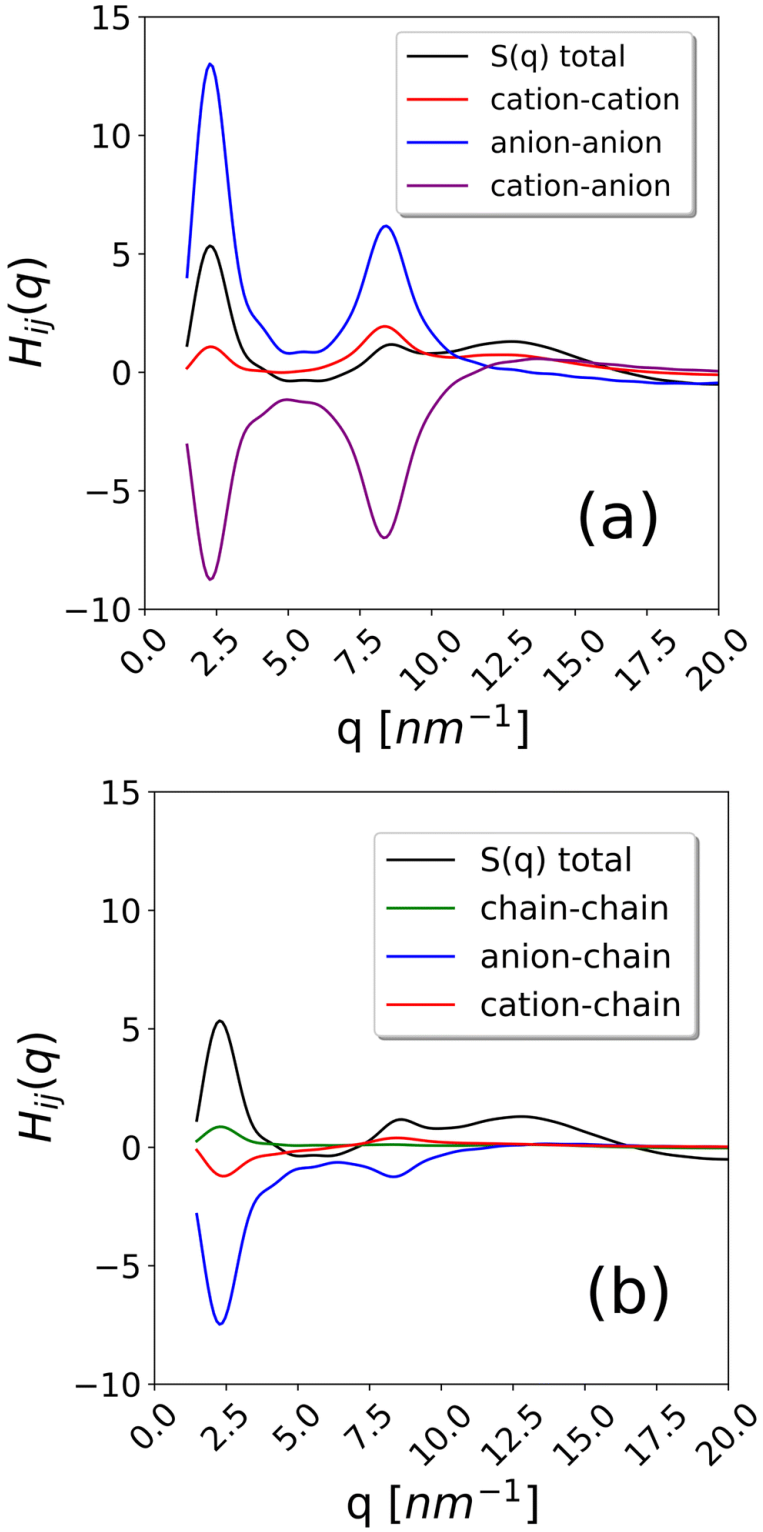

Figure 35 Partial structure factor $H_{ij}(q)$ for selected pairs to evaluate their contribution to $S(q)$ for the system $\chi_{C_{12}}$ = 0.8. (a) The anion–anion (N–N), cation–cation (C_2–C_2) and anion–cation (N–C_2) contributions and (b) the chain–chain (C_{12}'–C_{12}'), anion–chain (N–C_{12}') and cation–chain (C_2–C_{12}') contributions. The total $S(q)$ is also shown for comparison.

Finally, the position of the pre-peak as a function of the cubic root of C_{12} volume fraction, $\phi_{C_{12}}^{1/3}$, is depicted in Figure 36, where we observe a linear dependence of the pre-peak position on the parameter $\phi_{C_{12}}^{1/3}$. This trend, reported by Russina and coworkers in Ref. [125], is

reproduced almost quantitatively and might be attributed to the fact that alkyl domains on average stay closer as the content of C_{12} increases. Their structuring effect on the polar network then results in a closer packing of ions around the hydrophobic domains which is reflected in a larger value of the scattering vector. This interpretation of the results is supported by the RDFs shown in Figure 30 which highlights a closer ionic interaction as the content of C_{12} increases.

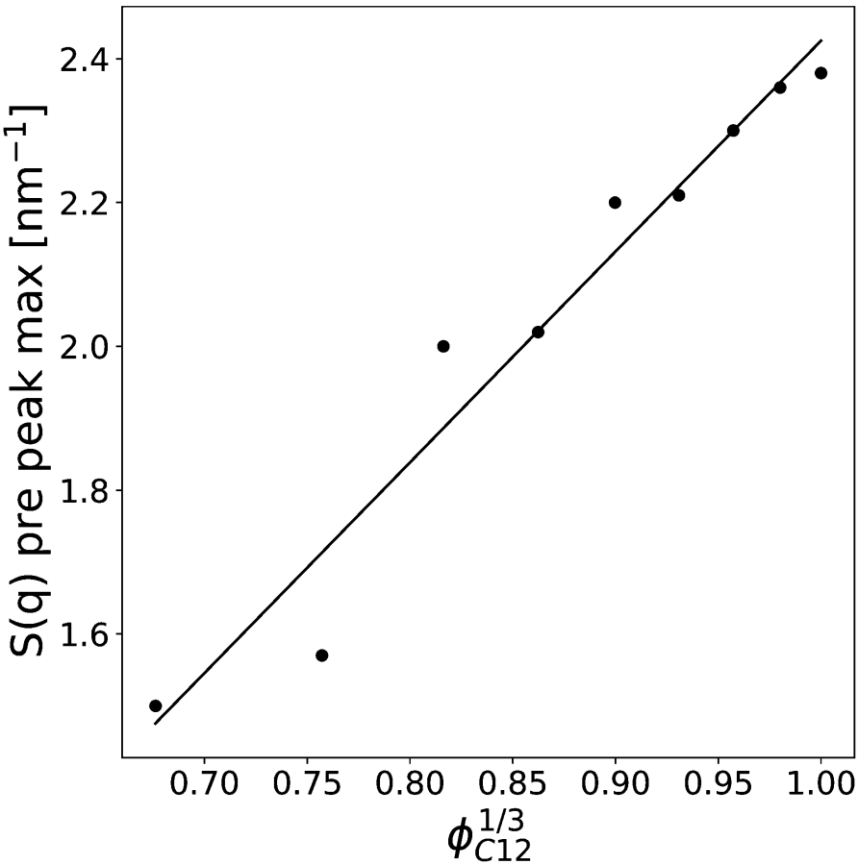

Figure 36 The pre-peak position of the simulated systems (except for $\chi_{C_{12}}$ of 0.1 and for pure C_1) are reported against the cubic root of the C_{12} volume fraction, $\phi_{C_{12}}^{1/3}$.

In Figure 37 we show the diffusion coefficients *D* obtained by a linear fit of the MSD for the three types of ions present in the mixtures. The diffusion coefficients appear to decrease rather smoothly with increasing C_{12} mole fraction because heavier cations make the movements of all ions slower. $D(C_{12})$ is scaled by a factor of about 0.50 compared to $D(C_1)$ while it appears to be scaled by a factor of about 0.75 compared to the bistriflimide anion, see Table 13. This is something that can be expected based on the Stokes–Einstein relation for the diffusion coefficient *D* of a particle with radius *r* in a medium with viscosity η,

$$D = \frac{k_B T}{6\pi\eta r}$$

and the sizes of the three particles which are in the order $C_1 < Tf_2N < C_{12}$. In fact, a quantum chemical calculation of the volume of each molecule at the **B3LYP/6-31G**** level of theory gave 101.3, 199.7 and 336.2 Å^3 mol^{-1} for C_1, [Tf_2N] and C_{12}, respectively, which corresponds to a ratio of the corresponding radii (assuming a spherical shape) of 0.67 and 0.80, respectively. The trend is qualitatively correct even though the approximation of a spherical particle appears particularly problematic for C_{12}. $D(Tf_2N)$ is intermediate compared to the

diffusion coefficients of the two cations. As can be seen in Figure 37, for pure C_{12}, the anions diffuse faster than the cations, while for pure C_1, anions diffuse slower.

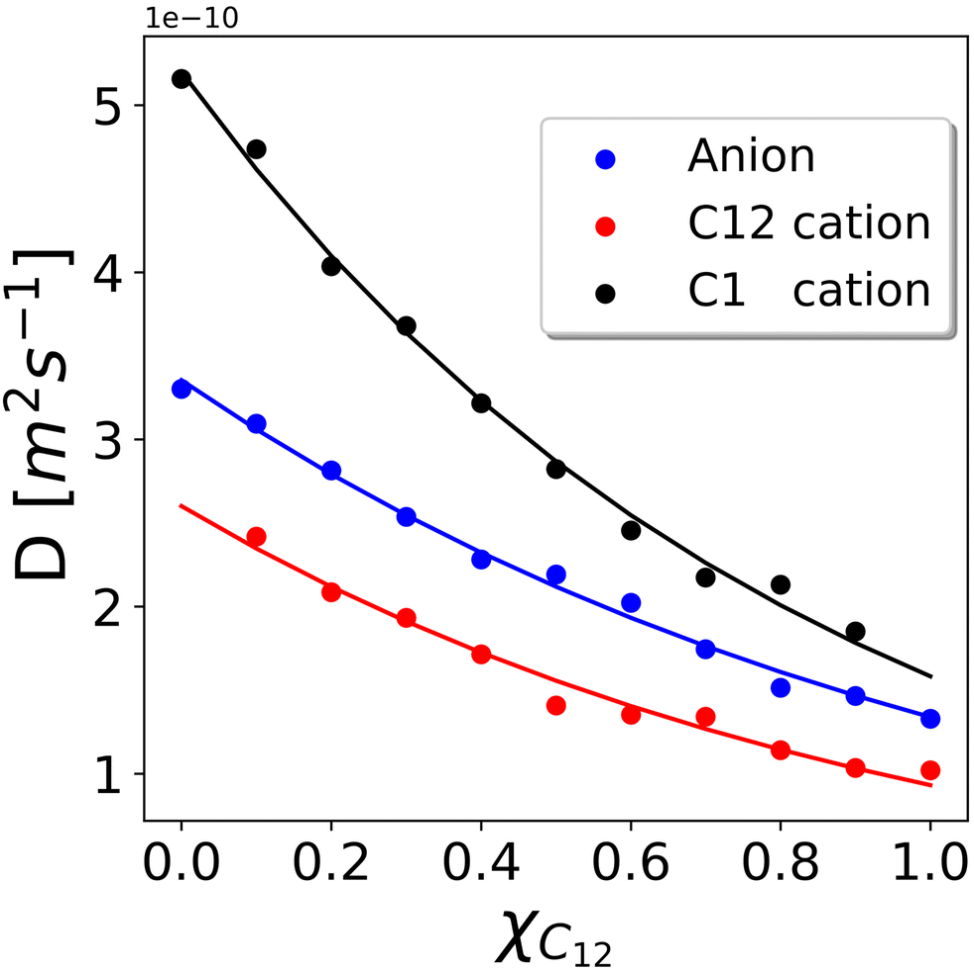

Figure 37 Diffusion coefficients D calculated according to the MSD of the C_2 atoms representing cations and the MSD of the N atoms representing anions. The error bar has been estimated to be ±0.1 × 10^{-10} m^2 s^{-1} by running three independent runs of the $\chi_{C_{12}}$ = 0.5 system. Solid lines are the fitting using the Grunberg and Nissan mixing law given in

$\chi_{C_{12}}$	$D(C_{12})/D(C_1)$	$D(C_{12})/D(Tf_2N)$	$D(C_1)/D(Tf_2N)$
1.0		0.77	
0.9	0.56	0.71	0.79
0.8	0.54	0.75	0.71
0.7	0.62	0.77	0.80
0.6	0.55	0.69	0.82
0.5	0.50	0.64	0.78
0.4	0.53	0.75	0.71
0.3	0.53	0.76	0.69
0.2	0.52	0.74	0.70
0.1	0.51	0.78	0.65
0.0			0.64

Table 13 Ratio of the diffusion coefficients of the different species

The solid lines in Figure 37 represent a fitting using the Grunberg and Nissan mixing law [126] which only involves the viscosities, η_1 and η_2, of the two pure phases to predict the viscosity η of the mixture:

$$log_{10}(\frac{1}{\eta}) = log_{10}(\frac{1}{\eta_1}) + log_{10}(\frac{1}{\eta_2})$$

Assuming the validity of the Stokes–Einstein relation for the diffusion coefficient, can be easily recast in a similar expression for *D* of a given molecule in the mixture as a function of *D* of the same molecule in the pure systems. This also allows estimating the infinite dilution limit of the diffusion coefficient of C_1 in pure C_{12} and that of C_{12} in pure C_1, which are not available from the simulations. The values in the pure systems obtained from the fitting are reported in Table 14.

	Pure C_{12}	Pure C_1
[Tf_2N]	1.34	3.35
C_{12}	0.93	2.60
C_1	1.58	5.20

Table 14 Diffusion coefficients of the ions in the pure compounds obtained from the fitting of the simulated data, 10^{-10} m^2 s^{-1}

Although the values of the diffusion coefficients qualitatively match the expected behaviour for different sizes of the ions and the viscosity of the mixture, it is worth mentioning that an unusual

trend has been observed both from experiments[127] and simulations in some ILs, where the larger cations have been observed to diffuse faster than the smaller anions, as an example in 3-ethyl-1-metylimidazolium tetrafluoroborate. The existence of partially arrested states, where the anions form a glassy network while the cations are still fluid, has been proposed as an explanation for such behaviour [128]. In the present case, however, we expect to be far from the glass transition so that normal behaviour simply depends on the viscosity and the molecular size observed. In fact, the ratio of the three diffusion coefficients is quite constant through various compositions (see Table 13), suggesting that they are simply rescaled by the viscosity of the mixture that varies as a function of the composition. The overall picture is that the dynamic properties of the constituent ions are not significantly affected by the nano-segregation and heterogeneous structure of the mixed systems. The very same behaviour was experimentally observed in mixtures of [$C_{12}C_1$im] with 1-ethyl-3-methylimidazolium salts (while in our simulations and in the experiments of Ref [125]. the long-chain dodecylimidazolium is mixed with dimethylimidazolium) and bistriflimide [129] . Similar to our results, the diffusion coefficients of the short- and long-chain cations varied smoothly with the composition following the viscosity change, while the anion was found in all cases to have an intermediate diffusion coefficient between the two cations [129] .

During the first and second year of my PhD course me and my supervisor collaborated with prof. Satoh Katsuhiko on the study of mixtures of spherical particles (LJ) and oblate discotic particles (GB) as models for liquid crystals. We produced and published two papers: the first that considers the particles interactions only as function of the particles' shape [130] and the second in which also the electrostatic interactions were taken into consideration to properly represent a model of a ILCs [131]. The second work is the natural prosecution of the first, in which charges are considered for the GB and LJ particles which are the cationic and ionic constituents of the ILCs, respectively.

Pure nematic behaviour and the effect of non-nematic particles. uncharged GBLJ

In this section, first we will briefly describe the results of the simulations for the pure GB system, then we will present a detailed discussion of two representative systems, the 3:1 system (χ_{GB} of 0.75.) and the 1:3 system (χ_{GB} of 0.25), as representative of GB-rich mixtures and LJ-rich mixtures. Transition temperatures for all systems are collected in Table 15. All systems, as already mentioned, have been simulated at the same packing fraction η of 0.5023, that is at different number densities, since composed by a different number of particles of different volume. We anticipate, however, that after the systems undergo de-mixing, the two phases in the box do not necessarily have both the packing fraction of the box, since this one is calculated for a homogeneous mixture.

		T^*_{N-I}				$T^*_{Col_h-N}$				T^*_{dem}			
GB:LJ	χ_{GB}	**heat**	**cool**	**avg**	**err**	**heat**	**cool**	**avg**	**err**	**heat**	**cool**	**avg**	**err**
Pure GB	**1.00**	15.750	15.750	15.750	0.250	4.250	4.250	4.250	0.250				
4:1	**0.80**	12.625	12.375	12.500	0.125	4.250	3.750	4.008	0.250	4.250	3.750	4.008	0.250
3:1	**0.75**	11.875	11.875	11.875	0.125	4.000	3.750	3.877	0.125	3.750	4.000	3.877	0.250
2:1	**0.67**	10.625	10.875	10.750	0.125	4.250	4.000	4.127	0.125	4.000	4.000	4.000	0.125
1:1	**0.50**	8.925	9.125	9.025	0.125	4.750	4.250	4.507	0.250	5.000	5.000	5.000	0.125
4:6	**0.40**	8.375	8.125	8.250	0.125	5.750	5.000	5.388	0.375	7.250	7.250	7.250	0.125
1:2	**0.33**	8.125	8.125	8.125	0.125	5.250	6.250	5.772	0.500	7.750	7.750	7.750	0.125
1:3	**0.25**	8.875	8.875	8.875	0.125	6.000	6.500	6.255	0.250	9.000	9.000	9.000	0.125
1:4	**0.20**	9.875	9.875	9.875	0.125	7.000	6.250	6.636	0.375	10.000	10.000	10.000	0.125
1:9	**0.10**	14.375	13.875	14.125	0.125	8.750	7.500	8.149	0.625	14.000	14.000	14.000	0.125

Table 15 For all systems studied we report here: GB disks : LJ spheres ratio, GB mole fraction, nematic-to-isotropic transition temperature, columnar-to-nematic transition temperature, de-mixing temperature. For each temperature we report the values obtained during the heating run, the cooling run, the average value and the associated error.

The pure GB discotic system has been simulated in order to have a reference to be compared with the remaining mixtures. As can be easily observed in Figure 38 the pure GB system is isotropic for scaled temperatures above T^*_{N-I} = 15.75 ± 0.25 ($\langle P_2 \rangle \approx 0$ and $\langle \psi_6 \rangle \approx 0$).

For lower temperatures it undergoes a transition into a nematic phase ($\langle P_2 \rangle > 0$ and $\langle \psi_6 \rangle \approx 0$) which is stable up to a temperature of T^* = 4.25 ± 0.25 and then a columnar hexagonal (Col$_h$) phase is observed ($\langle P_2 \rangle > 0$ and $\langle \psi_6 \rangle > 0$). For the range of scaled temperatures investigated (from 2.0 to 20.0) the scaled pressure varies from a minimum 0.5 to a maximum of 750. These results are consistent with the original work of Bates and Luckhurst [46] though they used *NpT* simulations. For example, our packing fraction corresponds to a volume per particle of 0.359: at T^* = 2.50 we obtain an average scaled pressure p^* of 24.3 and a Col$_h$ phase with an orientational order parameter of 0.92. In Ref. [46] Bates and Luckhurst, for a scaled pressure of 25.0 observe a Col$_h$ phase at = 2.50 with an average volume per particle of 0.362 and of 0.91.

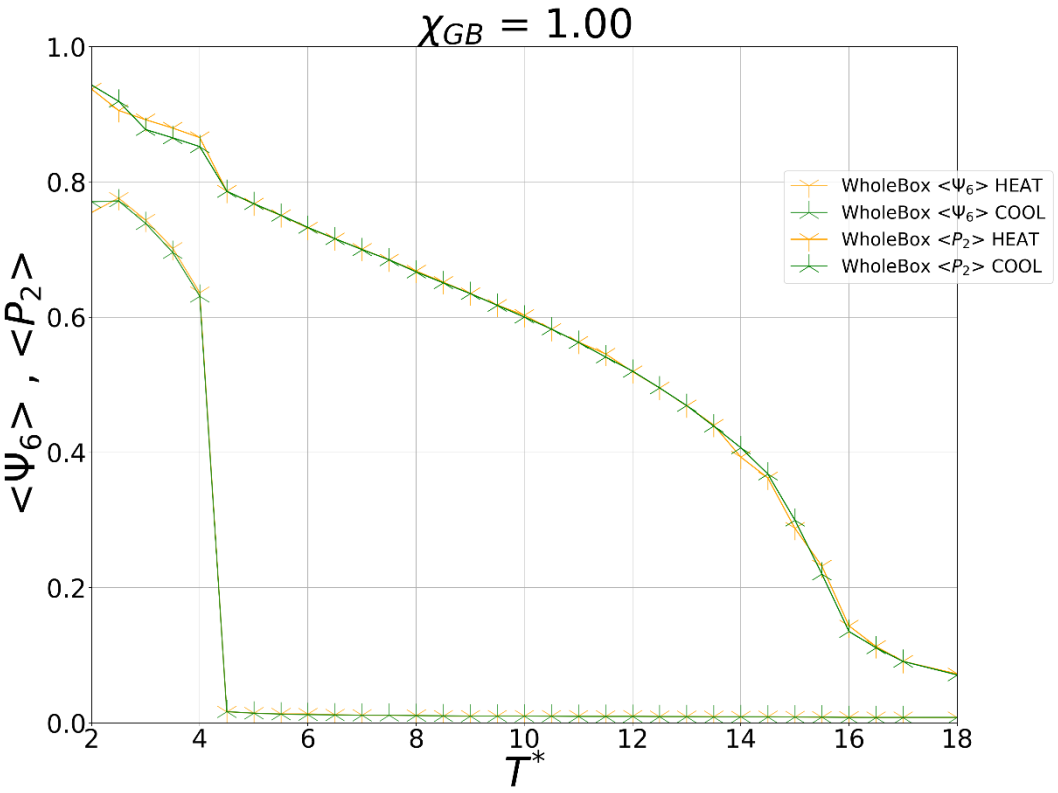

Figure 38 Second rank orientational order parameter, $\langle P_2 \rangle$, and hexatic order parameter $\langle \psi_6 \rangle$ calculated for the system composed solely of GB particles

While the jump in the hexatic order parameter is quite evident, from 0 to 0.63 (corresponding to a finite jump in the scaled energy), the isotropic-to-nematic transition is much weaker with the orientational order parameter varying smoothly and increasing up to 0.79 just before the transition into the Col$_h$ phase. The same behaviour is observed for the GB-rich systems, therefore, in order to have an estimate of the isotropic-to-nematic transition temperature we considered $\langle P_2 \rangle$ of 0.22 as the onset of the nematic phase.

The behaviour of the 3:1 system, here described in detail, is qualitatively similar to all systems having a composition with an excess of GB particles. All these systems, in the high temperature range appear to be closely related to the pure GB discotic mesogen since they all exhibit a transition from a homogeneous mixed isotropic phase to a homogeneous mixed nematic phase. On further cooling, they undergo a de-mixing into an LC phase and an isotropic phase while, at the same time, the LC phase changes from nematic to columnar hexagonal. For the 3:1 composition the isotropic-to-nematic transition is estimated to be at T^*_{N-I}= 11.875 ± 0.125 while $T^*_{dem} = T^*_{Col_h - N} = 3.88 \pm 0.125$, the analogous data for the other systems can

be found in Table 15. In Figure 39 we show some properties of the system: the temperature dependence of the HOP parameter, clearly highlighting the de-mixing; representative snapshots; and finally the mole fractions of GB particles in the various phases at different temperatures. Interestingly, the composition of the two phases, below the de-mixing temperature, is quite different from the overall composition of the box. The solubility of LJ particles in the LC Phase appears to be rather limited, since the LJ mole fraction in the LC phase, that can be obtained as $\chi_{LJ}^{LC} = 1 - \chi_{GB}^{LC}$, is below 0.05. In contrast, the solubility of GB particles in the isotropic phase, though strongly temperature dependent, is relatively high at temperatures close to the columnar-to-nematic transition point. The effect of orientational and hexatic order parameters as a function of the scaled temperature is reported in Figure 40. As we can see, the columnar-to-nematic transition is a clear first order transition, as indicated by the large jump in the hexatic order parameter, and it is accompanied by de-mixing. We also note a small hysteresis at the nematic-to-columnar transition. Instead, the nematic-to-isotropic transition shows a much less defined jump in the orientational order parameter suggesting a very weak first order transition; moreover, no hysteresis is detected at the clearing point. The identification of the phases through the order parameters is supported by the inspection of the parallel and perpendicular RDF as defined in the Computational Section. These are shown in Figure 41 and confirm the assignment of the phases.

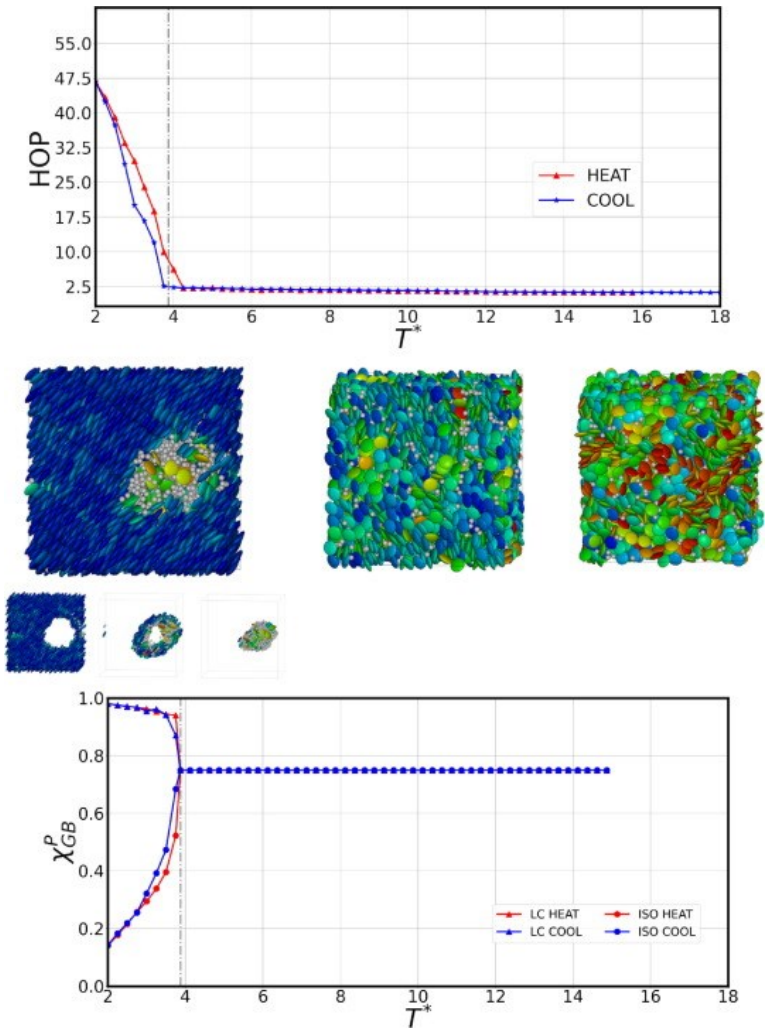

Figure 39 (Top panel) HOP parameter highlighting the de-mixing at $T_{dem}^{*} = 3.877 \pm 0.25$, vertical grey line. (Middle panel): snapshots of the 3:1 mixture ($\chi_{GB} = 0.75$) at: (left) $T^* = 2.00$, biphasic system Col$_h$ + Iso; (middle) $T^* = 7.00$, monophasic system nematic; (right) $T^* = 14.00$, monophasic system isotropic. For the low temperature biphasic system, we also show the representation of the

separated boxes of the LC phase, interphase (not characterized) and isotropic phase used for the calculation of the properties. (Bottom panel): the mole fraction of GB particles in the LC phase χ_{GB}^{LC}, (triangles) and ISO phase χ_{GB}^{ISO} (circles), for temperatures lower than T_{dem}^{*}. For higher temperatures there is only one phase in the box, so the mole fraction is constant.

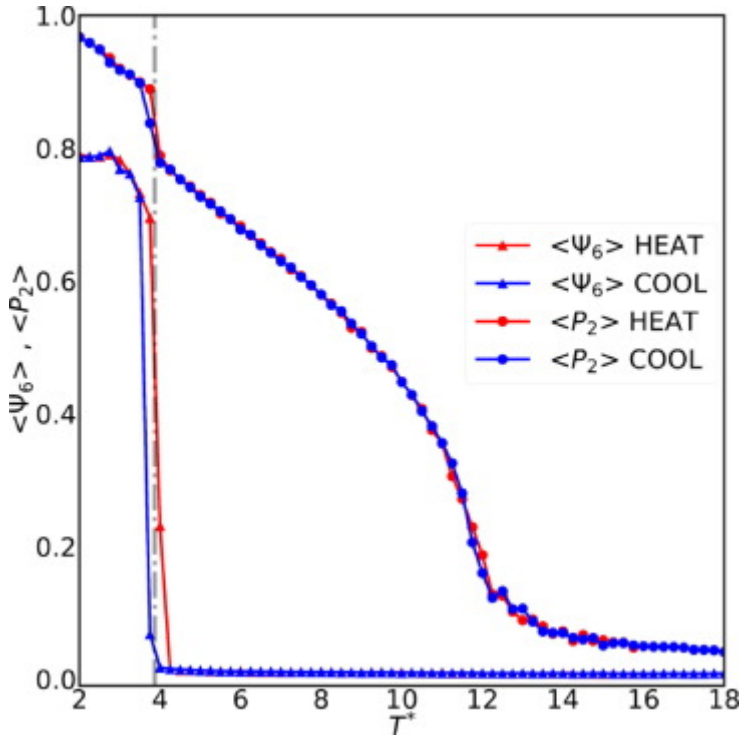

Figure 40 Orientational, $\langle P_2 \rangle$, and hexatic, $\langle \psi_6 \rangle$, order parameters for the 3:1 mixture ($\chi_{GB} = 0.75$) as a function of the scaled temperature. Below the de-mixing temperature (grey vertical line) the order parameters are calculated over the liquid crystal phase only. (red) heating run, (blue) cooling run.

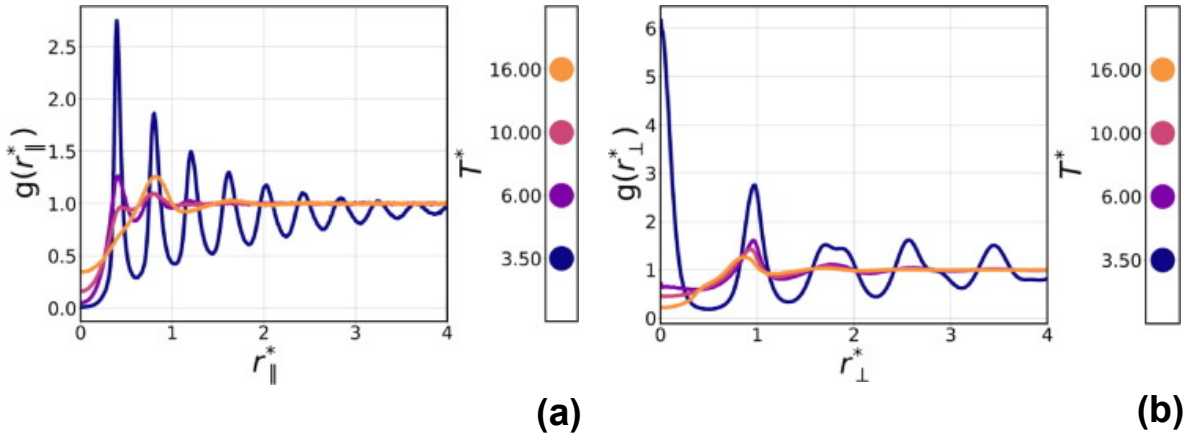

*Figure 41 RDF, as defined in the Analysis section, of the distance between two GB particles, resolved parallel to the director and perpendicular to the director, **(a)** and **(b)** respectively. Four representative temperatures are selected.*

The systems rich in LJ mole fraction have a completely different behaviour. In contrast to the previously discussed type of mixtures, now the de-mixing occurs at relatively high scaled

temperatures, see Table 15, almost concomitant with the transition of the GB particles into a nematic phase. Moreover, since the phase transition is accompanied by de-mixing, the jump in the orientational order parameter is now quite evident. For the 1:3 system, that we describe here in full detail, the transition temperatures are as follows: $T^*_{N-I} = 8.875 \pm 0.125$, $T^*_{dem} = 9.0 \pm 0.125$ and $T^*_{Col_h-N} = 6.26 \pm 0.25$. Both transitions are clearly first order. In Figure 42 we show some properties of the system: the temperature dependence of the HOP parameter, clearly highlighting the de-mixing; representative snapshots; finally, the mole fractions of GB particles in the various phases at different temperatures. In contrast with the previous case, now the solubility of LJ particles in the LC phase below the de-mixing point is indeed higher since the LJ mole fraction ($\chi^{LC}_{LJ} = 1 - \chi^{LC}_{GB}$) in the LC nematic phase is around 0.4–0.2. It becomes much lower in the columnar phase. At the same time, the solubility of the GB particles in the isotropic phase is smaller than for the 3:1 case discussed previously. The orientational and hexatic order parameters are reported in Figure 43, while the parallel and perpendicular RDF are shown in Figure 44**(a)** and **(b)**, respectively. All the data confirm the assignment of the phases as nematic and columnar, respectively. Both transitions are now clearly first order.

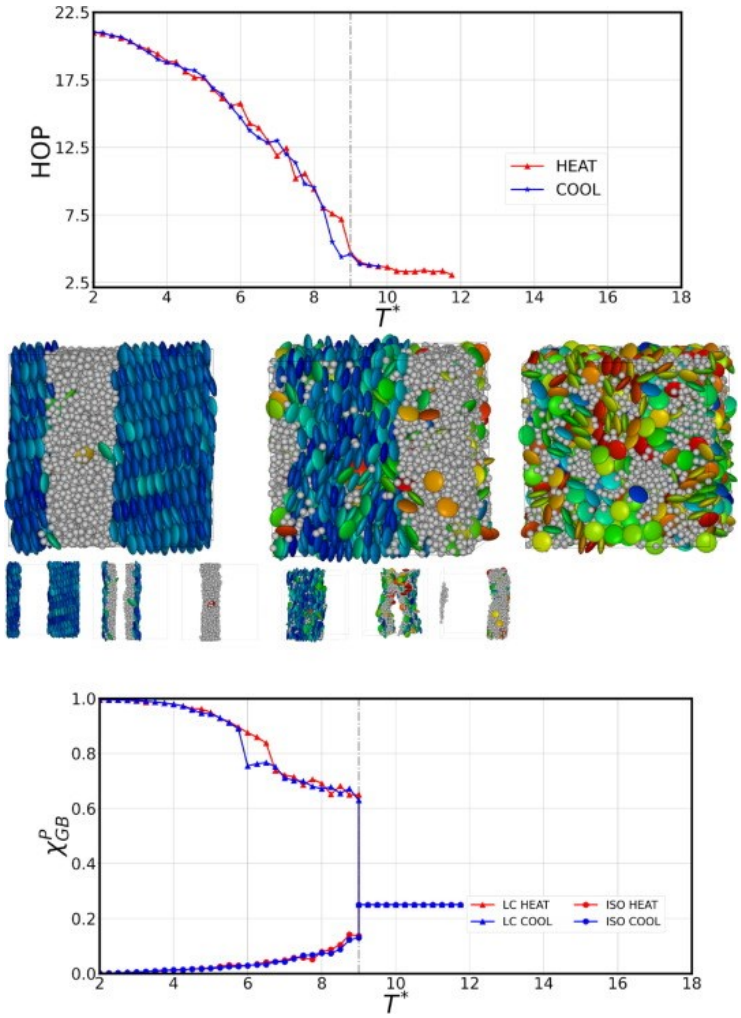

Figure 42 (Top panel) HOP parameter highlighting the de-mixing at $T^*_{dem} = 9.000 \pm 0.125$, vertical grey line. (Middle panel): snapshots of the 1:3 mixture ($\chi_{GB} = 0.25$) at: (left) $T^* = 3.00$, biphasic system Col_h + Iso; (middle) $T^* = 6.00$, biphasic system N + Iso; (right) $T^* = 9.75$, monophasic system isotropic. For the low temperature biphasic systems, we also show the representation of the separated boxes of the LC phase, interphase (not characterized) and isotropic phase. (see Supplementary Material for an enlarged version) used for the calculation of the properties. (Bottom panel): the mole fraction of GB particles in the LC phase, χ^{LC}_{GB} (triangles) and ISO phase χ^{ISO}_{GB} (circles), for temperatures lower than T^*_{dem}. For higher temperature there is only one phase in the box so the mole fraction is constant.

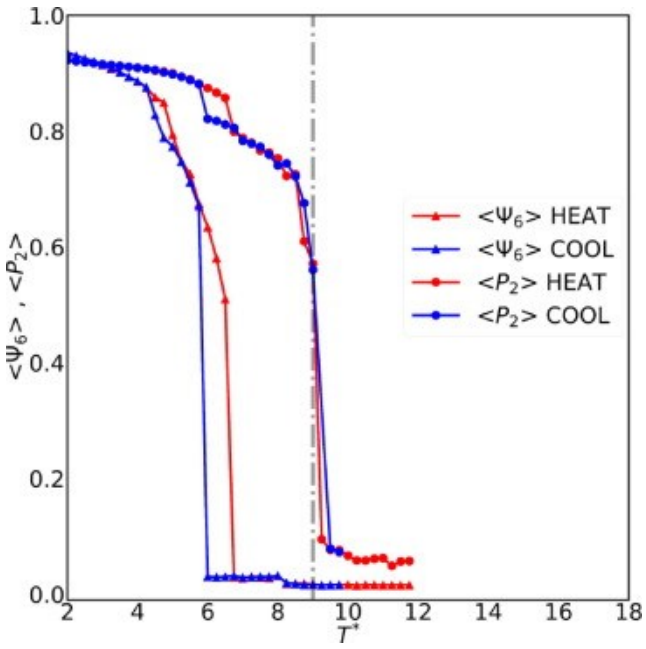

Figure 43 Orientational, $\langle P_2 \rangle$, and hexatic, $\langle \psi_6 \rangle$, order parameters for the 1:3 mixture ($\chi_{GB} = 0.25$) as a function of the scaled temperature. Below the de-mixing temperature (grey vertical line) the order parameters are calculated over the liquid crystal phase only. (red) heating run, (blue) cooling run.

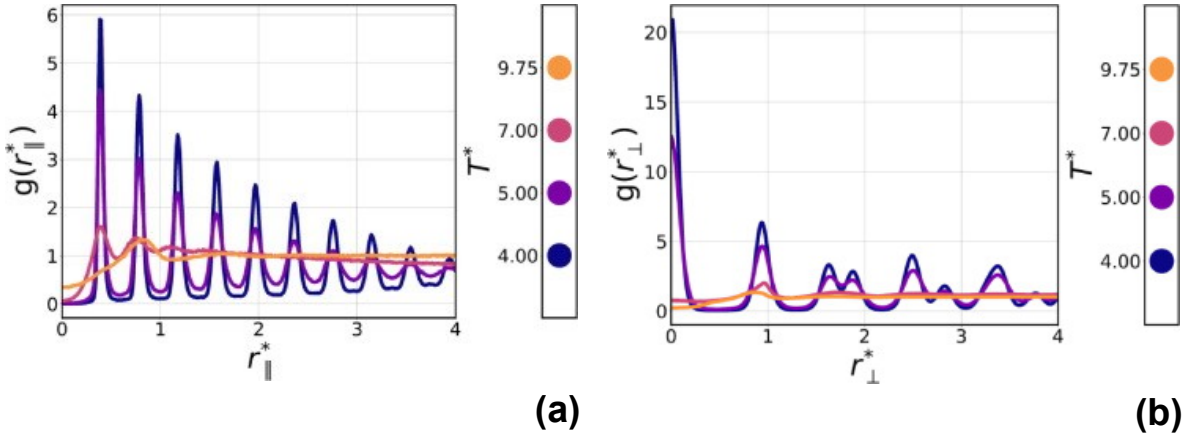

*Figure 44 RDF, as defined in the Analysis Section, of the distance between two GB particles, resolved parallel to the director and perpendicular to the director, **(a)** and **(b)** respectively. Four representative temperatures are selected.*

The phase behaviour of the systems as a function of the GB mole fraction is reported in Figure 45**.**

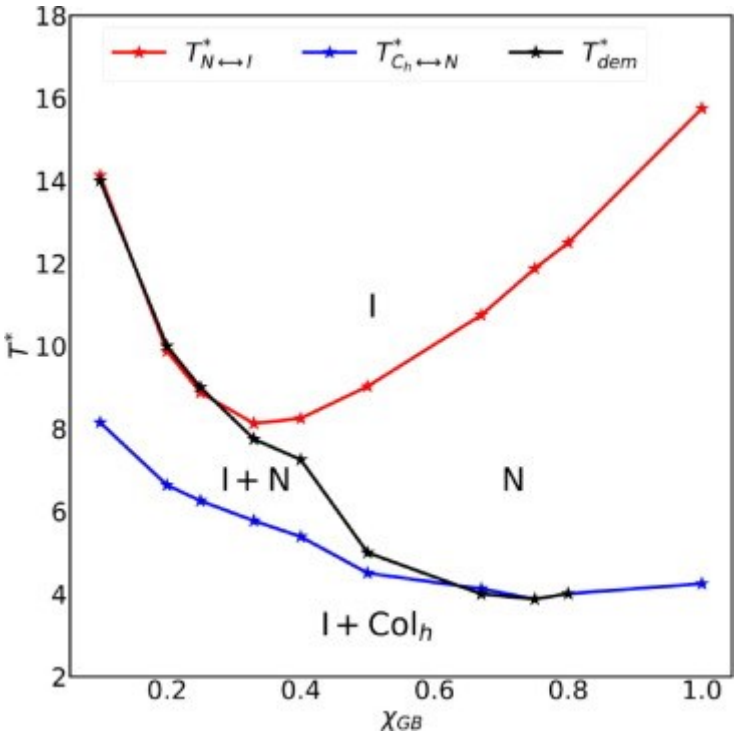

Figure 45 Phase behaviour of the studied mixtures at constant packing fraction η = 0.5023. "I" indicates the isotropic phase; "N" the nematic and "Col$_h$" the columnar hexagonal. Above the black curve the system is mono-phasic while below the black curve it is bi-phasic with a GB-rich liquid crystal phase in equilibrium with a LJ-rich isotropic phase. χ_{GB} is the mole fraction of the box.

At all compositions the GB disks exhibit the usual phase sequence, on cooling from high temperature, of isotropic-nematic-columnar hexagonal as observed in the pure GB case. However, there are two main effects to consider: the first one is the lowering of the isotropic-to-nematic transition temperature as LJ spheres are added to the GB disks. This decrement appears to be almost linear at least for GB mole fractions between 1 and 0.67; the low-temperature nematic phase consists of LJ spheres dissolved in the nematic GB phase keeping the system in single phase. In contrast, the transition from nematic to columnar hexagonal phase is almost unaffected by the presence of LJ spheres, as long as these are the minor component of the mixture and such transition occurs with a concomitant de-mixing. This latter result is in agreement with the experimental observations of Ref.[132] where the transition to a columnar phase in a mixture of triphenylene with a low molar mass solute occurred together with a phase separation on cooling from a mono-phasic isotropic phase. The depression of the isotropic-to-nematic transition temperature by the addition of LJ spheres, which has been also observed in other simulations of mixtures of anisotropic and spherical particles,[133], [134], is just a result of a perturbation of the average GB-GB interactions: [135] this can be acknowledged by plotting the orientational order parameter, $\langle P_2 \rangle$, as a function of the reduced temperature,$T_{red} = T^*/T^*_{N-I}$. As we can see in Figure 46, all GB-rich mixtures define a single curve at the nematic-to-isotropic transition. The various data are almost perfectly overlapped with the only exception of the 1:1 system which is slightly deviating. Noting that the scaled temperature T^* is defined with respect to the energy interaction parameter, see Coarse grained simulations of liquid crystals and ionic liquid crystals section, the overlap of the curves with respect to the reduced temperature suggests that the systems with a relatively small fraction of LJ spheres behaves just like the pure GB with a different energy interaction strength between the GB particles.

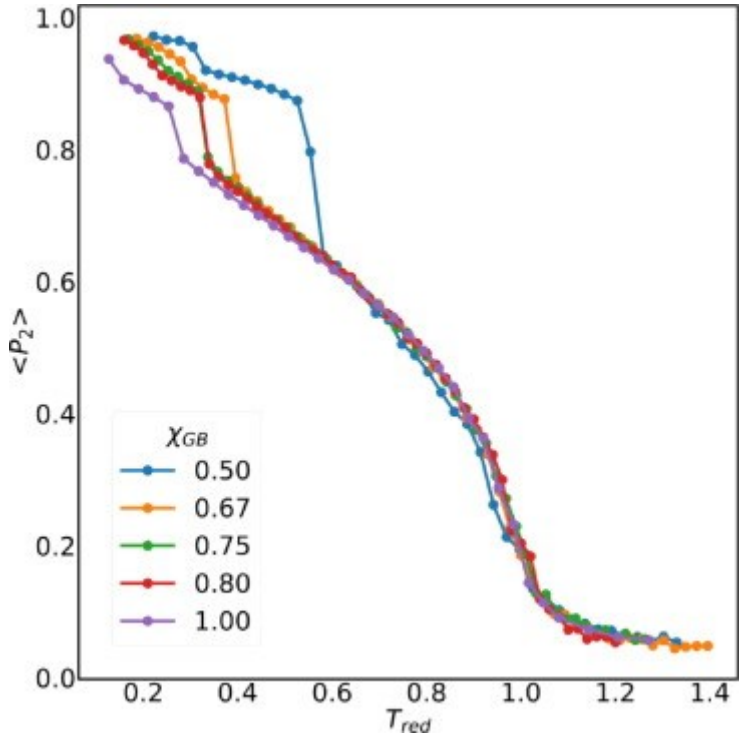

Figure 46 Dependence of the orientational order parameter, $\langle P_2 \rangle$, as a function of the reduced temperature, for the GB-rich systems.

The opposite behaviour is observed for systems with a large mole fraction of LJ spheres. Here the de-mixing occurs at the isotropic-to-nematic transition and both transition temperatures, particularly T^*_{N-I}, grow with increasing LJ content of the box. The different behaviour is a result of the different scaled pressure experienced by the systems as the ratio of GB and LJ particles is changed by keeping the same packing fraction. In Figure 47 we can see that the scaled pressure at the isotropic-to-nematic transition is roughly constant for the GB-rich systems (where GB and LJ particles remain homogeneously mixed in a single phase at the nematic-to-isotropic transition) but increases dramatically when the phase separation occurs together with the transition. The increased scaled pressure reduces the voids available in the LC phase to host the LJ sphere, and increases its order, consequently stabilizing more ordered phases.

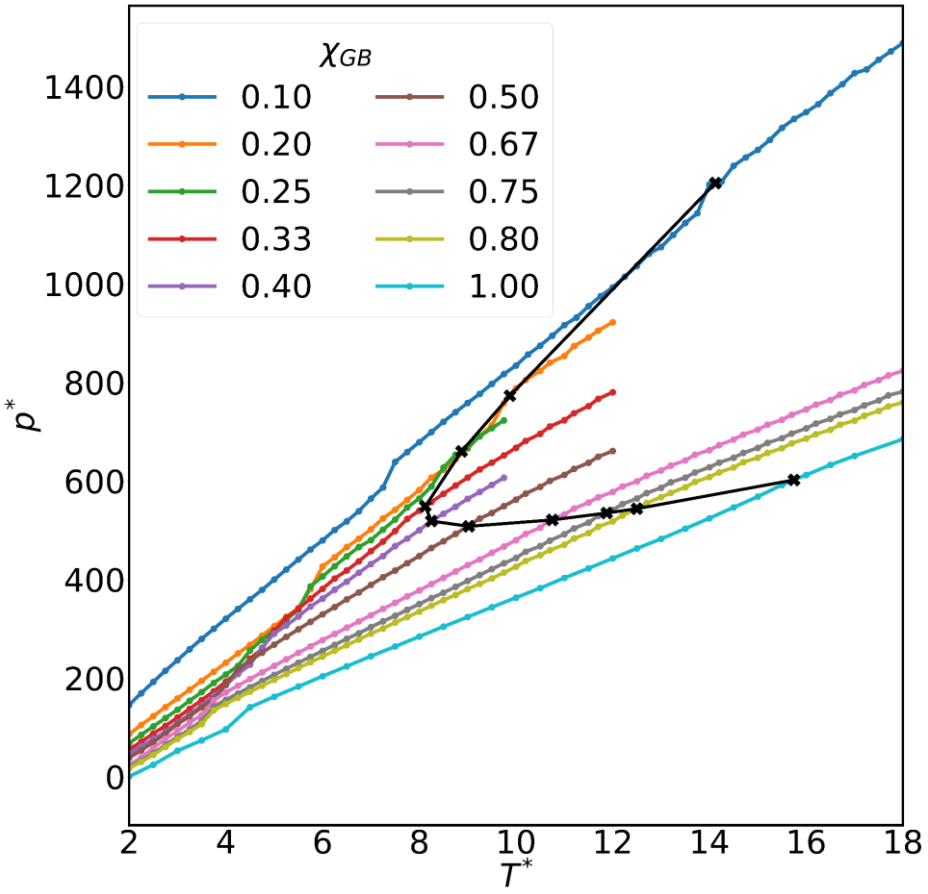

Figure 47 scaled pressure p^* as a function of scaled temperature T^* for all the systems, black crosses indicate the transition temperatures T^*_{N-I}

Finally, we should mention that the LJ particles, when phase separated, always appear as isotropic. In fact, the phase diagram of a pure LJ fluid having the same packing fraction of our systems, that corresponds to a number density of 0.9593, exhibits a liquid phase down to temperatures below 1.5.[136] In Figure 48 we plot χ_{GB}^{LC} as a function of the orientational order parameter $\langle P_2 \rangle$. With the exception of two data points for the 4:6 mixture ($\chi_{GB} = 0.40$), all data lie on a well-defined curve. For the LJ-rich systems, the orientational order parameter reaches a maximum of about 0.90 with a pure LC (*Col*$_h$) phase; for the GB-rich systems, where the de-mixing occurs at lower temperatures, the orientational order parameter grows higher even at slightly lower GB mol fractions. In short, in the *Col*$_h$ phase of GB-rich systems there is still some amount of LJ particles dissolved, while for the LJ-rich systems the low-temperature *Col*$_h$ phase is a pure GB phase. The different behaviour can be traced back to a different average pressure of the systems. In Figure 47, we show the average scaled pressure for all systems as a function of the scaled temperature. It is clear that increasing the LJ content of the mixtures, leads to an increased average scaled pressure at the same scaled temperature. Despite the fact that we used the same packing fraction, the different shape of the particles and strength of the interaction potential results in a different scaled pressure of the system.

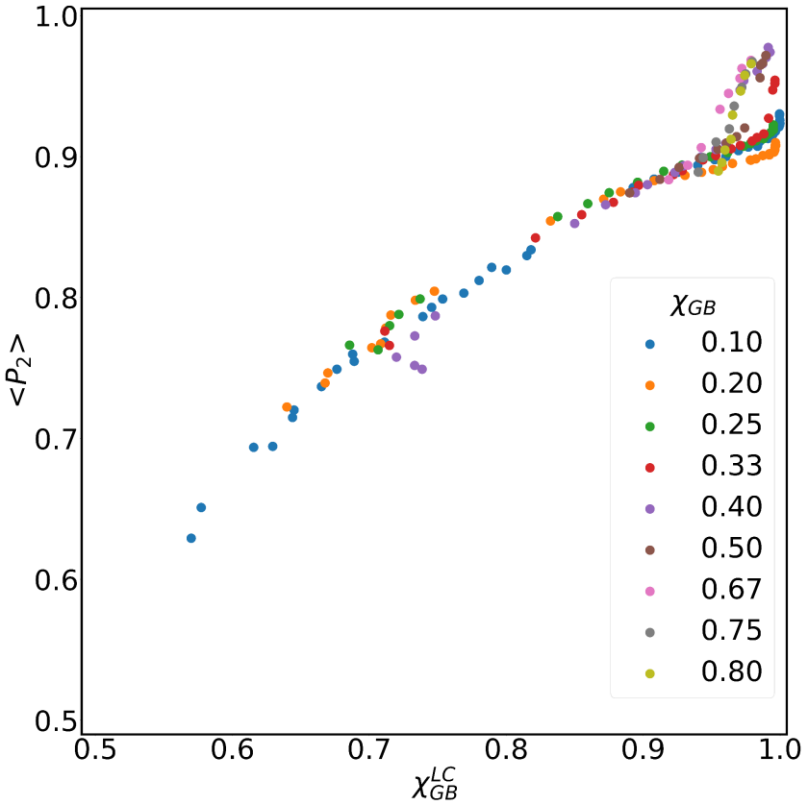

Figure 48 Mole fraction of GB particles in the LC phase, χ_{GB}^{LC}, as a function of the orientational order parameter, $\langle P_2 \rangle$ for all the systems. Data are taken during the heating runs

Effect of charges on nematogenic behaviour of stoichiometric mixtures of GB and LJ particles: a model for ILCs

The inclusion of electrostatic interaction deeply changes the behaviour and arrangement of the GB and LJ particles within the systems. The systems studied are a subset of selected stoichiometries(GB:LJ= 1:2, 1:1 and 2:1) with different charge combinations. No demixing process is found in any of the charged systems studied due to electrostatic interactions. Moreover, different structured phases are produced. This work is the natural prosecution of our previous work [130], extensively discussed above. We will discuss the systems starting from the systems with lowest GB content and then the 1:1 mixtures will be discussed. Finally, the systems with the highest GB content will be presented. In the end a brief overall discussion will be presented.

The phase behaviour of the systems with stoichiometry GB : LJ = 1 : 2 (modelling an ionic liquid crystal with a discotic divalent cation and a spherical monovalent anion) is shown in Figure 49 for the various scaled charges used, where we report the $\langle P_2 \rangle$ and $\langle \psi_6 \rangle$ order parameters as a function of the scaled temperature. Representative snapshots can be found in Figure 50. The charged systems with $q^*_{GB} = 0.50$ and $q^*_{GB} = 1.00$ have a similar qualitative behaviour. At high reduced temperatures they are in an isotropic and homogeneously mixed phase, see Figure 50**(a)**, for $q^*_{GB} = 1.00$, and the order parameters $\langle P_2 \rangle$ and $\langle \psi_6 \rangle$ are close to zero. By lowering T^* we observe an increase in the orientational order of the disks, while $\langle \psi_6 \rangle$ remains close to zero, therefore the phase observed is a nematic discotic, see Figure 50 **(b)**. In this case, when the orientational order parameter is above 0.4 the phase is considered nematic, while for $\langle P_2 \rangle < 0.2$ It is considered isotropic. When $\langle P_2 \rangle$ values are between 0.2 and 0.4 we observe the formation of nematic domains of GB particles within the box which, however, do not coherently align all in the same direction, resulting in a low orientational order parameter. This is partly due to a short-ranged microphase separation (especially for the low-charge system $q^*_{GB} = 0.50$) with the formation of domains of LJ particles that can also be seen in Figure 50 **(b)**. This explains the stable formation of an intermediate phase (observed on heating and cooling) with a low orientational order parameter. With these boundaries set, the transition temperatures isotropic-to-intermediate ($T^*_{Iso-Int}$) phase and intermediate-to-nematic ($T^*_{Int-Nem}$) are determined and their values are reported in Table 16 together with the Nem-to-Col transition temperatures ($T^*_{Nem-Col_h}$), which will be discussed later. The systems do not show hysteresis when undergoing Iso-to-Nem transition as can be seen from the $\langle P_2 \rangle$ in Figure 49, since the results of the cooling and heating run are superimposable.

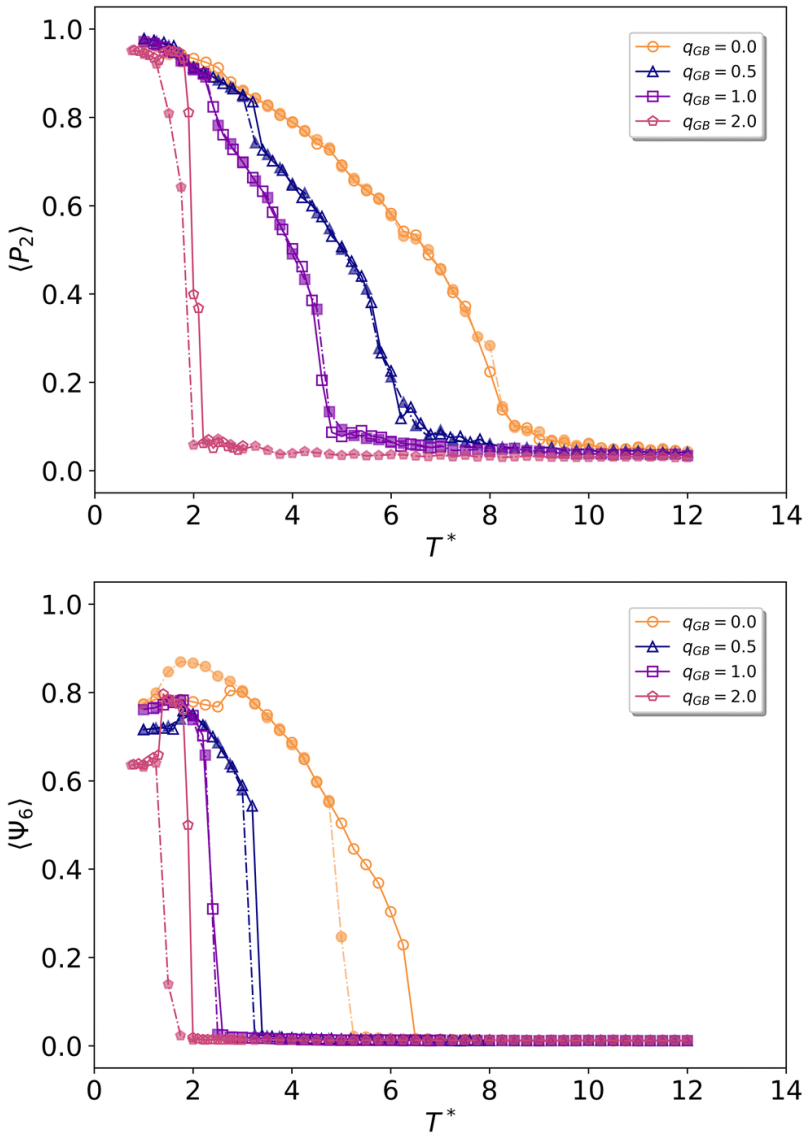

Figure 49 Order parameters $\langle P_2 \rangle$ (top) and $\langle \psi_6 \rangle$ (bottom) as a function of T^*, calculated for the GB : LJ = 1 : 2 systems with different charges. Filled markers connected by dashed lines are for cooling runs, empty markers connected by solid lines are for heating runs. These figures feature also the data of the uncharged systems for comparison

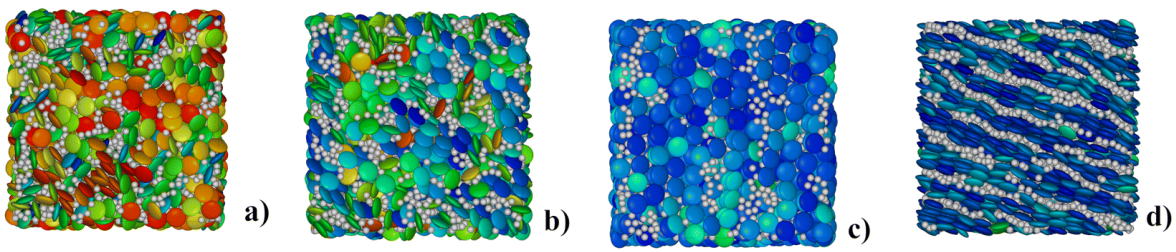

Figure 50 Snapshots representing the three main phases observed for the GB : LJ 1 : 2 system, $q^*_{GB} = 1.00$. (a): isotropic, $T^* = 6.00$, $\langle P_2 \rangle = 0.06$; (b): discotic nematic, $T^* = 4.00$, $\langle P_2 \rangle = 0.51$; (c and d): lamellar/hexagonal columnar, $T^* = 2.00$, $\langle P_2 \rangle = 0.90$, top view (c) and side view (d).

GB : LJ	$q^*_{GB}: q^*_{LJ}$	$T^*_{Iso-Int}$	$T^*_{Int-Nem}$	$T^*_{Nem-Col_h}$
1 : 2	0.0 : 0.0	8.125	7.25	5.772
	0.5 : −0.25	6.750	5.626	3.250
	1.0 : −0.5	4.800	4.500	2.400
	2.0 : −1.0	2.150	2.100	1.300
1 : 1	0.0 : 0.0	9.025	7.75	4.507
	0.5 : −0.5	8.000	7.250	2.675
	1.0 : −1.0	6.750	5.750	2.125
	2.0 : −2.0	2.000	1.500	1.250
2 : 1	0.0 : 0.0	10.75	9.25	4.127
	0.5 : −1.0	9.750	9.000	2.775
	1.0 : −2.0	8.400	7.800	2.250
	2.0 : −4.0	4.400	4.000	1.900

Table 16 Transition temperatures $T^*_{Iso-Int}$, $T^*_{Int-Nem}$, $T^*_{Nem-Col_h}$ of all the simulated charged systems alongside the transition temperatures for the uncharged systems presented before.

Further cooling of the $q^*_{GB} = 0.50$ and 1.00 systems, enhances the orientational order, thus increasing $\langle P_2 \rangle$ values. Moreover, they undergo a transition to another phase, as can be seen in Figure 50**(c)** (for $q^*_{GB} = 1.00$). The phase transition can be detected by the small jump in the $\langle P_2 \rangle$ values and by the large jump in the $\langle \psi_6 \rangle$ trends reported in Figure 49. This indicates a clear first order transition to a columnar hexagonal phase. As can be seen in Figure 50 **(d)** this is accompanied by a significant micro-phase segregation between disks and spheres resulting in a lamellar-like structure. This issue will be discussed more in details below. The systems show a hysteresis in the Nem-to-Col transitions when the particles bear no charges. This is due to the phase separation of GB and LJ particles that takes place in the zero-charge systems as it has been discussed before. In contrast, when $q^*_{GB} = 0.50$ and 1.00 they possess small or negligible hysteresis in the Nem-to-Col transition due to the electrostatic interactions that oppose the particle-demixing process. The net jumps in $\langle \psi_6 \rangle$ coincide with the transition temperature nem-to-Col ($T^*_{Nem-Col_h}$) for the system with $q^*_{GB} = 0.50$ and 1.00. Further cooling shows another small jump in $\langle P_2 \rangle$ values other than the one for Nem-to-Col transition suggesting the formation of a crystalline phase that is not further investigated.
The RDF of the different particle pairs within the system are reported in Figure 51. In panel**(a)** we note the lack of long-range correlation typical of an isotropic phase. Similar profiles are observed for the nematic phase, which also lacks any positional order. In contrast, in Figure 51**(c)** we see a strong correlation for the GB–GB pairs indicating the presence of long-range positional order. It is noteworthy, however, that the disks are not perfectly stacked face-to-face in the columnar hexagonal phase. In fact, by looking at the GB–GB trace, the first peak is found at r^* greater than 0.345 (which is the diameter of the spheres and the short axis of the ellipsoids), thus indicating that the disks' centres do not perfectly stack on top of each other. Moreover, the columnar hexagonal phase is not characterized by long columns since these

are limited by the layered structure, see Figure 50**(d)**. This point will be discussed in more details below. While the systems with $q^*_{GB} = 0.50$ and 1.00 behave in a qualitatively similar way and show analogous phase sequence, the system with $q^*_{GB} = 2.00$ behaves somewhat differently. The isotropic mixed phase is strongly stabilized by the larger charge. As the T^* is lowered, $\langle P_2 \rangle$ shows a net jump, suggesting a first order transition, but the nematic phase appears to be stable for a small range of T^* before undergoing the Nem-to-Col transition. Moreover, there is a significant hysteresis between the cooling and heating runs, see Figure 49. This different behaviour can be certainly ascribed to a stronger electrostatic interaction which favours the formation of tightly interacting ion pairs (which are actually formed by two LJ spheres and one GB disk because of the stoichiometry of the phase).

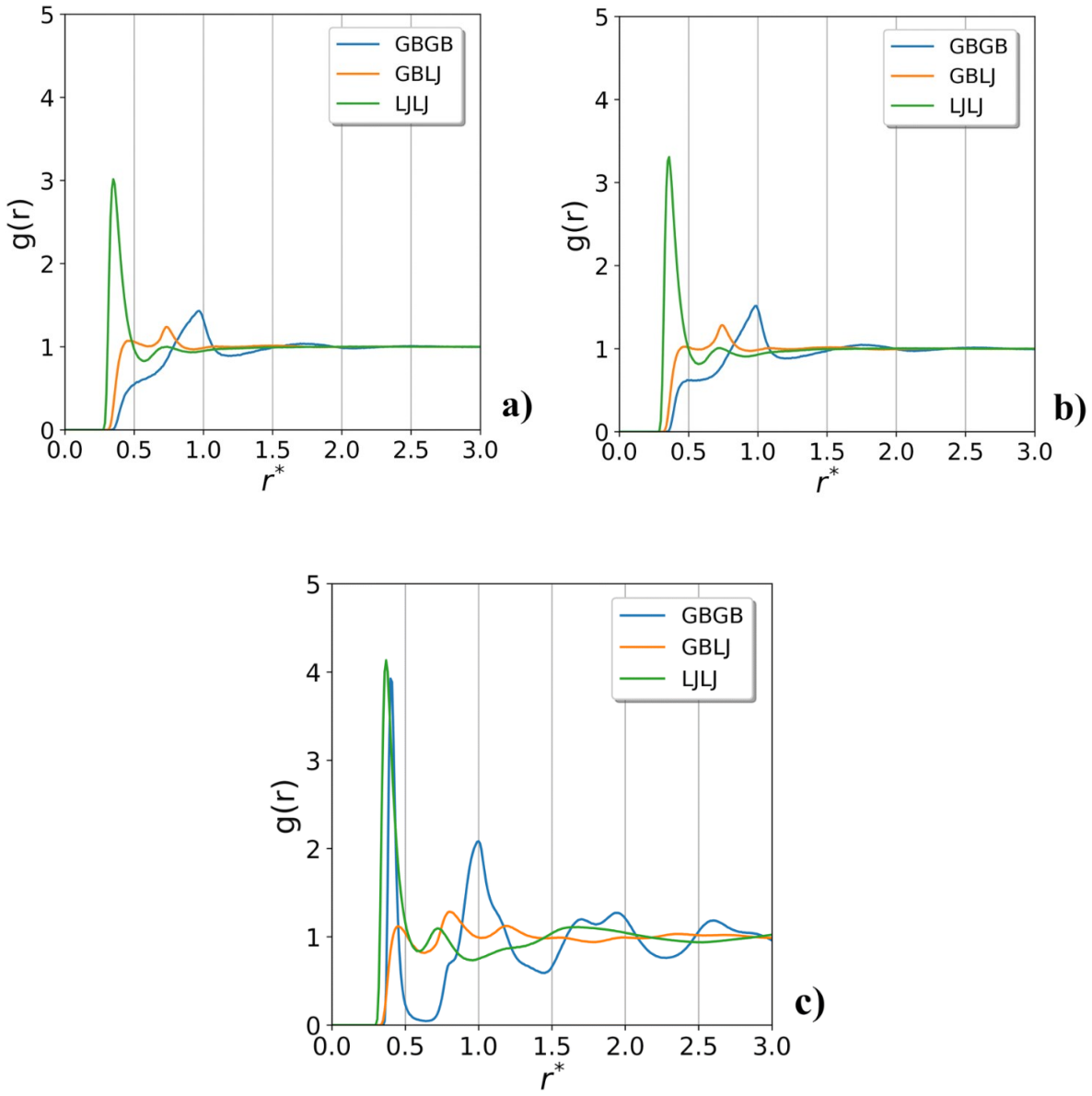

Figure 51 The radial distribution functions, $g(r^*)$, of the different particle pairs, GB–GB, LJ–LJ and GB–LJ, at selected T^* for the system GB : LJ = 1 : 2 and $q^*_{GB} = 1.00$. (a): $T^* = 6.00$, isotropic phase; (b):$T^* = 4.00$, nematic discotic phase; (c):$T^* = 2.00$, hexagonal columnar phase.

To summarize, the introduction of electrostatic interactions disfavors the phase separation observed in the non-charged systems. Nonetheless, a tendency in the segregation of the GB and the LJ particles is still present and it is manifested, as shown above, by the formation of

layers of oppositely charged particles in a similar fashion to lyotropic lamellar phases [137] or smectic phases of rod-like LCs. A similar alternation of layers was reported also in Ref.[138] where a system of oppositely charged discotic particles was investigated. The Authors observed the formation of a “smectic” phase where each alternating layer consisted of disks of the same charge. On the other hand, charged colloidal spherical particles were also found to exhibit a fluid layered structure[139], as well as the so-called inverse patchy colloids[140] modeled by a sphere with two charged regions at the poles and an oppositely charged equatorial belt. These observations point to the charge as the main ordering mechanism responsible for the layer's formation, while the particle's shape is likely to play a minor role.
Representative low T^* snapshots of GB : LJ = 1 : 2 systems are reported in Figure 52 to clearly highlight the effect of the charge. It appears that increasing the charge has the effect of reducing the thickness of the lamellae, therefore producing more intercalated discotic phases. This effect can be ascribed to the increased repulsion between like particles (forming a given layer) for higher charges. We calculated the layers thickness of the GB and LJ layers by inspection of the density profile projected along the nematic director, see Figure 53. The width at half height of the LJ and GB density profile can be taken as a measure of the thickness of the respective layers; these values are also reported in Table 17.

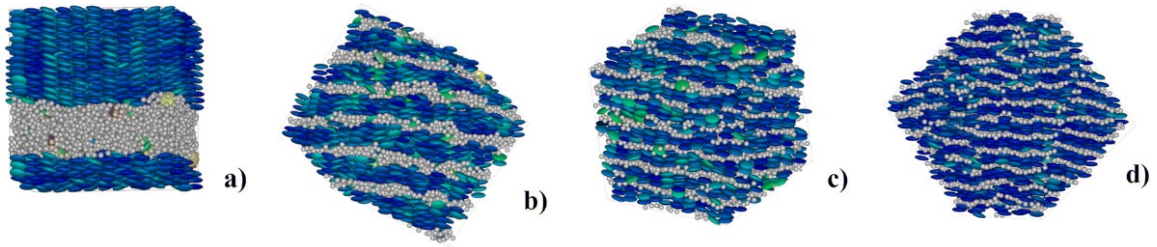

Figure 52 Low-temperature snapshots of the systems GB : LJ = 1 : 2 for different GB particles charge. (a): $q^*_{GB} = 0.00$; (b): $q^*_{GB} = 0.50$; (c): $q^*_{GB} = 1.00$; (d): $q^*_{GB} = 2.00$. The temperature,T^*, orientational, $\langle P_2 \rangle$, and hexatic, $\langle \psi_6 \rangle$, order parameters of these systems are respectively (a): 2.00, 0.91, 0.96; (b): 2.00, 0.91, 0.75; (c): 2.00, 0.91, 0.73; (d): 1.00, 0.94, 0.63.

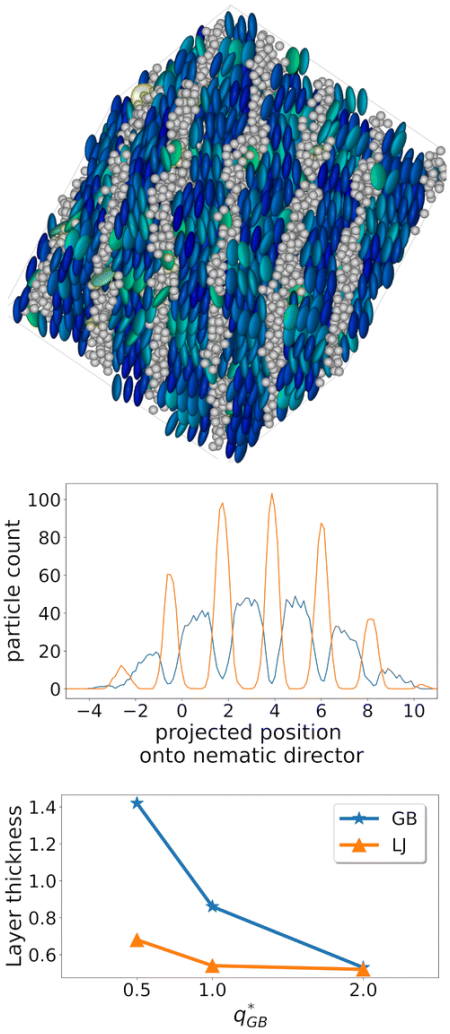

Figure 53 (Top) representative box with layered structure (GB : LJ = 1 : 2; $q^*_{GB} = 0.00$; $T^* = 2.00$); (middle) density profile projected along the director; (bottom) dependence of the layer thickness of the GB and LJ layers on the scaled charge.

	$q^*_{GB} = 0.50$	$q^*_{GB} = 1.00$	$q^*_{GB} = 2.00$
GB layer	1.42	0.86	0.53
LJ layer	0.68	0.54	0.52

Table 17 Thickness of the GB and LJ layers for the low-temperature systems with different q^*_{GB} charges

Finally, in Figure 54 we report the RDF of GB–GB distance resolved parallel and perpendicular to the director, $g(r^*_{\parallel})$ and $g(r^*_{\perp})$, respectively. They confirm the assignment of the phases in agreement with the isotropic RDF of Figure 51, while giving some additional information concerning the ordered phase. The in-plane correlation is typical of a hexagonal arrangement: for an ideal case of planar hexagonal lattice of disks we would observe a peak at 1.00 (the first shell) and a double peak at 1.732 and 2.00 (the second shell). These are clearly visible in all the isotropic RDFs and $g(r^*_{\perp})$, though the peaks are slightly scaled down because of some

degree of interdigitation of the disks. More interesting is the parallel component: for the $q^*_{GB} = 0.50$ system, the lack of a long range structure in the $g(r^*_{\parallel})$ (Figure 54**(a)**) clearly suggests that the short columns existing within each discotic layer do not correlate with the columns in the next discotic layer. In contrast, for the thinner layers of the systems with higher charge the columns are correlated through the whole box (Figure 54 **(c)** and **(e)**).

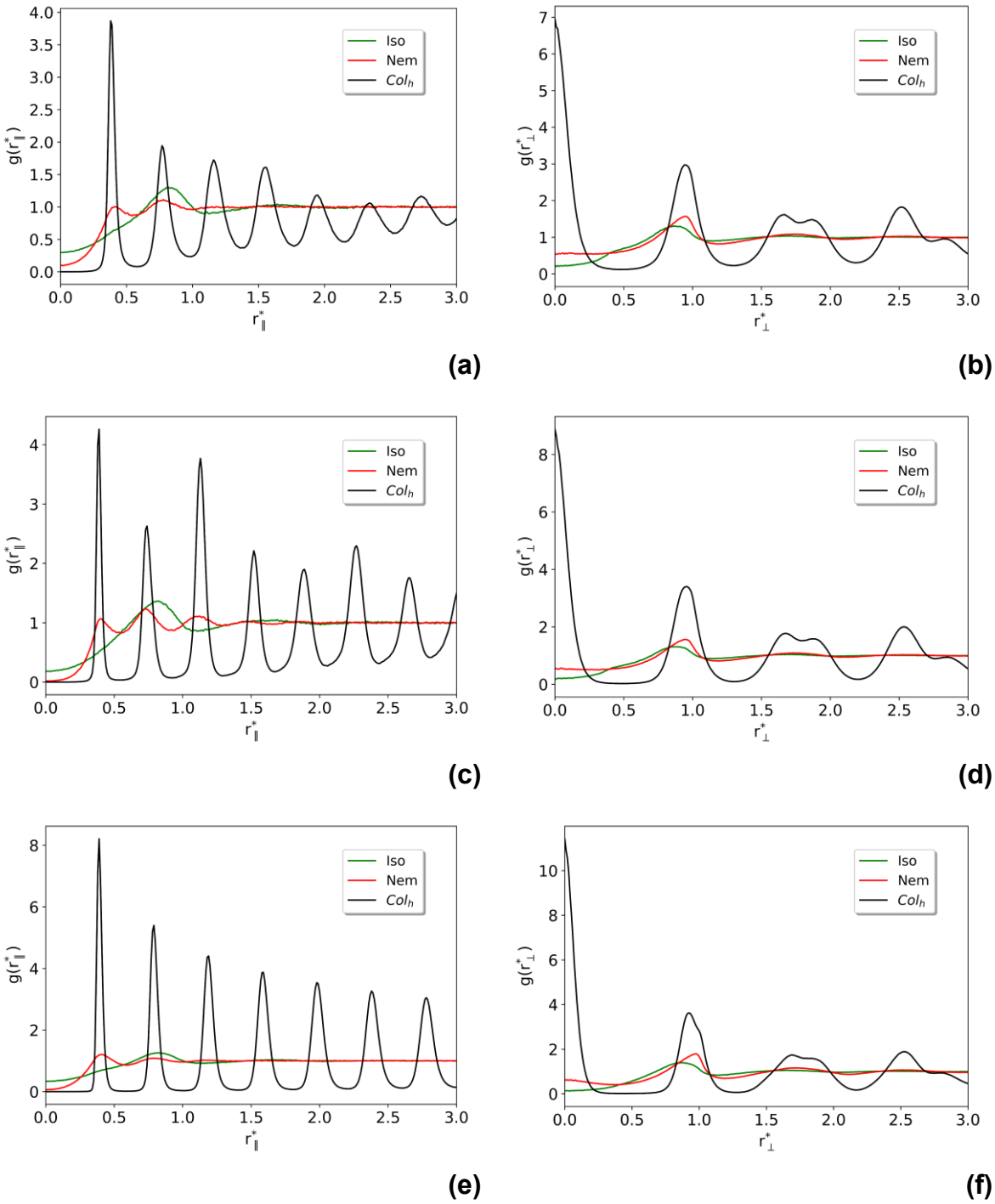

Figure 54 Parallel, left, and perpendicular, right, radial distribution functions of the discotic particles, $g(r^*_{\parallel})$ and $g(r^*_{\perp})$ respectively, resolved along the director for the Isotropic, nematic and Columnar hexagonal phases. The two figures on the top refer to the systems at $q^*_{GB} = 0.50$ while the two in the center are for $q^*_{GB} = 1.00$ and the two on the bottom are for $q^*_{GB} = 2.00$

We now consider the GB : LJ = 1 : 1 systems. Again, they have similar trends when q^*_{GB} are 0.00, 0.50 and 1.00. These systems do not possess order at high T^* ($\langle P_2 \rangle$ and $\langle \psi_6 \rangle$) both close to zero, seeFigure 55), thus being isotropic and homogeneously mixed, *e.g.* seeFigure 56**(a)** for some representative snapshots. Moreover, the radial distribution functions, not presented, do not show any long-range order for the different particle pairs, thus confirming an isotropic mixed phase. As the T^* is lowered, all the systems undergo a transition to a more ordered phase as can be appreciated by looking again at the relevant snapshot in Figure 56**(b)**. As for the GB : LJ = 1 : 2, the systems show negligible hysteresis in the Iso-to-Nem transition (transition temperatures are reported in Table 16). By continuing to lower T^* we bring the systems into a columnar hexagonal phase (Figure 56**(c)**). The transition Nem-to-Col is a sharp first order transition, as can be seen for $\langle \psi_6 \rangle$ trends in Figure 55. The systems with $q^*_{GB} = 0.50$ and 1.00 show negligible hysteresis in the Nem-to-Col transition, while the system with zero-charge shows a small hysteresis due to the demixing process of uncharged particles as already shown previously.

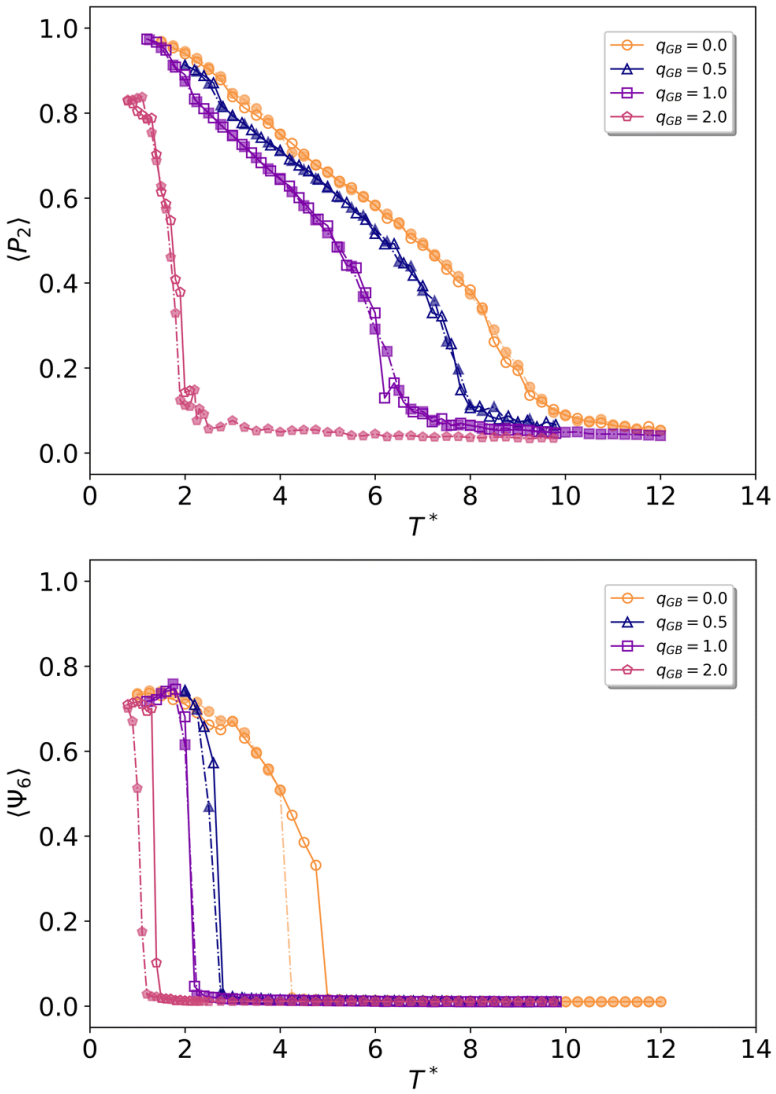

Figure 55 Order parameters $\langle P_2 \rangle$ (top) and $\langle \psi_6 \rangle$ (bottom) as a function of T^*, calculated for the GB : LJ = 1 : 1 systems with different charges. Filled markers connected by dashed lines are for cooling runs, empty markers connected by solid lines are for heating runs. These figures feature also the data of the uncharged systems for comparison

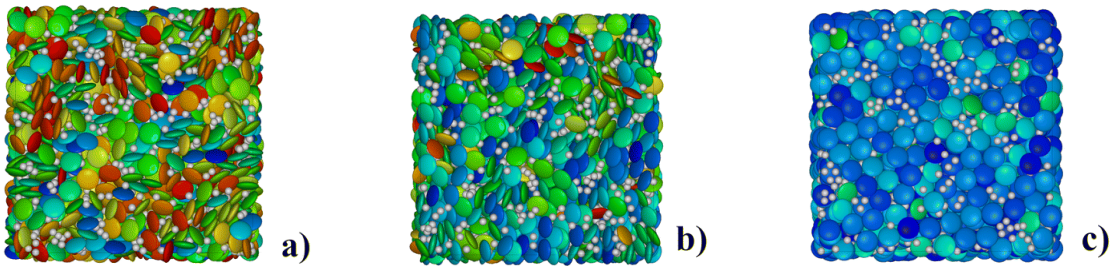

Figure 56 Snapshots representing the three main phases observed for the GB : LJ 1 : 1 system, $q^*_{GB} = 1.00$. (a): isotropic, $T^* = 8.00$, $\langle P_2 \rangle = 0.06$; (b): nematic discotic, $T^* = 5.00$, $\langle P_2 \rangle = 0.52$; (c): hexagonal columnar, $T^* = 2.00$, $\langle P_2 \rangle = 0.87$

The system with $q^*_{GB} = 2.00$ has, again, a partly different behaviour compared to the system with $q^*_{GB} = 0.50$ and 1.00, nonetheless it behaves similarly to the system with $q^*_{GB} = 2.00$ and GB : LJ = 1 : 2 stoichiometry. It is isotropic for a broad range of temperatures, as can be seen from Figure 55 the $\langle P_2 \rangle$ and $\langle \psi_6 \rangle$ order parameters are close to 0, down to $T^* = 2.00$. As the T^* is lowered the system undergoes two distinct first order phase transitions with sharp jumps in $\langle P_2 \rangle$ and $\langle \psi_6 \rangle$ values. The nematic phase has a small thermal range of existence and it shows no hysteresis in the Iso-to-Nem transition. On the other hand, the Nem-to-Col transition shows a small hysteresis (see Table 16). The low T^* snapshots of GB : LJ = 1 : 1 and all the different charges are reported in Figure 57. The macroscopic phase separation of uncharged LJ and GB occurs at low T^* and two distinct phases are found: a columnar hexagonal one and an isotropic one. The introduction of charges disfavors the de-mixing process and the segregation of phases. However, for the relatively small charge of 0.5, see Figure 57**(b)**, we still observe a clear short-range microphase segregation between disks and spheres, while increasing the value of q^* leads to a more homogeneous distribution of spheres within the GB matrix.

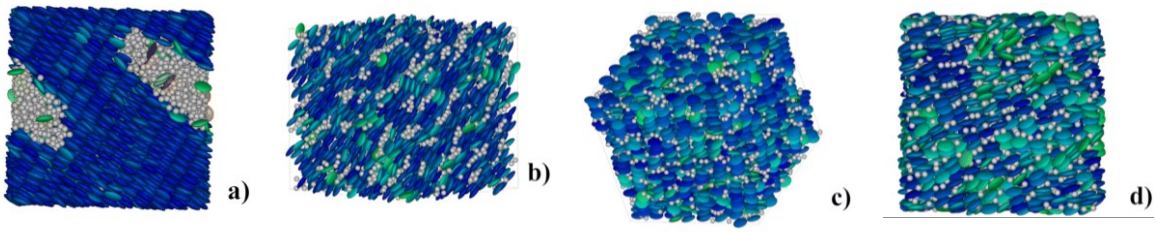

Figure 57 Low-temperature snapshots of the systems GB : LJ = 1 : 1 for different GB particles charge. (a): $q^*_{GB} = 0.00$; (b): $q^*_{GB} = 0.50$; (c): $q^*_{GB} = 1.00$; (d): $q^*_{GB} = 2.00$. The temperature, T^*, orientational, $\langle P_2 \rangle$, and hexatic, $\langle \psi_6 \rangle$, order parameters of these systems are respectively: 2.00, 0.94, 0.72 (a); 2.00, 0.91, 0.74 (b); 2.00, 0.87, 0.67 (c), 1.00, 0.83, 0.51 (d).

In contrast to the previous stoichiometry, however, the amount of spheres is not sufficient to promote the formation of separate layers of LJ particles, rather relatively small domains with finite size are formed. Moreover, as the GB disks charge increases ($q^*_{GB} = 1.00$ and $q^*_{GB} = 2.00$ in Figure 57**(c)** and **(d)**) the structure of columnar hexagonal phase boxes varies. The electrostatic interactions between GB–GB particles disfavour the face-to-face configuration and the even distribution of disks within the box produces columns with some disorder. Nonetheless, the GB particles form planes of disks arranged in a hexagonal fashion (see Figure Figure 57**(c)**) for a top view). These observations are confirmed by the parallel and perpendicular RDF in Figure 54 while for the systems with small and medium charge ($q^*_{GB} = 1.00$ and $q^*_{GB} = 0.50$) there is a clear long-range structure of $g(r^*_{\parallel})$. For the systems with $q^*_{GB} = 2.00$ we note a less clear pattern indicating a loss of correlation for the face-to-face stacking of disks within a column.

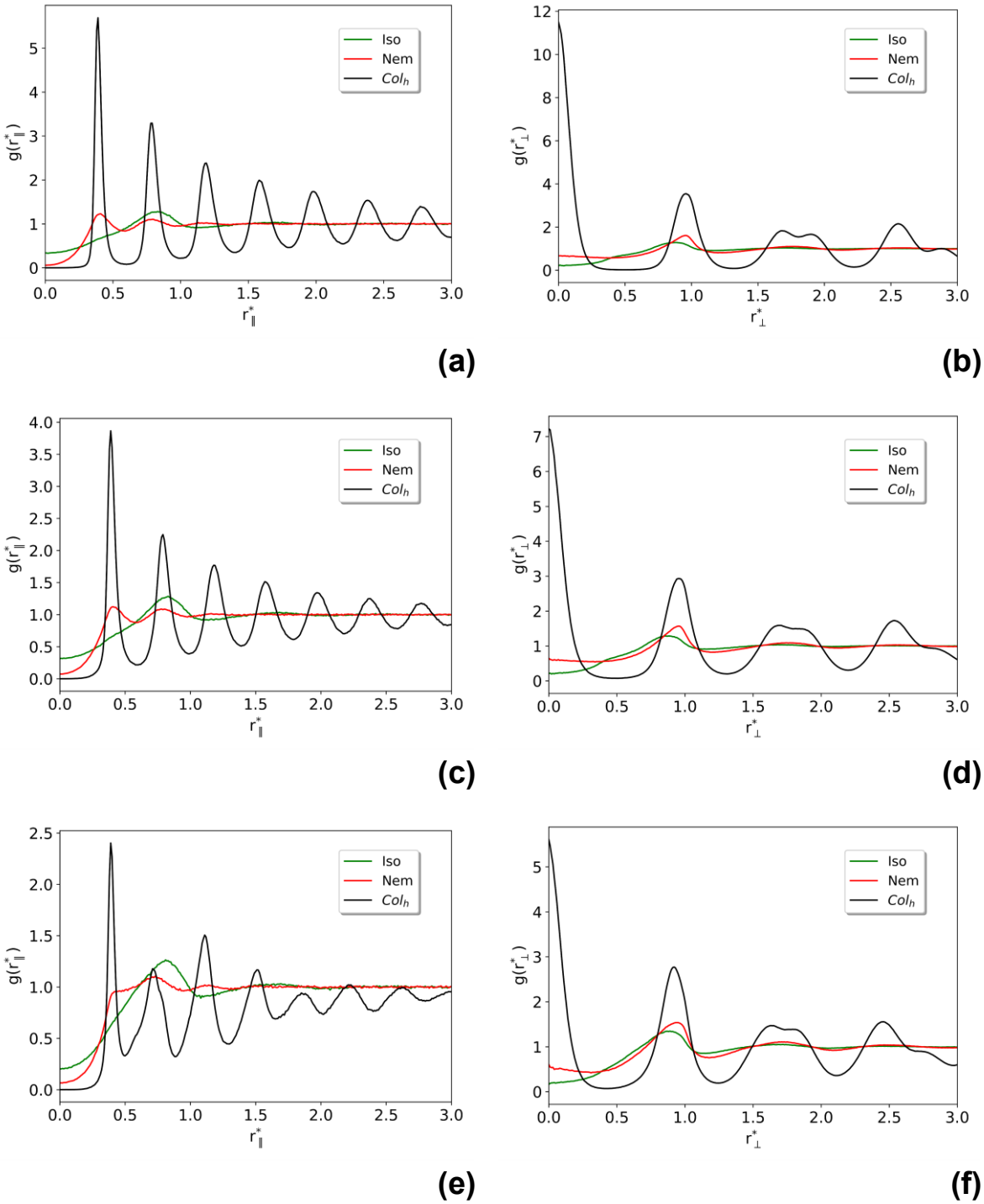

Figure 58 Parallel, left, and perpendicular, right, radial distribution functions of the discotic particles, $g(r_\parallel^*)$ and $g(r_\perp^*)$ respectively, resolved along the director for the Isotropic, nematic and Columnar hexagonal phases. The two figures on the top refer to the systems at $q_{GB}^* = 0.50$ while the two in the center are for $q_{GB}^* = 1.00$ and the two on the bottom are for $q_{GB}^* = 2.00$

Finally, we discuss the results for the GB : LJ = 2 : 1 systems. A behaviour qualitatively similar to the previous stoichiometries is found for the systems with $q_{GB}^* = 0.00$, 0.50 and 1.00. At high T^*, an isotropic mixed phase is present in all the systems, as can be seen in Figure 59 since $\langle P_2 \rangle$ and $\langle \psi_6 \rangle$ order parameters are close to 0. A snapshot of the box in Figure 60**(a)**

confirms the assignment as well as the RDFs of the particles' pairs, not reported here, show no long-range positional order. Cooling down the temperature results in the discotic nematic phase followed by a hexagonal columnar phase, see Figure 60**(c), (d)** and Table 16. The systems show negligible hysteresis for the Iso-to-Nem transitions and small hysteresis in the Nem-to-Col transition. Low-temperature trends of $\langle P_2 \rangle$ suggest the transition to other liquid crystalline phases which are not further investigate. For this case with GB : LJ = 2 : 1, at variance with the previously discussed stoichiometries, the system with a relatively high charge, $q^*_{GB} = 2.00$, appears to behave qualitatively in a similar way to its homologues with low-charge, see Figure 59. Likely, the abundance of GB particles stabilizes the nematic phase resulting in a wider T^* range of thermal stability of the discotic nematic phase. Moreover, the onset of a columnar hexagonal phase occurs at a higher T^*compared to the other stoichiometries. The system shows no hysteresis in the Iso-to-Nem transition, while a small hysteresis is found when the system has a Nem-to-Col transition.

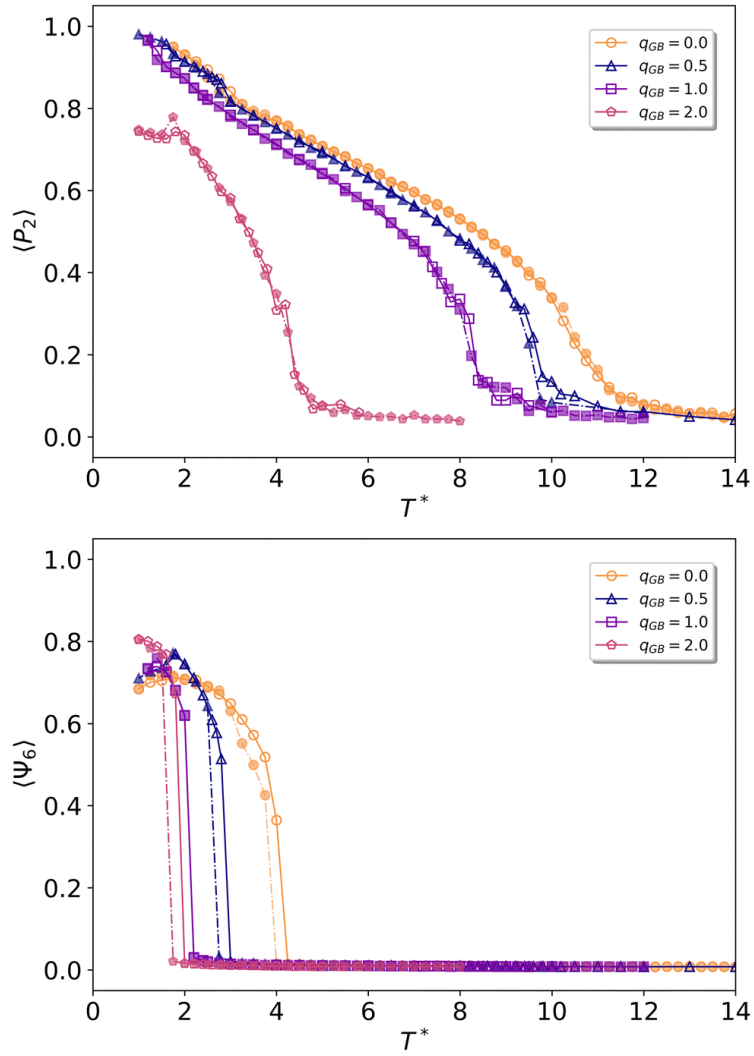

Figure 59 Order parameters $\langle P_2 \rangle$ (top) and $\langle \psi_6 \rangle$ (bottom) as a function of T^*, calculated for the GB : LJ = 2 : 1 systems with different charges. Filled markers connected by dashed lines are for cooling runs, empty markers connected by solid lines are for heating runs. These figures feature also the data of the uncharged systems for comparison

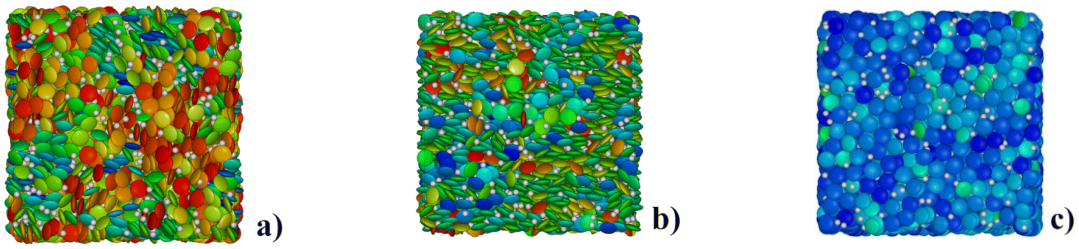

Figure 60 Snapshots representing the three main phases observed for the GB : LJ 2: 1 system, $q^*_{GB} = 1.00$. (a): isotropic, $T^* = 10.00$, $\langle P_2 \rangle = 0.06$; (b): nematic discotic, $T^* = 6.50$, $\langle P_2 \rangle = 0.52$; (c): hexagonal columnar, $T^* = 1.60$, $\langle P_2 \rangle = 0.90$

As for the other two stoichiometries investigated, we check the morphology of the low-temperature phases. The snapshots of the boxes with different charges are reported in Figure 61 and, as we can appreciate, the hexagonal columnar order is present in all cases. Moreover, except for the uncharged systems, the microphase segregation is quite inhibited.

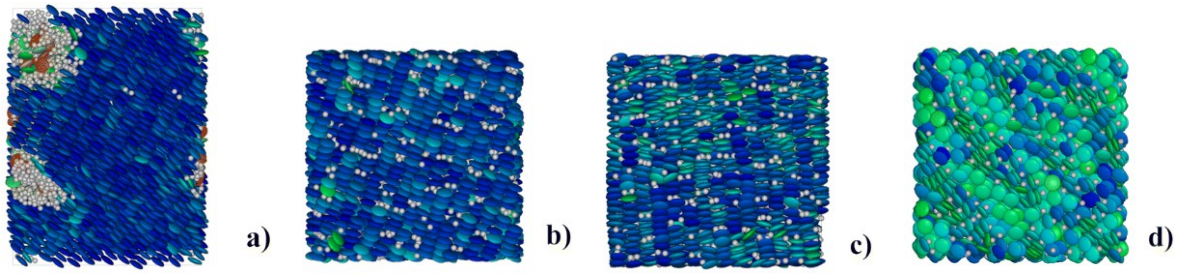

Figure 61 Low-temperature snapshots of the systems GB : LJ = 2 : 1 for different GB particles charge. (a): $q^*_{GB} = 0.00$; (b): $q^*_{GB} = 0.50$; (c): $q^*_{GB} = 1.00$; (d): $q^*_{GB} = 2.00$. The temperature, T^*, orientational, $\langle P_2 \rangle$, and hexatic, $\langle \psi_6 \rangle$, order parameters of these systems are respectively 2.00, 0.93, 0.71 (a); 1.50, 0.96, 0.73 (b); 1.25, 0.96, 0.73 (c), 1.20, 0.74, 0.78 (d).

Introducing the charge ($q^*_{GB} = 0.50$, Figure 61**(b)**), improves the dispersion of LJ particles within the box. The relatively low charge on GB particles enables the disks to be stacked face-to-face, producing highly aligned columns surrounded by negatively charged LJ particles. When the charge on GB particles increases ($q^*_{GB} = 1.00$, Figure 61 **(c)**) the columns tend to be made of tilted disks, since LJ particles,$q^*_{LJ} = -2.00$, act like the system at GB : LJ = 1 : 1 and $q^*_{GB} = 2.00$, Figure 61 **(d)**). Interestingly, the $q^*_{GB} = 2.00$ system forms a unique structure at low T^* values with a $\langle P_2 \rangle$ that never exceed 0.8 (as indicated by the more green shades of the particles), suggesting looser stacking of the disks, as can be seen in Figure 61 **(d)**. The LJ particles are evenly distributed within the simulation box. Moreover, two GB particles assemble into a “V” shaped motif with a LJ sphere in-between the “V” formed by two disks. In Figure 62 we show the same snapshot also presented in Figure 61 **(d)**, but using a different colouring scheme for the disks. These are now green or red depending on the sign of the tilt of the disk axis with respect to the director. Using these colours it appears clear that there is an alternation of layers with a different tilt in the hexagonal columnar phase.

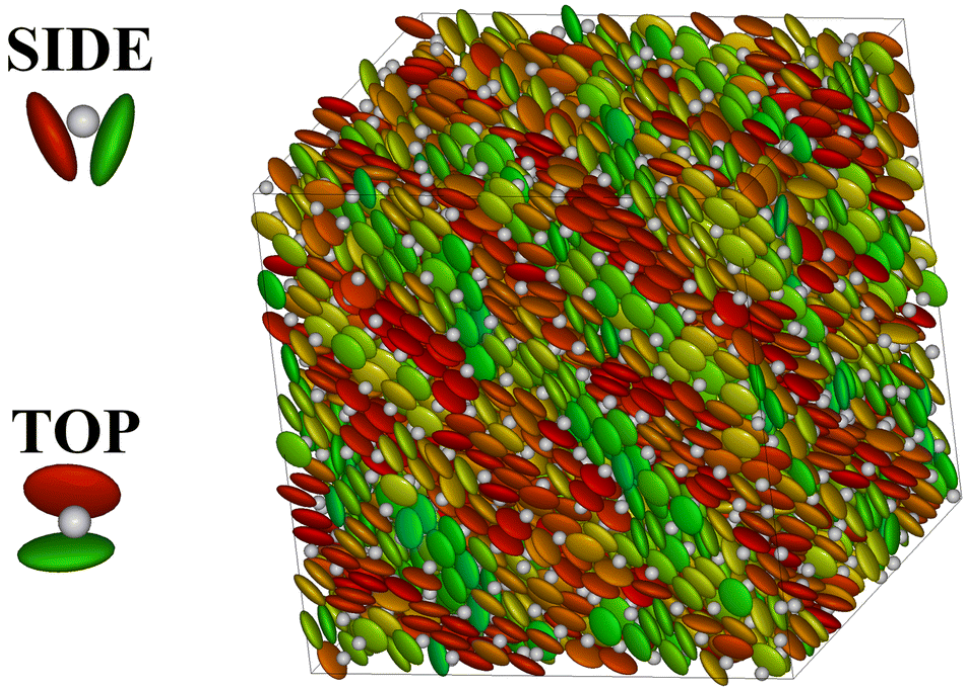

*Figure 62 The "V" motif is represented on the left, while on the right the same snapshots as in Figure 61**(d)** is shown. The slight deviations from the nematic director are highlighted in red and green depending on the direction of the tilt.*

The parallel RDF in Figure 63**(e)** confirms a complex arrangement of the disks in the frustrated columnar phase of the 2 : 1 system with $q^*_{GB} = 2.00$ in contrast with the systems with a lower charge where the columns are well defined (see Figure 63**(a)** and **(c)**). In particular, the peak in $g(r^*_{\parallel})$ at $r^*_{\parallel} \approx 0.6$, which is observed only in this system, corresponds to two disks arranged as the insert of Figure 62.

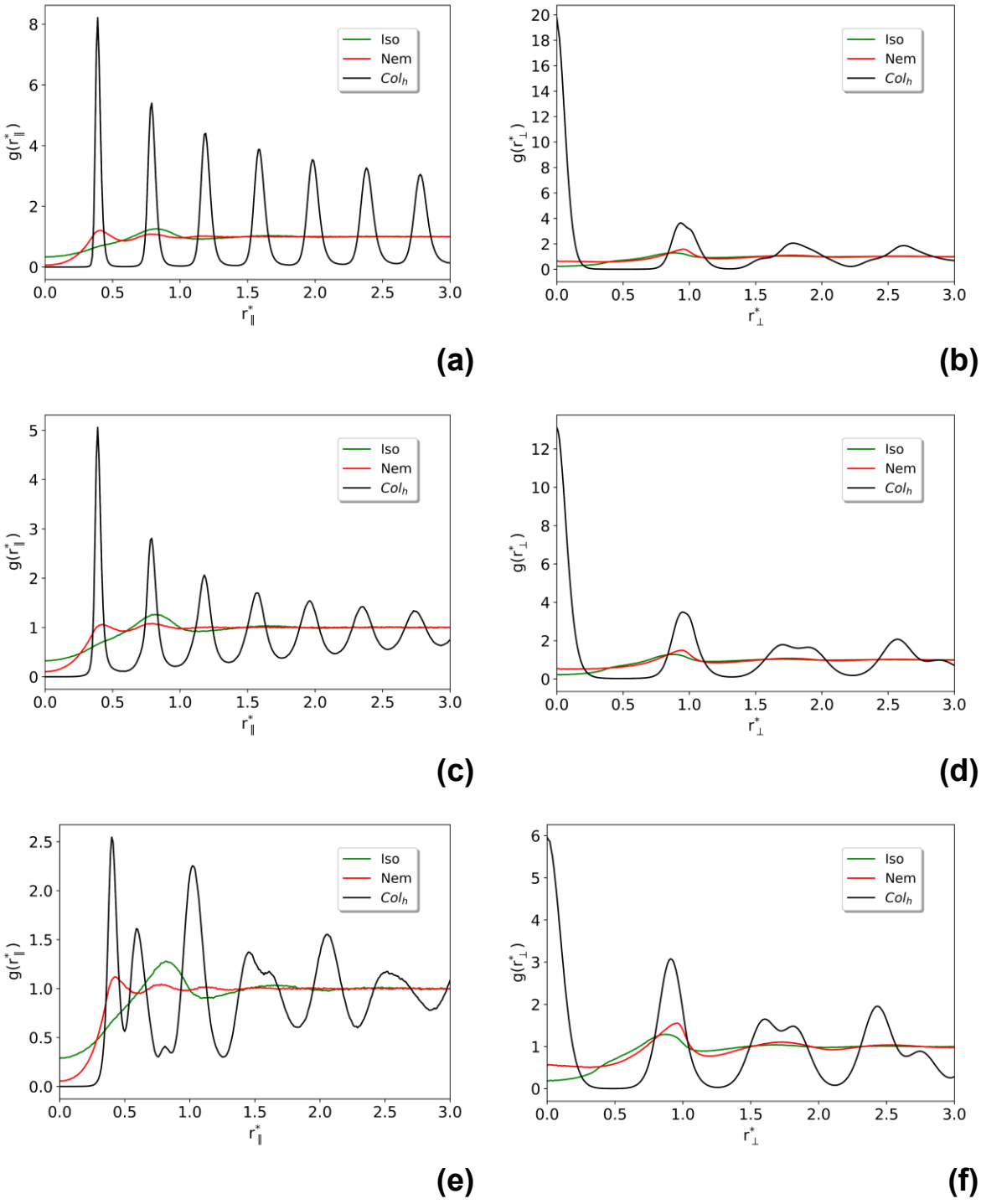

Figure 63 Parallel, left, and perpendicular, right, radial distribution functions of the discotic particles, $g(r_\parallel^*)$ and $g(r_\perp^*)$ respectively, resolved along the director for the Isotropic, nematic and Columnar hexagonal phases. The two figures on the top refer to the systems at $q_{GB}^* = 0.50$ while the two in the center are for $q_{GB}^* = 1.00$ and the two on the bottom are for $q_{GB}^* = 2.00$

To compare the results obtained we group together the important information in Figure 64. The thermal ranges of existence of the different phases are indicated with different colours for the various of GB : LJ stoichiometries and q_{GB}^* charge. The systems are all characterized by a high T^* isotropic phase and a low T^* columnar hexagonal phase. In between these two boundaries

the systems develop discotic nematic order. The overall effect of the introduction of charges is to lower all the transition temperatures, both $T^*_{Iso-Nem}$and $T^*_{Nem-Col_h}$. Moreover, the GB-rich systems have a nematic phase extending for a broader range of temperatures compared to the GB-poor ones. This is reasonable since the GB disks are the nematogenic particles. On the other hand, the columnar hexagonal order and $T^*_{Nem-Col_h}$ is somewhat affected by the GB content having all the transition T*comparable among all the systems. The effect is, however, to reduce the thermal range of the columnar phase in the GB-rich systems.

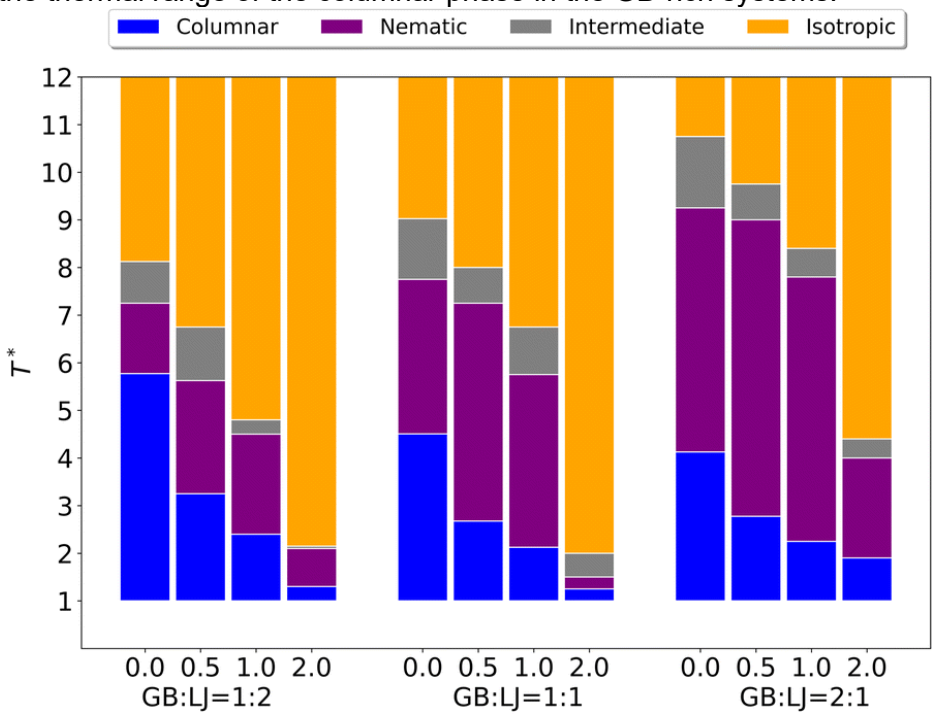

Figure 64 Diagram of the transition temperatures (see Table 16) of all the systems studied as a function of GB : LJ stoichiometry and q^*_{GB}. On the left GB : LJ = 1 : 2, in the centre GB : LJ = 1 : 1 and on the right GB : LJ = 2 : 1 stoichiometries are reported. Each GB : LJ stoichiometry consists of 4 different charges: q^*_{GB}, 0.00, 0.50, 1.00 and 2.00. Each color represents the phase in which the system is found: isotropic (yellow), nematic (purple), columnar (blue). The grey area is the intermediate region with weak nematic order.

The state points investigated cover a wide range of scaled pressures. Similar values were found for the non-charged mixtures as well as for the pure discotic GB investigated by Bates and Luckhurst [46]. We also report in Table 18 a summary of the type of columnar mesophases formed, for an easier reference. We focus on the Col phase since all systems exhibit similar isotropic and nematic phases, the main differences among them being in the degree of nano-segregation, which is absent for the highly charged cases and not-negligible (even though limited in scale) for the weakly charged ones.

GB:LJ | q^*_{GB}	**0.5**	**1.0**	**2.0**
1 : 2	Thick Lam, Hex Col within GB layers, no correlation between different layers	Medium Lam, columns correlated through several layers	Thin Lam, columns correlated through several layers
1 : 1	Hex Col, average correlation along a column	Hex Col, weak correlation along a column	Hex Col, very weak correlation along a column
2 : 1	Hex Col, high correlation along a column	Hex Col, high correlation along a column	Frustrated Hex Col with modulated tilt of the director

Table 18 Summary of the columnar phases observed for the systems investigated. Lam indicates lamellar structure, Hex Col a hexagonal columnar structure. All systems also exhibit a Nem and Iso phase though not indicated in Table

All atom simulations of anisotropic ILCs based on Gallic Acid derivatives

The results of the MD simulations of the Gallic Acid derivatives are presented here. The ones for the smaller systems are reported first, to show the thermotropic behaviour of the ILCs and the effect of using scaled charges. After a preliminary discussion on the smaller systems, the bigger systems will be presented to show how the water and water concentration affect the columnar structures.

The BzNMe3 system is presented as an example of smaller systems. The columns of the columnar liquid crystal structure are ionic channels made of anions, [BF_4], and cations, gallic acid ammonium derivatives. They appear as in Figure 65, where the anionic species are depicted as blue tetrahedra while the N atoms of the cations are shown as red spheres. They make the core of the channels and due to their ionic nature they create a region which is highly hydrophilic. On the contrary the hydrophobic moieties, which are made up of alkyl chains and aromatic rings represented as cyan lines and pink hexagons, respectively, act as spacers between columns.

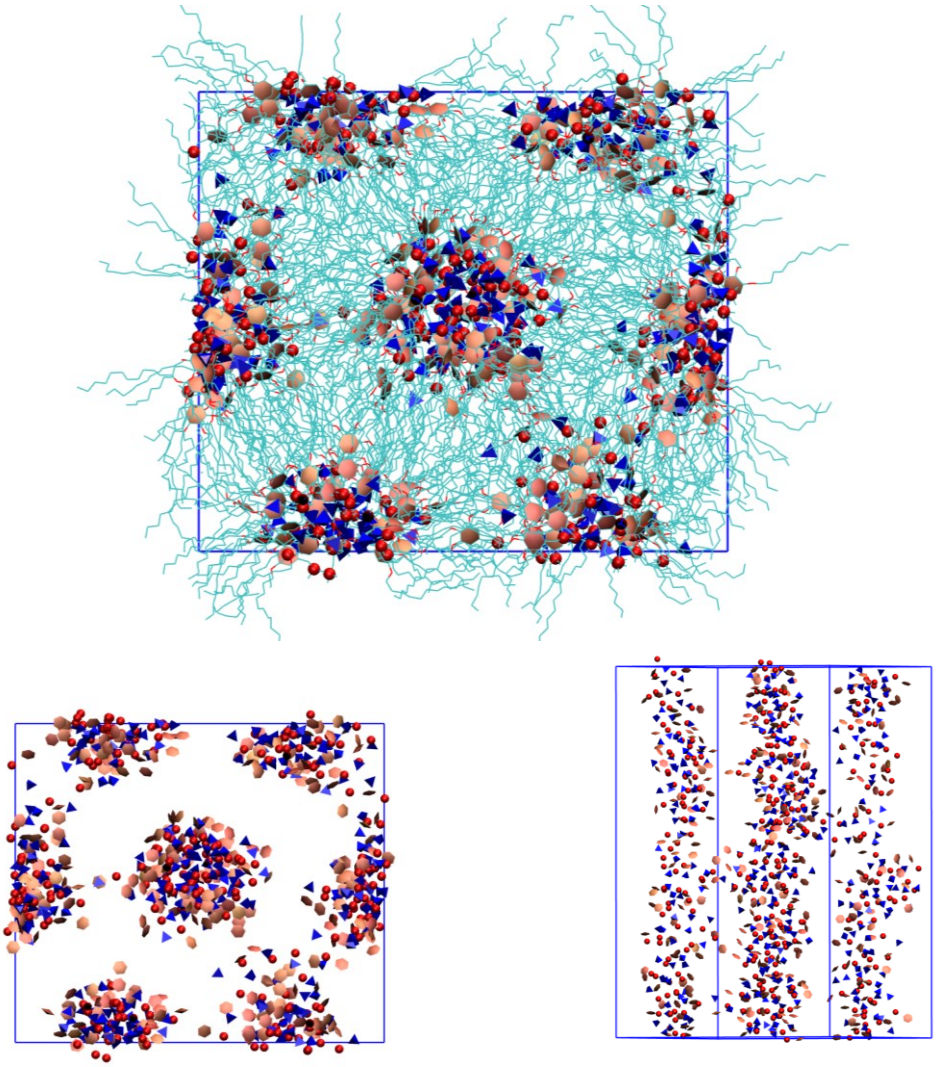

Figure 65 Columnar structure as seen from above (top figure) with the alkyl chains colored in cyan, the anions in blue, the N atoms of cation in red and the aromatic rings in pink. The two figures on the bottom highlight only the ionic moiety of the system and two different perspectives are shown, top view on the left and side view on the right . The temperature is 350 K

The box contains 4 independent columns and it is built starting from unit cells of a hexagonal lattice containing 1 column each as illustrated in the Figure 66(right). Four hexagonal lattice unit cells are employed to build a rectangular system using periodic boundary conditions with columns arranged in an hexagonal fashion, as illustrated on Figure 66(left). Thus, the smaller systems presented contain 4 columns.

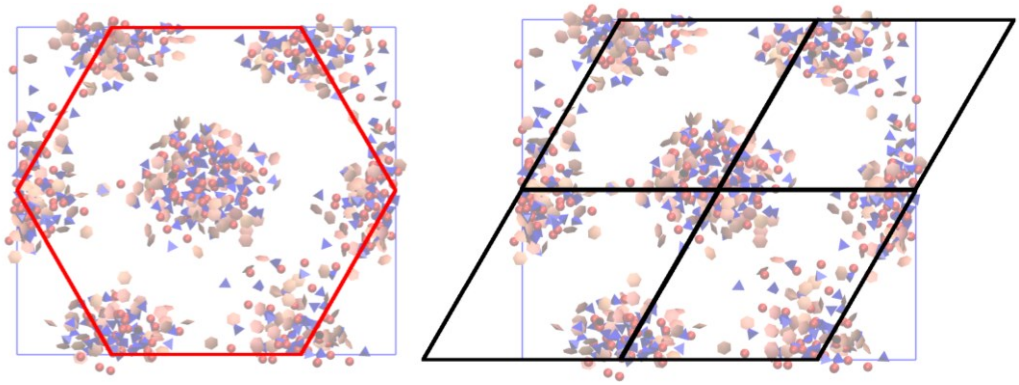

Figure 66 The hexagonal arrangement of columns is indicated as the red line on the left. Four hexagonal lattice unit cells, depicted on the right with black lines, are the minimum numbers of elementary units to build a rectangular system with periodic boundary conditions that contains hexagonal ordered columns. The snapshot is the same presented in Figure 65, bottom left

The close range ordering of ionic species is evaluated by looking at the radial distribution functions, reported in Figure 67, between B-B, N-N and N-B pairs of all the different Gallic Acid derivatives. It is noteworthy to mention that the microstructure of the ionic pairs attains to the same pattern in both the full charge and scaled charge systems when regarding the same species among those studied. As we can see later, the full charge systems have a weaker response to temperature, simulating the column's existence above the melting temperature of the ICLs and more viscous behaviour. Nonetheless, the columns appear similar in all systems with subtle differences in the microstructure given by the additional CH2 group on the BzNEt3 system. In fact PhNMe3 and BzNMe3 have an almost identical ionic pairs pattern, while BzNEt3 differs from the other two. The scaled charge systems' results will be presented as examples for both the full and scaled charge. The cation RDFs, red lines in Figure 67, show a first peak at 0.63 nm for both the trimethylated species while the triethyl ammonium derivative have a first peak at slightly higher distance, 0.74 nm, due to the presence of the additional CH2 group. The second peak is around 1 nm for all the systems but appears well defined in both the PhNMe3 and BzNMe3, while in the case of BzNEt3 it is more like a shoulder. A third broad peak is spotted at around 1.36 nm in all the systems. It displays the typical structure of ionic liquids where the cation-cation and anion-anion RDFs have a maximum in correspondence of the minimum of the cation-anion pairs.

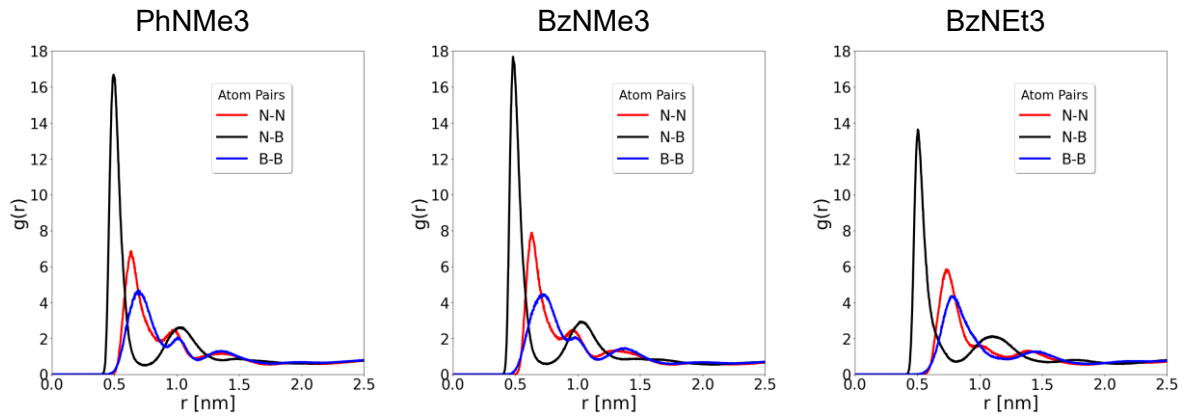

Figure 67 Radial distribution functions, g(r), between the ionic species of the different systems. N-N, N-B and B-B pairs are represented in red, black and blue respectively.

The first peak represents the average distance between the nitrogen atom of two adjacent Gallic Acid units laying on the same plane. Moreover, this distance is also the stacking distance of two units along the column. This information is clearly depicted in Figure 68: 4 gallic units form a supramolecular discotic unit, on the left. Two of them, on the right, are stacked one on top of the other.

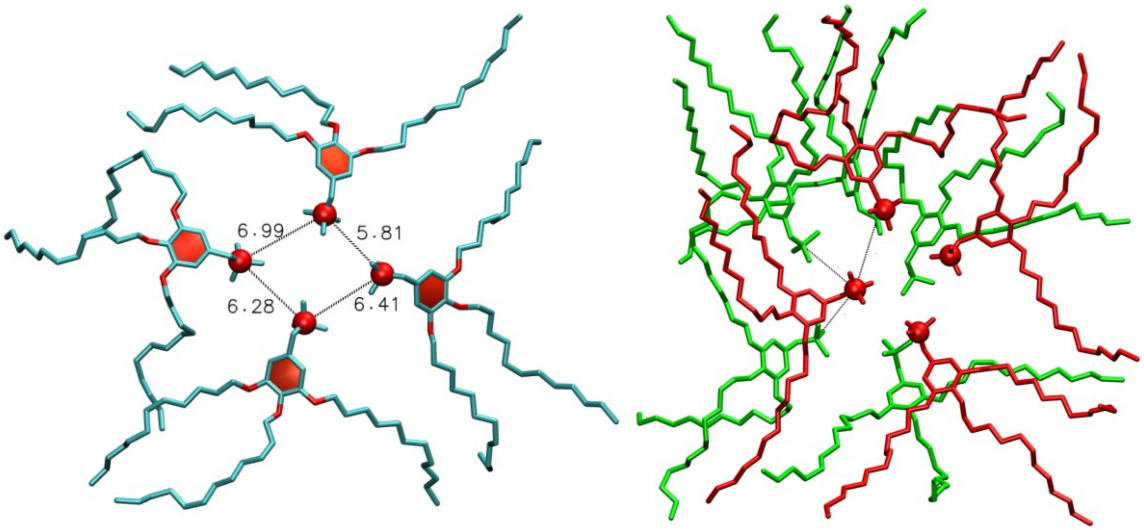

Figure 68 The in-plane organization of Gallic Acid units, on the left, with the distance of two adjacent N indicated in Å. On the right it is represented in red the same discotic unit that is on the left with the addition of the discotic unit beneath represented in green. The black lines on the right are the distances between the nitrogen atom of a given unit and the nitrogen atom of the units below. Their values are not indicated to avoid confusion but they are in the range of the first peak distance. The snapshots represented are for the scaled charge system at $T = 350\ K$

The second peak, at around 1 nm, is the peak that corresponds to the N-N distance of the Gallic Acid units on the opposite side of the same discotic unit, as can be seen in the Figure 69. This distance also corresponds to the N-N distance of two Gallic Acid units being on opposite sides of the two closest discotic units. Concerning the anions (B-B) RDFs, blue lines in Figure 67, an analogous behaviour is spotted as for the cation RDFs. The shape of the RDFs for both the trimethylated systems is similar with a first peak at 0.72 nm, a second peak at

around 1 nm and a third broad peak at 1.35 nm. The triethyl ammonium derivative system is missing the peak at around 1 nm, which is more like a side shoulder of the first one. Moreover, its first peak is shifted at longer distances, 0.79 nm, compared to the previous systems. This is due to the hindrance of the additional CH2 group.
While cations are less mobile and their structure could be ascribed to precise arrangement of the units, anions are more fluid and less constrained. For this reason the first and second peak are not directly related to the in-plane and interplane organization of [BF_4]. The RDF of anion-anion suggests that the [BF_4] act as spacers for cationic units.The mixed RDFs N-B, black curves in Figure 67, are similar for all three systems presenting a first sharp peak at 0.5 nm and a second peak at around 1 nm for the trimethylated systems and at 1.10 nm for the tri-ethylated one. It is worth to note that the discotic units are not covalently bonded and in these images the anion arrangement is missing. Moreover, it is important to bear in mind the twofold nature of these molecules: on one side the thermotropic LC nature is responsible of the ordering of the elementary units and the formation of columns, while the IL nature is responsible of the existence of regions of space with fluid mobile ionic pairs, especially for [BF_4] anions. The long alkyl chains act as spacers between the charges due to their hydrophobicity, thus producing segregation of ionic regions. The alkyl chains act also as a promoter of mesogenic behaviour. Since they are thermotropic mesogens the phase transition is a temperature-driven process and there exists a temperature at which the columnar order is not present anymore.

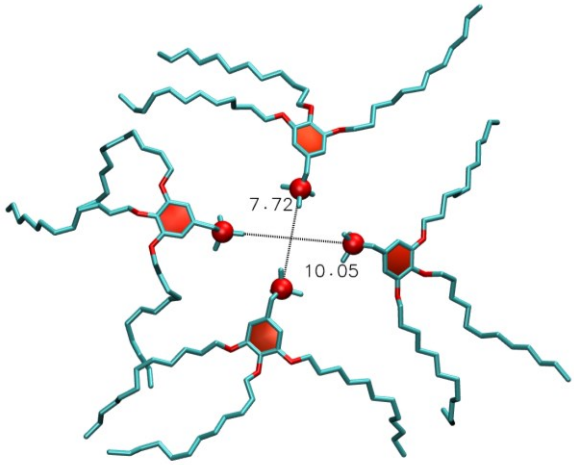

Figure 69 Same discotic unit represented in Figure 68, left, with the distance of opposite N-N indicated in Å

While the close range order of ionic species between the scaled and full charge systems appears to be almost identical, the diffusion coefficients present considerable differences. The anion and cation diffusion coefficients for the scaled charge systems are reported in Figure 70**.** The behaviour of all these three systems is evaluated as a function of the inverse of the temperature. Starting from the lowest temperature, the diffusion of cations and anions in the plane and along the columns are comparable. Once the temperature is risen the two components of the diffusion become different with the Z component being higher than the XY component, suggesting an anisotropy of mass transport properties along the columns with higher diffusion rate. As the temperature continues to rise there is a temperature at which the XY and Z components of the diffusion coefficients are equal to the isotropic one. Here the systems are considered to be in an isotropic phase with columnar order not present anymore. The comparison between full and scaled charge systems is presented in Figure 71, where diffusion coefficients are reported for the BzNMe3 systems. Here it can be seen that the full charge system appears more viscous with respect to the scaled charge one, having lower values of D. Moreover, the 2D and 1D diffusion coefficients are different from the 3D isotropic

one, suggesting that the anisotropic diffusion persists above the 600 K temperature, temperature at which the systems should be an isotropic ionic melt with no macroscopic ordering and no privileged direction of diffusion.

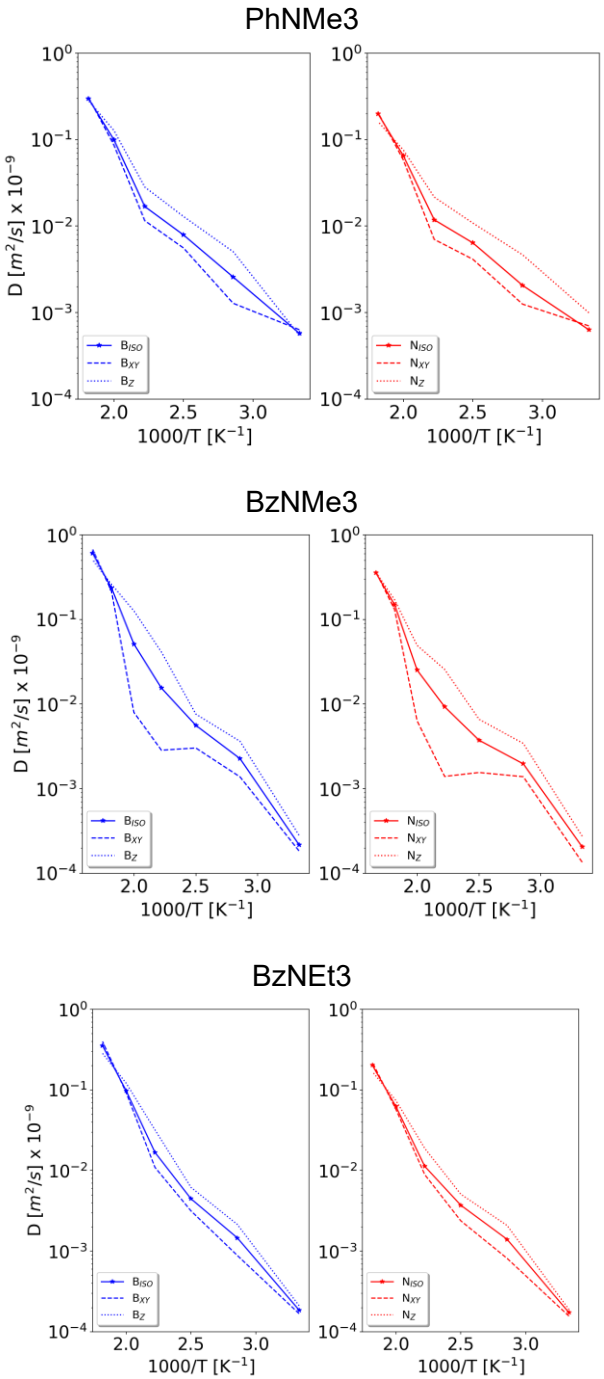

Figure 70 Diffusion coefficients for anion, blue curves, and cation, red curves, as a function of the inverse of temperature. The solid lines with markers are the isotropic (3D) diffusion coefficients. The dashed lines are the XY in-plane (2D) diffusion coefficients, while the dotted lines are the Z diffusion coefficients calculated along the column's length (1D). The y scale is logarithmic

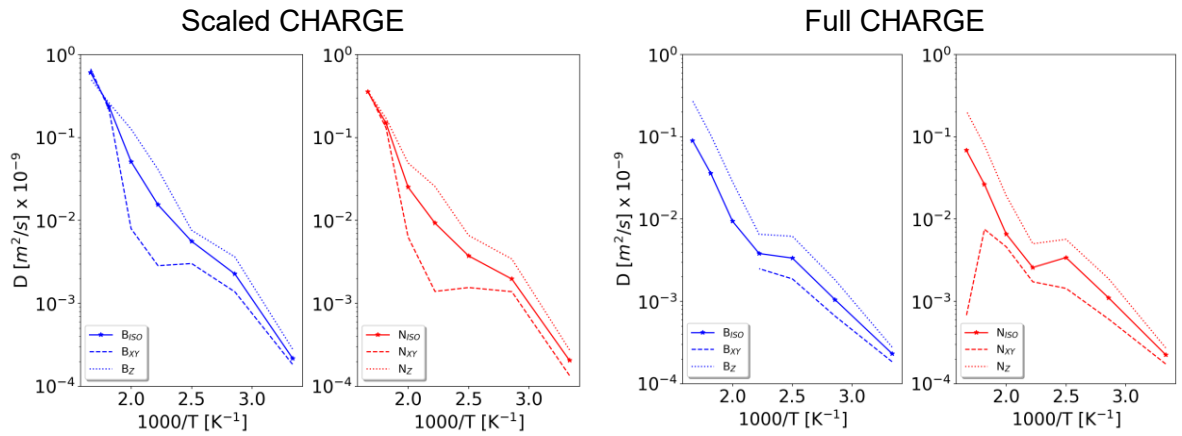

Figure 71. Diffusion coefficients for anion, blue curves, and cations, red curves, as a function of the inverse of temperature. The same color code as Figure 70 is used. The BzNMe3 system is taken as an example. The in-plane anion diffusion, B_{XY}, for the full charge system misses the temperature 500, 550 and 600 due to a poor linear fitting of the msd and they are omitted. Nonetheless, the in-plane diffusion coefficients are way lower than that of 1D diffusion coefficients suggesting the existence of a faster path along the columns.

The visual inspection of high temperature (600 K) full charge systems' snapshots, not presented here, indicates the persistence of columns at temperatures above the experimental isotropic transition temperature. This is also confirmed by the RDFs of N-N pairs resolved in the plane parallel to the columns (XY), Figure 72. Here, two distinct trends could be observed. On the left, scaled charge, it can be seen a temperature at which the RDFs flatten to 1, orange and yellow curves, suggesting a loss of in-plane ordering and a destruction of columns in the temperature range of experimental transition temperature. On the right, the full charge systems preserve the in-plane ordering and the columns still exist at temperatures far higher than that of the transition temperature.

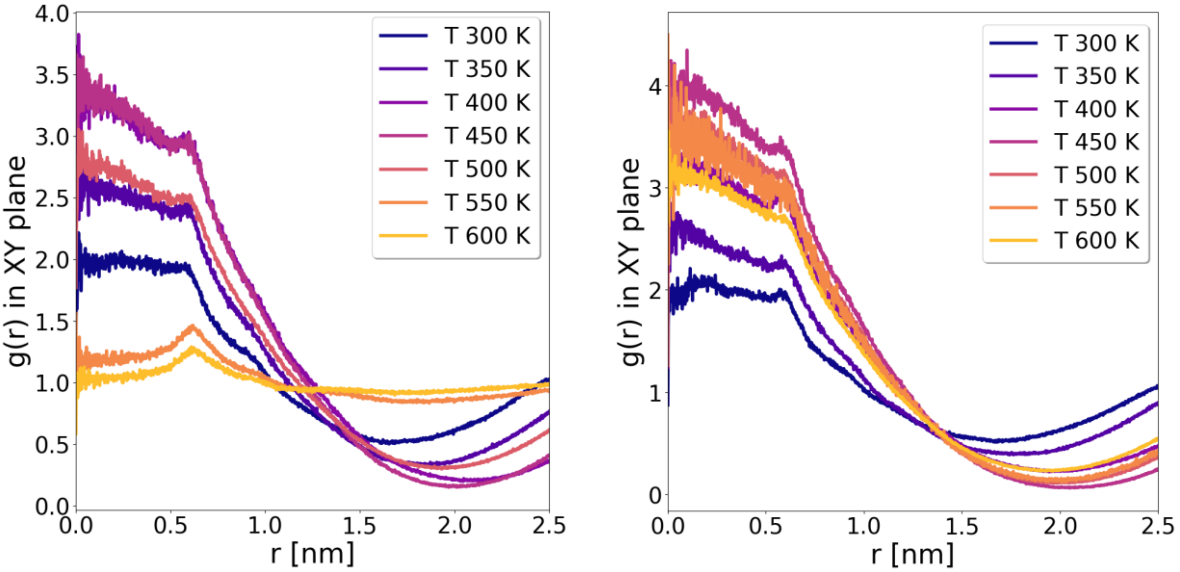

Figure 72 Radial distribution functions of the N-N pairs resolved in the XY plane, perpendicular to the columns. Scaled and full charge systems are shown respectively on the left and right. The yellow and orange lines on the left show a loss of in-plane ordering suggesting the transition of the system to an isotropic phase

For these reasons the full charge systems' FF is not suitable to simulate these systems' behavior and the scaled charge performs better and it is chosen as the preferred one. This strategy is a common workaround in the simulations of structural and dynamical properties of ILs and it is well known in literature [141]. Moreover, a recent study of Washizu and coworkers on $BzNEt_3$/ $[BF_4]$ [43]found out that the rescaling of charges by a factor of ≈ 0.8; as a reasonable rescaling factor that permitted to account for polarizability effects even though the FF employed is not polarizable. From now on, the results presented implicitly refers to the scaled charge systems if not stated otherwise.

To determine transition temperatures the in-plane RDFs and orientational order parameter $\langle P_2 \rangle$ are evaluated. The loss of in-plane ordering, as in Figure 72(left), suggest that the columns are not present in the XY plane and it is confirmed by the 2D and 1D diffusion coefficient that both tend to 1 like in the isotropic. These results combined with the evaluation of $\langle P_2 \rangle$ parameters, calculated using the vectors perpendicular to the aromatic ring as defined in the Analysisection,provides a robust esteem in the determination of the phases. $\langle P_2 \rangle$ itself gives a clue about the overall orientation of the aromatic rings within the system. The more its value is close to 0 the more the rings are randomly distributed, thus the molecules are not aligned along a preferred direction and the system is isotropic. On the other hand, the more this parameter is close to 1 the more the orientation of the disks is perfectly aligned, determining a macroscopic orientation of the phase along a certain vector, called director. Following these ideas and looking at Figure 73**,** it can be determined a temperature range, in the heating runs, at which the $\langle P_2 \rangle$ value drops to values less than 0.1 and very close to 0. Here the columnar to isotropic transition takes place. The transition temperature is calculated as the average value between the two temperatures and these values are reported in the Table 19 for all the systems.

PhNMe3

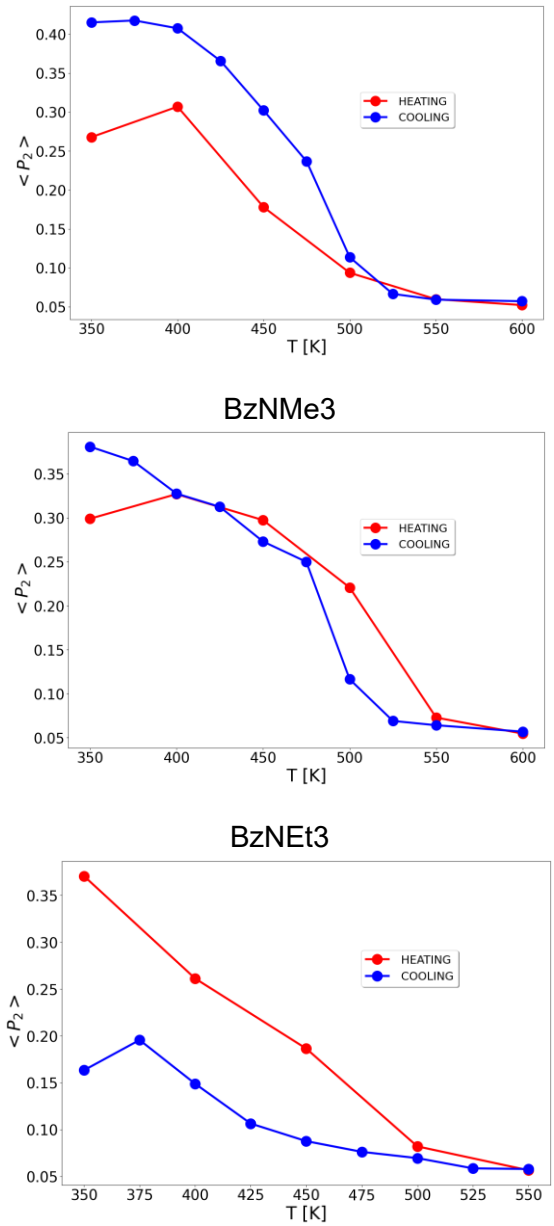

Figure 73. Orientational order parameters, $\langle P_2 \rangle$, in heating (red circles) and cooling (blue circles) run. The lines are a guide to the eye.

	expt	calcd.	Ref.
PhNMe3	196 °C // 469.15 °K	475.5 °K	[142]
BzNMe3	206 °C // 479,15 °K	525 °K	[2]
BzNEt3	126 °C // 399.15 °K	475.5 °K	[2]

Table 19 ***Ttransit*** *Experimental and calculated columnar-to-isotropic transition temperature for all of the systems studied.*

After the system reaches its isotropic phase it is cooled down back to 350 K. It can be appreciated that the columnar order within the system is restored, moreover a small hysteresis is found in the transition Iso-Col when regarding the BzNMe3 system. The PhNMe3 system also retrieves the column order while the system is cooled down. The BzNEt3 system, indeed, does not reach the column order again while cooled down, presenting channels that are distributed within the box with regions of interconnected structures. It is important to stress the trend of the orientational order parameter. The same value of $\langle P_2 \rangle$ is retrieved, for BzNMe3 system, after the cooling run indicating the restore of a columnar order, as can be appreciated in the Figure 74. It is also important to note that retrieving order from an isotropic phase is not a simple task, especially for non polarizable all atoms FF

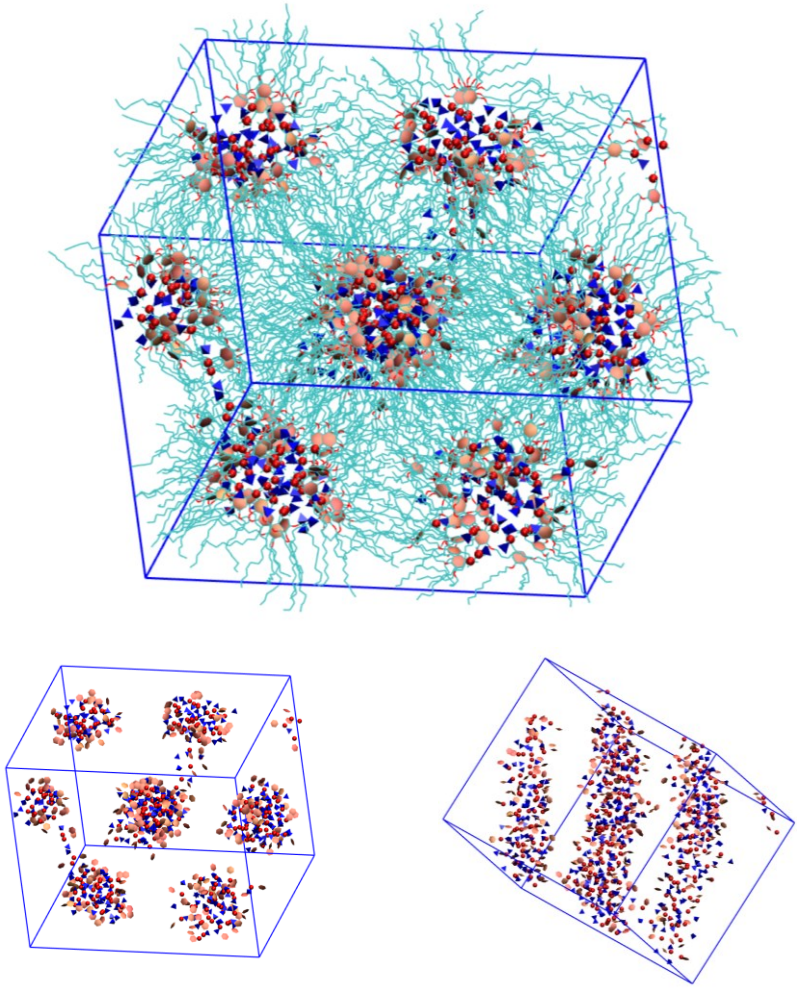

Figure 74 Columnar structure formed from the isotropic melt as seen from above (top figure) with the alkyl chains colored in cyan, the anion in blue, the N atom of cation in red and the aromatic ring in pink. The two figures on the bottom highlight only the ionic parts of the system and two different perspectives are shown. The temperature is 350 K and the BzNMe3 systems is represented

The bigger systems were built starting from the smaller ones taking the configurations from the 400 K simulations in heating. The systems were doubled in the x and y direction, that is in the plane perpendicular to the columns, using the nearest 4 periodic images. The close range order of ionic pairs of bigger systems is like the one shown for the smaller ones. The cation RDFs of trimethylated derivatives, N-N pairs, show two distinct peaks at 0.7 and 1 nm and a broader peak at around 1.30 nm, while the triehtylated system shows a sharp peak at 0.75 nm and a small shoulder at 1 nm with a broad peak centered at 1.5 nm. The in-plane RDFs show a similar trend to the yet shown RDFs in Figure 72**(left),** where it is possible to see the

modulation in the XY plane, perpendicular to the columns, of ionic species. Using the FWHM of the second peak, referred to N-N or B-B pairs, it is possible to give an estimate on the diameter of the columns which is around 2 nm for the trimethylated systems while 2.6 nm for the BzNEt3. Measuring the distance from the first two peaks gives a measure of the column-column distance in the XY plane. The precise diameters and column-column distance values are reported in Table 20**,** where both the N-N and B-B pairs are employed in the determination of the columns' size and inter-column distances.

	PhNMe3	BzNMe3	BzNEt3
columns' diameter	1.83 nm (diameter) N-N 2.00 nm (diameter) B-B	1.87 nm (diameter) N-N 1.94 nm (diameter) B-B	2.5 nm (diameter) N-N 2.77 nm (diameter) B-B
Column-Column distance	3.8 nm	4 nm	3.90 nm

Table 20 Esteem of the columns' diameter using the FWHM of the second peak of the in-plane RDFs for the N-N and B-B pairs, first row. Measure of the column-column distance evaluated using the distance in the XY RDFs between the first two peaks, second row.

The analysis of the $\langle P_2 \rangle$ parameter on these bigger systems confirms the presence of an ordered phase. The $\langle P_2 \rangle$ values range between 0.25 and 0.40, values obtained also in the smaller systems simulations. The columns are stable and the columnar ordering is maintained. To study the channels behaviour and dynamics, a series of simulations with different concentrations of water are carried out using the configurations obtained from the bigger box as starting configurations. The water interferes with the microstructural ordering of ionic pairs producing looser ionic pairs as the water concentration increases. Moreover, the channel dimension is affected by the water that preferentially resides into the hydrophilic ionic channel that builds a core channel of water that populates as more water is added without changing the space extension of the water channel. The bigger systems of BzNMe3 with the smallest content of water appear as in Figure 75**.** Here, the close range order of species is weakly affected by the water, nonetheless the water occupies the central zone of the ionic channels. As the water content is increased, the water channels do not enlarge their extent and the water inside the channel constitutes the core of the ionic columns. On the contrary, higher water concentrations increase the average distance between ionic species resulting in bigger channels as can be seen in Figure 76**,** depicting the same ionic liquid with higher water content. Nonetheless, the water itself does not expand or increases its dimension, the ionic moieties, on the contrary, act as containers of the water channel.

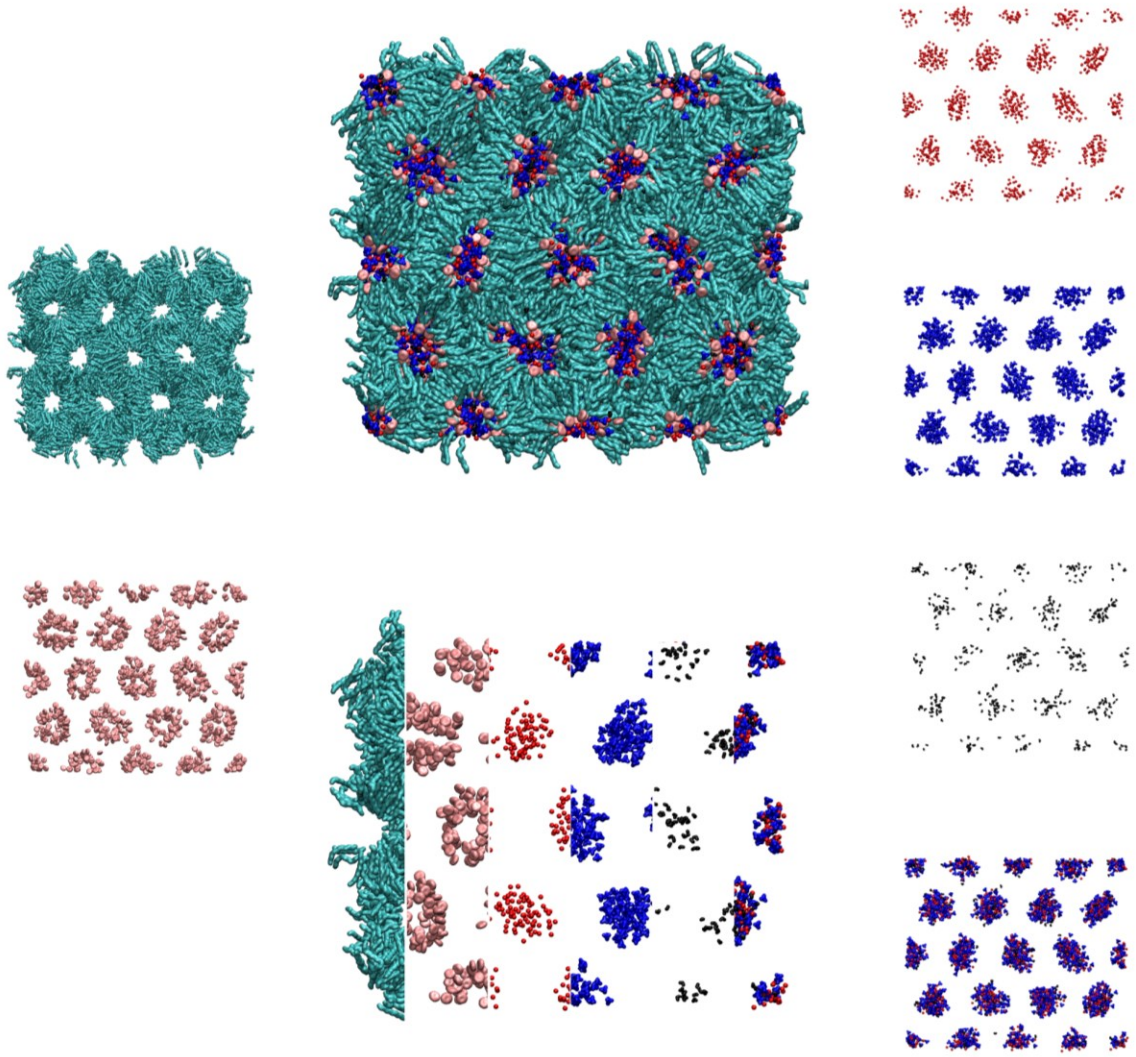

Figure 75Snapshot of the different species present in the system with the smallest content of water. The central panel shows the whole system on the top, while on the bottom different slices are depicted to show how the system is made. The left panel shows only the hydrophobic moieties of the Gallic Acid derivative: alkyl chains in cyan, top left, and aromatic ring in pink, bottom left. In the right panel, the hydrophilic parts of the system are represented. Starting from the top: N in red, [BF_4] in blue and water in black. The last of the four figures on the right side shows the whole ionic channels, composed of N, [BF_4] and water.

As can be appreciated by the Figures, the channels increase in size and the N-N and B-B close range order loosen, resulting in cation and anions being more distant than the system with smaller water content. The water preferentially resides inside the channel and makes up the core of the columns. This evidence is also supported by the RDFs of the ionic species, Figure 77**.** The cation-anion average distance is not heavily affected, the cation-cation average distances are slightly affected and the anion-anion distances are strongly affected, resulting in a broadening of the first peak with a shift to bigger distance values. Moreover, in the highest water content system the anion-anion RDF shows a loss of the first peak with a larger broadening of the peak due to a solubilization of [BF_4] inside the water moiety

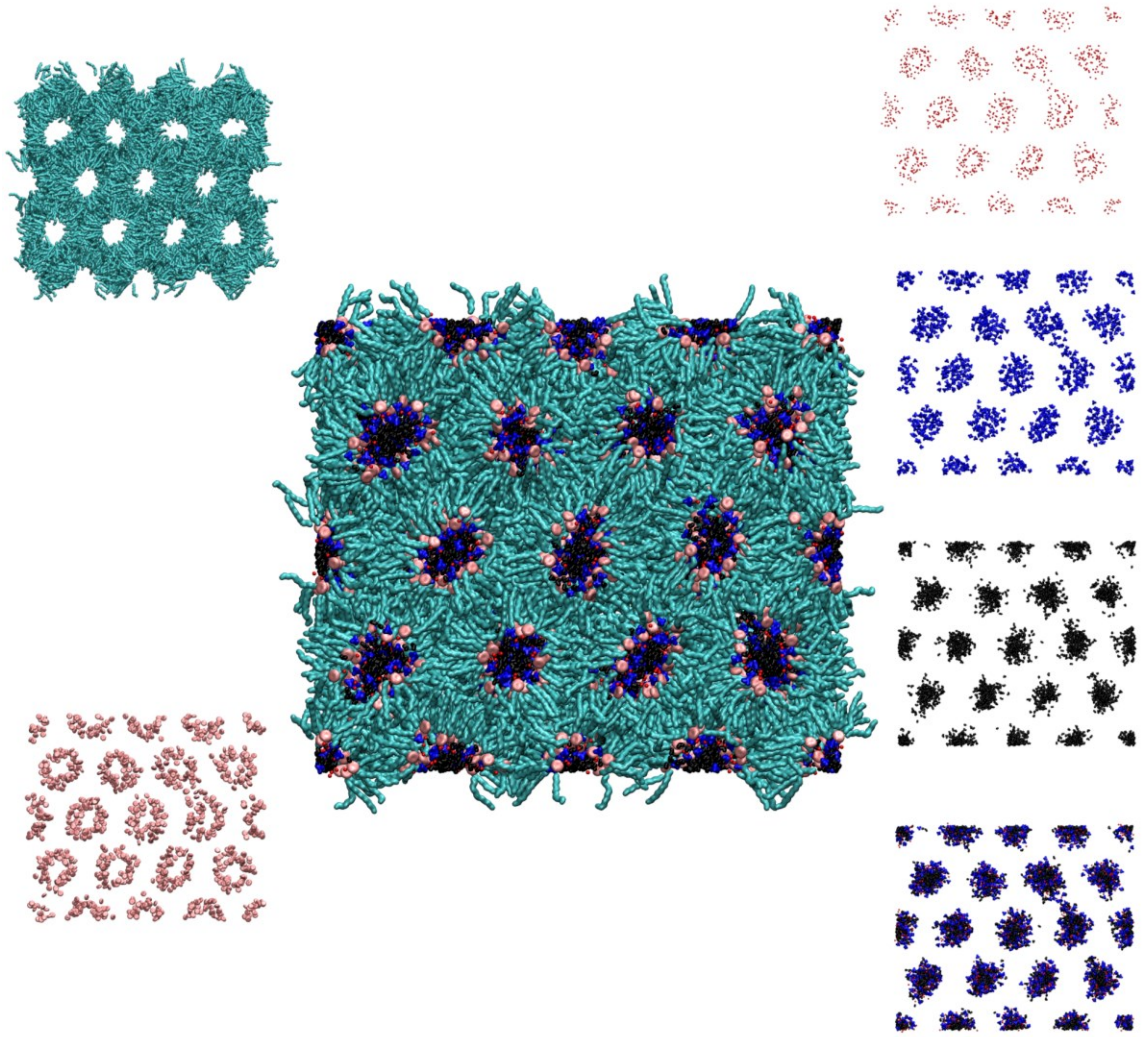

Figure 76 Snapshot of the different species present in the system with the highest content of water. The central panel shows the whole system. The left panel shows only the hydrophobic moieties of the Gallic Acid derivative: alkyl chains in cyan, top left, and aromatic ring in pink, bottom left. In the right panel, the hydrophilic parts of the system are represented. Starting from the top: N in red, [BF_4] in blue and water in black. The last of the four figures on the right side shows the whole ionic channels, composed of N, [BF_4] and water.

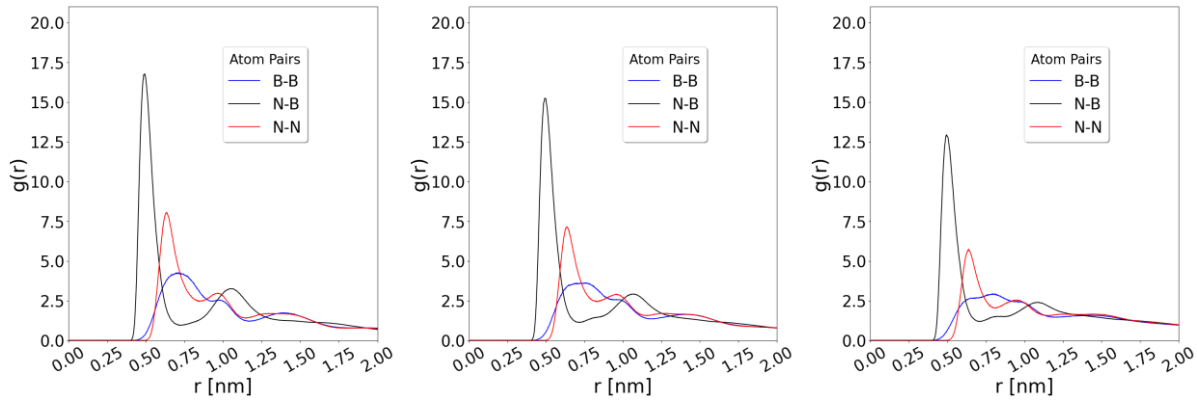

Figure 77 RDFs of ionic pairs in the hydrated systems of BzNMe3. From left to right the water content increases

The effect of water concentration is mainly to enlarge the ionic channel by preferentially residing in the central part of the columns with a small increase in water's channel dimension. In Table 21 it can be seen that: as the water concentration is increased the diameter of water columns remains almost constant for the BzNMe3 and being of about 1.70 nm in diameter. On the contrary, for the system PhNMe3, as the water is increased the water column diameter decreases not monotonically. The BzNEt3 systems with higher water content do not remain perfectly columnar, they lose their columnar order and diameters and inter-columns distance cannot be estimated. In Table 22 the inter-columnar distances are estimated from the distance between two successive peaks in the planar RDF of the species within the systems.

	PhNMe3	BzNMe3	BzNEt3
without water	1.83 nm N-N 2.00 nm B-B	1.87 nm N-N 1.94 nm B-B	2.5 nm N-N 2.77 nm B-B
0.39 M	1.74 nm O-O 1.85 nm N-N 2.00 nm B-B	1.70 nm O-O 1.90 nm N-N 2.03 nm B-B	2.47 nm (NN) 2.52 nm (OO) 2.78 nm (BB)
1.15 M	1.57 nm (O-O) 1.96 nm (NN) 2.10 nm (BB)	1.70 nm O-O 2.05 nm N-N 2.18 nm B-B	columnar order lost
3.32 M	1.68 nm (OO) 2.55 nm (NN) 2.70 nm (BB)	1.73 nm O-O 2.54 nm N-N 2.65 nm B-B	columnar order lost

Table 21 Esteem of the columns' diameter using the FWHM of the second peak of the in-plane RDFs for the N-N and B-B and O-O pairs as a function of water content. The temperature at which this diameters are evaluated is 380 K

The average distance between columns is about 3.9 nm, a slightly higher value compared to experimental measurement, [31] suggesting that alkyl moieties act as spacers between ionic channels in a similar manner between the three different systems. It is noticeable that the

highest colum-column distances are obtained for the BzNMe3 system. This suggests that the columns packing is loose for this system compared to the others.

	PhNMe3	BzNMe3	BzNEt3
without water	3.8 nm	4 nm	3.90 nm
0.39 M	3.80 nm (OO) 3.75 nm (BB) 3.77 nm (NN)	4.00 nm (NN, BB, OO)	3.93 nm (NN) 3.92 nm (BB) 3.93 nm (OO)
1.15 M	3.83 nm (BB) 3.87 nm (NN) 3.89 nm (OO)	4.08 nm B-B 4.10 nm N-N 4.12 nm O-O	columnar order lost
3.32 M	4.30 nm (OO) 4.24 nm (BB) 4.27 nm (NN)	4.45 nm N-N 4.44 nm B-B 4.50 nm O-O	columnar order lost

Table 22 Measure of the column-column distance evaluated using the distance in the XY RDFs between the first two peaks as a function of water content. The temperature at which these distances are evaluated is 380 K

Regarding dynamic properties as a function of water content for the BzNMe3 systems it can be seen that the diffusion of both the anion and cation are enhanced when the water is present, because of the diminished viscosity of the water that favors the motion of other species within the system. The Figure 78 shows how the diffusion coefficient of all the species in the system varies as a function of temperature by changing the water content. For the least concentrated water system, Figure 78**(top)**, the cation and anion diffusion coefficient are comparable: they have the same order of magnitude of the anhydrous systems, the $D_{cation} \simeq D_{anion}$ for the hydrated one and the anisotropically diffusion along the Z axis is not so favored compared to the in-plane diffusion for both cation and anion. The longitudinal diffusion of water is higher than the planar diffusion. Increasing the water content, Figure 78**(center)**, enhances the overall diffusion of anion but does not alter significantly the one for the cations. The longitudinal diffusion is increased compared to the planar one and the water diffusion is highly increased even at low temperatures. The system with highest water concentration, Figure 78**(bottom)**, has the D_{anion} increased by an order of magnitude compared to the D_{anion} with the lowest water content. Moreover, the reduced viscosity of the ionic channel enhances the anisotropic diffusion along the longitudinal axis for both the water and $[BF_4]$. The water diffusion seems not to be altered with the increasing temperature of this system. Increasing the water content enhances the diffusion anisotropy of water within the channel. By doing so the water drag with itself anion with its motion, producing an enhanced mobility also for anion. This is obtained only for systems with enough water to permit the formation of a region of bulk-like organization of water that permits the solubilization of $[BF_4]$ with its first solvation shell inside the channel.
The role of the ions within the channels was investigated using a different kind of anion with respect to the $[BF_4]$. Cl was chosen to substitute the $[BF_4]$ inside the channel as counterions of the gallic acid ammonium derivatives. Cl has a higher density of charge, thus making Cl more hydrophilic with respect to the $[BF_4]$. The structural and dynamical behaviour are presented to compare the difference between the systems.

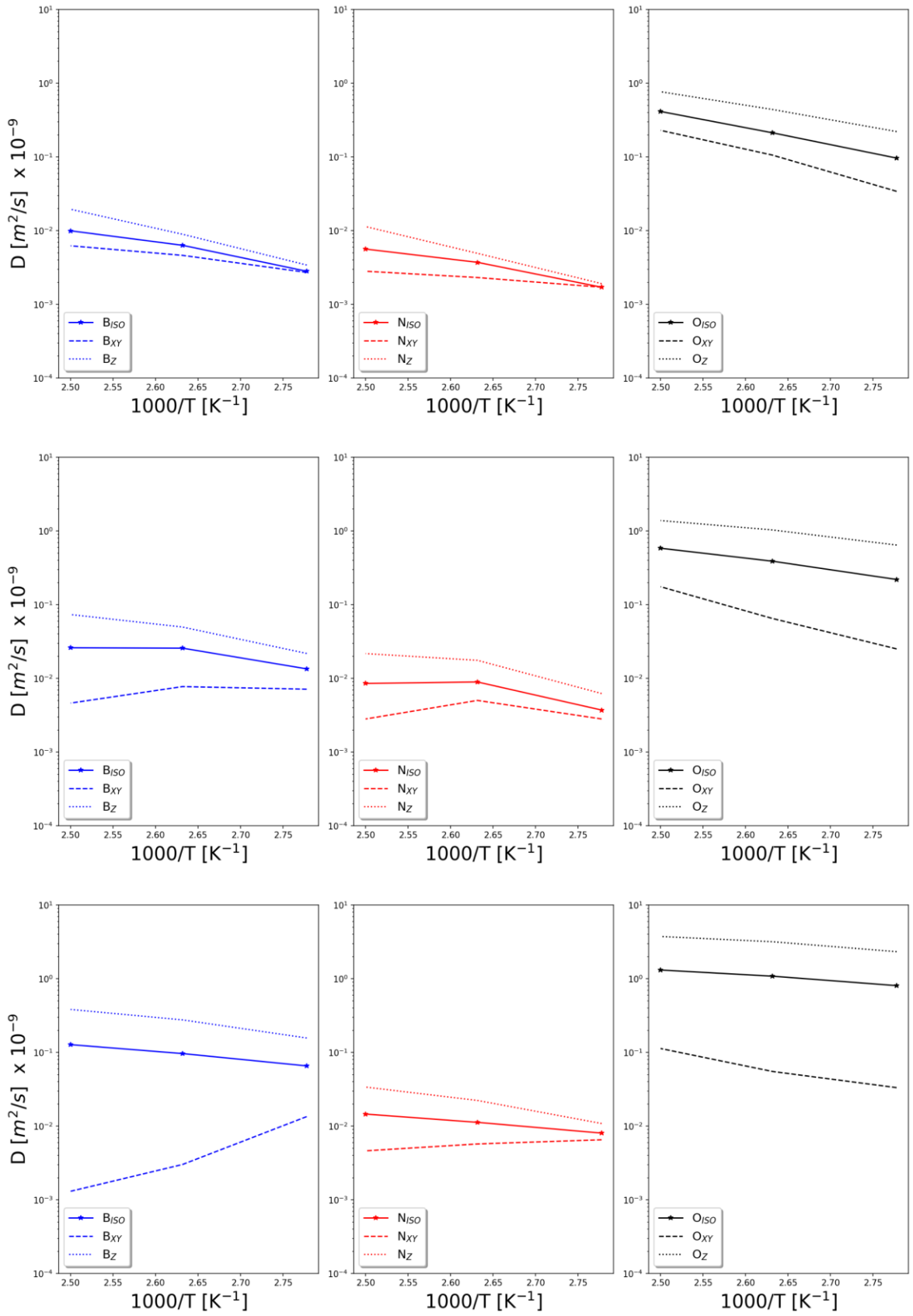

Figure 78. Diffusion coefficient and their planar (XY) and longitudinal (Z) components for the anion, blue on the left, cation, red on the center and water, black on the right as a function of the reciprocal of temperature. The three different graphs represent different water concentrations: from the top to the bottom the water concentration increases.

The close range order of ionic species is evaluated using the RDFs reported in Figure 79**.** It can be seen that the anhydrous systems possess a similar arrangement of ionic species, with a shift to smaller distances due to the reduced size of the Cl atom with respect to [BF_4]. The introduction of water strongly affects the ionic interaction and the close range ordering of the species within the channels varies. The system with the smallest water content does not alter significantly the arrangements of the ionic species, since the water is not enough to form a core of bulk-like water. Starting from the 1.15M systems the anion-anion order differs from that of the anhydrous systems, with a three peaked profile in the RDF or the BzNMe3//Cl, while the [BF_4] one possess a broad peak due to the bigger size of the [BF_4] anions. The cation-cation RDF presents a better resolved second peak in the system with Cl with respect to the [BF_4] one. This behaviour is ascribed to the addition of water and the presence of a smaller counterion. The systems with the highest water concentration and Cl as anion possess a small range Cl-Cl ordering of about 0.40 nm as indicated by the first peak in Figure 79**,** 3.32 top**.** This peak coincides also with the Anion-Cation ordering. Moreover, the structure of the anion-cation presents a three peak profile for the system with Cl as anion while the [BF_4] systems have a broad ordering of the species due to the anion hindrance and less hydrophilicity compared to Cl.

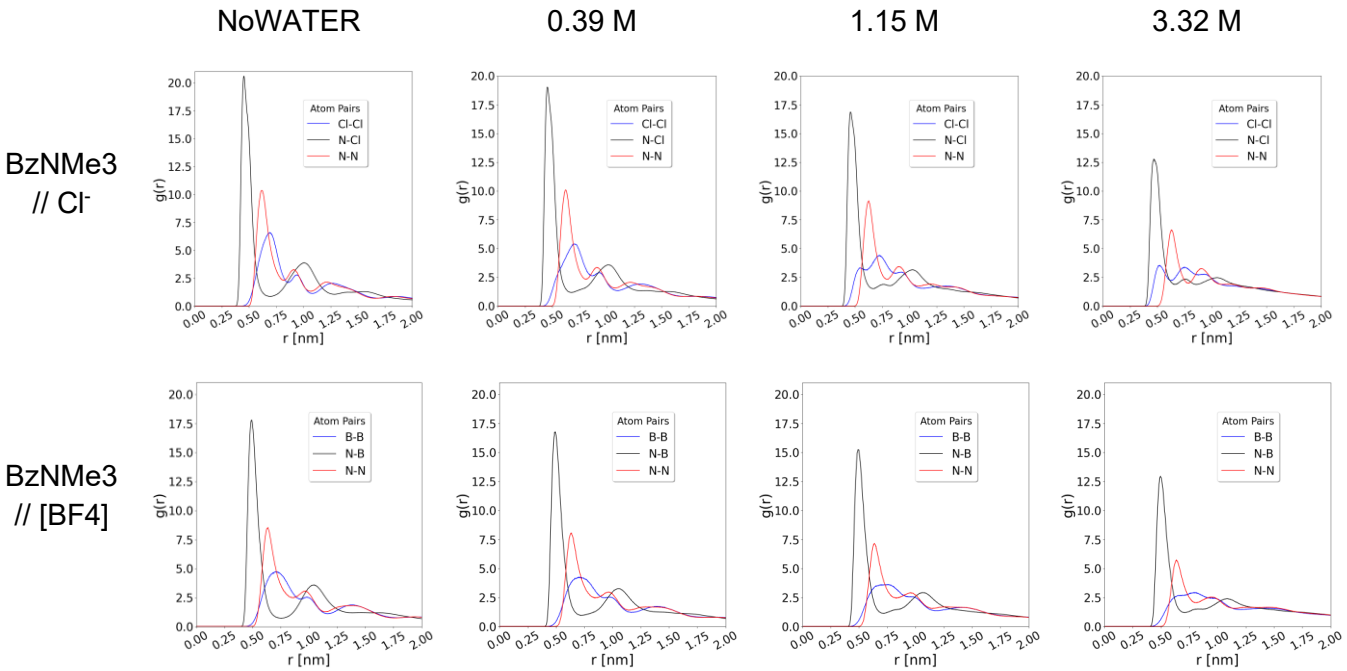

Figure 79.Radial distribution function between ionic species for the BzNMe3 systems with two different anions, [BF_4] and Cl, on top and bottom respectively. Red curves are the cation-cation pairs, blue curves are the anion-anion pairs and black curves are the cation-anion pairs.

The most important interactions are the anion-water interactions, shown in Figure 80 for the systems with different anions and different water concentrations. Here it is more evident that the ionic liquid with Cl has a stronger anion-water interaction than that of the ionic liquid with [BF_4] due to the Cl higher hydrophilicity, thus, the water-water interaction is weakened by the Cl. On the contrary [BF_4] possesses a lower hydrophilicity and its interaction with water is milder compared to the systems with Cl. Moreover, the interaction of [BF_4] with water permits the water to interact more with itself, producing higher values of g(r) in the first peak of the water-water RDF compared to the one obtained for the systems with Cl. The structure of the water inside the channel is disturbed by the Cl which does not permit forming channels in which the water builds networks of hydrogen bonds that resemble the one of the bulk phase.

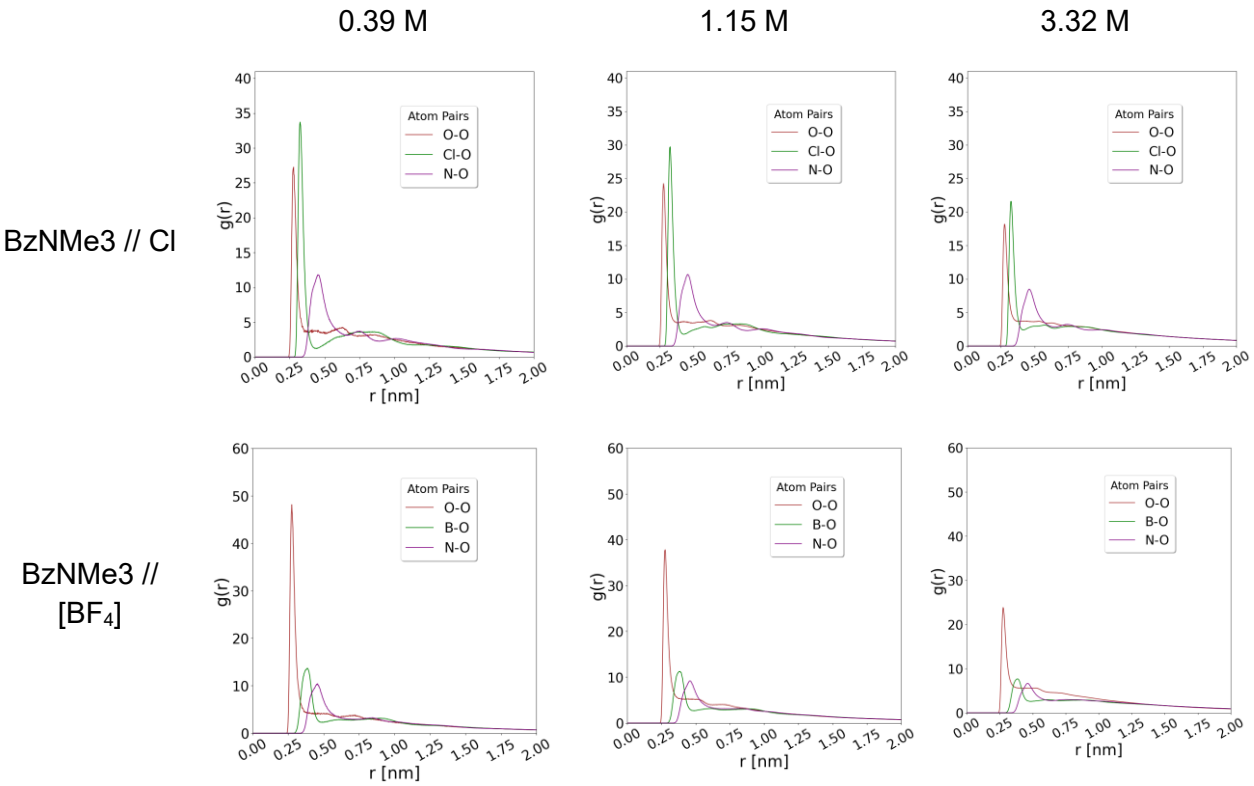

Figure 80. Radial distribution function between ionic species and the water's oxygen for the BzNMe3 systems with two different anions, [BF_4] and Cl^-, on top and bottom respectively. Red curves are the water-water pairs, green curves are the anion-warter pairs and purple curves are the cation-water pairs.

The dynamical behaviour is evaluated by considering the diffusion coefficient of the different species as a function of water concentrations and the inverse of temperature. Moreover, the planar and longitudinal components are evaluated to assess the anisotropy of mass transport within the membrane. In Figure 78 the diffusion coefficients are reported for the ionic liquid with [BF_4], while the Figure 81 reports the diffusion coefficients for the ionic liquid with Cl as anion. The two systems appear to behave similarly: the introduction of water lowers the viscosity inside the channel, thus increasing the diffusion coefficient of the anion with the one for the cation slightly increasing. The diffusion coefficients of cations in both the systems are comparable with similar values. The anions' diffusion coefficient also has the same order of magnitude for both the ionic liquids studied with an increase in value as the water concentration is increased. The water appears to be more mobile in the [BF_4] system. This is ascribed to the preferential interaction of water molecules with themselves, producing a core of water inside the channel that acts as bulk-like water, with its typical network of hydrogen bonds. This explains the enhanced diffusivity of water through the channel. Moreover the longitudinal component of diffusion, dotter black curve on the bottom panel of Figure 78 and Figure 81, is higher for the systems with [BF_4] and its value is twice as large as the one for the system with Cl as anion. It is important to stress that the introduction of Cl as a counterion destabilizes the columns and the more water is added the more the systems produce defects inside the columns. This evidence supports the fact that the [BF_4] is a better counterion to build these specific membranes because it permits the water to interact more with itself and thus providing an ulterior structuring effect operated by the water inside the channels. The Cl does not heavily alter the anion-cation close range order but its effect is totally ascribed to the interaction with water.

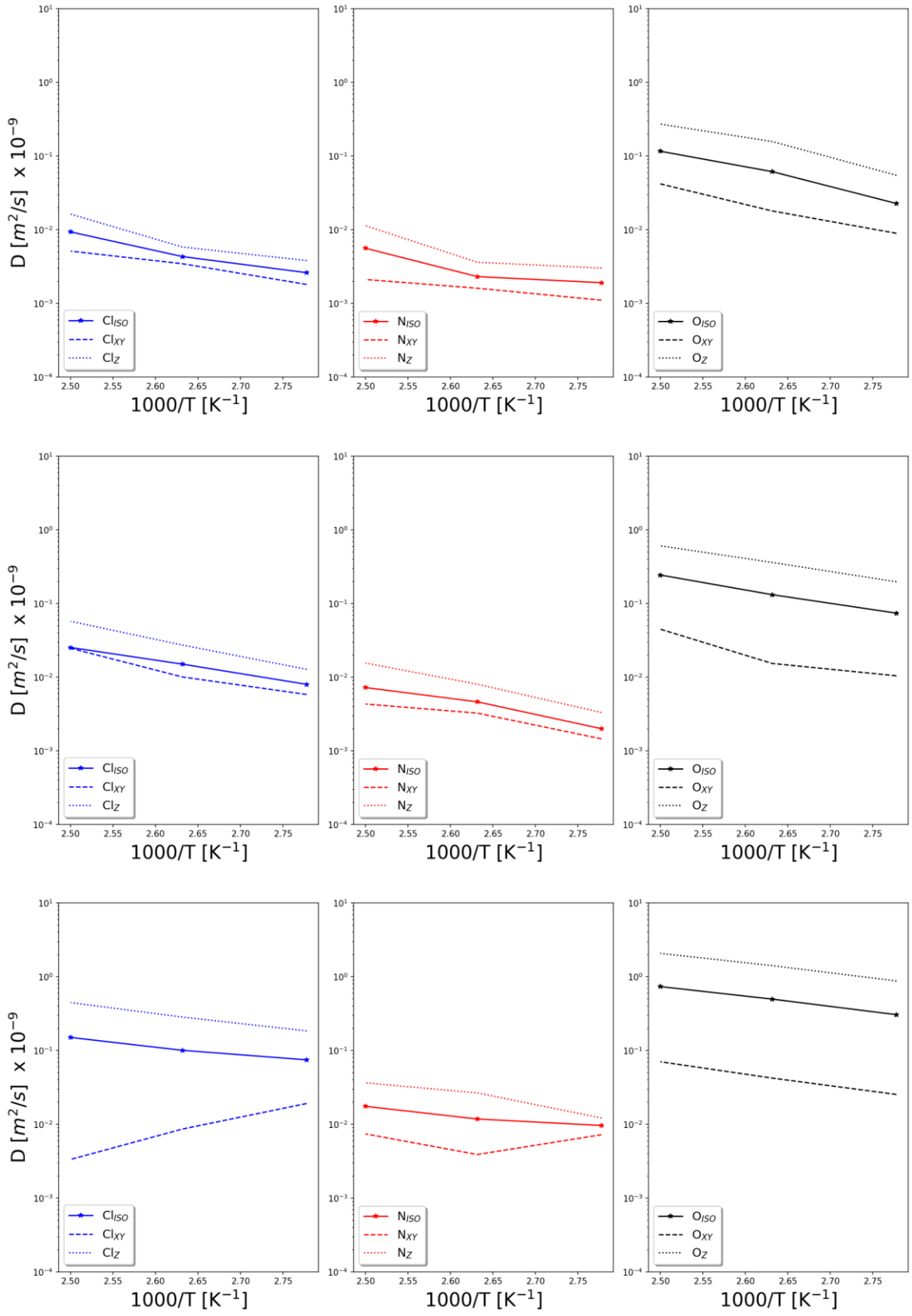

Figure 81. Diffusion coefficient and their planar (XY) and longitudinal (Z) components for the anion, blue on the left, cation, red on the center and water, black on the right as a function of the reciprocal

of temperature. The three different graphs represent different water concentrations: from the top to the bottom the water concentration increases.

As illustrated by the 2D density probability maps shown in Figure 82 it can be seen that the water forms the inner part of the ionic channel both in low and high water concentration of the BzNMe3//B4 systems and as the water content is increased the nitrogen starts to surround the water, forming the outer crust of the ionic channels. Moreover, the [BF_4] seems to be pushed in the peripheral regions of the channel, suggesting the formation of a domain of highly hydrophilic nature. Here the most hydrophilic molecule is the water itself that prefers to be surrounded by other water molecules. The water prevalently interacts with itself constituting a core of water that is maintained together thanks to the instauration of a network of hydrogen bonds. The more hydrated system shows a higher probability of finding water inside the channel. The Figure 83 shows the same map of the highest water content system, yet reported in Figure 82**,** for the water molecule within the box. On the same image there are depicted the hydrogen bonds, in black, and the water molecules of a single configuration to show how they are arranged. The core of the ionic channels is contained inside the nitrogen of the cations and the driving force of water channel formation is the enhanced interaction between water-water molecules.

	0.39 M	3.32 M
chains	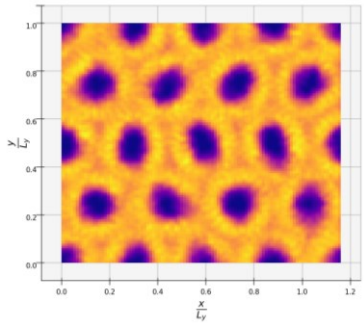	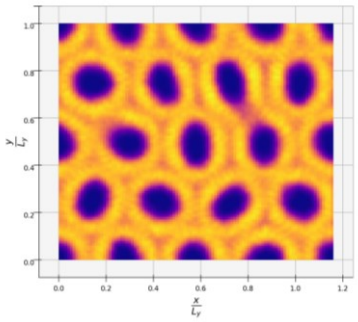
B	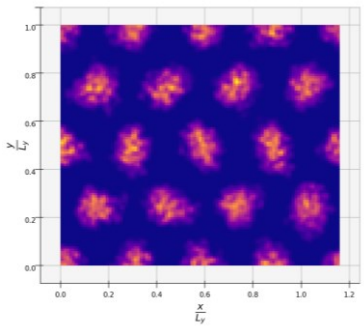	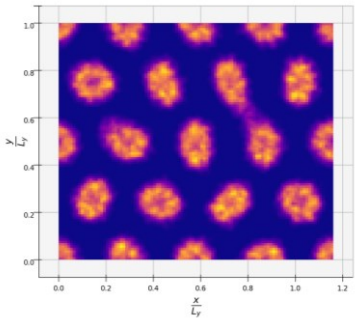
N	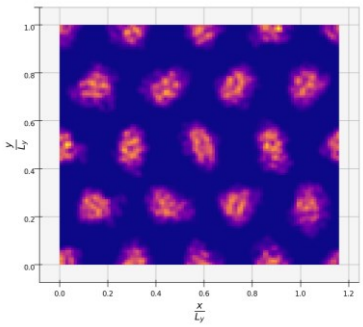	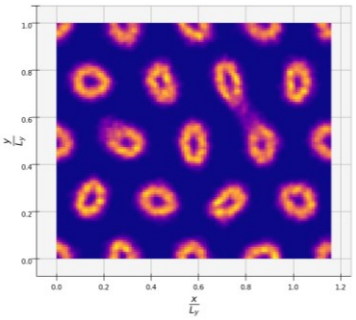
water	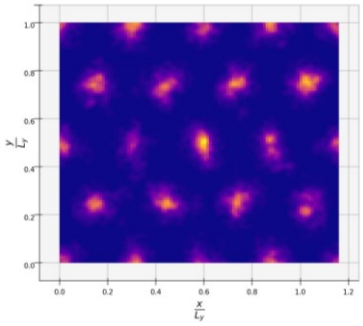	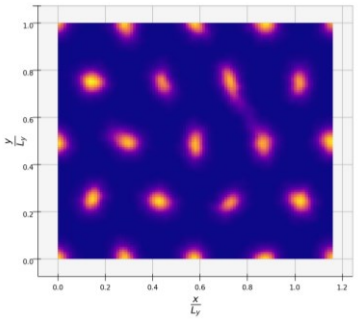

Figure 82 Probability density of the position in the XY plane for different species of atoms inside the system BzNMe3 with low, left, and high, right, water content. Blue is for low probability and yellow for high probability. Starting from the top the chains, B, N and water maps are reported. The dimensions of the reported box are obtained by normalizing the position by the smaller dimension of the box (L_y), obtaining box's dimensions of 1.16 and 1 for x and y respectively.

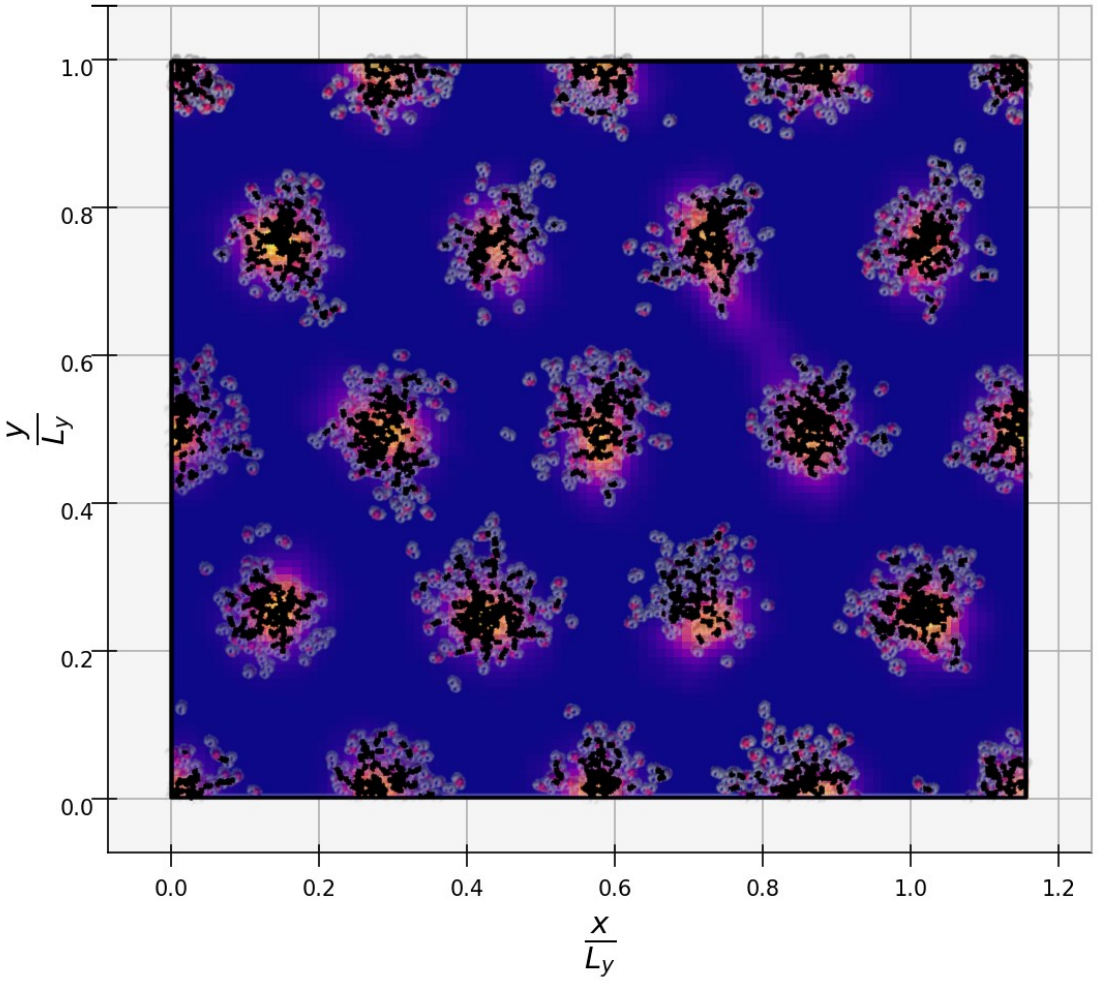

Figure 83 ***WaterMaps_hbonds*** *Probability density map of the water inside the BzNMe3//[BF_4] system with the highest water content. Black dots represent the hydrogen bond network of the single configuration shown beneath.*

Membrane Model with two different Salts

The final step in the modeling of Gallic Acid derivatives membranes is the simulation of a system made of a central slab of columnar ionic channels with a 0.5 M solution of two different salts commonly found in seawater: NaCl and $MgSO_4$. Only one of the three different gallic acid derivatives was chosen to build the membrane model: the $BzNMe_3$ one. The simulated systems appear as in Figure 84**,** where the $MgSO_4$ is dispersed within the aqueous layer**.** In the beginning the charges for the ions of NaCl and $MgSO_4$ salt were taken into account as integer values, -1 and -2 for Cl and SO_4 and +1 ad +2 for Na and Mg respectively. However the electrostatic interactions between ionic pairs of salts were too strong and in the system with $MgSO_4$ a crystal like structure is obtained. For this reason the scaling of the charges by a factor of 0.831 is applied also on the ions of the salts.

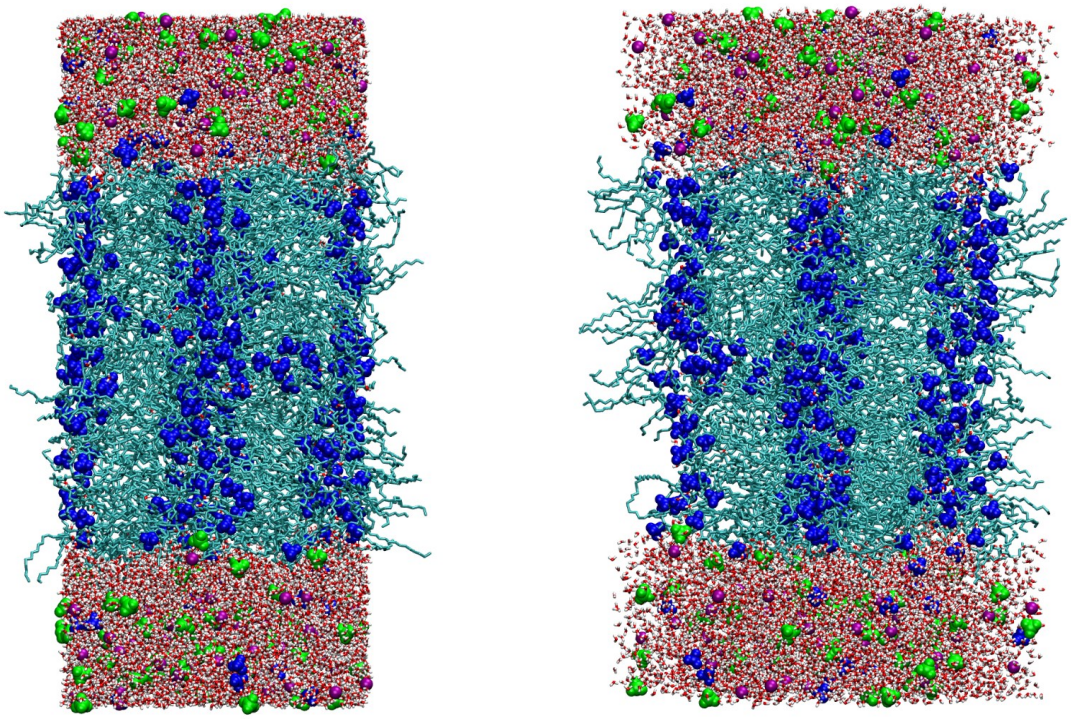

Figure 84 Snapshots of the membrane model for $MgSO_4$ featuring $BzNMe_3$ and $[BF_4]$ as ILCs of the central slab. $BzNMe_3$ cations are depicted in cyan while $[BF_4]$ anions are blue. Water is represented in red and white and inside the water there are dissolved purple spheres and green spheres representing Mg^{++} and SO_4^{2-} ions, respectively. Hydrogens of $BzNMe_3$ are omitted for clarity. Two perspectives of the same box are represeted

Why simulate such salts? As reported in the work of Kato and coworkers [31], the rejection rate of the two salts, NaCl and $MgSO_4$, are 73% and 30%, respectively. This means that 27% of NaCl and 70% of $MgSO_4$ passes through the ionic channels and reaches the opposite end of the columns. This is a curious behaviour since if only geometrical considerations are taken into account it is expected that the Cl^- anion should be more prone to cross the ionic channel than the SO_4^{2-} because of its smaller radius. Moreover, the additional charge on SO_4^{2-} ion should hinder the crossing more than that of Cl^-. Following these reasoning, rejection rate of

$MgSO_4$ should be higher than that of NaCl. Nonetheless, the experimental results go in the opposite direction. To shed light on the mechanisms of ionic crossing these simulations were performed on a long timescale, of about 0.5 μs, for all-atoms simulations. Initial configurations were set with the ionic channels completely empty and the salt dispersed inside the water. The inspection of the produced trajectories does not show any crossing of the salts for the whole duration of the simulations, neither from NaCl or $MgSO_4$, suggesting a rejection rate of 100% for both the salt testes at the different temperatures simulated. Some of the Cl^- ions enter the channel from one end, nonetheless, they escape from the same end some ns after. Some of the $[BF_4]$ anions that made up the ILCs escape the channels and go into the water with no significant destruction of the columnar structure. During July 2023 I participated in the International congress on membranes and membranes processes (ICOM2023), and I had the opportunity to met in person Prof. Kato Takashi which pioneered the field of gallic acid derivatives ILCs for membrane application. The issue of the $[BF_4]$ depletion inside the channel is still not understood and met no experimental evidence, for now. Since the ILCs units are made of polymerized cations and freely moving anions it is possible, for the anions, to go inside water and be solvated. The water, on the contrary, enters the ionic channels and after some time the number of molecules inside the columns stabilizes. The analysis of water's loading inside the ionic channels is evaluated fitting the exponential equation:

$$y = A \cdot (1 - e^{-\frac{t}{\tau}})$$

Counting the number of water molecules inside the channel as a function of simulation time. The parameters A and τ, obtained from the fit, are the mean number of water molecules inside a single ionic channel and the characteristic time of channel's filling. Figure 85 shows the fitted curve, as a dashed red line, and the instantaneous number of water molecules inside the channel at different time intervals as a blue curve.

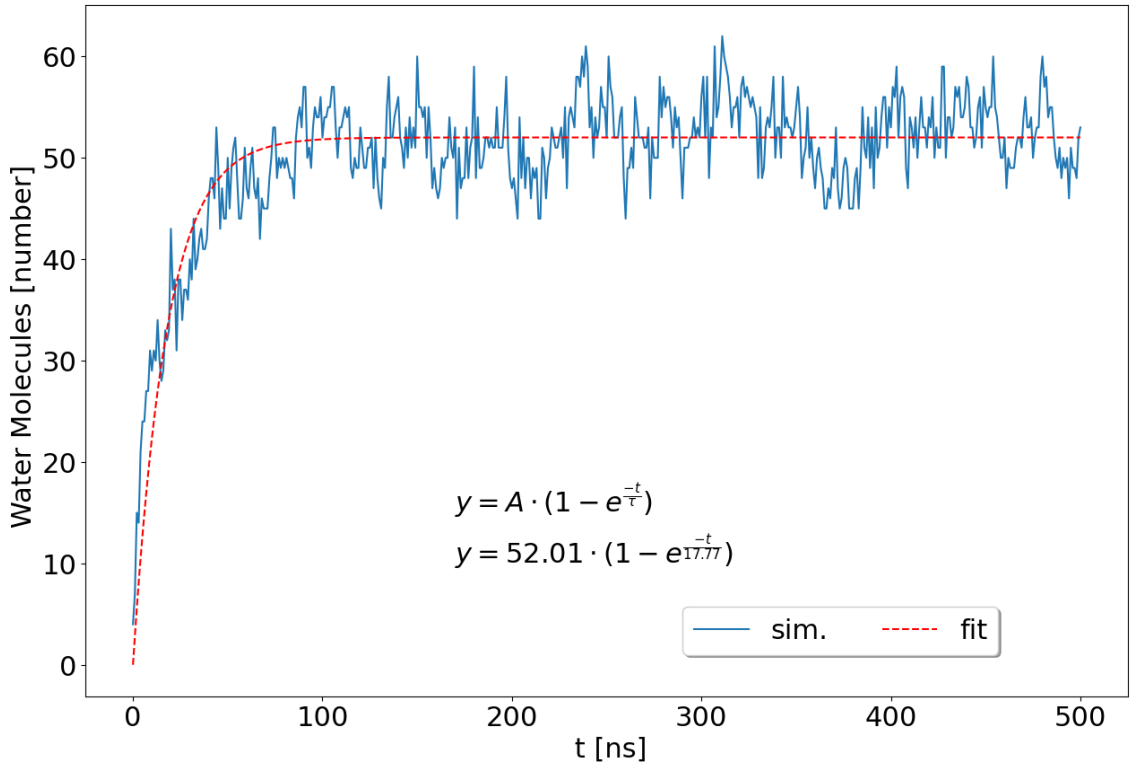

Figure 85 Number of water molecules inside the ionic channel as a function of the simulation time, blue, and exponential fit. This figure refers to the simulation of a membrane containing 4 columns with $MgSO_4$ dissolved in water at T=350 K

Parameters A and τ are calculated for the different systems simulated and their values are reported in Table 23 and Table 24 for the NaCl and $MgSO_4$, respectively The values obtained from the simulations of A and τ suggests that the average number of water molecules inside the channel is similar between the systems with NaCl and $MgSO_4$ with the one for the NaCl being slightly higher. Moreover the characteristic time of channel's filling is comparable between the systems with different salts meaning that the ions do not interfere with the water loading inside the columns. The number of water molecules inside the channels is comparable with the number of water molecules inside the systems with 0.39 M yet illustrated.

$BzNMe_3/[BF_4]$ (4 columns) NaCl (full charge)	A	τ
T= 350 K	60.54	11.01
T= 400 K	74.51	3.4
$BzNMe_3/[BF_4]$ (4 columns) NaCl (scaled charge)		
T= 300 K	55.31	76.25
T= 350 K	61.8	14.84
T= 400 K	77.43	3.61
Extended $BzNMe_3/[BF_4]$ (16 columns) NaCl (scaled charge)		
T= 350 K	58.63	11.59
T= 400 K	75.55	2.4

Table 23 Parameter of the exponential fit obtained from the simulation at different conditions: full and scaled charges for the systems containing only 4 columns and scaled charges for the extended systems containing 16 columns

$BzNMe_3/[BF_4]$ (4 columns) $MgSO_4$ (scaled charge)	A	τ
T= 300 K	45.18	62.63
T= 350 K	52.01	17.77
T= 400 K	64.29	3.7
Extended $BzNMe_3/[BF_4]$ (16 columns) $MgSO_4$ (scaled charge)		
T= 350 K	64.11	13.85
T= 400 K	84.8	2.11

Table 24 Parameter of the exponential fit obtained from the simulation at different conditions: systems containing only 4 columns and for the extended systems containing 16 columns. Just the scaled charges of $MgSO_4$ are considered here.

Conclusion

During the PhD course I had the opportunity to start and develop a project, from scratch, on the study of the ordered phases of ILCs. Most of the studies pursued, presented in this thesis, were propaedeutic to the simulations and analysis of the systems based on gallic acid derivatives. Nonetheless, they have their own worth alone and for some of them an article has been published.

Starting with the *n*-alkanes systems, the densities obtained as a function of temperature and as a function of different chain's length are reproduced quantitatively. Dynamical properties, like the diffusion coefficients, were found to be in agreement with the experimental values. The obtained chemical shifts of ^{129}Xe on extracted clusters is evaluated and compared with experiments providing an overestimation of the calculated chemical shifts, with respect to the experimental one, of about 60 ppm. The overestimation of calculated chemical shifts is found also in the different systems investigated, dihalomethanes and Xe@PIM-EA-TB, thus the protocol employed provides a systematic shift at higher chemical shifts values obtained from calculations due to the compromise of the selected level of theory employed in the DFT calculations and the performance in the calculations ascribed to the computational time. The study of the chemical shifts of ^{129}Xe in different dihalomethanes was published in the second year of my PhD and was a joint study conducted with the group of Prof. Castiglione [107] which provided the experimental measurements. The study of Xe@PIM-EA-TB was a fully computational study in collaboration with dr. Tocci which was conducted in the headquarters of ITM-CNR in Rende, Italy. We plan to publish the results of this study in a paper which is in preparation. Here the effect of the ^{129}Xe is rationalized by evaluating the mean dimension of the pocket in which the xenon atom is found. Also for these systems the calculated values appear to give an overestimation of the chemical shift values which is ascribed to the systematic error of the method and it is rationalized bearing in mind the results obtained for simpler systems. By doing so, the chemical shift values appear comparable to the experimental values.

The results of ^{125}Te chemical shifts for different organutellurium halides provided a good protocol in the calculation of NMR spectroscopic properties over a broad range of compounds and functionals tested

The analysis on the mixtures of uncharged GB and LJ particles highlighted the demixing behavior of alike-particles for systems with excess of non nematogenic particles. The determination of a liquid crystalline phase and an isotropic phase within the simulation box and their discrimination was a task I put effort into during the first year of my PhD course. The result of this study was, later, published at the end of the first year of my PhD [130]. This study was a preliminary study to set the reference for the successive study in which also the electrostatic interactions were considered. During the second year of my PhD course we published a paper concerning the simulations of charged stoichiometric mixtures of GB and LJ particles with different charges [131]. The results produced show significant changes compared to the uncharged systems. The phases explored were different and the effect of the charges was to disfavors the separation of alike-particles producing nematic regions intercalated by spheres of layer, in the case of systems with excess of LJ particles, or twisted nematic phase composed of units made of two disks and a sphere, like in the case of the system GB:LJ =2:1 and $q^*_{GB} = 2.00$. Moreover the phase behaviour as a function of temperature is evaluated for both the uncharged and charged systems, providing a reduced temperature window of nematogenic existence for the systems simulated with the highest charges.

During the second year of my PhD course I worked on the simulation and analysis of imidazolium based ionic liquids with different alkyl content and the results are published in a paper in collaboration with Prof. Wang [119]. The results obtained are consistent with the experimental results providing a quantitative agreement on the existence and position of the pre-peak in the structure factor, which arises from the modulation of the ionic domains inside

the systems operated by the lipophilic alkyl domains acting as spacers, this feature is also found in the gallic acid derivatives systems. The dynamical properties were rationalized in terms of diffusion coefficients, which follow a simple viscosity dependence on the mixture composition. The growing network of polar domains and alkyl chain aggregates does not seem to impact the diffusion of cations and anions except for the increased viscosity of the mixture. The gallic acid derivative systems results are not included in any published paper, however a manuscript is in preparation for the results concerning smaller and bigger systems simulation which describes the approach adopted for the building of the columnar systems and the FF parameter employed in the simulations. The main results concerning these systems are the effectiveness of scaling the partial atomic charges which led to an almost quantitative agreement between the transition temperature from columnar phase to isotropic phase. Another important result is the establishment of a hexagonal columnar phase from an high-temperature isotropic melt retrieving back the correct arrangement of molecules within the systems, a typical behaviour of thermotropic LCs. The microstructural close-range ordering of the anion-cation pairs in different systems is evaluated and linked to the dimension of the channels which are in agreement with experimental data. The effect of hydration on ionic columns is evaluated, suggesting that the morphology of the channel varies as the content of water is changed. The behaviour of water inside the channel is different among the hydrated systems with the low water content systems possessing a confined water behaviour inside the channel while for the high content water systems the water behaves like bulk water in the inside. Diffusion coefficients were determined and their planar and longitudinal components were analyzed suggesting an enhancement of transport properties along the columnar axis as expected for such structures. The effect of another anion different from [BF_4] is evaluated in all the system, suggesting that the more hydrophilic Cl^- anion interferes with the close range ordering of the units. Moreover, the water dynamics inside the channels is slowed down in the presence of Cl^-.

The model of a membrane gives the characteristic time of channels' filling and the average number of water molecules that reside inside the channels which is in agreement with the aforementioned simulation of bulk-like systems, reported in the All atom simulations of anisotropic ILCs based on Gallic Acid derivatives Section. However no ions cross the channel, as expected by the experiments, nor for NaCl nor for $MgSO_4$. This study poses the basis for further studies on the behaviour of the membrane since the FF building was pursued from scratch giving results in good agreement with experimental results.

References

[1] K. Salikolimi, A. A. Sudhakar, and Y. Ishida, “Functional Ionic Liquid Crystals,” *Langmuir*, vol. 36, no. 40, pp. 11702–11731, Oct. 2020, doi: 10.1021/acs.langmuir.0c01935.

[2] T. Ichikawa *et al.*, “Induction of Thermotropic Bicontinuous Cubic Phases in Liquid-Crystalline Ammonium and Phosphonium Salts,” *J Am Chem Soc*, vol. 134, no. 5, pp. 2634–2643, Feb. 2012, doi: 10.1021/ja209010m.

[3] T. Sakamoto *et al.*, “Development of Nanostructured Water Treatment Membranes Based on Thermotropic Liquid Crystals: Molecular Design of Sub-Nanoporous Materials,” *Advanced Science*, vol. 5, no. 1, Jan. 2018, doi: 10.1002/advs.201700405.

[4] G. Saielli and K. Satoh, “A coarse-grained model of ionic liquid crystals: the effect of stoichiometry on the stability of the ionic nematic phase,” *Physical Chemistry Chemical Physics*, vol. 21, no. 36, pp. 20327–20337, 2019, doi: 10.1039/C9CP03296G.

[5] T. Margola, K. Satoh, and G. Saielli, “Comparison of the Mesomorphic Behaviour of 1:1 and 1:2 Mixtures of Charged Gay-Berne GB(4.4,20.0,1,1) and Lennard-Jones Particles,” *Crystals (Basel)*, vol. 8, no. 10, p. 371, Sep. 2018, doi: 10.3390/cryst8100371.

[6] G. Saielli, T. Margola, and K. Satoh, “Tuning Coulombic interactions to stabilize nematic and smectic ionic liquid crystal phases in mixtures of charged soft ellipsoids and spheres,” *Soft Matter*, vol. 13, no. 30, pp. 5204–5213, 2017, doi: 10.1039/C7SM00612H.

[7] T. Margola, G. Saielli, and K. Satoh, “MD simulations of mixtures of charged Gay-Berne and Lennard-Jones particles as models of ionic liquid crystals,” *Molecular Crystals and Liquid Crystals*, vol. 649, no. 1, pp. 50–58, May 2017, doi: 10.1080/15421406.2017.1303918.

[8] W. L. Jorgensen, D. S. Maxwell, and J. Tirado-Rives, “Development and Testing of the OPLS All-Atom Force Field on Conformational Energetics and Properties of Organic Liquids,” *J Am Chem Soc*, vol. 118, no. 45, pp. 11225–11236, Nov. 1996, doi: 10.1021/ja9621760.

[9] Lindahl, Abraham, Hess, and van der Spoel, “GROMACS 2020.7 Source code,” Feb. 2022, doi: 10.5281/ZENODO.5938877.

[10] H. J. C. Berendsen, D. van der Spoel, and R. van Drunen, “GROMACS: A message-passing parallel molecular dynamics implementation,” *Comput Phys Commun*, vol. 91, no. 1–3, pp. 43–56, Sep. 1995, doi: 10.1016/0010-4655(95)00042-E.

[11] M. J. Abraham *et al.*, “GROMACS: High performance molecular simulations through multi-level parallelism from laptops to supercomputers,” *SoftwareX*, vol. 1–2, pp. 19–25, Sep. 2015, doi: 10.1016/j.softx.2015.06.001.

[12] S. W. I. Siu, K. Pluhackova, and R. A. Böckmann, “Optimization of the OPLS-AA Force Field for Long Hydrocarbons,” *J Chem Theory Comput*, vol. 8, no. 4, pp. 1459–1470, Apr. 2012, doi: 10.1021/ct200908r.

[13] M. Bohn, J. Fischer, and F. Kohler, “Prediction of excess properties for liquid mixtures: results from perturbation theory for mixtures with linear molecules,”

Fluid Phase Equilib, vol. 31, no. 3, pp. 233–252, Jan. 1986, doi: 10.1016/0378-3812(86)87010-8.

[14] H. J. C. Berendsen, J. P. M. Postma, W. F. van Gunsteren, A. DiNola, and J. R. Haak, “Molecular dynamics with coupling to an external bath,” *J Chem Phys*, vol. 81, no. 8, pp. 3684–3690, Oct. 1984, doi: 10.1063/1.448118.

[15] G. Bussi, D. Donadio, and M. Parrinello, “Canonical sampling through velocity rescaling,” *J Chem Phys*, vol. 126, no. 1, Jan. 2007, doi: 10.1063/1.2408420.

[16] L. Martínez, R. Andrade, E. G. Birgin, and J. M. Martínez, “P <scp>ACKMOL</scp> : A package for building initial configurations for molecular dynamics simulations,” *J Comput Chem*, vol. 30, no. 13, pp. 2157–2164, Oct. 2009, doi: 10.1002/jcc.21224.

[17] W. L. Jorgensen and J. Tirado-Rives, “Potential energy functions for atomic-level simulations of water and organic and biomolecular systems,” *Proceedings of the National Academy of Sciences*, vol. 102, no. 19, pp. 6665–6670, May 2005, doi: 10.1073/pnas.0408037102.

[18] L. S. Dodda, I. Cabeza de Vaca, J. Tirado-Rives, and W. L. Jorgensen, “LigParGen web server: an automatic OPLS-AA parameter generator for organic ligands,” *Nucleic Acids Res*, vol. 45, no. W1, pp. W331–W336, Jul. 2017, doi: 10.1093/nar/gkx312.

[19] Berk Hess, Henk Bekker, Herman J. C. Berendsen, and Johannes G. E. M. Fraaije, “ LINCS: A linear constraint solver for molecular simulations ,” *J Comput Chem*, vol. 18, no. 12, pp. 1463–1472, 1998.

[20] V. Mazzilli, Y. Wang, and G. Saielli, “Correction: The structuring effect of the alkyl domains on the polar network of ionic liquid mixtures: a molecular dynamics study,” *Physical Chemistry Chemical Physics*, vol. 24, no. 45, pp. 28080–28080, 2022, doi: 10.1039/D2CP90215J.

[21] T. Köddermann, D. Paschek, and R. Ludwig, “Molecular Dynamic Simulations of Ionic Liquids: A Reliable Description of Structure, Thermodynamics and Dynamics,” *ChemPhysChem*, vol. 8, no. 17, pp. 2464–2470, Dec. 2007, doi: 10.1002/cphc.200700552.

[22] J. N. Canongia Lopes and A. A. H. Pádua, “Molecular Force Field for Ionic Liquids III: Imidazolium, Pyridinium, and Phosphonium Cations; Chloride, Bromide, and Dicyanamide Anions,” *J Phys Chem B*, vol. 110, no. 39, pp. 19586–19592, Oct. 2006, doi: 10.1021/jp063901o.

[23] Dassault Systèmes, “BIOVIA.” Dassault Systèmes, San Diego, 2019.

[24] H. Sun, “COMPASS: An ab Initio Force-Field Optimized for Condensed-Phase ApplicationsOverview with Details on Alkane and Benzene Compounds,” *J Phys Chem B*, vol. 102, no. 38, pp. 7338–7364, Sep. 1998, doi: 10.1021/jp980939v.

[25] D. N. Theodorou and U. W. Suter, “Atomistic modeling of mechanical properties of polymeric glasses,” *Macromolecules*, vol. 19, no. 1, pp. 139–154, Jan. 1986, doi: 10.1021/ma00155a022.

[26] D. N. Theodorou and U. W. Suter, “Detailed molecular structure of a vinyl polymer glass,” *Macromolecules*, vol. 18, no. 7, pp. 1467–1478, Jul. 1985, doi: 10.1021/ma00149a018.

[27] M. Heuchel, D. Fritsch, P. M. Budd, N. B. McKeown, and D. Hofmann, “Atomistic packing model and free volume distribution of a polymer with intrinsic

microporosity (PIM-1)," *J Memb Sci*, vol. 318, no. 1–2, pp. 84–99, Jun. 2008, doi: 10.1016/j.memsci.2008.02.038.
[28] E. Tocci *et al.*, "Molecular Modeling and Gas Permeation Properties of a Polymer of Intrinsic Microporosity Composed of Ethanoanthracene and Tröger's Base Units," *Macromolecules*, vol. 47, no. 22, pp. 7900–7916, Nov. 2014, doi: 10.1021/ma501469m.
[29] A. J. Stone, "Distributed multipole analysis, or how to describe a molecular charge distribution," *Chem Phys Lett*, vol. 83, no. 2, pp. 233–239, Oct. 1981, doi: 10.1016/0009-2614(81)85452-8.
[30] X. Feng *et al.*, "Scalable Fabrication of Polymer Membranes with Vertically Aligned 1 nm Pores by Magnetic Field Directed Self-Assembly," *ACS Nano*, vol. 8, no. 12, pp. 11977–11986, Dec. 2014, doi: 10.1021/nn505037b.
[31] T. Sakamoto *et al.*, "Development of Nanostructured Water Treatment Membranes Based on Thermotropic Liquid Crystals: Molecular Design of Sub-Nanoporous Materials," *Advanced Science*, vol. 5, no. 1, Jan. 2018, doi: 10.1002/advs.201700405.
[32] C. M. Breneman and K. B. Wiberg, "Determining atom-centered monopoles from molecular electrostatic potentials. The need for high sampling density in formamide conformational analysis," *J Comput Chem*, vol. 11, no. 3, pp. 361–373, Apr. 1990, doi: 10.1002/jcc.540110311.
[33] MJ Frisch, GW Trucks, and HB Schlegel, "Gaussian 16." Gaussian Inc., Wallingford, 2016.
[34] G. A. Petersson, A. Bennett, T. G. Tensfeldt, M. A. Al-Laham, W. A. Shirley, and J. Mantzaris, "A complete basis set model chemistry. I. The total energies of closed-shell atoms and hydrides of the first-row elements," *J Chem Phys*, vol. 89, no. 4, pp. 2193–2218, Aug. 1988, doi: 10.1063/1.455064.
[35] G. A. Petersson and M. A. Al-Laham, "A complete basis set model chemistry. II. Open-shell systems and the total energies of the first-row atoms," *J Chem Phys*, vol. 94, no. 9, pp. 6081–6090, May 1991, doi: 10.1063/1.460447.
[36] M. J. Frisch, M. Head-Gordon, and J. A. Pople, "A direct MP2 gradient method," *Chem Phys Lett*, vol. 166, no. 3, pp. 275–280, Feb. 1990, doi: 10.1016/0009-2614(90)80029-D.
[37] M. J. Frisch, M. Head-Gordon, and J. A. Pople, "Semi-direct algorithms for the MP2 energy and gradient," *Chem Phys Lett*, vol. 166, no. 3, pp. 281–289, Feb. 1990, doi: 10.1016/0009-2614(90)80030-H.
[38] S. Sæbø and J. Almlöf, "Avoiding the integral storage bottleneck in LCAO calculations of electron correlation," *Chem Phys Lett*, vol. 154, no. 1, pp. 83–89, Jan. 1989, doi: 10.1016/0009-2614(89)87442-1.
[39] M. Head-Gordon and T. Head-Gordon, "Analytic MP2 frequencies without fifth-order storage. Theory and application to bifurcated hydrogen bonds in the water hexamer," *Chem Phys Lett*, vol. 220, no. 1–2, pp. 122–128, Mar. 1994, doi: 10.1016/0009-2614(94)00116-2.
[40] M. Head-Gordon, J. A. Pople, and M. J. Frisch, "MP2 energy evaluation by direct methods," *Chem Phys Lett*, vol. 153, no. 6, pp. 503–506, Dec. 1988, doi: 10.1016/0009-2614(88)85250-3.
[41] T. H. Dunning, "Gaussian basis sets for use in correlated molecular calculations. I. The atoms boron through neon and hydrogen," *J Chem Phys*, vol. 90, no. 2, pp. 1007–1023, Jan. 1989, doi: 10.1063/1.456153.

[42] R. A. Kendall, T. H. Dunning, and R. J. Harrison, “Electron affinities of the first-row atoms revisited. Systematic basis sets and wave functions,” *J Chem Phys*, vol. 96, no. 9, pp. 6796–6806, May 1992, doi: 10.1063/1.462569.
[43] Y. Ishii, N. Matubayasi, G. Watanabe, T. Kato, and H. Washizu, “Molecular insights on confined water in the nanochannels of self-assembled ionic liquid crystal,” *Sci Adv*, vol. 7, no. 31, Jul. 2021, doi: 10.1126/sciadv.abf0669.
[44] S. V. Sambasivarao and O. Acevedo, “Development of OPLS-AA Force Field Parameters for 68 Unique Ionic Liquids,” *J Chem Theory Comput*, vol. 5, no. 4, pp. 1038–1050, Apr. 2009, doi: 10.1021/ct900009a.
[45] R. K. Mishra, K. Kanhaiya, J. J. Winetrout, R. J. Flatt, and H. Heinz, “Force field for calcium sulfate minerals to predict structural, hydration, and interfacial properties,” *Cem Concr Res*, vol. 139, p. 106262, Jan. 2021, doi: 10.1016/j.cemconres.2020.106262.
[46] M. A. Bates and G. R. Luckhurst, “Computer simulation studies of anisotropic systems. XXVI. Monte Carlo investigations of a Gay–Berne discotic at constant pressure,” *J Chem Phys*, vol. 104, no. 17, pp. 6696–6709, May 1996, doi: 10.1063/1.471387.
[47] R. Berardi, C. Fava, and C. Zannoni, “A Gay–Berne potential for dissimilar biaxial particles,” *Chem Phys Lett*, vol. 297, no. 1–2, pp. 8–14, Nov. 1998, doi: 10.1016/S0009-2614(98)01090-2.
[48] W. M. Brown, M. K. Petersen, S. J. Plimpton, and G. S. Grest, “Liquid crystal nanodroplets in solution,” *J Chem Phys*, vol. 130, no. 4, Jan. 2009, doi: 10.1063/1.3058435.
[49] S. Nosé, “A molecular dynamics method for simulations in the canonical ensemble,” *Mol Phys*, vol. 52, no. 2, pp. 255–268, Jun. 1984, doi: 10.1080/00268978400101201.
[50] W. G. Hoover, “Canonical dynamics: Equilibrium phase-space distributions,” *Phys Rev A (Coll Park)*, vol. 31, no. 3, pp. 1695–1697, Mar. 1985, doi: 10.1103/PhysRevA.31.1695.
[51] R. W. Hockney and J. W. Eastwood, *Computer Simulation Using Particles*. CRC Press, 2021. doi: 10.1201/9780367806934.
[52] E.J. Baerends *et al.*, “ADF2017.” SCM, Vrije Universiteit, Amsterdam, 2017.
[53] G. te Velde *et al.*, “Chemistry with ADF,” *J Comput Chem*, vol. 22, no. 9, pp. 931–967, Jul. 2001, doi: 10.1002/jcc.1056.
[54] E. van Lenthe, E. J. Baerends, and J. G. Snijders, “Relativistic total energy using regular approximations,” *J Chem Phys*, vol. 101, no. 11, pp. 9783–9792, Dec. 1994, doi: 10.1063/1.467943.
[55] E. van Lenthe, A. Ehlers, and E.-J. Baerends, “Geometry optimizations in the zero order regular approximation for relativistic effects,” *J Chem Phys*, vol. 110, no. 18, pp. 8943–8953, May 1999, doi: 10.1063/1.478813.
[56] E. van Lenthe, R. van Leeuwen, E. J. Baerends, and J. G. Snijders, “Relativistic regular two-component Hamiltonians,” *Int J Quantum Chem*, vol. 57, no. 3, pp. 281–293, 1996.
[57] E. van Lenthe, J. G. Snijders, and E. J. Baerends, “The zero-order regular approximation for relativistic effects: The effect of spin–orbit coupling in closed shell molecules,” *J Chem Phys*, vol. 105, no. 15, pp. 6505–6516, Oct. 1996, doi: 10.1063/1.472460.

[58] G. Saielli, A. Bagno, F. Castiglione, R. Simonutti, M. Mauri, and A. Mele, “Understanding Cage Effects in Imidazolium Ionic Liquids by ^{129}Xe NMR: MD Simulations and Relativistic DFT Calculations,” *J Phys Chem B*, vol. 118, no. 48, pp. 13963–13968, Dec. 2014, doi: 10.1021/jp511207s.

[59] A. Bagno and G. Saielli, “DFT Study of the NMR Properties of Xenon in Covalent Compounds and van der Waals Complexes—Implications for the Use of 129Xe as a Molecular Probe,” *Chemistry - A European Journal*, vol. 9, no. 7, pp. 1486–1495, Apr. 2003, doi: 10.1002/chem.200390168.

[60] A. D. Becke, “Density-functional exchange-energy approximation with correct asymptotic behavior,” *Phys Rev A (Coll Park)*, vol. 38, no. 6, pp. 3098–3100, Sep. 1988, doi: 10.1103/PhysRevA.38.3098.

[61] C. Lee, W. Yang, and R. G. Parr, “Development of the Colle-Salvetti correlation-energy formula into a functional of the electron density,” *Phys Rev B*, vol. 37, no. 2, pp. 785–789, Jan. 1988, doi: 10.1103/PhysRevB.37.785.

[62] B. G. Johnson, P. M. W. Gill, and J. A. Pople, “The performance of a family of density functional methods,” *J Chem Phys*, vol. 98, no. 7, pp. 5612–5626, Apr. 1993, doi: 10.1063/1.464906.

[63] T. V. Russo, R. L. Martin, and P. J. Hay, “Density functional calculations on first-row transition metals,” *J Chem Phys*, vol. 101, no. 9, pp. 7729–7737, Nov. 1994, doi: 10.1063/1.468265.

[64] M. Straka, P. Lantto, and J. Vaara, “Toward Calculations of the ^{129}Xe Chemical Shift in Xe@C_{60} at Experimental Conditions: Relativity, Correlation, and Dynamics,” *J Phys Chem A*, vol. 112, no. 12, pp. 2658–2668, Mar. 2008, doi: 10.1021/jp711674y.

[65] M. Swart, A. W. Ehlers, and K. Lammertsma *, “Performance of the OPBE exchange-correlation functional,” *Mol Phys*, vol. 102, no. 23–24, pp. 2467–2474, Dec. 2004, doi: 10.1080/00268970420002750 17.

[66] F. Zaccaria, L. P. Wolters, C. Fonseca Guerra, and L. Orian, “Insights on selenium and tellurium diaryldichalcogenides: A benchmark DFT study,” *J Comput Chem*, vol. 37, no. 18, pp. 1672–1680, Jul. 2016, doi: 10.1002/jcc.24383.

[67] A. D. Becke, “Density-functional exchange-energy approximation with correct asymptotic behavior,” *Phys Rev A (Coll Park)*, vol. 38, no. 6, pp. 3098–3100, Sep. 1988, doi: 10.1103/PhysRevA.38.3098.

[68] J. P. Perdew, “Density-functional approximation for the correlation energy of the inhomogeneous electron gas,” *Phys Rev B*, vol. 33, no. 12, pp. 8822–8824, Jun. 1986, doi: 10.1103/PhysRevB.33.8822.

[69] T. W. Keal and D. J. Tozer, “The exchange-correlation potential in Kohn–Sham nuclear magnetic resonance shielding calculations,” *J Chem Phys*, vol. 119, no. 6, pp. 3015–3024, Aug. 2003, doi: 10.1063/1.1590634.

[70] C. Adamo and V. Barone, “Exchange functionals with improved long-range behavior and adiabatic connection methods without adjustable parameters: The mPW and mPW1PW models,” *J Chem Phys*, vol. 108, no. 2, pp. 664–675, Jan. 1998, doi: 10.1063/1.475428.

[71] J. P. Perdew *et al.*, “Atoms, molecules, solids, and surfaces: Applications of the generalized gradient approximation for exchange and correlation,” *Phys Rev B*, vol. 46, no. 11, pp. 6671–6687, Sep. 1992, doi: 10.1103/PhysRevB.46.6671.

[72] T. V. Russo, R. L. Martin, and P. J. Hay, “Density functional calculations on first-row transition metals,” *J Chem Phys*, vol. 101, no. 9, pp. 7729–7737, Nov. 1994, doi: 10.1063/1.468265.
[73] B. G. Johnson, P. M. W. Gill, and J. A. Pople, “The performance of a family of density functional methods,” *J Chem Phys*, vol. 98, no. 7, pp. 5612–5626, Apr. 1993, doi: 10.1063/1.464906.
[74] C. Lee, W. Yang, and R. G. Parr, “Development of the Colle-Salvetti correlation-energy formula into a functional of the electron density,” *Phys Rev B*, vol. 37, no. 2, pp. 785–789, Jan. 1988, doi: 10.1103/PhysRevB.37.785.
[75] A. D. Becke, “Density-functional exchange-energy approximation with correct asymptotic behavior,” *Phys Rev A (Coll Park)*, vol. 38, no. 6, pp. 3098–3100, Sep. 1988, doi: 10.1103/PhysRevA.38.3098.
[76] M. Swart, M. Solà, and F. M. Bickelhaupt, “Switching between OPTX and PBE exchange functionals,” *Journal of Computational Methods in Sciences and Engineering*, vol. 9, no. 1–2, pp. 69–77, Jul. 2009, doi: 10.3233/JCM-2009-0230.
[77] M. Swart, M. Solà, and F. M. Bickelhaupt, “A new all-round density functional based on spin states and SN2 barriers,” *J Chem Phys*, vol. 131, no. 9, Sep. 2009, doi: 10.1063/1.3213193.
[78] M. Brehm, M. Thomas, S. Gehrke, and B. Kirchner, “TRAVIS—A free analyzer for trajectories from molecular simulation,” *J Chem Phys*, vol. 152, no. 16, Apr. 2020, doi: 10.1063/5.0005078.
[79] M. Brehm and B. Kirchner, “TRAVIS - A Free Analyzer and Visualizer for Monte Carlo and Molecular Dynamics Trajectories,” *J Chem Inf Model*, vol. 51, no. 8, pp. 2007–2023, Aug. 2011, doi: 10.1021/ci200217w.
[80] Y. Wang and G. A. Voth, “Molecular Dynamics Simulations of Polyglutamine Aggregation Using Solvent-Free Multiscale Coarse-Grained Models,” *J Phys Chem B*, vol. 114, no. 26, pp. 8735–8743, Jul. 2010, doi: 10.1021/jp1007768.
[81] D. R. Nelson and B. I. Halperin, “Dislocation-mediated melting in two dimensions,” *Phys Rev B*, vol. 19, no. 5, pp. 2457–2484, Mar. 1979, doi: 10.1103/PhysRevB.19.2457.
[82] E. K. Lindenberg and G. N. Patey, “Melting point trends and solid phase behaviors of model salts with ion size asymmetry and distributed cation charge,” *J Chem Phys*, vol. 143, no. 2, Jul. 2015, doi: 10.1063/1.4923344.
[83] M. Brehm, H. Weber, M. Thomas, O. Hollóczki, and B. Kirchner, “Domain Analysis in Nanostructured Liquids: A Post-Molecular Dynamics Study at the Example of Ionic Liquids,” *ChemPhysChem*, vol. 16, no. 15, pp. 3271–3277, Oct. 2015, doi: 10.1002/cphc.201500471.
[84] A. P. Thompson *et al.*, “LAMMPS - a flexible simulation tool for particle-based materials modeling at the atomic, meso, and continuum scales,” *Comput Phys Commun*, vol. 271, p. 108171, Feb. 2022, doi: 10.1016/j.cpc.2021.108171.
[85] C. R. Harris *et al.*, “Array programming with NumPy,” *Nature*, vol. 585, no. 7825, pp. 357–362, Sep. 2020, doi: 10.1038/s41586-020-2649-2.
[86] P. Virtanen *et al.*, “SciPy 1.0: fundamental algorithms for scientific computing in Python,” *Nat Methods*, vol. 17, no. 3, pp. 261–272, Mar. 2020, doi: 10.1038/s41592-019-0686-2.
[87] N. Michaud-Agrawal, E. J. Denning, T. B. Woolf, and O. Beckstein, “MDAnalysis: A toolkit for the analysis of molecular dynamics simulations,” *J*

Comput Chem, vol. 32, no. 10, pp. 2319–2327, Jul. 2011, doi: 10.1002/jcc.21787.
[88] R. Gowers *et al.*, “MDAnalysis: A Python Package for the Rapid Analysis of Molecular Dynamics Simulations,” 2016, pp. 98–105. doi: 10.25080/Majora-629e541a-00e.
[89] W. Humphrey, A. Dalke, and K. Schulten, “VMD: Visual molecular dynamics,” *J Mol Graph*, vol. 14, no. 1, pp. 33–38, Feb. 1996, doi: 10.1016/0263-7855(96)00018-5.
[90] A. T. Gabriel, T. Meyer, and G. Germano, “Molecular Graphics of Convex Body Fluids,” *J Chem Theory Comput*, vol. 4, no. 3, pp. 468–476, Mar. 2008, doi: 10.1021/ct700192z.
[91] The GIMP development Team, “GIMP.” The GIMP development Team, 2019. Accessed: Oct. 01, 2023. [Online]. Available: https://www.gimp.org
[92] “C3P.” Accessed: Oct. 01, 2023. [Online]. Available: http://wwwdisc.chimica.unipd.it/c3p-wiki/index.php/C3P
[93] “CINECA g100.” Accessed: Oct. 01, 2023. [Online]. Available: https://www.hpc.cineca.it/hardware/galileo100
[94] “CINECA m100”, Accessed: Oct. 01, 2023. [Online]. Available: https://www.hpc.cineca.it/hardware/galileo100
[95] “CloudVeneto.” Accessed: Oct. 01, 2023. [Online]. Available: http://userguide.cloudveneto.it/en/latest/
[96] W. D. Cornell *et al.*, “A Second Generation Force Field for the Simulation of Proteins, Nucleic Acids, and Organic Molecules,” *J Am Chem Soc*, vol. 117, no. 19, pp. 5179–5197, May 1995, doi: 10.1021/ja00124a002.
[97] A. Aucejo, M. C. Burguet, R. Munoz, and J. L. Marques, “Densities, Viscosities, and Refractive Indices of Some n-Alkane Binary Liquid Systems at 298.15 K,” *J Chem Eng Data*, vol. 40, no. 1, pp. 141–147, Jan. 1995, doi: 10.1021/je00017a032.
[98] I. Cibulka, “Saturated liquid densities of 1-alkanols from C1 to c10 and n-alkanes from C5 to C16: A critical evaluation of experimental data,” *Fluid Phase Equilib*, vol. 89, no. 1, pp. 1–18, Aug. 1993, doi: 10.1016/0378-3812(93)85042-K.
[99] ESDU international, “Critical densities on n-alkanes.” Accessed: Oct. 01, 2023. [Online]. Available: https://www.esdu.com/cgi-bin/ps.pl?sess=unlicensed_1230913145507wdm&t=doc&p=esdu_87010a
[100] D. Ambrose and J. Walton, “Vapour pressures up to their critical temperatures of normal alkanes and 1-alkanols,” *Pure and Applied Chemistry*, vol. 61, no. 8, pp. 1395–1403, Jan. 1989, doi: 10.1351/pac198961081395.
[101] D. C. Douglass and D. W. McCall, “Diffusion in Paraffin Hydrocarbons,” *J Phys Chem*, vol. 62, no. 9, pp. 1102–1107, Sep. 1958, doi: 10.1021/j150567a020.
[102] J. Winkelmann, “Self-diffusion coefficient of hexane,” in *Diffusion in Gases, Liquids and Electrolytes*, Berlin, Heidelberg: Springer Berlin Heidelberg, 2017, pp. 299–302. doi: 10.1007/978-3-540-73735-3_167.
[103] M. Holz, S. R. Heil, and A. Sacco, “Temperature-dependent self-diffusion coefficients of water and six selected molecular liquids for calibration in accurate 1H NMR PFG measurements,” *Physical Chemistry Chemical Physics*, vol. 2, no. 20, pp. 4740–4742, 2000, doi: 10.1039/b005319h.

[104] M. Holz and H. Weingartner, “Calibration in accurate spin-echo self-diffusion measurements using 1H and less-common nuclei,” *Journal of Magnetic Resonance (1969)*, vol. 92, no. 1, pp. 115–125, Mar. 1991, doi: 10.1016/0022-2364(91)90252-O.
[105] G. L. Pollack, R. P. Kennan, J. F. Himm, and D. R. Stump, “Diffusion of xenon in liquid alkanes: Temperature dependence measurements with a new method. Stokes–Einstein and hard sphere theories,” *J Chem Phys*, vol. 92, no. 1, pp. 625–630, Jan. 1990, doi: 10.1063/1.458413.
[106] P. Morgado, R. Bonifácio, L. F. G. Martins, and E. J. M. Filipe, “Probing the Structure of Liquids with ^{129} Xe NMR Spectroscopy: *n* -Alkanes, Cycloalkanes, and Branched Alkanes,” *J Phys Chem B*, vol. 117, no. 30, pp. 9014–9024, Aug. 2013, doi: 10.1021/jp4060507.
[107] M. Boventi, V. Mazzilli, R. Simonutti, F. Castiglione, and G. Saielli, “Exploring the structure of halomethanes with xenon: An NMR and MD investigation,” *J Mol Liq*, vol. 382, p. 122011, Jul. 2023, doi: 10.1016/j.molliq.2023.122011.
[108] S. Valkai, J. Liszi, and I. Szalai, “Temperature dependence of the refractive index for three chloromethane liquids at 514.5 nm and 632.8 nm wavelengths,” *J Chem Thermodyn*, vol. 30, no. 7, pp. 825–832, Jul. 1998, doi: 10.1006/jcht.1998.0349.
[109] OxyChem, “Methylene chloride Temperature vs. Density Table.” Accessed: Oct. 01, 2023. [Online]. Available: https://www.oxy.com/globalassets/documents/chemicals/products/chlorinated-organics/tech-methylene_chloride_temp-density_table.pdf
[110] A. Reddy, H. Nagar, B. Satyavathi, and V. Aniya, “Phase equilibria and thermophysical properties of dibromomethane: Measurement and correlation studies,” *J Mol Liq*, vol. 306, p. 112917, May 2020, doi: 10.1016/j.molliq.2020.112917.
[111] V. Griffing, M. A. Cargyle, L. Corvese, and D. Eby, “Temperature Coefficients of Viscosity of Some Halogen Substituted Organic Compounds,” *J Phys Chem*, vol. 58, no. 11, pp. 1054–1056, Nov. 1954, doi: 10.1021/j150521a032.
[112] Y. H. Lim and A. D. King, “NMR chemical shifts of xenon-129 dissolved in liquid n-alkanes and their mixtures,” *J Phys Chem*, vol. 97, no. 47, pp. 12173–12177, Nov. 1993, doi: 10.1021/j100149a012.
[113] G. A. Casagrande, C. Raminelli, E. S. Lang, and S. de S. Lemos, “A novel organotellurium halide with tellurium presenting mixed oxidation states: Synthesis and structural characterization,” *Inorganica Chim Acta*, vol. 365, no. 1, pp. 492–495, Jan. 2011, doi: 10.1016/j.ica.2010.09.053.
[114] J. P. A. Souza *et al.*, “Synthesis, Mechanism Elucidation and Biological Insights of Tellurium(IV)-Containing Heterocycles,” *Chemistry – A European Journal*, vol. 27, no. 58, pp. 14427–14437, Oct. 2021, doi: 10.1002/chem.202102287.
[115] R. K. Chadha and J. M. Miller, “^{125} Te Fourier transform nuclear magnetic resonance studies of tellurium compounds,” *Can J Chem*, vol. 60, no. 17, pp. 2256–2258, Sep. 1982, doi: 10.1139/v82-320.
[116] C. R. Princival *et al.*, “Stability Study of Hypervalent Tellurium Compounds in Aqueous Solutions,” *ACS Omega*, vol. 2, no. 8, pp. 4431–4439, Aug. 2017, doi: 10.1021/acsomega.7b00628.
[117] J. Beckmann, D. Dakternieks, A. Duthie, C. Mitchell, and M. Schürmann, “Observation of Te…π and X…X Bonding in para-Substituted Diphenyltellurium

Dihalides, (p-Me2NC6H4)(p-YC6H4)TeX2 (X = Cl, Br, I; Y = H, EtO, Me2N)," *Aust J Chem*, vol. 58, no. 2, p. 119, 2005, doi: 10.1071/CH04268.
[118] M. R. Detty, W. C. Lenhart, P. G. Gassman, and M. R. Callstrom, "X-ray photoelectron spectroscopy and tellurium-125 NMR studies of organotellurium compounds. II. Oxatellurolylium halides and dioxatellurapentalenes and their products of oxidative halogen addition," *Organometallics*, vol. 8, no. 4, pp. 866–870, Apr. 1989, doi: 10.1021/om00106a002.
[119] V. Mazzilli, Y. Wang, and G. Saielli, "The structuring effect of the alkyl domains on the polar network of ionic liquid mixtures: a molecular dynamics study," *Physical Chemistry Chemical Physics*, vol. 24, no. 31, pp. 18783–18792, 2022, doi: 10.1039/D2CP02786K.
[120] S. M. Urahata and M. C. C. Ribeiro, "Structure of ionic liquids of 1-alkyl-3-methylimidazolium cations: A systematic computer simulation study," *J Chem Phys*, vol. 120, no. 4, pp. 1855–1863, Jan. 2004, doi: 10.1063/1.1635356.
[121] Y. Wang and G. A. Voth, "Unique Spatial Heterogeneity in Ionic Liquids," *J Am Chem Soc*, vol. 127, no. 35, pp. 12192–12193, Sep. 2005, doi: 10.1021/ja053796g.
[122] J. N. A. Canongia Lopes and A. A. H. Pádua, "Nanostructural Organization in Ionic Liquids," *J Phys Chem B*, vol. 110, no. 7, pp. 3330–3335, Feb. 2006, doi: 10.1021/jp056006y.
[123] A. Triolo, O. Russina, H.-J. Bleif, and E. Di Cola, "Nanoscale Segregation in Room Temperature Ionic Liquids," *J Phys Chem B*, vol. 111, no. 18, pp. 4641–4644, May 2007, doi: 10.1021/jp067705t.
[124] H.-Q. Zhao, R. Shi, and Y.-T. Wang, "Nanoscale Tail Aggregation in Ionic Liquids: Roles of Electrostatic and van der Waals Interactions," *Commun Theor Phys*, vol. 56, no. 3, pp. 499–503, Sep. 2011, doi: 10.1088/0253-6102/56/3/19.
[125] O. Russina, F. Lo Celso, N. V. Plechkova, and A. Triolo, "Emerging Evidences of Mesoscopic-Scale Complexity in Neat Ionic Liquids and Their Mixtures," *J Phys Chem Lett*, vol. 8, no. 6, pp. 1197–1204, Mar. 2017, doi: 10.1021/acs.jpclett.6b02811.
[126] L. GRUNBERG and A. H. NISSAN, "Mixture Law for Viscosity," *Nature*, vol. 164, no. 4175, pp. 799–800, Nov. 1949, doi: 10.1038/164799b0.
[127] A. Noda, K. Hayamizu, and M. Watanabe, "Pulsed-Gradient Spin−Echo ^{1}H and ^{19}F NMR Ionic Diffusion Coefficient, Viscosity, and Ionic Conductivity of Non-Chloroaluminate Room-Temperature Ionic Liquids," *J Phys Chem B*, vol. 105, no. 20, pp. 4603–4610, May 2001, doi: 10.1021/jp004132q.
[128] P. E. Ramírez-González, L. E. Sanchéz-Díaz, M. Medina-Noyola, and Y. Wang, "Communication: Probing the existence of partially arrested states in ionic liquids," *J Chem Phys*, vol. 145, no. 19, Nov. 2016, doi: 10.1063/1.4967518.
[129] M. E. Di Pietro, F. Castiglione, and A. Mele, "Anions as Dynamic Probes for Ionic Liquid Mixtures," *J Phys Chem B*, vol. 124, no. 14, pp. 2879–2891, Apr. 2020, doi: 10.1021/acs.jpcb.0c00026.
[130] V. Mazzilli, K. Satoh, and G. Saielli, "Mixtures of discotic and spherical soft particles: de-mixing, liquid crystal behaviour and relative solubility," *J Mol Liq*, vol. 347, p. 117973, Feb. 2022, doi: 10.1016/j.molliq.2021.117973.

[131] V. Mazzilli, K. Satoh, and G. Saielli, “Phase behaviour of mixtures of charged soft disks and spheres,” *Soft Matter*, vol. 19, no. 18, pp. 3311–3324, 2023, doi: 10.1039/D3SM00223C.
[132] B. Brandl and J. H. Wendorff, “Eutectic mixtures with plastic columnar discotics: molecular structure, phase morphology and kinetics of phase separation,” *Liq Cryst*, vol. 32, no. 5, pp. 553–563, May 2005, doi: 10.1080/02678290500125616.
[133] S. D. Peroukidis, A. G. Vanakaras, and D. J. Photinos, “Liquid crystalline phases and demixing in binary mixtures of shape-anisometric colloids,” *J Mater Chem*, vol. 20, no. 46, p. 10495, 2010, doi: 10.1039/c0jm01692f.
[134] G. Cinacchi, E. Velasco, and L. Mederos, “Entropic segregation in smectic phases of hard-body mixtures,” *Journal of Physics: Condensed Matter*, vol. 16, no. 19, pp. S2003–S2014, May 2004, doi: 10.1088/0953-8984/16/19/012.
[135] “A statistical theory of liquid crystalline mixtures: phase separation,” *Proceedings of the Royal Society of London. A. Mathematical and Physical Sciences*, vol. 352, no. 1668, pp. 41–56, Dec. 1976, doi: 10.1098/rspa.1976.0162.
[136] E. A. Mastny and J. J. de Pablo, “Melting line of the Lennard-Jones system, infinite size, and full potential,” *J Chem Phys*, vol. 127, no. 10, Sep. 2007, doi: 10.1063/1.2753149.
[137] A. K. Singh *et al.*, “Nanosize Carriers for Drug and Vaccine Delivery: Advances and Challenges,” *Nanoscience & Nanotechnology-Asia*, vol. 11, no. 6, Dec. 2021, doi: 10.2174/2210681211666210505115217.
[138] G. C. Ganzenmüller and G. N. Patey, “Charge Ordering Induces a Smectic Phase in Oblate Ionic Liquid Crystals,” *Phys Rev Lett*, vol. 105, no. 13, p. 137801, Sep. 2010, doi: 10.1103/PhysRevLett.105.137801.
[139] F. Smallenburg and M. Dijkstra, “Phase diagram of colloidal spheres in a biaxial electric or magnetic field,” *J Chem Phys*, vol. 132, no. 20, May 2010, doi: 10.1063/1.3425734.
[140] E. G. Noya, I. Kolovos, G. Doppelbauer, G. Kahl, and E. Bianchi, “Phase diagram of inverse patchy colloids assembling into an equilibrium laminar phase,” *Soft Matter*, vol. 10, no. 42, pp. 8464–8474, 2014, doi: 10.1039/C4SM01559B.
[141] Z. Sun, Z. Gong, L. Zheng, P. Kalhor, Z. Huai, and Z. Liu, “Molecular modelling of ionic liquids: General guidelines on fixed-charge force fields for balanced descriptions,” *Journal of Ionic Liquids*, vol. 2, no. 2, p. 100043, Dec. 2022, doi: 10.1016/j.jil.2022.100043.
[142] B. Soberats *et al.*, “Ionic Switch Induced by a Rectangular–Hexagonal Phase Transition in Benzenammonium Columnar Liquid Crystals,” *J Am Chem Soc*, vol. 137, no. 41, pp. 13212–13215, Oct. 2015, doi: 10.1021/jacs.5b09076.